SOLUTION BEHAVIOR AND CHARGE TRANSFER KINETICS OF MACROMOLECULAR RADICALS FOR ENERGY STORAGE

A Dissertation

by

ALEXANDRA DANIELLE EASLEY

Submitted to the Graduate and Professional School of
Texas A&M University
in partial fulfillment of the requirements for the degree of

DOCTOR OF PHILOSOPHY

Chair of Committee,	Jodie L. Lutkenhaus
Committee Members,	Lei Fang
	Emily Pentzer
	Karen L. Wooley
Head of Department,	Ibrahim Karaman

May 2022

Major Subject: Materials Science and Engineering

ABSTRACT

Within a few decades, lithium-ion batteries (LIBs) have revolutionized technologies facilitating the rapid development of new portable devices and electric vehicles. However, this rapid technology growth has exceeded the ability to address issues associated with mining lithium, cobalt, and other mineral ore resources. To reduce this reliance on strategic elements, organic-based electroactive materials have received considerable attention as alternative electrode materials for LIBs. Recently, one class to gain considerable attention is polymers with redox-active groups. One polymer that is popular in literature is poly(TEMPO methacrylate) (PTMA), which has nitroxide radicals that can reversibly store energy through a reduction/oxidation mechanism. Although the investigation of PTMA and fully polymeric batteries is found in literature, there is little consideration for the composite materials, nanostructured fabrication, recyclability of the redox-active polymers, or the anodic polymers redox mechanism. This dissertation focuses on improving the use of redox-active polymers, such as PTMA, in batteries to create safe and recyclable alternatives. Broken into four main objectives and five chapters: (1) design PTMA-based electrodes that exhibit improved performance, (2) fabricate and characterize nanostructured redox-active coatings, (3) use degradable redox-active polymers to improve the recyclability of fully polymeric batteries, and (4) characterize the electron and mass transport of polymers containing viologen groups.

The main findings will be briefly summarized. When designing PTMA-based composite electrodes, identifying materials with similar hydrogen bonding and dispersion Hansen solubility parameters is key to producing electrodes with improved performance. To fabricate nanostructured nitroxide-based thin films, oppositely charged polymers both containing the nitroxide radical should be utilized and the charge of the terminating layer will determine the ion transport mechanism during oxidation and reduction.

ACKNOWLEDGMENTS

I would like to thank my research advisor, Prof. Jodie Lutkenhaus, and my committee members, Prof. Lei Fang, Prof. Emily Pentzer, and Prof. Karen Wooley for their guidance, support, and mentorship throughout this research.

I would also like to thank my lab mates, friends, and colleagues for making my time at Texas A&M University a great experience. I would like to thank Alison Hoe for helping to keep me sane throughout the writing and defense processes. Also, a very large thanks to my counselor and doctor that helped me manage my mental health and stress.

Finally, thanks to my family for their encouragement and patience and my fiancé for the bagels and laughs.

CONTRIBUTORS AND FUNDING SOURCES

Contributors

This work was supervised by a committee consisting of Professor Jodie Lutkenhaus (chair) of the Artie McFerrin Department of Chemical Engineering, Professor Emily Pentzer of the Department of Materials Science and Engineering, and Professors Lei Fang and Karen Wooley of the Department of Chemistry. In Chapter 2, Paraskevi Flouda conducted X-ray photoelectron spectroscopy, and Lillian Vukin, Dylan Howard, and Jose Pena contributed to the data collection. In Chapter 3, the polymers and chemical characterizations were provided by Steven Regen and Sayali Shaligram of Lehigh University, the atomic force microscope images were provided by Ian Echols, and thermal gravimetric analysis was conducted by Kevin Nixon. Finally, in Chapters 4 and 5 Karen Wooley, Tan Nguyen, and Shih-Guo Li provided the polypeptides and their chemical characterization. Daniel Tabor and Cheng-Han Li conducted all simulations.

Funding Sources

Graduate studies were supported by Texas A&M University's Graduate and Professional Studies Diversity Fellowship (1st year and 4th – 5th year) and the National Science Foundation Graduate Research Fellowship (2nd- 4th year). An acknowledgment is made to the Donors of the American Chemical Society Petroleum Research Fund for partial support of this work (solubility studies and viscosity work). This work was financially supported by the U.S. Department of Energy Office of Science (DE-SC0014006, electrochemical measurements).

TABLE OF CONTENTS

Page

LIST OF FIGURES

Page

LIST OF TABLES

Page

1. INTRODUCTION

Due to the rapid expansion of electronics with rechargeable batteries in recent years, the demand for lithium-ion batteries (LIBs) has also grown drastically.[1] LIB demand has been focused on two main storage scales: 1) small scale storage, such as wearable electronics and wireless headphones and 2) large scale storage, like electric vehicles.[2] With more countries targeting 100% zero-emission vehicles and increasing consumer incentives to purchase electric vehicles, demand for LIBs will continue to rise.[3] The increased demand motivates the identification of additional and alternative electrode chemistries to meet production goals.[2]

Currently, commercial LIBs typically utilize a graphite anode and lithium cobalt oxide ($LiCoO_2$) cathode (**Figure 1.1 a**).[2,4] Although there are some health concerns due to the processing of the graphite, the production of the anode can meet the growing demand.[1] In contrast, there are concerns associated with the supply and acquisition of cobalt used in the cathode. Cobalt is a strategic element that is mainly mined in the Democratic Republic of the Congo and processed in China.[5] Due to current political tensions, the global supply, and United States' access is unstable. Additionally, the increased global demands for cobalt are predicted to deplete, and hit global deficits in supply, by 2030 (**Figure 1.1 b**).[1] Further accelerating the depletion is the low recycling rates of LIBs, which is currently < 3 %.[6,7] If the recycling rates of LIBs were increased to 90 %, the global deficit would be reduced albeit still present by 2030.[8] Due to the supply concerns associated with cobalt, alternative lithium metal oxides such as XXX have been investigated. However, supply and demand issues have also been reported for lithium.[9]

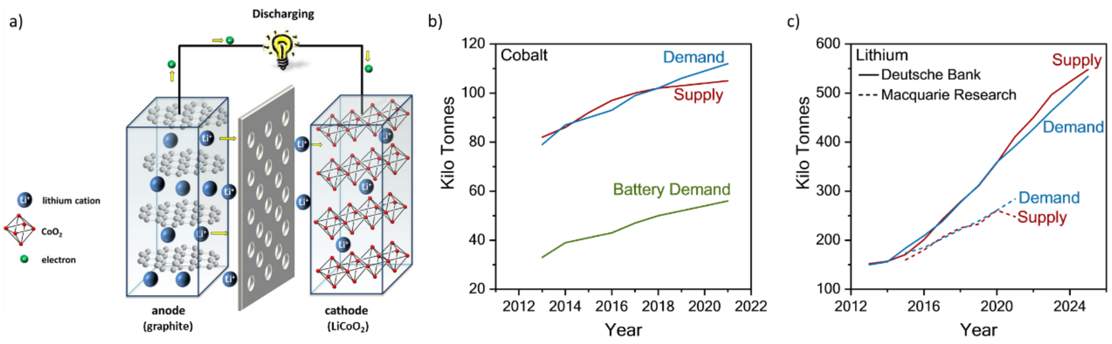

Figure 1.1. a) The most common Lithium-ion battery chemistry with a graphite anode and $LiCoO_2$ cathode. The supply and demand for b) cobalt and c) lithium by year. a) Adapted with permission from ref [4]. Copyright 2016 American Chemical Society. b) and c) Adapted with permissions from ref [9]. Copyright 2019 American Chemical Society.

Due to this persistent deficit, alternatives to metal oxide cathodes are required to meet global demand for LIBs. The identified alternatives should also seek to increase the recycling rate while removing reliance on the strategic elements. With these criteria, an attractive alternative that has increased interest in recent years is organic-based redox-active polymers for battery cathodes.[10-16] There are two main classes of redox-active polymers that have been previously investigated: conjugated polymers and macromolecular radicals (**Figure 1.2**).

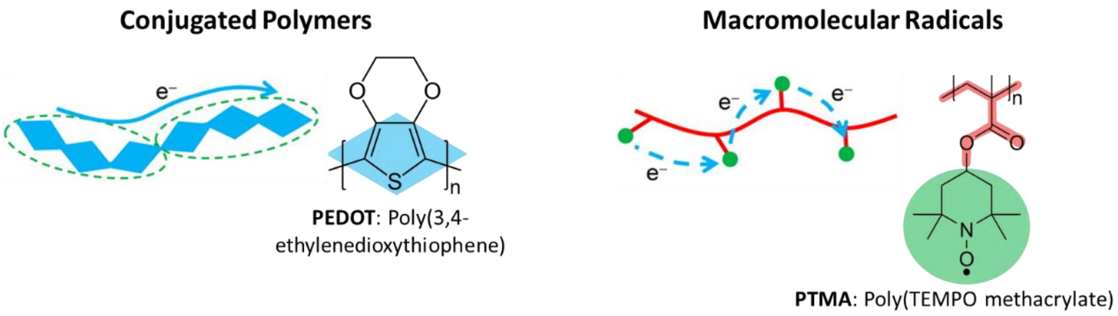

Figure 1.2. Comparison of the electron transport mechanism and chemical structures of conjugated polymers and macromolecular radicals. Adapted with permission from ref [17]. Copyright 2015 American Chemical Society. The ref can be found https://pubs.acs.org/doi/10.1021/jacs.5b02290. Any permissions related to the material excerpted should be directed to the ACS.

Conjugated polymers, such as poly(3,4-ethylenedioxythiophene) (PEDOT), are class of redox-active polymers that all have conjugated backbones. These polymers conduct electrons through the overlapping π-orbitals of the conjugated backbone. Due to the delocalized electrons, these polymers typically exhibit high electronic conductivity values from 10^{-4} – 10^{-9} S/cm in their undoped state and up to 1500 S/cm in certain doped states, which is appealing for battery applications.[16] However, conductivity is also strongly dependent on the morphology of the polymer, with high regioregularity and crystallinity favoring increased conductivity.[16] One downside arising from highly regioregularity and long conjugation lengths is processing difficulties due to their poor solubility in common organic solvents.[4]

In contrast to conjugated polymers, recently macromolecular radicals, such as poly(2,2,6,6-tetramethylpiperidinyloxy-4-yl) (PTMA), have been reported for use in battery cathodes.[4,10-12,18] Macromolecular radicals have linear, aliphatic backbones that have redox-active pendant groups.[19] This class of polymer conducts electrons *via* a site-to-site hopping mechanism from the redox of the pendant groups.[20] Due to their aliphatic backbones, these polymers typically exhibit significantly lower conductivities compared to conjugated polymers, varying from 10^{-2} – 10^{-11} S/cm depending on the polymer backbone.[21,22] Unlike conjugated polymers, macromolecular radicals are soluble in common organic solvents stemming from their aliphatic backbone's.[23] This is beneficial in the solution processing of battery electrodes, however, it also leads to fading of battery performance due to dissolution into the electrolyte during operation.[24,25]

The energy storage mechanism for the $LiCoO_2$ cathodes differ from those of the macromolecular radical cathode. The $LiCoO_2$ cathodes store energy through an intercalation/deintercalation reaction that occurs at *ca.* 4.0 V *vs*. Li/Li^+ (**Figure 1.3 a**).[26] The theoretical capacity of $LiCoO_2$ is *ca.* 273 mAh/g (with insertion of 1 Li ion), however, experimentally only 140 mAh/g can be achieved reversibly.[26] Unlike $LiCoO_2$, macromolecular nitroxide radicals store energy through the reversible reduction-oxidation reaction of the pendant nitroxide which occurs at *ca.* 3.7 V *vs.* Li/Li^+ (**Figure 1.3 b**).[4,10] The most commonly used macromolecular nitroxide radical in battery cathodes is PTMA, which has a theoretically capacity 111 mAh/g.[4,10] In contrast to $LiCoO_2$ cathodes, the theoretical capacity is experimentally achievable for PTMA-based electrodes.[4,10] The similar capacity and output voltage makes PTMA an appealing alternative to $LiCoO_2$ for Li-ion battery cathodes that are not reliant on strategic elements.

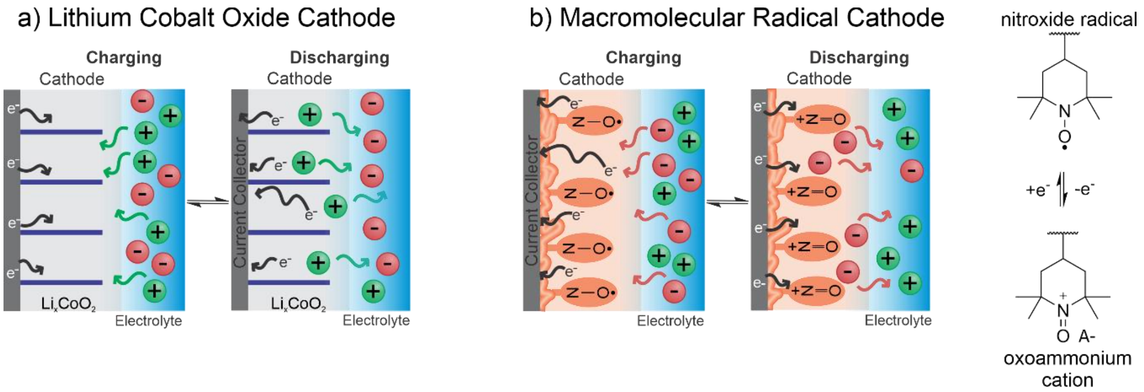

Figure 1.3. a) The intercalation/deintercalation charge storage mechanism for lithium cobalt oxide cathodes. b) The reduction-oxidation charge storage mechanism for macromolecular nitroxide radical cathodes.

PTMA-based cathodes are a more environmentally friendly alternative to $LiCoO_2$ but the insulating backbone of PTMA necessitates the addition of conductive additives, such as Super P carbon black, to facilitate electron transport.[27] In addition to conductive additives, binder polymers, such as poly(vinylidene fluoride) (PVDF), are added to ensure the cohesion of the components and to prevent dissolution of PTMA during battery cycling. The most common composition is 30 wt% PTMA, 60 wt% Super P carbon black, and 10 wt% PVDF. Although these PTMA-composites are common cathodes, very little research has focused on quantifying the interactions between the components or identifying alternative conductive additives and binder polymers to improve the performance of the electrode.[23]

Although PTMA is more environmentally friendly, compared to $LiCoO_2$, mechanical recycling of PTMA-based electrodes has not yet been demonstrated and the non-degradable aliphatic backbone prevents the chemical recycling of PTMA. Due to dissolution of PTMA during battery cycling and the composite nature of PTMA-based electrodes, mechanical recycling will be difficult and have low yields.

The results of this dissertation aim to explore alternative materials for LIBs, namely polymer-based electrodes, and batteries (**Figure 1.4**). **Chapter 2** seeks to quantify the interactions between composite electrode components and improve the cohesion between components to improve the performance of PTMA-based cathodes. **Chapter 3** explores the assembly of nanoarchitectonics of charged nitroxide-based polymers to produce thin electroactive coatings. **Chapter 4** focuses on incorporating degradable redox-active polypeptides as the anode and cathode material to produce a metal-free fully polymeric battery, with degradable active materials. **Chapter 5** investigates the structure-property relationship for electron transfer in anodic polypeptides. Finally, **Chapter** 6 discusses ongoing work studying the anion mass transport and effect of ion valency in crosslinked redox-active polymer electrodes and studies of solution state conformations of PTMA.

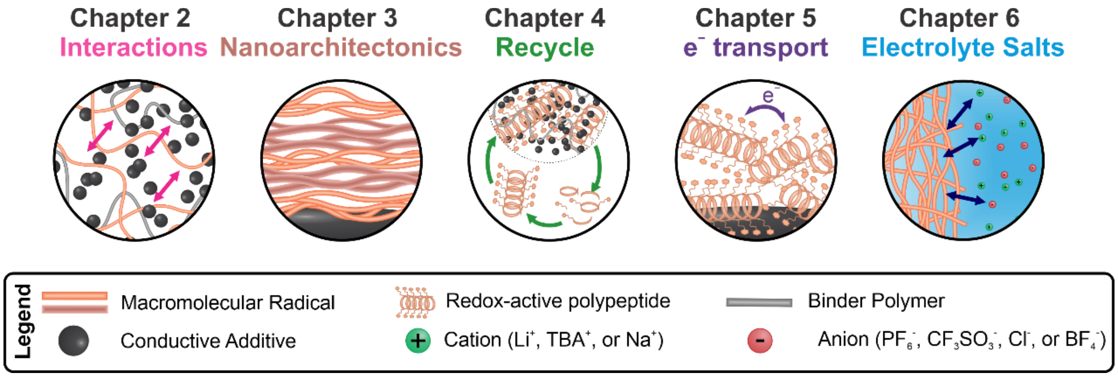

Figure 1.4. Objectives for each chapter related to macromoelcular radicals, their material's interactions, thin film fabrication, recyclability, and electroon and mass transport.

Taken together, this work seeks to provides the groundwork for next-generation polymer-based batteries that may outperform LIBs electrode materials while retaining recyclability. This is accomplished through elucidation of component interactions in PTMA-based electrodes, determination of charge and mass transport mechanisms and domains for anodic redox-active polymers, and demonstration of metal-free degradable polymer-based batteries. By replacing traditional LIB materials, this work can reduce the reliance of the U.S. energy market on foreign powers, a natural source of instability, and commit to more sustainable, environmentally friendly alternatives that can provide commensurate or better performance.

1.1. References

1. Turcheniuk, K., Bondarev, D., Singhal, V. & Yushin, G. Ten years left to redesign lithium-ion batteries. *Nature* **559**, 467-470 (2018).

2. Manthiram, A. A reflection on lithium-ion battery cathode chemistry. *Nature Communications* **11**, 1550 (2020).

3. (IEA), I. E. A. Global EV Outlook 2020. (2020).

4. Muench, S., Wild, A., Friebe, C., Häupler, B., Janoschka, T. & Schubert, U. S. Polymer-Based Organic Batteries. *Chem. Rev.* **116**, 9438-9484 (2016).

5. van den Brink, S., Kleijn, R., Sprecher, B. & Tukker, A. Identifying supply risks by mapping the cobalt supply chain. *Resources, Conservation and Recycling* **156**, 104743 (2020).

6. Zeng, X., Li, J. & Singh, N. Recycling of Spent Lithium-Ion Battery: A Critical Review. *Critical Reviews in Environmental Science and Technology* **44**, 1129-1165 (2014).

7. Olivetti, E. A., Ceder, G., Gaustad, G. G. & Fu, X. Lithium-Ion Battery Supply Chain Considerations: Analysis of Potential Bottlenecks in Critical Metals. *Joule* **1**, 229-243 (2017).

8. Dias, P. A., Blagoeva, D., Pavel, C. & Arvanitidis, N. (Publications Office of the European Union, 2018).

9. Eftekhari, A. Lithium Batteries for Electric Vehicles: From Economy to Research Strategy. *ACS Sustainable Chemistry & Engineering* **7**, 5602-5613 (2019).

10. Nishide, H., Iwasa, S., Pu, Y.-J., Suga, T., Nakahara, K. & Satoh, M. Organic radical battery: nitroxide polymers as a cathode-active material. *Electrochim. Acta* **50**, 827-831 (2004).

11. Kim, J.-K., Ahn, J.-H., Cheruvally, G., Chauhan, G. S., Choi, J.-W., Kim, D.-S., Ahn, H.-J., Lee, S. H. & Song, C. E. Electrochemical properties of rechargeable organic radical battery with PTMA cathode. *Metals and Materials International* **15**, 77-82 (2009).

12. Janoschka, T., Hager, M. D. & Schubert, U. S. Powering up the Future: Radical Polymers for Battery Applications. *Adv. Mater.* **24**, 6397-6409 (2012).

13. Wild, A., Strumpf, M., Häupler, B., Hager, M. D. & Schubert, U. S. All-Organic Battery Composed of Thianthrene- and TCAQ-Based Polymers. *Advanced Energy Materials* **7**, 1601415 (2017).

14. Lopez, J., Mackanic, D. G., Cui, Y. & Bao, Z. Designing polymers for advanced battery chemistries. *Nature Reviews Materials* **4**, 312-330 (2019).

15. Mike, J. F. & Lutkenhaus, J. L. Electrochemically Active Polymers for Electrochemical Energy Storage: Opportunities and Challenges. *ACS Macro Letters* **2**, 839-844 (2013).

16. Mike, J. F. & Lutkenhaus, J. L. Recent advances in conjugated polymer energy storage. *J. Polym. Sci., Part B: Polym. Phys.* **51**, 468-480 (2013).

17. Liang, Y., Chen, Z., Jing, Y., Rong, Y., Facchetti, A. & Yao, Y. Heavily n-Dopable π-Conjugated Redox Polymers with Ultrafast Energy Storage Capability. *Journal of the American Chemical Society* **137**, 4956-4959 (2015).

18. Kim, J.-K., Cheruvally, G., Ahn, J.-H., Seo, Y.-G., Choi, D. S., Lee, S.-H. & Song, C. E. Organic radical battery with PTMA cathode: Effect of PTMA content on electrochemical properties. *Journal of Industrial and Engineering Chemistry* **14**, 371-376 (2008).

19. Wang, S., Easley, A. D. & Lutkenhaus, J. L. 100th Anniversary of Macromolecular Science Viewpoint: Fundamentals for the Future of Macromolecular Nitroxide Radicals. *ACS Macro Letters* **9**, 358-370 (2020).

20. Sato, K., Ichinoi, R., Mizukami, R., Serikawa, T., Sasaki, Y., Lutkenhaus, J., Nishide, H. & Oyaizu, K. Diffusion-Cooperative Model for Charge Transport by

Redox-Active Nonconjugated Polymers. *Journal of the American Chemical Society* **140**, 1049-1056 (2018).

21. Zhang, Y., Park, A., Cintora, A., McMillan, S. R., Harmon, N. J., Moehle, A., Flatté, M. E., Fuchs, G. D. & Ober, C. K. Impact of the synthesis method on the solid-state charge transport of radical polymers. *Journal of Materials Chemistry C* **6**, 111-118 (2018).

22. Joo, Y., Agarkar, V., Sung, S. H., Savoie, B. M. & Boudouris, B. W. A nonconjugated radical polymer glass with high electrical conductivity. *Science* **359**, 1391 (2018).

23. Easley, A. D., Vukin, L. M., Flouda, P., Howard, D. L., Pena, J. L. & Lutkenhaus, J. L. Nitroxide Radical Polymer–Solvent Interactions and Solubility Parameter Determination. *Macromolecules* **53**, 7997-8008 (2020).

24. Wang, S., Li, F., Easley, A. D. & Lutkenhaus, J. L. Real-time insight into the doping mechanism of redox-active organic radical polymers. *Nature Materials* **18**, 69-75 (2019).

25. Zhang, K., Hu, Y., Wang, L., Fan, J., Monteiro, M. J. & Jia, Z. The impact of the molecular weight on the electrochemical properties of poly(TEMPO methacrylate). *Polymer Chemistry* **8**, 1815-1823 (2017).

26. Liu, C., Neale, Z. G. & Cao, G. Understanding electrochemical potentials of cathode materials in rechargeable batteries. *Mater. Today* **19**, 109-123 (2016).

27. Schubert, U. S., Friebe, C. & Lex-Balducci, A. Sustainable Energy Storage: Recent Trends and Developments toward Fully Organic Batteries. *ChemSusChem* **0** (2019).

2. NITROXIDE RADICAL POLYMER-SOLVENT INTERACTIONS AND SOLUBILITY PARAMETER DETERMINATION*

2.1. Introduction

In recent years, the desire for sustainable alternatives to lithium-ion batteries has led to increased interest in organic radical batteries (ORBs), in which macromolecular radicals comprise the cathode and/or anode. The most commonly investigated macromolecular radical is poly(2,2,6,6-tetramethylpiperidinyloxy methacrylate) (PTMA) owing to its simple synthesis, high theoretical capacity (111 $mA \cdot h \cdot g^{-1}$), and fast charge-discharge kinetics.[4,10,11,18,28-30] ORBs use common lithium ion battery electrolytes, such as linear and cyclic carbonates. However, a large number of studies have observed dissolution of the macromolecular radical into the electrolyte (see **Table S2.1** for specific examples), resulting in pronounced capacity fade with cycling.[4,11,13,18,25,28,29,31-34] Therefore, it is important to identify non-dissolving electrolytes for practical ORB design. Unfortunately, the PTMA-solvent interactions have not been quantified, and the solubility parameter of PTMA is unknown.

More specifically, a capacity fade of *ca.* 75% was reported for linear PTMA in 1 M $LiPF_6$ in EC/DEC (1/1, v/v) electrolyte over the course of 25 cycles.[35] Additionally, a study by Wang *et al.* showed quantitative results for the dissolution of PTMA during

---

* Reprinted with permission from ref. 23. Easley, A. D., Vukin, L. M., Flouda, P., Howard, D. L., Pena, J. L. & Lutkenhaus, J. L. Nitroxide Radical Polymer–Solvent Interactions and Solubility Parameter Determination. *Macromolecules* **53**, 7997-8008 (2020). Copyright 2020 American Chemical Society.

cyclic voltammetry and Zhang *et al.* demonstrated the solubility limit of PTMA in a DEC-based electrolyte to vary from 3.0 to 65.1 mg·mL^{-1} depending on PTMA's molar mass.[24,25]

In addition to dissolution during ORB cycling, solution-processing of PTMA should be conducted using a dissolving solvent that yields homogenous films or electrodes. This is especially important when considering the solid-state properties of PTMA-based films, since defects or morphological changes can alter the properties.[36] For the production of homogenous PTMA-based electrodes, solvents and additives (binder and conductive additives) must be selected to dissolve or favorably interact with each other to optimize performance.[37,38] Most commonly, *N*-methyl-2-pyrrolidone (NMP) is used as the dissolving medium; however, the need for more environmentally friendly alternatives has focused attention to other solvents. This highlights the complementary need to identify dissolving solvents for PTMA, where solution processing or solution-based applications are desired.

Therefore, we focus upon identifying the solubility parameter of PTMA to estimate the Flory-Huggins interaction parameter, which is used to quantify polymer-solvent interactions.[39] **Equation 2.1** shows the formulation for the Flory-Huggins, χ, interaction parameter:

$$\chi = \frac{V_1}{RT}(\delta_1 - \delta_2)^2 + 0.34$$

Equation 2.1

where V_1 is the molar volume of the solvent (cm^3·mol^{-1}), R is the gas constant (8.314 cm^3·MPa·K^{-1}·mol^{-1}), T is temperature (K), and δ_1 and δ_2 are the solubility parameters

($MPa^{1/2}$) of the solvent and polymer, respectively. Solubility parameters for solvents are measured through direct methods and many databases exist that present the values for most solvents.[24] Traditional methods of determination for a polymer's solubility parameter include group contribution,[40-42] solubility spectrum,[42] viscosity measurements,[43,44] and turbidity titrations.[45,46] Otherwise, the Flory-Huggins interaction parameter, instead of the solubility parameter, may be determined using membrane osmometry and quartz crystal microbalance with dissipation (QCM-D).[47]

Two common solubility parameters used to calculate χ are the Hildebrand and total Hansen solubility parameter. The Hildebrand solubility parameter condenses all structural information into one representative value.[48] This reduced dimensionality makes experimental determination and group contribution calculations simpler but can misidentify solubility due to differences in polarity or hydrogen bonding affinity.[48] To improve upon these short comings, the Hansen solubility parameters δ_h, δ_p, and δ_d, which account for the hydrogen bonding, polarity, and dispersion forces, respectively,[49] were developed. These parameters can also be combined to calculate a total Hansen solubility parameter (δ_t).[50]

Herein, we report the determination of PTMA's solubility parameter for the first time. This is accomplished by comparing the solubility behavior of poly(2,2,6,6-tetramethyl-4-piperidyl methacrylate) (PTMPM, which is PTMA's precursor), PTMA with two different oxidation levels, and oxidized PTMA (poly(2,2,6,6-tetramethyl-4-oxoammonium tetrafluoroborate methacrylate, or $PTMA^+$). These four macromolecules are analyzed using solubility spectrums, group contribution methods, and turbidity titrations. Using the measured solubility parameters, we suggest non-dissolving and dissolving solvents that may be used either for ORB operation or for solution-processing, respectively.

2.2. Experimental

2.2.1. Materials

The following materials were received from Sigma Aldrich and used without further purification: 2-phenol-2-propyl benzodithioate (CTA), toluene, tetrahydrofuran (THF), *N*-methyl-2-pyrrolidone (NMP), 4-hydroxy-2,2,6,6-tetramethylpiperidine-1-oxyl (4-OH-TEMPO), poly(methyl methacrylate) (PMMA, 1.25 dL/g inherent viscosity), acetonitrile, *N,N*-dimethylformamide (DMF), *meta*-chloroperoxybenzoic acid (*m*CPBA, 77 %), propylene carbonate (PC), sodium tungstate dihydrate (Na_2WO_4 $2H_2O$), ethylenediaminetetraacetic acid disodium salt dihydrate (Na_2EDTA $2H_2O$), tetrafluoroboric acid solution (48 wt%), decane, dodecane, xylenes, dimethylacetamide, acetonitrile, 1,2-propanediol, ethanol, and dimethyl sulfoxide. 2,2′-azobis(2-methylpropionitrile) (AIBN) was received from Sigma Aldrich and was recrystallized from ethanol before use. The following materials were received from VWR BDH Chemicals and used without any further purification: hexanes, chloroform, dichloromethane (DCM), acetone, hydrogen peroxide solution (30 wt%), methanol, diethyl ether, ethyl acetate, and isopropyl alcohol. 2,2,6,6-tetramethyl-4-piperidyl methacrylate (TMPM) was received from TCI America and used without purification. NaClO CP-722 Solution (~12 wt%) was used as received from CANI Inc. Triethylamine was used as received from Acros Organics. Ultrapure water (water) was collected from a Milli-Q® water purification system (18 MΩ·cm). Super P® Carbon Black (Super P) was purchased from TIMCAL Graphite & Carbon. Polyvinylidene fluoride (PVDF, MW = 600,000 g·mol^{-1}) was purchased from MTI Corporation. Lithium metal and 2-butoxyethyl acetate (BCA) were purchased from Alfa-Aesar.

2.2.2. Synthesis of PTMPM

Following the protocol previously published by Rostro *et al.*, PTMA was synthesized using a RAFT polymerization method.[51] In brief, in a 250-mL Schlenk flask 10.0 g (44 mmol) of TMPM, 30 mg of AIBN (0.18 mmol), 40 mg (0.13 mmol) of CTA, and 20 mL of toluene were combined in an argon atmosphere glovebox. Resulting in a monomer : initiator : CTA molar ratio of 330 : 1.4 : 1. The flask was then sealed and transferred out of the glovebox, heated to 75°C, and left to react for 12 hrs. The reaction was then cooled to room temperature and exposed to ambient air to terminate the reaction. The reaction solution was then precipitated in hexanes and the resulting polymer, poly(2,2,6,6-tetramethyl-4-piperidyl methacrylate) with CTA end groups (or PTMPM-CTA), was collected *via* vacuum filtration and vacuum dried overnight.

The CTA end group was removed by reacting 2.50 g (11 mmol of repeat unit) PTMPM-CTA with an excess of AIBN (2.50 g, 15 mmol) in 50 mL of toluene at 75 °C for 12 hrs. The reaction was then cooled to room temperature and exposed to ambient air to terminate the reaction. The reaction solution was precipitated in hexanes and the resulting white polymer, poly(2,2,6,6-tetramethyl-4-piperidyl methacrylate) (PTMPM), was collected *via* vacuum filtration and vacuum dried overnight. PTMPM was oxidized using *m*CPBA and H_2O_2 as previously described.[21,24,51]

2.2.3. Synthesis of PTMA-*m*CPBA

For *m*CPBA oxidation, a solution consisting of 3.06 g (17 mmol) of *m*CPBA dissolved in DCM (15 mL) was added dropwise to a solution of 1.50 g (7 mmol of repeat unit) of PTMPM in DCM (15 mL).[24] The reaction was carried out at ambient conditions for 3 hours, after which the reaction solution was washed with water and saturated sodium bicarbonate solution, and then dried over sodium sulfate.[24] The filtrate was collected after gravity filtration and precipitated in hexanes. Finally, the resulting orange solid (PTMA-*m*CPBA) was vacuum dried overnight.

2.2.4. Synthesis of PTMA-H_2O_2

For H_2O_2 oxidation, 0.60 g (3 mmol) of PTMPM, 219 mg (0.7 mmol) of Na_2WO_4 $2H_2O$, 116 mg (0.3 mmol) of Na_2EDTA $2H_2O$, and 30 mL of methanol were added to a 150-mL round-bottom flask with a condenser.[21] The solution was stirred at 60 °C for 5 min, followed by the dropwise addition of 3 mL of 30 wt% aqueous H_2O_2 solution.[21] The mixture was further reacted at 60 °C for 24 h. The solid precipitate was dissolved in DCM and washed with water (three times).[21] The solution was concentrated under reduced vacuum and precipitated in cold hexanes. The orange solid (PTMA-H_2O_2) was collected *via* vacuum filtered and vacuum dried overnight.

2.2.5. Synthesis of PTMA$^+$

Poly(2,2,6,6-tetramethyl-4-oxoammonium tetrafluoroborate methacrylate) (here called “PTMA$^+$”) was synthesized following previous reports.[52-54] In brief, 1.50 g (6.2

mmol of repeat unit) of PTMA-*m*CPBA was combined with 3.5 mL of water in a 25 mL-round bottom flask. Once mixed, 0.8 mL of tetrafluoroboric acid solution was added dropwise under ambient conditions. The reaction mixture was then cooled to 0 °C. After cooling, 1.6 mL of NaClO solution (~12 wt%) was added dropwise. The reaction was left to react at 0 °C for an additional hour. Finally, the reaction mixture was washed with ice-cold water three times, followed by vacuum filtration to collect the polymer precipitate. The collected yellow polymer ($PTMA^+$) was dried under vacuum overnight.

2.2.6. Characterization

After synthesis, all polymers were characterized within 40 days. For NMR, 10 mg of the polymer, PTMPM-CTA or PTMPM, was dissolved in 1 mL of deuterated DCM and a 400 MHz Bruker NMR was used to collect the ^{1}H-NMR spectra. For UV-vis spectroscopy, 5-10 mg of each polymer, PTMPM-CTA or PTMPM, were dissolved in 1 mL of chloroform with spectra collected in 1 nm increments from 800 to 300 nm using a Hitachi U-4100 UV-Vis-NIR spectrophotometer (341-F). Pure CTA (1.8 mg/mL in chloroform) was used as a control to determine whether the end group was successfully removed. Size exclusion chromatography (SEC) was performed on a TOSOH EcoSEC (HLC-8320GPC) with UV (254 nm) and RI detectors at 40 °C with THF as the eluent with a flow rate of 0.35 mL min^{-1}. The SEC sample was prepared by dissolving 5 mg of PTMA-*m*CPBA or PTMA-H_2O_2 in 1.5 mL of THF. The molecular weights were calculated using a calibration curve based on polystyrene standards. The SEC columns were TSKgel SuperHM-M and TSKgel SuperH-RC. EPR was performed on a Bruker Elexsys at room temperature. A reference solution of 1 mM of 4-OH-TEMPO and 1 mM of polymer repeat unit (PTMPM, PTMA-*m*CPBA, PTMA-H2O2, and PTMA$^+$) were prepared in chloroform.

Following a previous report by Aqil *et al.*, UV-vis spectroscopy was utilized to generate a calibration curve by varying the concentration of the standard, 4-OH-TEMPO, from 0.01 to 0.04 M in chloroform.[55] The PTMA sample was prepared at a concentration of 0.03 M (repeat unit basis) in chloroform. The oxidation percentage of the PTMA sample was calculated using the standard calibration curve at 462 nm.

Attenuated total reflectance-Fourier transform infrared (ATR-FTIR) spectra were recorded for powder samples of the polymers using a Shimadzu Corp. IR Prestige 21 system and analyzed using IRsolution v. 1.40 software. All spectra were normalized to the C=O stretching vibration, which is attributed to the ester linkages in the side chain, (~1750 cm^{-1}). Finally, XPS spectra were collected on powder samples of the polymers (unless otherwise stated) using an Omicron XPS with an Argus detector using a monochromated Mg X-ray source (hm = 1253.6 eV). Survey scans were performed with an analyzer pass energy of 150 – 1150 eV (1.0 eV steps, 50 ms dwell time). High-resolution scans of nitrogen (N 1s), chlorine (Cl 2p), and fluorine (F 1s) were collected with a pass energy of 150 eV (0.05 eV steps, 200 ms dwell time). All spectra were calibrated using the C 1s photoemission peak (sp^2-hybridized carbons) at 284.5 eV. Curve fitting of N 1s spectra was conducted using a Gaussian-Lorentzian peak shape after a Shirley-type background correction and the FWHM of the deconvoluted peaks was constrained. XPS for PTMA-*m*CPBA was collected on a spin coated thin film on ITO-coated glass.

2.2.7. Solvent Spectrum

The solvent spectrums were prepared by making solutions with a concentration of 25 mg·mL^{-1} for each polymer in solvents of increasing δ value. The solvents used were decane, hexane, triethylamine, diethyl ether, dodecane, xylene, toluene, ethyl acetate, THF, chloroform, DCM, acetone, dimethylacetamide, NMP, isopropyl alcohol, acetonitrile, dimethylformamide, 1,2-propanediol, ethanol, PC, methanol, dimethyl sulfoxide, and water to vary the δ value from 13.5 MPa$^{1/2}$ (decane) to 47.9 MPa$^{1/2}$ (water). The solutions were then classified as soluble if the powder completely dissolved and insoluble if the polymer did not dissolve in solution or formed a gel. The $\delta_{polymer}$ was calculated by averaging the δ values for the solvents in which the polymer was soluble. This approach was used to estimate the Hildebrand and Hansen solubility parameters. The calculated Hansen solubility parameters were used as the center point and the radius of the Hansen solubility sphere was determined by drawing a circle in the δ_h *vs.* δ_p projection to enclose as many dissolving solvents as possible, while excluding non-dissolving solvents.

2.2.8. Group Contribution

The Hoy and Fedors group contribution methods were utilized to estimate the Hildebrand solubility parameter of PTMPM, PTMA-*m*CPBA, PTMA-H_2O_2, and PTMA$^+$.[40,42] The three Hansen parameters (δ_d, δ_h, and δ_p) and the total Hansen solubility parameter (δ_t) were estimated for all four polymers using the group contribution values presented by Meusberger.[41]

2.2.9. Turbidity Titrations

A solution of polymer dissolved in solvent (THF, chloroform, DCM, acetone, NMP, or DMF) was prepared at a concentration of 30 mg·mL^{-1}. Two separate titrations were performed for each polymer solution. A solvent of higher solubility parameter, dimethyl sulfoxide, and separately a solvent of lower solubility parameter, decane (for PTMPM) or diethyl ether (for PTMA-*m*CPBA and PTMA-H_2O_2), were slowly added and the volume fraction at the turbid point was recorded for both. Using the Hildebrand solubility parameters of the higher and lower solvents, and volume fraction at the turbid points for both titrations, the theoretical Hildebrand solubility parameter of the polymer (δ_2') was then calculated using **Equation 2.2**,

$$\delta_2' = \frac{\left(V_{ml}^{1/2}\delta_{ml} + V_{mh}^{1/2}\delta_{mh}\right)}{\left(V_{ml}^{1/2} + V_{mh}^{1/2}\right)}$$

Equation 2.2

where $V_{ml\ or\ mh} = V_{ds}V_{nds}/(\theta_{nds}V_{ds} + \theta_{ds}V_{nds})$ and $\delta_{ml\ or\ mh} = \theta_{ds}\delta_{ds} + \theta_{nds}\delta_{nds}$ estimate the mixed solvent molar volume (V_m) and Hildebrand solubility parameter (δ_m), respectively. V is the molar volume ($cm^3\ mol^{-1}$) and θ is the volume fraction of the dissolving solvents (ds) or non-dissolving (nds) solvents at the turbid point, respectively, for both higher (h) and lower (l) solubility parameter solvents. Each titration was repeated three times to determine the error using standard error propagation.

The turbidity after every non-dissolving solvent addition was calculated using **Equation 2.3**, where the % transmittance at 750 nm was obtained *via* UV-vis spectroscopy. 750 nm was chosen for analysis because it represents a non-absorbing wavelength common for all three polymers. The turbid point was determined as the addition which resulted in a significant increase in turbidity.

$$Turbidity = -\ln\frac{I_T}{I_0}$$

Equation 2.3

2.2.10. Electrochemical Testing

PTMA-*m*CPBA based composite electrodes were fabricated using the PMMA or PVDF polymer binder, conductive additive (Super P), and processing solvent. The electrode slurry was prepared by grinding Super P (60 wt%), PTMA-*m*CPBA (30 wt%), and PMMA (10 wt%) in BCA with a mortar and pestle. Using the same preparation method control electrodes were fabricated with a composition Super P (60 wt%), PTMA-*m*CPBA (30 wt%), and PVDF (10 wt%) in NMP. The slurries were doctor-bladed onto aluminum foil with a blade thickness of 200 μm using an automated film applicator (Elcometer 4340 Automatic applicator). The electrodes were dried at r.t. for 24 hrs and 40°C under ambient pressure for two days before drying under vacuum at 40°C for 24 h. After drying, 16 mm diameter electrodes were cut for use. Electrode thickness was determined after drying using a utilized TESA μ-HITE instrument. The mass loading and thickness of the resulting electrodes were 0.66 $mg\cdot cm^2$ and 10.2 μm, respectively.

The electrodes were used as working electrodes in a half-cell with a lithium metal foil reference/counter electrode, Celgard separator, and 1 M $LiPF_6$ in EC/DEC (1/1, v/v) electrolyte. Cyclic voltammetry (50 cycles at 10 $mV\cdot s^{-1}$) and galvanostatic charge-discharge (5 cycles each at 1, 2, 5, 10 and 20 C followed by 10 cycles at 1 C) were performed using a Solartron Electrochemical Interface 1287 potentiostat/galvanostat. All cells were assembled in an argon-filled glovebox.

2.3. Results and Discussion

2.3.1. Synthesis of PTMPM, PTMA-*m*CPBA, PTMA-H_2O_2, and PTMA$^+$.

PTMPM was synthesized using a reversible addition–fragmentation chain transfer (RAFT) polymerization method (**Figure S2.1 – Figure S2.2**) as reported by Rostro *et al.*[51] RAFT polymerization resulted in PTMPM with chain-transfer agent (CTA) end groups (PTMPM-CTA) that were removed prior to oxidation.[51] **Figure S2.3 – Figure S2.4** show ^{1}H-NMR and UV-vis spectra before and after CTA end group removal (PTMPM-CTA and PTMPM, respectively). UV-vis spectra showed a decrease in the shoulder associated with the CTA end groups (between 300 and 400 nm), and ^{1}H-NMR spectra showed that peaks associated with the CTA end groups (between 7 and 7.5 ppm) disappeared. The changes in UV-vis and NMR spectra confirmed the successful removal of the CTA end groups to produce PTMPM.

After removing the CTA end groups, the PTMPM precursor was oxidized with either *meta*-chloroperoxybenzoic acid (*m*CPBA) or hydrogen peroxide in the presence of catalytic sodium tungstate (H_2O_2/Na_2WO_4), resulting in PTMA-*m*CPBA and PTMA-H_2O_2, respectively.[19,21,25] From size exclusion chromatography (SEC) the molar mass (M_n) of PTMA-*m*CPBA was 66 kDa with a dispersity of 2.2, whereas the M_n of PTMA-H_2O_2 was 67 kDa with a dispersity of 1.7. Additionally, PTMA-*m*CPBA was oxidized to produce the oxoammonium cation using tetrafluoroboric acid and sodium hypochlorite solutions, resulting in a polymer here called “PTMA$^+$”.[52-54]

The radical loadings of PTMA-*m*CPBA, PTMA-H_2O_2 and PTMA$^+$ were quantified utilizing UV-vis spectroscopy, X-ray photoelectron spectroscopy (XPS), and electron paramagnetic resonance (EPR) spectroscopy, summarized in **Figure S2.5 – Figure S2.7 and Table S2.2**. The average radical loadings for PTMA-*m*CPBA, PTMA-H_2O_2, and PTMA$^+$ were 62 %, 69 %, and 45 %, respectively.

Macromolecular nitroxide radicals will possess a combination of amine, nitroxide radical, and oxoammonium cation groups depending on synthesis and oxidation method.[19] XPS was used to determine the elemental composition of each polymer, as well as the distribution of these functional groups, **Figure S2.6 d - Figure S2.7** and **Table S2.3**. The survey scans indicate that all polymers contained similar amounts of carbon, oxygen, and nitrogen. Additionally, high resolution Cl 2p and F 1s scans confirmed that the counter anion for PTMA-*m*CPBA was the chlorine-containing ion conjugate base of *m*CPBA,[56] whereas the counter anion for PTMA$^+$ was tetrafluoroborate, confirmed by the respective appearances of chlorine and fluorine signatures.[52,53] Deconvolution of the high resolution N 1s scan was used to determine the fractions of amine (~399.8 eV), nitroxide radical (~401.3 eV), and oxoammonium cation (~405.6 eV) functionalities for the polymers studied.[56] PTMPM, as expected, consisted entirely of amine functional groups, whereas PTMA-*m*CPBA, PTMA-H_2O_2, and PTMA$^+$ bore different fractions of all three functional groups (**Figure 2.1** and **Table S2.3**).

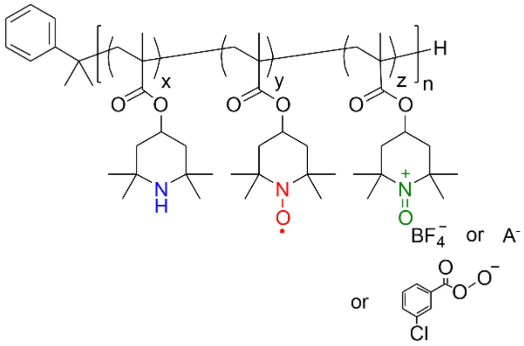

where A^- is a component of H_2O_2, Na_2WO_4, or Na_2EDTA

PTMPM	x = 1.0	y = 0.0	z = 0.0
PTMA-*m*CPBA	x = 0.36	y = 0.51	z = 0.13
PTMA-H_2O_2	x = 0.27	y = 0.67	z = 0.06
PTMA$^+$	x = 0.15	y = 0.65	z = 0.20

Figure 2.1. Distribution of functional groups for the polymers studied.

2.3.2. Solubility Spectrum.

We first examined the polymers' solubility parameters using a solvent or solubility spectrum. Here, the solubility spectrums for PTMPM, PTMA-*m*CPBA, PTMA-H_2O_2, and PTMA$^+$ were prepared at 25 mg·mL^{-1} for a variety of solvents, **Figure S2.8**. The resulting mixtures were classified as "soluble" if the polymer dissolved completely or "insoluble" if the polymer formed a polymer precipitate or gel. **Figure 2.2** shows a subset of the solubility spectrums for PTMPM, PTMA-*m*CPBA, PTMA-H_2O_2, and PTMA$^+$ in the solvents utilized for later for turbidity titrations.

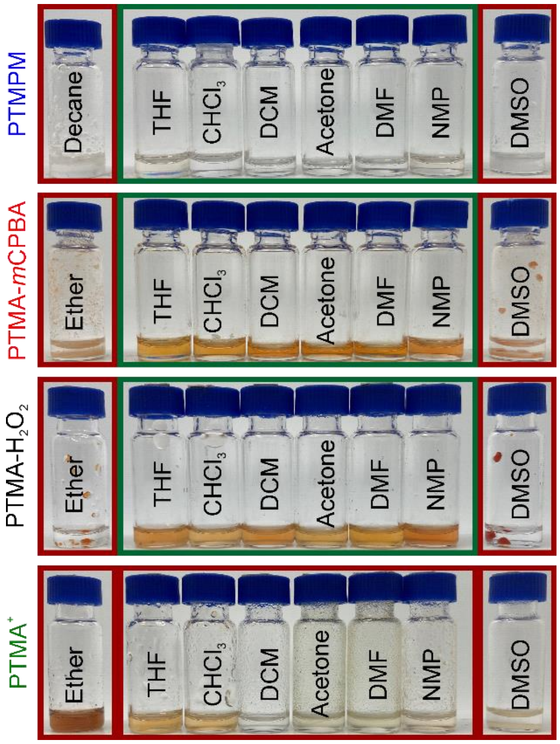

Figure 2.2. Dissolving (green) and non-dissolving (red) solvents used for turbidity titrations. No turbidity titrations were performed for $PTMA^+$ because of its insolubility in the investigated solvents.

In general, PTMPM exhibited solubility in more solvents than PTMA-*m*CPBA, PTMA-H_2O_2, or $PTMA^+$. This difference in solubility was especially evident for solvents with strong hydrogen bonding affinity, such as isopropyl alcohol, 1,2-propanediol, ethanol, and methanol (**Figure S2.8**), where PTMPM exhibited enhanced solubility. However, none of the polymers studied (including PTMPM) were water-soluble, which is in good agreement with previous work.[57] The solubility of PTMPM in these strong hydrogen bonding affinity solvents is attributed to the hydrogen bonding capability of the amine of the 2,2,6,6-tetramethylpiperidine pendant group. Additionally, $PTMA^+$ was insoluble in all the solvents examined in this work.

Using the results from the solubility spectrum, both the Hildebrand and Hansen solubility parameters for PTMPM, PTMA-*m*CPBA, and PTMA-H_2O_2 were determined by averaging the solubility parameters of the solvents classified as "soluble" in **Figure S2.8**. The Hildebrand solubility parameter values were 21.7 $MPa^{1/2}$, 21.5 $MPa^{1/2}$, and 21.5 $MPa^{1/2}$ for PTMPM, PTMA-*m*CPBA, and PTMA-H_2O_2, respectively. The solubility parameter for $PTMA^+$ could not be determined because it was insoluble in all the solvents utilized. The Hildebrand solubility parameter condenses all structural information related to polymer solubility into one parameter and showed little variation among PTMPM, PTMA-*m*CPBA, and PTMA-H_2O_2, whereas PTMPM and PTMA (regardless of oxidation method) exhibited differences in solubility. Altogether, the Hildebrand solubility parameter failed to capture the true solution behavior of the polymers.

Instead, we found that the Hansen solubility parameters captured the polymers' solution behavior more descriptively. **Table 2.1** summarizes δ_h, δ_p, and δ_d for PTMPM, PTMA-*m*CPBA, and PTMA-H_2O_2, and **Figure 2.3** shows the corresponding surface projections (gray circles). The strongest indicator of each polymer's solubility was δ_h. For example, PTMPM bears a higher δ_h than PTMA, which supports the increased solubility of PTMPM in strong hydrogen bonding affinity (higher δ_h) solvents. The radii of the Hansen solubility spheres were also considered and found to be 10.5 $MPa^{1/2}$, 8.5 $MPa^{1/2}$, 8.5 $MPa^{1/2}$, and 4.0 $MPa^{1/2}$ for PTMPM, PTMA-*m*CPBA, PTMA-H_2O_2, and $PTMA^+$, respectively. Due to the insolubility of $PTMA^+$, the radius of the Hansen solubility sphere was determined by using the largest possible radius that excluded the insoluble points. PTMPM exhibits a larger solubility radius than PTMA, meaning that PTMPM dissolves in a wider range of solvents. $PTMA^+$ exhibits the smallest solubility sphere, suggesting it is soluble in very few solvents. This is confirmed in **Figure S2.8**, in which $PTMA^+$ was insoluble in each of the 23 solvents investigated.

Table 2.1. A summary of the measured and calculated solubility parameters for PTMPM, PTMA-*m*CPBA, PTMA-H_2O_2, PTMA$^+$, PMMA.

		Solubility Parameter (MPa$^{1/2}$)				
Method		**PMMA**[a]	**PTMPM**	**PTMA-*m*CPBA**	**PTMA-H_2O_2**	**PTMA$^+$**
Solubility Spectrum						
Hildebrand	δ	19.4	21.7	21.5	21.5	NA[b]
Hansen	δ_d	18.6	16.8	17.2	17.2	NA[b]
	δ_p	10.5	7.5	9.6	9.6	NA[b]
	δ_h	7.5	9.7	6.8	6.8	NA[b]
	δ_t	22.6	20.8	20.8	20.8	NA[b]
	R	11.1	10.5	8.5	8.5	4.0
Group Contribution						
Hildebrand	Hoy	18.0	18.8	19.4	19.6	19.5
Hildebrand	Fedors	20.3	18.8	20.5	21.0	21.0
Hansen	δ_d	17.5	20.5	19.4	21.1	21.3
	δ_p	5.7	2.9	3.4	3.6	3.6
	δ_h	7.8	7.2	10.7	11.5	11.6
	δ_t	22.7	22.0	23.9	24.3	24.5
New Group Contribution (from experimental input)						
Hildebrand	Hoy	NA	NA	20.8	21.6	21.3
Hildebrand	Fedors	NA	NA	21.1	21.7	21.7
Hansen	δ_d	NA	NA	20.3	20.6	20.1
	δ_p	NA	NA	4.7	4.7	5.4
	δ_h	NA	NA	7.5	7.7	7.6
	δ_t	NA	NA	22.1	22.5	22.1
Turbidity						
Hildebrand	δ	20.5	24.2	21.1	21.7	NA[b]
Average Hildebrand						
		19.6 ± 1.1	20.9 ± 2.6	20.6 ± 0.9	21.0 ± 0.9	20.3 ± 1.1

[a] Data on PMMA are from ref. [42,58,59]

[b] Unable to determine due to the insoluble nature

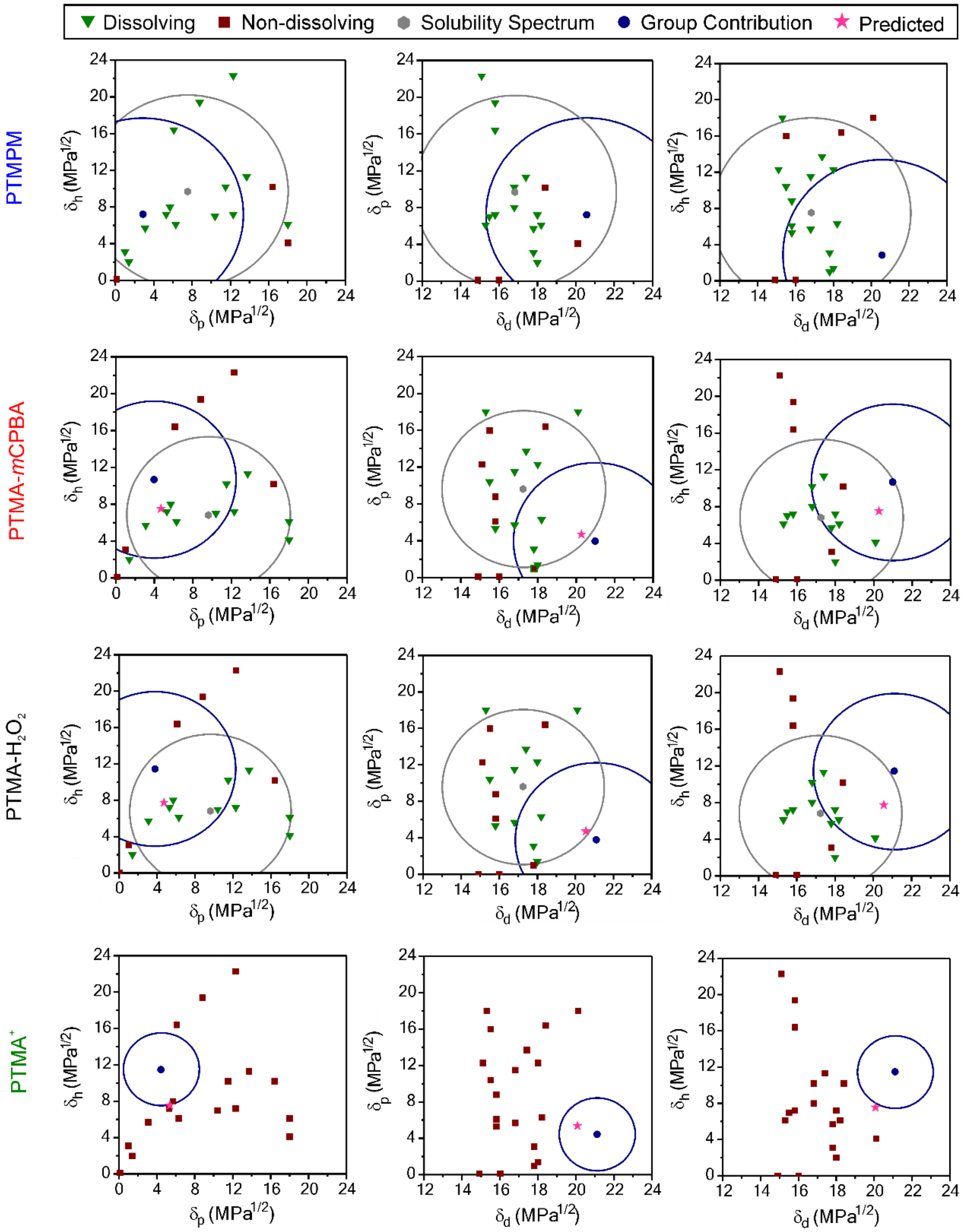

Figure 2.3. The solubility surface projections of the Hansen solubility parameters for PTMPM, PTMA-*m*CPBA, PTMA-H_2O_2, and PTMA$^+$. Values obtained from both the group contribution and solubility spectrums are used as sphere centers (except PTMA$^+$ which could not be estimated with solubility spectrum due to insolubility). The 3D solubility sphere is presented in Figure S12. Water is off the scale of the graphs due a large δ_h value of 42.4 MPa$^{1/2}$.

From **Figure 2.3**, we determined that the δ_h *vs.* δ_p plot most effectively distinguished dissolving and non-dissolving solvents for the studied polymers. This was concluded because for the three polymers, the δ_h *vs.* δ_p plot exhibited the lowest error for non-dissolving solvents enclosed in the solubility radius. In addition to δ_h indicating solvent compatibility, δ_h also showed the most variation for the three polymers. These results indicate that Hansen solubility parameters are more accurate than Hildebrand solubility for distinguishing macromolecular radical solubility behavior, consistent with past findings for other polymers.[60] From these results, we conclude that the major contributing factor to macromolecular radical solubility is hydrogen bonding interactions with the solvent.

2.3.3. Group Contribution.

In addition to experimental methods, group contribution calculations provide another method to estimate the solubility parameters of polymers. Here, the Hildebrand and Hansen solubility parameters of PTMPM (**Figure S2.9**), PTMA-mCPBA, PTMA-H2O2, and PTMA+ were determined utilizing three group contribution methods (Hoy, Fedors, and Hansen). There are no published group contributions for the nitroxide radical (N-O•) and oxoammonium cation (+N=O) groups, so we applied an estimate using a tertiary amine with a hydroxyl group (N-OH) and an amine with a double-bonded oxygen (-N=O), respectively (**Figure S2.10 – Figure S2.11**). Additionally, PTMA-mCPBA, PTMA-H2O2, and PTMA+ are tri-copolymers (**Figure 2.1**), so the fraction of each functional group was used in the group contribution calculations as a weighted average (**Table S2.4**).[61]

Table 2.1 summarizes the Hoy and Fedors methods estimates of the Hildebrand solubility parameter for PTPMP, PTMA-*m*CPBA, PTMA-H_2O_2, and PTMA$^+$. For PTMA-*m*CPBA, PTMA-H_2O_2, and PTMA$^+$, the estimated Hildebrand solubility parameters from the Hoy method was smaller than those from the Fedors method; a similar difference has been observed elsewhere for poly(methyl methacrylate) and polystyrene.[42,62] However, for PTMPM, these estimated values were equal, which has also been seen previously for a polystyrene derivative.[62]

Hansen solubility parameters (δ_h, δ_p, and δ_d) were also estimated *via* group contribution for the four polymers, **Table 2.1**. The group contribution estimation of the nitroxide and oxoammonium cation groups led to an overestimate of the hydrogen bonding parameter (δ_h) and the dispersion parameter (δ_d), but underestimated the polarity parameter (δ_p), compared to the results from the experimental solubility spectrum. **Figure 2.3.** The solubility surface projections of the Hansen solubility parameters for PTMPM, PTMA-*m*CPBA, PTMA-H_2O_2, and PTMA$^+$. Values obtained from both the group contribution and solubility spectrums are used as sphere centers (except PTMA$^+$ which could not be estimated with solubility spectrum due to insolubility). The 3D solubility sphere is presented in Figure S12. Water is off the scale of the graphs due a large δ_h value of 42.4 MPa$^{1/2}$. plots the solubility projections (in blue) based on these calculated Hansen solubility parameters, while assuming a radius identical to that found from the solubility spectrum.

The solubility parameters calculated from group contribution for PTMA$^+$ are most similar to PTMA-H_2O_2, thus suggesting that both polymers would exhibit similar solution behavior. However, $PTMA^+$ was insoluble in all the solvents used for the solubility spectrum. By comparison the Hansen solubility sphere radius of 4 $MPa^{1/2}$ for $PTMA^+$(**Figure 2.3**) was significantly smaller than the PTMPM or PTMA.

2.3.4. Turbidity Titrations.

For a more accurate experimental description for the polymer's solubility parameter, we next applied turbidity titrations.[45,46,62] In this method, a non-dissolving solvent is titrated into a polymer in a dissolving solvent while monitoring the turbidity using UV-vis spectroscopy. Each polymer was dissolved in six different dissolving solvents, with varying solubility parameters, **Figure 2.4** and **Figure S2.13** – **Figure S2.17**. For each dissolving solvent, two separate titrations were performed: a titration using a non-dissolving solvent of (1) higher solubility parameter and (2) lower solubility parameter. Decane was selected as the non-dissolving solvent with a lower solubility parameter for PTMPM, while diethyl ether (ether) was used for PTMA-*m*CPBA and PTMA-H_2O_2. Dimethyl sulfoxide (DMSO) was selected as the non-dissolving solvent with a higher solubility parameter for all three polymers.

Figure 2.4 shows representative UV-vis spectra and turbidities for PTMPM, PTMA-*m*CPBA, and PTMA-H_2O_2 dissolved in acetone. The turbid point of each of these titrations is indicated by a black colored point (and spectra). For all polymers, the peaks in the spectra between 300 and 350 nm are associated with the addition of the non-dissolving solvent. For PTMA-*m*CPBA and PTMA-H_2O_2, the characteristic absorbance at *ca*. 460 nm is associated with the TEMPO radical.[35] The turbid points for PTMPM occurred at 57 v% decane and 60 v% DMSO; PTMA-*m*CPBA solutions became turbid at

59 v% ether and 82 v% DMSO; and PTMA-H_2O_2 solutions became turbid at 83 v% ether and 80 v% DMSO.

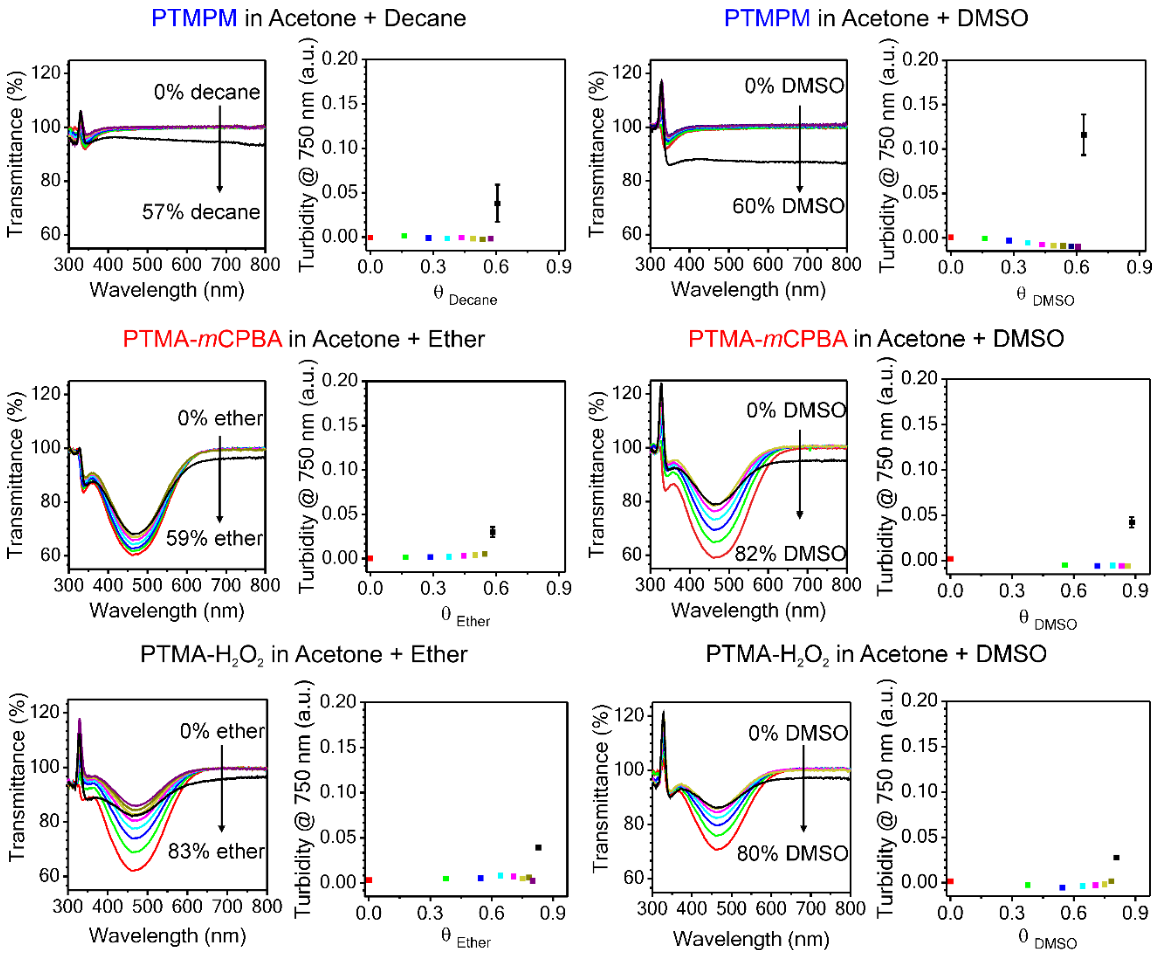

Figure 2.4. Representative UV-vis spectra for the turbidity titrations of PTMPM, PTMA-*m*CPBA, and PTMA-H_2O_2 dissolved in acetone. The turbid point is indicated by a black spectra and corresponding black point in the turbidity plot. θ is the volume fraction of the subscripted solvent.

The volume fraction of non-dissolving solvent at the turbid point was used to calculate the theoretical polymer solubility parameter (δ_2'), **Figure 2.5** and **Table S2.5 – Table S2.7**. δ_2' values were used to determine a line of best fit, and the intersection of that line with $\delta_2 = \delta_1$ was taken as the polymer's solubility parameter. As a result, the Hildebrand solubility parameters were 24.2 MPa$^{1/2}$ for PTMPM, 21.1 MPa$^{1/2}$ for PTMA-*m*CPBA, and 21.7 MPa$^{1/2}$ for PTMA-H_2O_2 (**Table 2.1**). An example calculation for PTMA-*m*CPBA in acetone is shown in **Figure S2.18**. Of the solvents examined in this work, the ones with the most similar solubility parameters are acetonitrile for PTMPM, acetone for PTMA-*m*CPBA, and dimethylformamide for PTMA-H_2O_2.

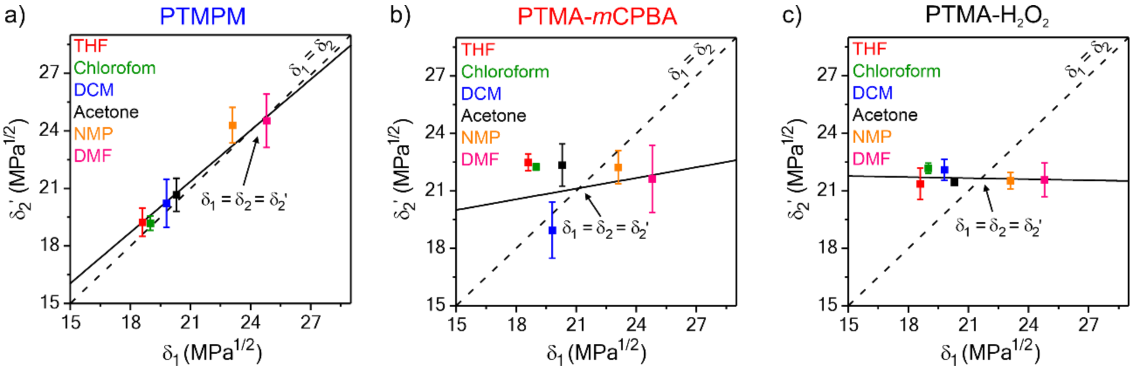

Figure 2.5. δ_2' values for a) PTMPM, b) PTMA-*m*CPBA, and c) PTMA-H_2O_2 plotted against the dissolving solvent used for the titration. The intersection of the line of best fit with $\delta_2 = \delta_1$ provides an estimate of the polymer's solubility parameter. Error bars were calculated using standard error propagation.

2.3.5. Calculation of Nitroxide and Oxoammonium Group Contribution Values.

Using the estimated values of the Hildebrand parameter from the turbidity titrations and the estimated Hansen solubility parameter values from the solubility spectrum, the group contribution values of the nitroxide group (N-O∙) and the oxoammonium cation (+N=O) were estimated. Here we chose to use the Hildebrand parameter determined from turbidity titrations due to improved sensitivity compared to the solubility spectrum, whereas the solubility spectrum must be used for the Hansen parameters.

For the nitroxide radical the molar volume contribution was assumed to match that of -N-O, or 19.0 $cm^3 \cdot mol^{-1}$ for the Hoy method and -5.2 $cm^3 \cdot mol^{-1}$ for the Fedors method, whereas the oxoammonium cation group molar volume contribution was assumed to match that of -N=O, or 18.9 $cm^3 \cdot mol^{-1}$ for the Hoy method and 8.8 $cm^3 \cdot mol^{-1}$ for the Fedors method. The resulting group contribution values for both groups are summarized in **Table 2.2**.

Table 2.2. The estimated group contribution values of the nitroxide radical group (N-O•) and the oxoammonium cation (+N=O) for the Hoy, Fedors, and Hansen methods. Details of the calculations and an example are in the Supplementary Information.

	Hoy Method	**Fedors Method**	**Hansen Method**		
Group	***F*** **($J^{1/2}\cdot cm^{3/2}\cdot mol^{-1}$)**	***U*** **($kJ\cdot mol^{-1}$)**	**F_d ($J^{1/2}\cdot cm^{3/2}\cdot mol^{-1}$)**	**F_p ($J^{1/2}\cdot cm^{3/2}\cdot mol^{-1}$)**	**U_h ($J\cdot mol^{-1}$)**
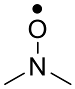	1410.0	39.7	10	801	5000
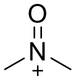	654.5	17.0	-409	1377	0

For the Hoy method, the nitroxide radical value is similar to a urethane group (-OCONH-) with a value of 1261.9 $J^{1/2}\cdot cm^{3/2}\cdot mol^{-1}$, whereas the value for the oxoammonium cation is similar to an ether (-O-), or 235.2 $J^{1/2}\cdot cm^{3/2}\cdot mol^{-1}$.[42] For the Fedors method, the nitroxide radical value is similar to a substituted urea (-NHCON<) with a value of 41.9 $kJ\cdot mol^{-1}$, while the oxoammonium cation estimate is similar to an *O*-hydroxylamine or 19.1 $kJ\cdot mol^{-1}$.[42]

Using the estimated values of the Hansen solubility parameters from the solubility spectrum, the F_d, F_p, and U_h group contribution values of the nitroxide group (N-O•) and the oxoammonium cation (+N=O) were estimated. For the nitroxide group estimate, the molar volume was assumed to match -N-O or -5.1 $cm^3\cdot mol^{-1}$, whereas the oxoammonium cation group molar volume was assumed to match -N=O or 7.8 $cm^3\cdot mol^{-1}$. The resulting dispersion, polarity, and hydrogen bonding group contribution values are summarized in **Table 2.2**.

Using the group contribution values determined above, new solubility parameter values were predicted for PTMA-*m*CPBA, PTMA-H_2O_2, and PTMA$^+$ using the Hoy, Fedors, and Hansen methods. These predicted Hansen solubility parameter values are indicated with a star in **Figure 2.3.**

2.3.6. Predictions Using the New Group Contribution Values and Applications of PTMA's Solubility Parameter.

Using the group contribution values determined above for the nitroxide radical, we predicted the hydrogen bonding and dispersion Hansen solubility parameters for other nitroxide-based macromolecular radicals, **Figure 2.6 a**. The macromolecular radicals considered were poly(TEMPO norbornene) (PTNB), poly (TEMPO acrylamide) (PTAm), poly (TEMPO vinyl ether) (PTVE), and poly (TEMPO ethylene oxide) (PTEO), assuming 100% radical functionalization, **Table S2.8**. However, 100% radical functionalization is rarely achieved in practice. These other macromolecular radicals had larger δ_h and δ_d values, as well as smaller δ_p values, than PTMA-H_2O_2 and PTMA-*m*CPBA. Specifically, the δ_h value of PTAm was the smallest, whereas PTNB had the largest δ_h value of the considered macromolecular radicals. Due to the large δ_h values, we would expect PTNB to dissolve in solvents of higher hydrogen bonding affinity as shown by Suga *et al.* in ethyl lactate (δ_h.= 12.5 MPa$^{1/2}$).[63]

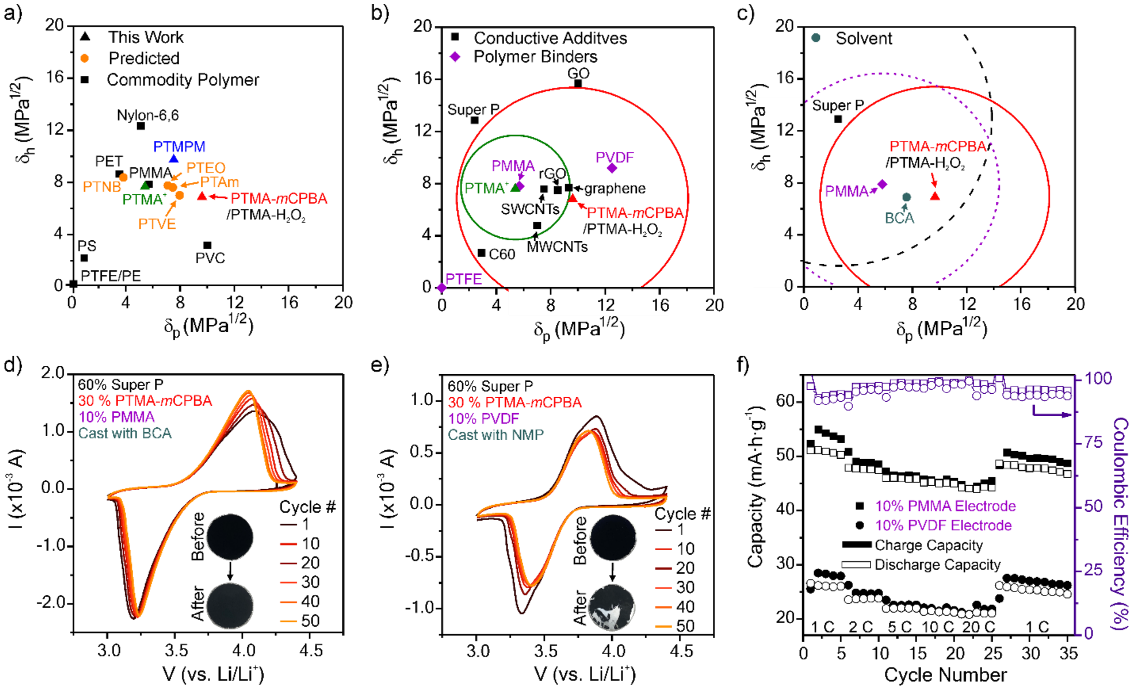

Figure 2.6. Hydrogen bonding and polar Hansen parameters for a) PTMPM (blue), PTMA-*m*CPBA (red), PTMA-H_2O_2 (same as PTMA-mCPBA here), PTMA$^+$ (green), for other macromolecular radicals as predicted in Table S8 (orange), and for other commodity polymers. Hanson parameters for b) Conductive additives and polymer binders compared to PTMA-*m*CPBA, PTMA-H_2O_2, and PTMA$^+$ and for c) 2-butoxyethyl acetate (BCA), which was the predicted "optimal" solvent for processing the proposed PTMA composite electrode with Super P and PMMA. Cyclic voltammetry at 10 mV·s^{-1} for a two-electrode lithium metal half-cell of a PTMA composite electrode containing d) the predicted PMMA binder and e) the control PVDF binder. f) The galvanostatic charge-discharge rate performance for the electrodes containing the predicted and control binders. The electrolyte was 1 M $LiPF_6$ in EC/DEC (1/1, v/v) and the counter and reference electrodes were lithium metal.

In addition to predicting the solubility parameters of other macromolecular radicals, the solubility parameters for PTMA and PTMA$^+$ were also used to evaluate common conductive additives, polymer binder, and processing solvents for the fabrication of homogenous PTMA-based composite electrodes, **Figure 2.6 b**. Here, we considered the Hansen solubility parameters for single-walled carbon nanotubes (SWCNTs),[37,64,65] multi-walled carbon nanotubes (MWCNTs),[66,67] graphene,[68] $Ti_3C_2T_x$ MXene nanosheets,[64,69] fullerene (C60),[64,70] Super P carbon black,[38] graphene oxide (GO),[64] and reduced graphene oxide (rGO) as conductive additives[64] and PVDF,[71] PTFE,[42] and PMMA as binder polymers.[72,73] Most of these have been used as additives in PTMA cathodes previously.[11,18,25,29,30,32,33,35,74-77] For the best interactions among components, the Hansen parameters should be similar (or have overlapping solubility spheres) to result in an increased cohesion among all the components and to promote the formation of a percolating network of conductive additives.[37,50]

From these considerations, the conductive additives with similar Hansen solubility parameters to both PTMA and $PTMA^+$ were SWCNTs, MWCNTs, rGO, and Super P. Additionally, the binder polymer with Hansen solubility parameters most similar to PTMA, $PTMA^+$, and Super P was PMMA, which has not yet been tested in PTMA-based electrodes. Finally, the projections of the three components (PTMA, Super P, and PMMA) were considered to identify a casting solvent with favorable interactions for all the components, **Figure 2.6 c.** By examination of the overlapping areas, we identified 2-butoxyethyl acetate (BCA) as a possible solvent for electrode fabrication. BCA has been previously used to fabricate electrodes with PMMA but not with PTMA or a composite of all three.[78,79] The resulting electrodes exhibited a characteristic quasi-reversible redox couple at 3.63 V *vs*. Li/Li^+ that is associated with PTMA. There was an increase in peak current for the predicted electrode and a decrease in peak current for the control electrode (containing PVDF and processed using NMP) over the 50 cyclic voltammetry cycles,

Figure 2.6 d-e. Finally, the control electrode exhibited a lower initial capacity of 28.5 mA·h·g^{-1} with 92% capacity retention after 35 cycles, whereas the predicted electrode exhibited an initial capacity of 54.9 mA·h·g^{-1} with 89% capacity retention after 35 cycles, **Figure 2.6 f**. These results confirm the importance of selecting appropriate additives and casting solvents for electrode processing.

Finally, we used the measured PTMA Hansen solubility parameters to recommend a non-dissolving electrolyte solvent. This work has so far identified that the hydrogen bonding Hansen solubility parameter (δ_h) is the largest factor impacting the dissolution of PTMA into the electrolyte. For example, many of the linear and cyclic carbonates currently used as electrolytes have δ_h values similar to that of PTMA (between 4.1 MPa$^{1/2}$ to 6.1 MPa$^{1/2}$ vs 6.8 MPa$^{1/2}$, respectively), so it is not surprising that dissolution has been a long-standing issue. **Figure 2.6 f** is one such example, in which capacity fade gradually occurred in EC/DEC solvent. However, solvents with larger δ_h values, such as isopropyl alcohol, 1,2-propanediol, ethanol, and dimethyl sulfoxide (DMSO), do not dissolve PTMA, but not all of these solvents are suitable battery electrolytes. Other considerations include the electrolyte's dielectric constant (ε) and electrochemical stability.[34,80-82] For example, DMSO is predicted to be a non-dissolving solvent and has been studied as an electrolyte solvent in Li-O_2 batteries.[83,84] However, our attempts with DMSO have yielded no PTMA electroactivity, possibly due to a reaction of the oxoammonium cation with the DMSO.[85] We also tested glycerol carbonate/dimethyl carbonate (DMC) electrolyte (DMC must be added to reduce the viscosity); however, the resulting electrochemical performance was still poor. These results indicate that solubility/non-solubility of the electrolyte solvent are important but must be balanced with the viscosity and electrolyte penetration for optimal electrochemical performance.

2.3.7. Comparison to PMMA.

The studied polymers' backbones are structurally similar to PMMA, so comparisons will provide insight into the effect of the side groups, **Table 2.1**. In general, the macromolecular radicals (and precursor PTMPM) had larger Hildebrand solubility parameters (by 0.7 to 1.4 $MPa^{1/2}$) than PMMA, which is attributed to the added side groups.[42,59] However, when considering the Hansen solubility parameters, both PTMA-*m*CPBA and PTMA-H_2O_2 exhibited a decrease or a similar (depending on method of determination) δ_h compared to PMMA. This decrease or unchanged value is due to the lack of hydrogen bonding from the TEMPO and oxoammonium cation groups. Despite the decreased or similar δ_h values, our general observation is that the two PTMA's are soluble in fewer solvents (as compared to PMMA) due to the smaller solubility sphere radii (8.5 $MPa^{1/2}$ *vs*. 11.1 $MPa^{1/2}$). In contrast, PTMPM was soluble in many solvents because of the increased δ_h-value attribute to the hydrogen bonding capability of the piperidine-based side group. In general, although PTMPM was more soluble than PTMA, PMMA is soluble in a greater number of solvents, due to its larger solubility sphere radii.

2.3.8. Limitations and Assumptions.

In this work assumptions were made that could lead to errors or limit the findings' scope. Perhaps the most influential assumption was that that the oxoammonium group's counter anion did not affect the solubility of the polymers. Specifically, the counter anion was not considered in the estimation of molar volumes for group contribution calculations.

Large changes in solubility have been observed for polymerized ionic liquids with various counterions, so similar effects could apply to this work.[86] Also of note, we considered only a single molar mass for each polymer, but solubility is heavily dependent on molar mass. Specifically, Zhang *et al.* previously demonstrated decreased PTMA solubility as molar mass increased.[25]

As for group contribution calculations, the contributions for the oxoammonium cation and nitroxide radical were not known *a priori*, so we approximated those groups as -N=O and N-OH, respectively, which was not an exact representation. Additionally, our method used to back-calculate the Hansen solubility group contribution values for the nitroxide radical and oxoammonium cation groups was limited because of the indirect experimental methods used.

Finally, the insoluble nature of PTMA$^+$ prevented experimental determination of the solubility parameter, which would be important because the fully oxidized form of PTMA is generated in energy storage and electronic applications during use. However, we do conclude that PTMA$^+$ would exhibit little-to-no dissolution in current electrolyte solvents (*i.e.*, acetonitrile and propylene carbonate), which is a desirable feature.

2.3.9. Conclusions

In summary, we determined the Hildebrand and Hansen solubility parameters of PTMPM, PTMA (from both *m*CPBA and H_2O_2 oxidation), and PTMA$^+$. This work indicates that the Hansen solubility parameters provide more descriptive insights for the studied polymer's solubility behavior. Specifically, the hydrogen bonding Hansen solubility parameter (δ_h) and the solubility sphere radii (R) provide the best prediction of the polymer's interactions with solvents and electrode additives. Furthermore, we used the experimentally determined Hildebrand and Hansen solubility parameters to determine group contribution values for the nitroxide and oxoammonium cation, which may be used to determine the solubility parameters of other nitroxide-based macromolecular radicals for the future. Finally, we used the determined solubility parameters to select electrode additives and casting solvents to fabricate a PTMA-based composite electrode that out-performed a control-based electrode.

Future studies should focus on studying the oxidized form in-depth to better identify potential electrolytes and on examining the effect of counter anion type on the solubility behavior (not considered in this work). Identification of future electrolyte solvents should focus on increasing the δ_h-value of the electrolyte solvent in addition to the dielectric constant to prevent dissolution and related capacity fade of PTMA from PTMA-based electrodes.

2.4. References

4. Muench, S., Wild, A., Friebe, C., Häupler, B., Janoschka, T. & Schubert, U. S. Polymer-Based Organic Batteries. *Chem. Rev.* **116**, 9438-9484 (2016).

10. Nishide, H., Iwasa, S., Pu, Y.-J., Suga, T., Nakahara, K. & Satoh, M. Organic radical battery: nitroxide polymers as a cathode-active material. *Electrochim. Acta* **50**, 827-831 (2004).

11. Kim, J.-K., Ahn, J.-H., Cheruvally, G., Chauhan, G. S., Choi, J.-W., Kim, D.-S., Ahn, H.-J., Lee, S. H. & Song, C. E. Electrochemical properties of rechargeable organic radical battery with PTMA cathode. *Metals and Materials International* **15**, 77-82 (2009).

13. Wild, A., Strumpf, M., Häupler, B., Hager, M. D. & Schubert, U. S. All-Organic Battery Composed of Thianthrene- and TCAQ-Based Polymers. *Advanced Energy Materials* **7**, 1601415 (2017).

18. Kim, J.-K., Cheruvally, G., Ahn, J.-H., Seo, Y.-G., Choi, D. S., Lee, S.-H. & Song, C. E. Organic radical battery with PTMA cathode: Effect of PTMA content on electrochemical properties. *Journal of Industrial and Engineering Chemistry* **14**, 371-376 (2008).

19. Wang, S., Easley, A. D. & Lutkenhaus, J. L. 100th Anniversary of Macromolecular Science Viewpoint: Fundamentals for the Future of Macromolecular Nitroxide Radicals. *ACS Macro Letters* **9**, 358-370 (2020).

21. Zhang, Y., Park, A., Cintora, A., McMillan, S. R., Harmon, N. J., Moehle, A., Flatté, M. E., Fuchs, G. D. & Ober, C. K. Impact of the synthesis method on the solid-state charge transport of radical polymers. *Journal of Materials Chemistry C* **6**, 111-118 (2018).

23. Easley, A. D., Vukin, L. M., Flouda, P., Howard, D. L., Pena, J. L. & Lutkenhaus, J. L. Nitroxide Radical Polymer–Solvent Interactions and Solubility Parameter Determination. *Macromolecules* **53**, 7997-8008 (2020).

24. Wang, S., Li, F., Easley, A. D. & Lutkenhaus, J. L. Real-time insight into the doping mechanism of redox-active organic radical polymers. *Nature Materials* **18**, 69-75 (2019).

25. Zhang, K., Hu, Y., Wang, L., Fan, J., Monteiro, M. J. & Jia, Z. The impact of the molecular weight on the electrochemical properties of poly(TEMPO methacrylate). *Polymer Chemistry* **8**, 1815-1823 (2017).

28. Nakahara, K., Iwasa, S., Satoh, M., Morioka, Y., Iriyama, J., Suguro, M. & Hasegawa, E. Rechargeable batteries with organic radical cathodes. *Chem. Phys. Lett.* **359**, 351-354 (2002).

29. Nakahara, K., Iriyama, J., Iwasa, S., Suguro, M., Satoh, M. & Cairns, E. J. Cell properties for modified PTMA cathodes of organic radical batteries. *J. Power Sources* **165**, 398-402 (2007).

30. Wang, S., Park, A. M. G., Flouda, P., Easley, A. D., Li, F., Ma, T., Fuchs, G. D. & Lutkenhaus, J. L. Solution-Processable Thermally Crosslinked Organic Radical Polymer Battery Cathodes. *ChemSusChem* **13**, 2371 (2020).

31. Kim, J.-K., Cheruvally, G., Choi, J.-W., Ahn, J.-H., Lee, S. H., Choi, D. S. & Song, C. E. Effect of radical polymer cathode thickness on the electrochemical performance of organic radical battery. *Solid State Ionics* **178**, 1546-1551 (2007).

32. Nakahara, K., Iriyama, J., Iwasa, S., Suguro, M., Satoh, M. & Cairns, E. J. Al-laminated film packaged organic radical battery for high-power applications. *J. Power Sources* **163**, 1110-1113 (2007).

33. Nakahara, K., Iriyama, J., Iwasa, S., Suguro, M., Satoh, M. & Cairns, E. J. High-rate capable organic radical cathodes for lithium rechargeable batteries. *J. Power Sources* **165**, 870-873 (2007).

34. Gerlach, P. & Balducci, A. A critical analysis about the underestimated role of the electrolyte in batteries based on organic materials. *ChemElectroChem* **7**, 2364 (2020).

35. Bugnon, L., Morton, C. J. H., Novak, P., Vetter, J. & Nesvadba, P. Synthesis of Poly(4-methacryloyloxy-TEMPO) via Group-Transfer Polymerization and Its Evaluation in Organic Radical Battery. *Chem. Mater.* **19**, 2910-2914 (2007).

36. Suwa, K., Oyaizu, K., Segawa, H. & Nishide, H. Anti-Oxidizing Radical Polymer-Incorporated Perovskite Layers and their Photovoltaic Characteristics in Solar Cells. *ChemSusChem* **12**, 5207-5212 (2019).

37. Ata, S., Mizuno, T., Nishizawa, A., Subramaniam, C., Futaba, D. N. & Hata, K. Influence of matching solubility parameter of polymer matrix and CNT on electrical conductivity of CNT/rubber composite. *Scientific Reports* **4**, 7232 (2014).

38. Kwon, Y. H., Huie, M. M., Choi, D., Chang, M., Marschilok, A. C., Takeuchi, K. J., Takeuchi, E. S. & Reichmanis, E. Toward Uniformly Dispersed Battery Electrode Composite Materials: Characteristics and Performance. *ACS Applied Materials & Interfaces* **8**, 3452-3463 (2016).

39. Flory, P. J. *Principles of Polymer Chemistry*. (Cornell University Press, 1953).

40. Fedors, R. F. A method for estimating both the solubility parameters and molar volumes of liquids. *Polymer Engineering & Science* **14**, 147-154 (1974).

41. Meusburger, K. E. in *Pesticide Formulations* Vol. 371 *ACS Symposium Series* Ch. 14, 151-162 (American Chemical Society, 1988).

42. Barton, A. F. M. *CRC Handbook of Solubility Parameters and Other Cohesion Parameters, Second Edition*. (Taylor & Francis, 1991).

43. Mangaraj, D., Patra, S. & Roy, P. C. Cohesive energy density of high polymers. Part V. C. E. D. of polymethacrylates. *Die Makromolekulare Chemie* **81**, 173-179 (1965).

44. Mangarj, D., Bhatnagar, S. K. & Rath, S. B. Cohesive-energy-densities of high polymers. Part. III. Estimation of C. E. D. by viscosity measurements. *Die Makromolekulare Chemie* **67**, 75-83 (1963).

45. Suh, K. W. & Clarke, D. H. Cohesive energy densities of polymers from turbidimetric titrations. *Journal of Polymer Science Part A-1: Polymer Chemistry* **5**, 1671-1681 (1967).

46. Suh, K. W. & Corbett, J. M. Solubility parameters of polymers from turbidimetric titrations. *J. Appl. Polym. Sci.* **12**, 2359-2370 (1968).

47. Qian, J., Wiener, C. G., Zhu, Y. & Vogt, B. D. Swelling and plasticization of polymeric binders by Li-containing carbonate electrolytes using quartz crystal microbalance with dissipation. *Polymer* **143**, 237-244 (2018).

48. Howell, J., Roesing, M. & Boucher, D. A Functional Approach to Solubility Parameter Computations. *The Journal of Physical Chemistry B* **121**, 4191-4201 (2017).

49. Hansen, C. M. The three dimensional solubility parameter. *Danish Technical: Copenhagen* **14** (1967).

50. Seo, J., Singh, A. K., Zhang, Y., Ma, J., Bakis, C. E., Rahn, C. D. & Hickner, M. A. Electrolyte-resistant epoxy for bonding batteries based on sandwich structures. *J. Appl. Polym. Sci.* **135**, 46059 (2018).

51. Rostro, L., Baradwaj, A. G. & Boudouris, B. W. Controlled Radical Polymerization and Quantification of Solid State Electrical Conductivities of Macromolecules Bearing Pendant Stable Radical Groups. *ACS Applied Materials & Interfaces* **5**, 9896-9901 (2013).

52. Bobbitt, J. M. Oxoammonium Salts. 6.1 4-Acetylamino-2,2,6,6-tetramethylpiperidine-1-oxoammonium Perchlorate: A Stable and Convenient Reagent for the Oxidation of Alcohols. Silica Gel Catalysis. *The Journal of Organic Chemistry* **63**, 9367-9374 (1998).

53. Mercadante, M. A., Kelly, C. B., Bobbitt, J. M., Tilley, L. J. & Leadbeater, N. E. Synthesis of 4-acetamido-2,2,6,6-tetramethylpiperidine-1-oxoammonium tetrafluoroborate and 4-acetamido-(2,2,6,6-tetramethyl-piperidin-1-yl)oxyl and their use in oxidative reactions. *Nature Protocols* **8**, 666-676 (2013).

54. Khodeir, M., Ernould, B., Brassinne, J., Ghiassinejad, S., Jia, H., Antoun, S., Friebe, C., Schubert, U. S., Kochovski, Z., Lu, Y., Van Ruymbeke, E. & Gohy, J.-F. Synthesis and characterisation of redox hydrogels based on stable nitroxide radicals. *Soft Matter* **15**, 6418-6426 (2019).

55. Aqil, A., Vlad, A., Piedboeuf, M.-L., Aqil, M., Job, N., Melinte, S., Detrembleur, C. & Jérôme, C. A new design of organic radical batteries (ORBs): carbon nanotube buckypaper electrode functionalized by electrografting. *Chem. Commun.* **51**, 9301-9304 (2015).

56. Rostro, L., Wong, S. H. & Boudouris, B. W. Solid State Electrical Conductivity of Radical Polymers as a Function of Pendant Group Oxidation State. *Macromolecules* **47**, 3713-3719 (2014).

57. Liang, W. Effect of structure of polymeric hindered amines on the oxidation of polymers: Part 1—Syntheses of polymeric hindered piperidyl esters. *Polym. Degrad. Stab.* **31**, 353-364 (1991).

58. Koenhen, D. M. & Smolders, C. A. The determination of solubility parameters of solvents and polymers by means of correlations with other physical quantities. *J. Appl. Polym. Sci.* **19**, 1163-1179 (1975).

59. Barton, A. F. M. *CRC handbook of polymer-liquid interaction parameters and solubility parameters*. (1991).

60. Venkatram, S., Kim, C., Chandrasekaran, A. & Ramprasad, R. Critical Assessment of the Hildebrand and Hansen Solubility Parameters for Polymers. *Journal of Chemical Information and Modeling* **59**, 4188-4194 (2019).

61. Matsuura, T., Blais, P. & Sourirajan, S. Polar and nonpolar parameters for polymeric reverse osmosis membrane materials from liquid chromatographic data. *J. Appl. Polym. Sci.* **20**, 1515-1531 (1976).

62. Arichi, S. & Himuro, S. Solubility parameters of poly(4-acetoxystyrene) and poly(4-hydroxystyrene). *Polymer* **30**, 686-692 (1989).

63. Suga, T., Konishi, H. & Nishide, H. Photocrosslinked nitroxide polymer cathode-active materials for application in an organic-based paper battery. *Chem. Commun.*, 1730-1732 (2007).

64. Qin, J., Wang, X., Jiang, Q. & Cao, M. Optimizing Dispersion, Exfoliation, Synthesis, and Device Fabrication of Inorganic Nanomaterials Using Hansen Solubility Parameters. *ChemPhysChem* **20**, 1069-1097 (2019).

65. Bergin, S. D., Nicolosi, V., Streich, P. V., Giordani, S., Sun, Z., Windle, A. H., Ryan, P., Niraj, N. P. P., Wang, Z.-T. T., Carpenter, L., Blau, W. J., Boland, J. J., Hamilton, J. P. & Coleman, J. N. Towards Solutions of Single-Walled Carbon Nanotubes in Common Solvents. *Adv. Mater.* **20**, 1876-1881 (2008).

66. Clark, M. D. & Krishnamoorti, R. Dispersion of Functionalized Multiwalled Carbon Nanotubes. *The Journal of Physical Chemistry C* **113**, 20861-20868 (2009).

67. Detriche, S., Zorzini, G., Colomer, J.-F., Fonseca, A. & Nagy, J. B. Application of the Hansen Solubility Parameters Theory to Carbon Nanotubes. *Journal of Nanoscience and Nanotechnology* **8**, 6082-6092 (2008).

68. Hernandez, Y., Lotya, M., Rickard, D., Bergin, S. D. & Coleman, J. N. Measurement of Multicomponent Solubility Parameters for Graphene Facilitates Solvent Discovery. *Langmuir* **26**, 3208-3213 (2010).

69. Maleski, K., Mochalin, V. N. & Gogotsi, Y. Dispersions of Two-Dimensional Titanium Carbide MXene in Organic Solvents. *Chem. Mater.* **29**, 1632-1640 (2017).

70. Hansen, C. M. & Smith, A. L. Using Hansen solubility parameters to correlate solubility of C60 fullerene in organic solvents and in polymers. *Carbon* **42**, 1591-1597 (2004).

71. Bottino, A., Capannelli, G., Munari, S. & Turturro, A. Solubility parameters of poly(vinylidene fluoride). *J. Polym. Sci., Part B: Polym. Phys.* **26**, 785-794 (1988).

72. Camacho, J., Díez, E., Díaz, I. & Ovejero, G. Hansen solubility parameter: from polyethylene and poly(vinyl acetate) homopolymers to ethylene–vinyl acetate copolymers. *Polym. Int.* **66**, 1013-1020 (2017).

73. Bresser, D., Buchholz, D., Moretti, A., Varzi, A. & Passerini, S. Alternative binders for sustainable electrochemical energy storage – the transition to aqueous electrode processing and bio-derived polymers. *Energy & Environmental Science* **11**, 3096-3127 (2018).

74. Deng, L.-f., Li, X.-h., Xiao, L.-x. & Zhang, Y.-h. Synthesis and electrochemical properties of polyradical cathode material for lithium second batteries. *Journal of Central South University of Technology* **10**, 190-194 (2003).

75. Kim, J.-K., Cheruvally, G., Choi, J.-W., Ahn, J.-H., Choi, D. S. & Song, C. E. Rechargeable Organic Radical Battery with Electrospun, Fibrous Membrane-Based Polymer Electrolyte. *J. Electrochem. Soc.* **154**, A839 (2007).

76. Kim, Y., Jo, C., Lee, J., Lee, C. W. & Yoon, S. An ordered nanocomposite of organic radical polymer and mesocellular carbon foam as cathode material in lithium ion batteries. *J. Mater. Chem.* **22**, 1453-1458 (2012).

77. Guo, W., Yin, Y.-X., Xin, S., Guo, Y.-G. & Wan, L.-J. Superior radical polymer cathode material with a two-electron process redox reaction promoted by graphene. *Energy & Environmental Science* **5**, 5221-5225 (2012).

78. Ogihara, H., Kibayashi, H. & Saji, T. Microcontact Printing for Patterning Carbon Nanotube/Polymer Composite Films with Electrical Conductivity. *ACS Applied Materials & Interfaces* **4**, 4891-4897 (2012).

79. Park, J. W., Shin, D. K., Ahn, J. & Lee, J. Y. Thermal property of transparent silver nanowire films. *Semicond. Sci. Technol.* **29**, 015002 (2013).

80. Phadke, S., Cao, M. & Anouti, M. Approaches to Electrolyte Solvent Selection for Poly-Anthraquinone Sulfide Organic Electrode Material. *ChemSusChem* **11**, 965-974 (2018).

81. Yanliang Liang, Y. Y. Advancing Electrolytes Towards Stable Organic Batteries. *General Chemistry* **3**, 207-212 (2017).

82. Amanchukwu, C. V. The Electrolyte Frontier: A Manifesto. *Joule* **4**, 281-285 (2020).

83. Peng, Z., Freunberger, S. A., Chen, Y. & Bruce, P. G. A Reversible and Higher-Rate Li-O_2 Battery. *Science* **337**, 563 (2012).

84. Liu, B., Xu, W., Yan, P., Kim, S. T., Engelhard, M. H., Sun, X., Mei, D., Cho, J., Wang, C.-M. & Zhang, J.-G. Stabilization of Li Metal Anode in DMSO-Based Electrolytes via Optimization of Salt–Solvent Coordination for Li–O2 Batteries. *Advanced Energy Materials* **7**, 1602605 (2017).

85. Bobbitt, J. M. in *TCIMAIL* Vol. 146 (TCI America, 2011).

86. Hurisso, B. B., Lovelock, K. R. J. & Licence, P. Amino acid-based ionic liquids: using XPS to probe the electronic environment via binding energies. *Physical Chemistry Chemical Physics* **13**, 17737-17748 (2011).

3. LAYER-BY-LAYER NANOARCHITECTONICS OF ELECTROCHEMICALLY ACTIVE THIN FILMS COMPRISED OF RADICAL-CONTAINING POLYMERS[*]

3.1. Introduction

Electroactive coatings (EACs) are thin films that contain redox-active species that undergo reduction and oxidation. EACs are promising for improved device performance in corrosion protection, actuators,[88] organic electronics,[89,90] and energy storage.[91] In recent years, there has been an increased focus on developing EACs for organic energy storage devices, which utilize redox-active polymers as the coating material.[92] There are two main classes of redox-active polymers used in EACs, conjugated polymers (*e.g.*, polyaniline) and non-conjugated polymers (*e.g.*, poly(TEMPO methacrylate), PTMA). The majority of work on EACs has centered on conjugated polymers due to the ease of their synthesis and deposition, but conjugated polymers can be limited in their practical capacity due to incomplete charge transfer and self-discharge.[93] On the other hand, non-conjugated polymers bear near-theoretical capacities and less self-discharge.[94] This is because the redox activity of non-conjugated polymers is based upon the reversible oxidation-reduction of a pendant active group that bears electronic charge locally; in contrast, conjugated polymers accommodate charge in a delocalized fashion.

---

[*] Reproduced with permissions from ref. 87. Easley, A., Shaligram, S., Echols, I., Nixon, K., Regen, S. & Lutkenhaus, J. L. Layer-by-Layer Nanoarchitectonics of Electrochemically Active Thin Films Comprised of Radical-Containing Polymers. *J. Electrochem. Soc.* (2022).. Copyright the Electrochemical Society.

It is desirable to broaden EACs to include non-conjugated polymers, but literature indicates certain challenges exist. These challenges include dissolution of the active material, diffusion limitations, and low areal loading.[19,93] One approach demonstrated to prevent the dissolution of PTMA from EACs was the use of surface-initiated polymerization to polymerize PTMA as brushes from a conductive substrate.[95] This method resulted in coatings up to 84 nm thick, however, the authors demonstrated that as thickness was increased there was a decrease in observed galvanostatic charge-discharge capacity.[95] Another method that prevents dissolution and reduces the diffusion limitations in EACs was a PTMA-polystyrene copolymer that underwent self-assembly from solvent annealing.[96] The authors demonstrated that these 80 nm thin films showed stable galvanostatic cycling performance at high current densities (23.7 $\mu A/cm^2$), but exhibited self-discharge at lower current densities.[96] However, both methods can lead to reduced processability of PTMA and a reduced areal loading of the redox-active unit (due to initiators for surface polymerization and comonomers).

Non-conjugated, redox-active PTMA has been investigated in depth for organic energy storage devices due to PTMA’s synthetic simplicity and solution processability. However, PTMA and other TEMPO-containing polymers are subject to dissolution during operation, leading to a gradual loss of capacity. To prevent dissolution, previous work investigated TEMPO-containing polymers that bore a non-dissolving unit for >100 nm thick electrodes. For example, Tokue *et al.* demonstrated poly(TEMPO methacrylate -*co*-styrenesulfonyl(trifluoromethanesulfonyl)imide) with both TEMPO-containing repeat units and trifluoromethanesulfonylimide ($TFSI^-$) anion-containing repeat units that exhibited only slight capacity fade during battery operation.[97] In contrast, Aqil *et al.* produced ionic liquid homopolymers with both TEMPO and imidazolium cations; however, these polymers also exhibited some capacity fade after battery operation.[98,99] In our own work, we have addressed dissolution by introducing crosslinkable acrylate units.[100] However, none of these approaches addressed thin film applications, which have different challenges, including substrate adhesion and conformability.

As has been demonstrated for conjugated polymers,[101-106] the layer-by-layer (LbL) assembly technique can produce EACs with controllable thickness, good adhesion, and conformal deposition. In the LbL technique, oppositely charged polymers are alternately deposited onto a surface of interest from aqueous solutions, building up layers of polycations and polyanions in a stepwise fashion.[107,108] The internal structure of the film is often highly interdigitated, but stratified structures can be obtained as well.[109-111] Therefore, oppositely charged polymers that are soluble in water are required for strong electrostatic interactions to increase film stability and prevent polymer dissolution. This requirement presents a challenge for the LbL assembly of many non-conjugated redox active polymers because they are often neutral or insoluble in water. For these reasons, LbL assembly has not been widely investigated for non-conjugated redox active polymers, especially for those with TEMPO units. To the best of our knowledge, there exists only two reports of TEMPO-containing LbL films, where one study investigated an LbL film with a nitroxide-containing polyanion[112] and the other study investigated the use of a nitroxide-containing polycation.[113] However these films utilized a complementary polymer that was not redox active, thus diluting the radicals in the film and, therefore, the electroactivity. As of yet, nitroxide-containing polycations and anions have not yet been assembled together or evaluated as LbL thin films

Here, we report the synthesis and electrochemical characterization of a TEMPO-based polycation and polyanion that are suitable to LbL assembly to produce EACs consisting entirely of radical-containing polyelectrolytes. First, the solution-state electrochemical behavior of these charged polymers is considered. The rate constants for electron transfer are determined from cyclic voltammetry and chronoamperometry. Then, the oppositely charged polymers are assessed for their ability to form LbL assemblies of tunable thickness and mass. The LbL mass, spectroscopic, and thickness growth profiles are determined using quartz crystal microbalance, UV-Vis spectroscopy, and profilometry, respectively. Last, we evaluate the electrochemical performance of the LbL thin films using cyclic voltammetry and galvanostatic cycling. Overall, these results present an alternative method for producing TEMPO-based macromolecular radical thin films of tunable thickness and good adhesion.

3.2. Experimental

3.2.1. Materials

Dimethylammonium chloride, 4-oxo-TEMPO, $Ti(O^{i}Pr)_4$, poly(ethylene-alt-maleic anhydride) (M_w = 100,000 - 500,000 g/mol), 4-amino-TEMPO, anhydrous N,N-dimethylformamide, tetrahydrofuran, ethanol, pyridine, diethyl ether, sodium borohydride, branched polyethyleneimine (bPEI, M_w = 25,000 g/mol, M_n = 10,000 g/mol), and hydrochloric acid (HCl, 37% w/w) were purchased from Sigma-Aldrich and used as received. Poly(4-vinylbenzyl chloride) (PVBC) (M_w = 39,500 g/mol, M_n = 22,500 g/mol was purchased from Polymer Source Inc. and used without further purification. Acetone, methanol, dichloromethane (DCM), and sodium chloride (NaCl) from VWR BDH Chemicals were used without any further purification. Ultrapure water (MQ water) was collected from a Milli-Q® water purification system (18 MΩ·cm). Indium tin oxide (ITO)-coated glass (CUV5B) was purchased from Delta Technologies. Ti/Au quartz crystal microbalance 5 MHz substrates (part # 149257-1) were purchased from MAXTEK and cleaned with 5:1:1 MQ H_2O:ammonium hydroxide:hydrogen peroxide at 75 °C for 5 mins before use.

3.2.2. Synthesis of the nitroxide polycation (*1*)

The modified TEMPO group, 4-(*N*,*N*-dimethylamino)-TEMPO, was synthesized as previously described (**Scheme 3.1**).[114] A solution of poly(4-vinylbenzyl chloride) (PVBC), (0.30 g, 1.96 mmol repeat unit) and 4-(*N*,*N*-dimethylamino)-TEMPO (1.184 g, 5.92 mmol) in 8 mL of *N*,*N*-dimethylformamide was stirred at room temperature for 24 h. The mixture was then poured into 20 mL of diethyl ether to precipitate the polymer, followed by trituration (two times) with 20 mL of diethyl ether to give 500 mg (72%) of **1**. Anal. calcd. For $C_{20}H_{34}ClN_2O_2$ (monohydrate) C, 64.93; H, 9.26; Cl, 9,58; N, 7.57. Found: C, 63.48; H, 9.27; Cl, 8.73; N, 8.14.

Scheme 3.1. Synthetic route for the nitroxide polycation.

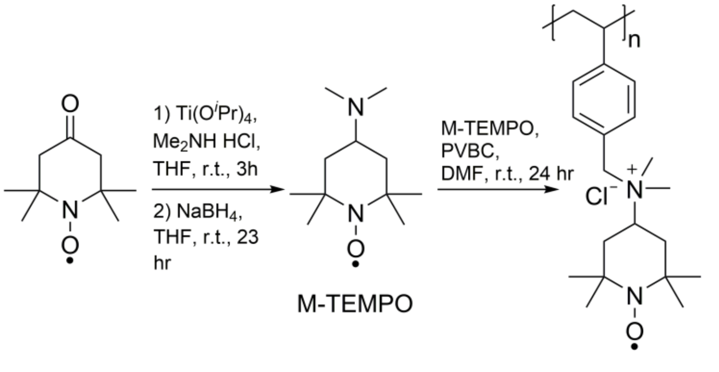

1
Nitroxide Polycation

3.2.3. Synthesis of the nitroxide polyanion (*2*)

The polyanion containing a pendant nitroxide group (nitroxide polyanion) was synthesized following a previous report by Lappan *et al* (**Scheme 3.2**).[115] In summary, a solution was prepared by stirring 0.50 g (3.96 mmol of repeat unit) of poly(ethylene-*alt*-maleic anhydride) in 10 mL of anhydrous pyridine for 3 h at 50°C under an argon atmosphere. To this solution a solution made from 1.71 g (10 mmol) of 4-amino-TEMPO plus 5 mL of anhydrous pyridine was added. The resulting solution was stirred at room temperature for 3 h under an argon atmosphere. The polymer was then isolated by precipitation into 60 mL of *n*-hexane. The polymer was purified by dissolving it in 15 mL of anhydrous pyridine followed by precipitation in 60 mL of *n*-hexane. Subsequent drying under reduced pressure for 24 h at room temperature afforded 1.12 g (94%) of **2**. Anal. calcd. for $C_{15}H_{25}N_2O_4$: C, 60.59; H, 8.47; N, 9.42. Found: C, 58.60; H, 8.90; N, 9.53.

Scheme 3.2. Synthetic route for the nitroxide polyanion (deprotonated carboxylic acid at pH 4).

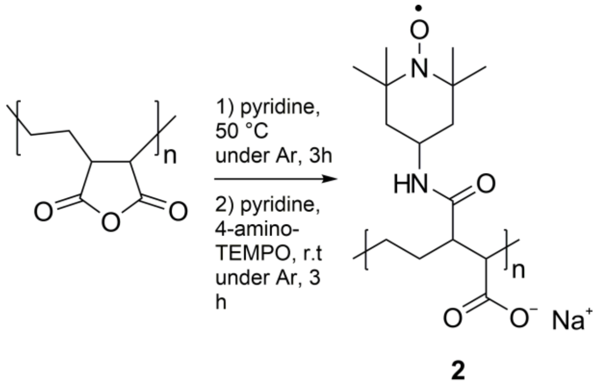

2
Nitroxide Polyanion

3.2.4. Chemical characterization

All IR spectra were recorded on solid samples using a Thermo Scientific Nicolet iS10 spectrometer in attenuated total reflection (ATR) mode. Elemental analysis was performed by Midwest Microlab. Thermal gravimetric analysis (TGA) was performed on a TA Instruments Q50 with a heating rate of 10 °C/ min from ambient temperature to 900 °C under a nitrogen environment (60 mL/min) to identify the 5% degradation temperature (T5d). Differential scanning calorimetry (DSC) was performed using a Q200 DSC (TA Instruments) with a heat–cool–heat cycle. The samples were ramped from −40 °C to T5d at a rate of 5 °C/min. The glass transition temperature was taken as the inflection point of the second heating cycle.

3.2.5. Preparation and characterization of nitroxide polyanion/nitroxide polycation LbL films

LbL films were prepared on ITO-coated glass, which were cleaned before use by subsequent sonication in soap water, water, DCM, methanol, and acetone. After cleaning, the ITO-coated glass was plasma treated for 10 minutes before immediate submersion into a bPEI solution (0.1 wt% in 0.1 M NaCl in H_2O) for 15 minutes followed by a 2-minute rinse in MQ water to generate a base layer on the substrate. After the rinse, the nitroxide polyanion/nitroxide polycation LbL films were deposited using an alternating immersion process. The bPEI-coated substrate was first immersed in a nitroxide polyanion solution (15 mM by polymer repeat unit, 0.1 M NaCl, pH 4) for deposition, followed by 2 min, 1 min, and 1 min rinses in 0.1 M NaCl, pH 4 water. After the three rinses, the substrate was submerged in a nitroxide polycation solution (15 mM by polymer repeat unit, 0.1 M NaCl, pH 4) for 15 min, followed by another three rinses. This cycle completed one layer pair. This process was repeated until the desired number of layer pairs was attained, resulting in bPEI-(nitroxide polyanion/nitroxide polycation)$_n$ films, where n is the number of layer pairs. After assembly, the films were dried at ambient conditions for 24 h. We observed that drying films under vacuum results in the loss of electrochemical activity due to kinetic trapping of the polymer chains.

3.2.6. Film characterization

UV–Vis spectra were collected from 300 nm to 800 nm using a Hitachi U-4100 UV–Vis–NIR spectrophotometer (341-F). Micrographs of the film morphology were collected using optical microscopy (Leica DM4 M) and atomic force microscopy (AFM, Bruker Dimension Icon AFM). Profilometric thickness and root-mean-square (RMS) roughness (R_q) of thin films were measured using a profilometer (KLA Tencor D-100). Quartz crystal microbalance (QCM) (MAXTEK RQCM Research) was used to determine the dry film composition during LbL assembly. The change in frequency was reported after each polymer was deposited and converted to mass using the Sauerbrey equation.

3.2.7. Electrochemical characterization

To confirm the redox behavior of the polymers, solution-state cyclic voltammetry (CV) and chronoamperometry (CA) were used with a three-electrode cell. The working electrode was the LbL film on ITO-coated glass, the counter electrode was platinum wire, and the reference electrode was Ag/AgCl (sat). CV from 0.3 to 1.1 V *vs.* Ag/AgCl for 45 cycles at 50 mV/s was used to determine the polymer's stability. Following the stability cycling, two cycles of CV at 2, 5, 10, 25, 50, and 100 mV/s were conducted, followed by CA with a step from 0.3 to 1.1 V *vs.* Ag/AgCl. The diffusion coefficient of electron transfer (D_{et}) was determined by using the Cottrell equation (**Equation 3.1**), assuming a semi-infinite condition[20]:

$$i = \frac{nFAC_E}{\sqrt{\pi t}}\sqrt{D_{et}} = \tau\frac{nFAC_E}{\sqrt{\pi}}\sqrt{D_{et}}$$

Equation 3.1

where i is the current output from CA (in mA), n is the number of electrons transferred per repeat unit (1 equiv mol^{-1}), A is the electrode area (in cm^2), and C_0^* is the total concentration of redox sites (or repeat units in mol/cm^3). With the determined D_{et} values, the apparent electron transfer rate constant ($k_{ex,app}$) was calculated using the Dahms-Ruff equation (**Equation 3.2**).

$$k_{ex,app} = \frac{6D_{et}}{C_0^* \delta^2}$$

Equation 3.2

where δ is the average site distance determined from MD simulations (discussed below). Finally, the heterogenous rate constant (k^0) was determined using the method of Nicholson (**Equation 3.3**) assuming the diffusion coefficient of the oxidized and reduced species are equal to D_{et}.

$$\psi = \frac{k^0}{(\pi D_{et} f \upsilon)^{1/2}}$$

Equation 3.3

where ψ is a dimensionless rate parameter (using the peak separation from 10 mV/s), *v* is the scan rate of CV (in V s^{-1}), and D_{et} is the diffusion of electron transfer from CA (in cm^2/s). Last, *f* = F/RT, where F is Faraday constant (or 96585 C/mol e^-), R is the gas constant (or 8.3124 J/mol K), and T is the temperature (in K).

To study the electrochemical properties of the LbL film, CV, CA, galvanostatic charge-discharge (GCD), and electrochemical impedance spectroscopy (EIS) were conducted in a similar three-electrode cell, but the working electrode was the LbL film of interest assembled on ITO-coated glass. CV from 0.3 to 1.1 V *vs.* Ag/AgCl was used to condition the films for 45 cycles at 50 mV/s. Following conditioning, two cycles of CV (from 0.3 to 1.1 V *vs.* Ag/AgCl) at 2, 5, 10, 25, 50, 100, 200, and 400 mV/s were conducted to determine a scan rate dependence. After CV testing, GCD was carried out for 5 cycles at 2, 5, 10, and 20 μA/cm^2, followed by 100 cycles at 2 μA/cm^2. Unless otherwise stated, a Solartron potentiostat (Solartron Electrochemical Interface 1287) was used for all electrochemical testing. EIS was conducted at a potential of 0.8 V *vs.* Ag/AgCl (sat.) with an amplitude of 10 mV in a frequency range of 0.1 to 5×10^6 Hz (10 steps per decade).

3.3. Results and Discussion

3.3.1. Synthesis and characterization of the nitroxide polycation and the nitroxide polyanion.

The nitroxide polycation (***1***) was synthesized by installation of 4-(N,N-dimethylamino)-TEMPO to poly(4-vinylbenzyl chloride) (PVBC) (**Scheme 3.1**).[114] 4-(N,N-dimethylamino)-TEMPO was collected from the amination of 4-oxo-TEMPO with dimethylamine hydrochloride, as seen from the appearance of the 1750 cm^{-1} vibration (**Figure S3.1**). Installation of 4-(N,N-dimethylamino)-TEMPO onto PVBC was confirmed by the appearance of the C-N stretching peaks (**Figure S3.2**). The resulting nitroxide polycation degree of polymerization and Đ was assumed to match that of the precursor PVBC (M_n ≈ 22.5 kDa and Đ ≈ 1.8) or 44.6 kDa (**Table 3.1**).

Table 3.1. Polymer and solution-state properties.

Physical property	**Nitroxide Polycation (*1*)**	**Nitroxide Polyanion (*2*)**
# of RUs	147[a]	-[b]
M_n or M_w (kDa)	$M_n = 44.6$	$M_w = 100\text{-}500$[b]
Đ	1.8[a]	-[b]
D_{et} (cm^2/s)	$1.7 \pm 0.3 \times 10^{-6}$	$25.2 \pm 12.3 \times 10^{-6}$
$k_{ex,app}$ (M^{-1} s)	$1.6 \pm 0.2 \times 10^{12}$	$23.6 \pm 11.6 \times 10^{12}$
k^0 (cm/s)	$8.2 \pm 0.6 \times 10^{-3}$	$30.8 \pm 7.8 \times 10^{-3}$

[a] From precursor polymer poly(4-vinylbenzyl chloride).

[b] M_w of the precursor polymer poly(ethylene-alt-maleic anhydride) from the manufacturer is listed. Because of the wide range, Đ and the number of repeat units were not estimated.

The nitroxide polyanion (***2***) was synthesized by the installation of 4-amino-TEMPO to poly(ethylene-alt-maleic anhydride) (**Scheme 3.2**). Successful installation of the TEMPO moieties was confirmed by the appearance of the COOH and $CONH_2$ peaks (**Figure S3.3**). For both the nitroxide polycation and polyanion, an excess of the nitroxide-containing moieties was used to prepare both polymers and the elemental analysis was consistent with a nitroxide being added to virtually all repeat units present.

From thermogravimetric analysis, the 5% decomposition temperature (T_{5d}) for the nitroxide polycation was 55.4 °C, whereas the T_{5d} for the nitroxide polyanion was 66.0 °C (**Figure S3.4**). From differential scanning calorimetry, the T_g of the nitroxide polycation and the nitroxide polyanion were -26.9 °C and -29.4 °C, respectively. These glass transitions are considerably lower than that of neutral PTMA (*ca.* 170 °C), perhaps because the charge groups on the nitroxide polyelectrolytes may provide extra free volume for faster segmental relaxation.

After confirming the polymer structures, the redox behavior of the polyelectrolytes was characterized using solution-state cyclic voltammetry (CV) and chronoamperometry (CA). From CV, the nitroxide polycation exhibited a redox couple at $E_{1/2}$ = 0.80 V *vs.* Ag/AgCl, whereas the nitroxide polyanion exhibited a redox couple at $E_{1/2}$ = 0.72 V *vs.* Ag/AgCl (**Figure 3.1 a-b**). The nitroxide polycation exhibited a smaller peak separation of 54 mV, compared to 74 mV for the nitroxide polyanion. The difference in peak separation suggests that the redox reaction for the nitroxide polycation is more reversible than the nitroxide polyanion. Additionally, the nitroxide polyanion shows a pronounced shoulder in oxidation and reduction. This shoulder can be attributed to anion self-doping that occurs during the electrochemical reaction. More specifically, nitroxide-based charged copolymers from Tokue *et al.* and neutral homopolymers from Wang *et al* exhibited similar features.[24,97] In addition, both the nitroxide polyanion and polycation here exhibited reasonable electrochemical stability with a slight fade in peak oxidation current (~13% fade) over 45 CV cycles for both polyelectrolytes, which could be a result of the nitroxide radical or oxoammonium cation oxidizing amines present in the polymer (**Figure S3.5**).[116,117] Both polymers showed an increase in peak current with increased scan rate that scaled linearly with the square root of the scan rate, indicative of a diffusion-limited reaction (**Figure 3.2 a-b**).

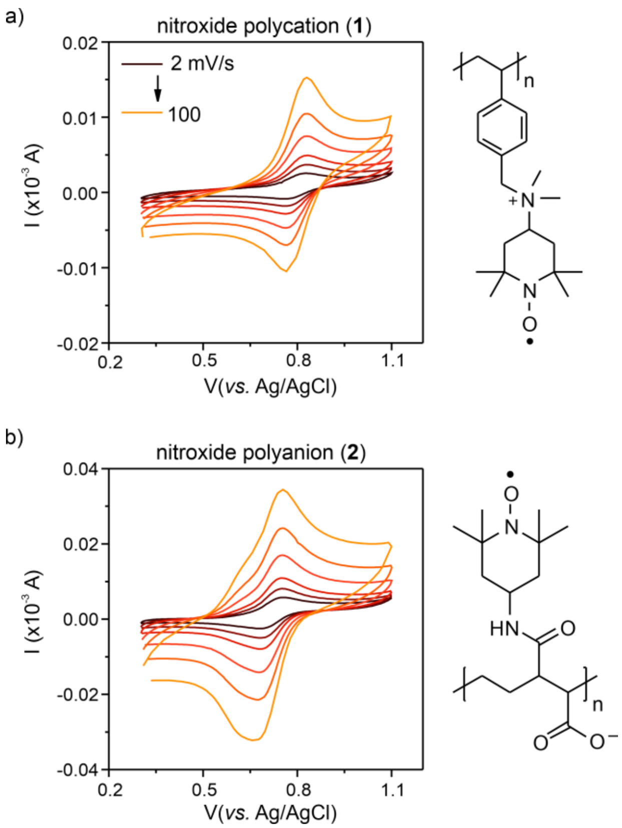

Figure 3.1. Solution state cyclic voltammograms at varying scan rates for the a) nitroxide polycation and b) nitroxide polyanion. The polymer was dissolved at 1 mM of repeat unit in 0.1 M NaCl aqueous solution. The polymer solution was tested in a three-electrode cell with a glassy carbon working electrode, a platinum wire counter electrode, and a Ag/AgCl (sat.) reference electrode. Legend in panel b) applies to panel a). Polymer structures are shown to the right of their corresponding cyclic voltammograms. A comparison of 2 mV/s for both polymers can be found in **Figure S3.6**.

In addition to CV, chronoamperometry studies were conducted to determine the solution-state electron transfer rate constants for both polymers (**Figure 3.2c-d**). The linear region of the Cottrell plots allowed for calculation of the diffusion coefficient of electron transfer (D_{et}) (**Table 3.1**). Once D_{et} was calculated, the apparent electron transfer rate constant ($k_{ex,app}$) and the heterogenous rate constant (k^0) were calculated using the

Dahms-Ruff equation and the method of Nicholson, respectively. The nitroxide polyanion exhibited significantly higher D_{et}, $k_{ex,app}$, and k^0 values compared to the nitroxide polycation. This enhanced rate of electron transfer for the nitroxide polyanion could be caused by the negative charge of the pendant group acting as a counter ion and negating the need for anion uptake, as previously hypothesized for bulk TEMPO-containing polymers.[24]

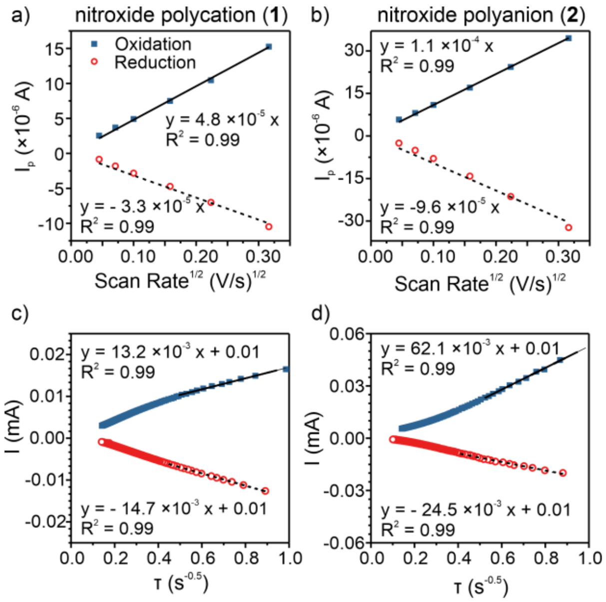

Figure 3.2. Solution-state peak current *vs*. square root scan rate for the a) nitroxide polycation and b) the nitroxide polyanion from CV. Solution-state Cottrell plots of chronoamperometry data for the c) nitroxide polycation and d) the nitroxide polyanion. The electrolyte solution was 1 mM of the nitroxide repeat unit in 0.1 M NaCl in water with a platinum wire counter electrode, Ag/AgCl (sat.) reference electrode, and a glassy carbon working electrode. Legend in panel a) applies to panels b-d.

3.3.2. Nitroxide polycation/nitroxide polyanion LbL Films.

Following confirmation of the polymers' solution-state electroactivity, LbL assembly of the nitroxide polycation and polyanion was carried out up to 10.5 layer pairs (LPs) (**Figure 3.3 a**), for which the polyanion was the terminating layer. Digital images of the films were taken with varying LPs, and a change in apparent film color with increasing number of LPs was visible (**Figure 3.3 b**). UV-Vis spectroscopy also showed an increase in the peak absorbance for the LbL films at a similar wavelength to that of the nitroxide radical (ca. 500 nm) (**Figure 3.3 c**).

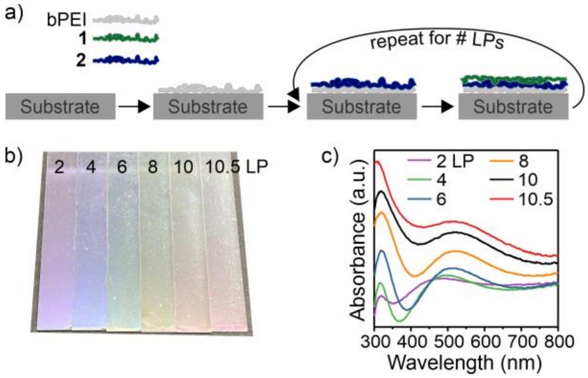

Figure 3.3. a) LbL assembly process including a branched polyethyleneimine (bPEI) base layer followed by alternating deposition of the nitroxide polyanion (***2***) and polycation (***1***) for the desired number of layer pairs (LPs). b) Digital images of the LbL films with increasing LPs. c) UV-Vis spectra for films with varying number of LPs.

To better characterize the surface of the LbL films with different terminating layers (polycation or polyanion), optical microscopy and atomic force microscopy (AFM) were used. From optical microscopy, there was little difference in surface morphology for the differing terminating layers (**Figure 3.4 a-b)**. Similar results were obtained from AFM, which showed that the surface morphologies of both the 10 and 10.5 LP films were similar with discrete agglomerates on the surface. The 10 LP film, with a polycation terminating layer, had an R_q of 53.1 nm, whereas the 10.5 LP film, with a polyanion terminating layer, had one of 107 nm.

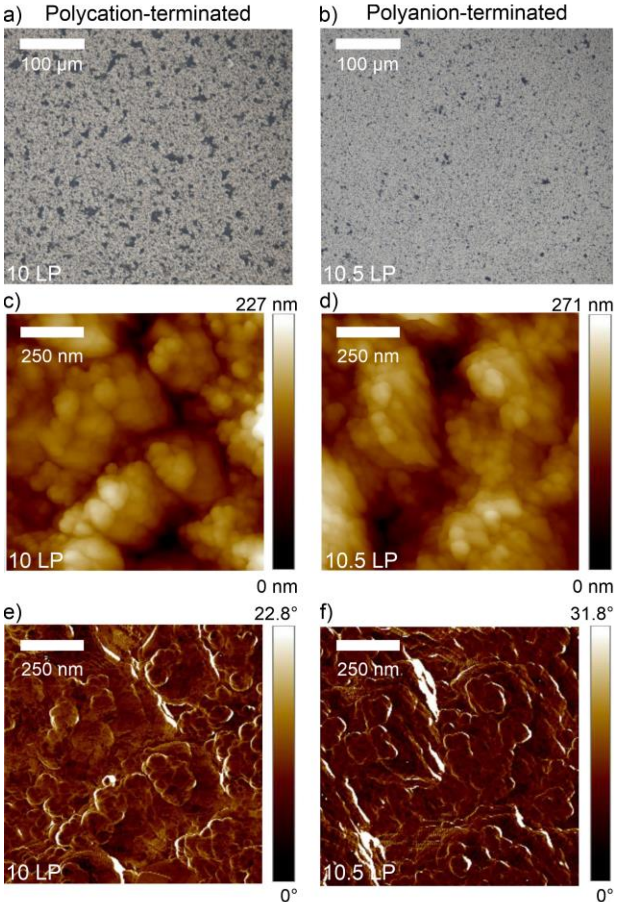

Figure 3.4. a) Optical micrographs of the 10 LP film and b) 10.5 LP film. AFM micrographs of the c-d) height and e-f) phase for the 10 LP film (c, e) and the 10.5 LP film (d, f). 10 LPs indicated polycation-terminated films and 10.5 LPs indicates polyanion-terminated films.

The growth profiles of the LbL films were monitored as a function of LP using UV-Vis absorbance at 500 nm, quartz crystal microbalance (QCM), and profilometry. The absorbance at 500 nm increased with increasing LPs and did not show a significant dependence on terminating layer (**Figure 3.5 a**). The profilometic thickness growth profile showed that the LbL films increased by 28.2 nm per LP (**Figure 3.5 b**). There was an observed increase in thickness and profilometric roughness for the 10.5 LP film with the polyanion terminating layer. Finally, the mass change during layer deposition was monitored with QCM and showed a linear increase of 2.74 ng/cm^2 per LP deposited (**Figure 3.5 c**). From the QCM mass growth profiles, the film composition was determined to be 62.7 ± 17.7 wt% of nitroxide polyanion. The resulting film density was 1.01 g/cm^3.

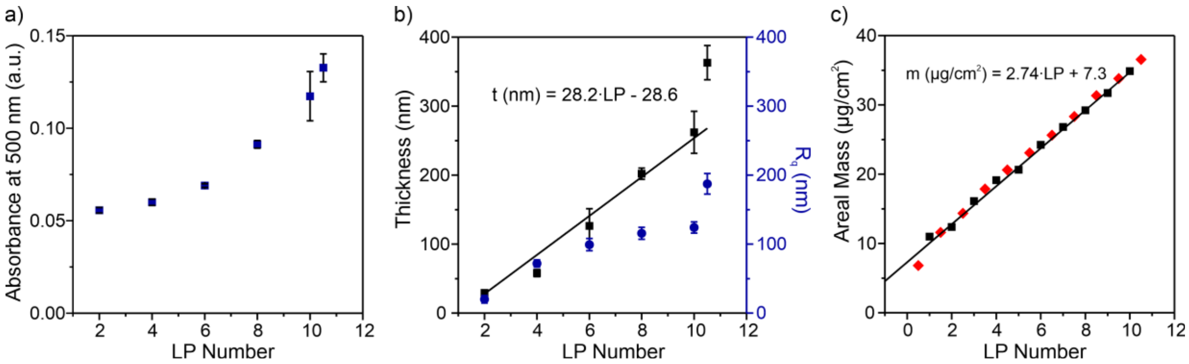

Figure 3.5. Growth profiles as a function of LP number from a) UV-Vis absorbance at 500 nm, b) profilometric thickness and root mean square roughness (R_q), and c) QCM areal mass deposition. UV-Vis spectra are from **Figure 3.3 c**. In panel c), the red diamonds correspond to polyanion deposition and the black squares to polycation deposition.

3.3.3. Electrochemical properties of nitroxide polycation/nitroxide polyanion LbL films.

To determine the nature of the redox reaction for the LbL films, CV and galvanostatic cycling were conducted in a 3-electrode beaker cell. From CV, both the 10 and 10.5 LP films exhibited a redox couple at $E_{1/2} = 0.65$ V *vs.* Ag/AgCl, (**Figure 3.6 a-b**). At 100 mV/s, the 10 LP film exhibited a smaller peak separation of 147 mV, compared to 216 mV for the 10.5 LP film. At low scan rates the 10 LP film shows peak splitting, whereas the 10.5 LP film did not (**Figure 3.6 c**). The observed peak splitting could be attributed to separate cation and anion transport events. Anion transport is suppressed in the 10.5 LP film due to Donnan exclusion of the chloride anion[118] or the reduced mobility of the film from the odd-even effect[119,120] caused by the polyanion terminating layer. This demonstrates that LbL assemblies can be utilized to manipulate the ion transport mechanism by changing the charge of the terminating layer. LbL assembly was also attempted here with the nitroxide polycation and poly(styrene sulfonate) (PSS); however, the negatively charged groups of PSS led to overoxidation of the nitroxide groups and prevented any appreciable electrochemical response.[121] The cyclic voltammogram results at 50 mV/s for the 10.5 LP film were compared to previous literature (**Table S3.1**). Our film was able to reach a greater thickness, which resulted in a larger peak current compared to other studies using nitroxide-based polyelectrolytes for LbL, indicating the added material led to greater energy storage.

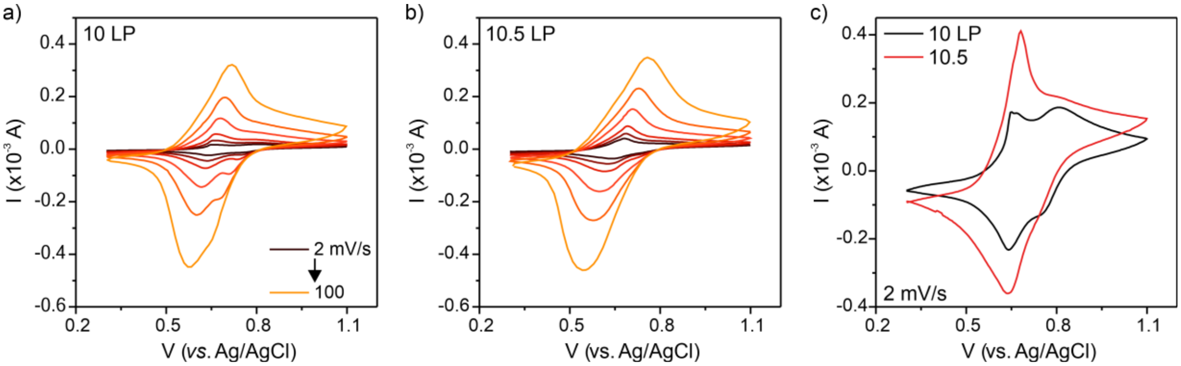

Figure 3.6. Cyclic voltammograms at various scan rates for a) a 10 LP film and b) a 10.5 LP LbL film consisting of the nitroxide polycation and the nitroxide polyanion. c) Cyclic voltammograms at 2 mV/s for 10 and 10.5 LP. Legend in panel a) applies to panel b).

In addition to CV, galvanostatic cycling was also conducted to consider the capacity performance of the LbL films (**Figure 3.7**). The theoretical capacities of the nitroxide polycation and polyanion are 76 mAh/g and 84 mAh/g, respectively. At the lowest current density (2 μA/cm^2), the 10.5 LP film exhibited significantly higher capacity (4.8 × 10^{-4} mAh/cm^2) than the 10 LP film (2.6 × 10^{-4} mAh/cm^2) (**Figure 3.7 a-b**). However, at current densities > 2 μA/cm^2, the two films showed similar capacities. In general, the capacities are low, which might be attributed to diffusion limitations, limited accessibility of the TEMPO groups due to the tightly ion-paired LbL film, or the low mass loading (36.5 μg/cm^2 for 10.5 LP film). In future work, this might be adjusted changing the assembly conditions to promote a more coiled chain conformation (such as added salt) which would produces films that are less dense.

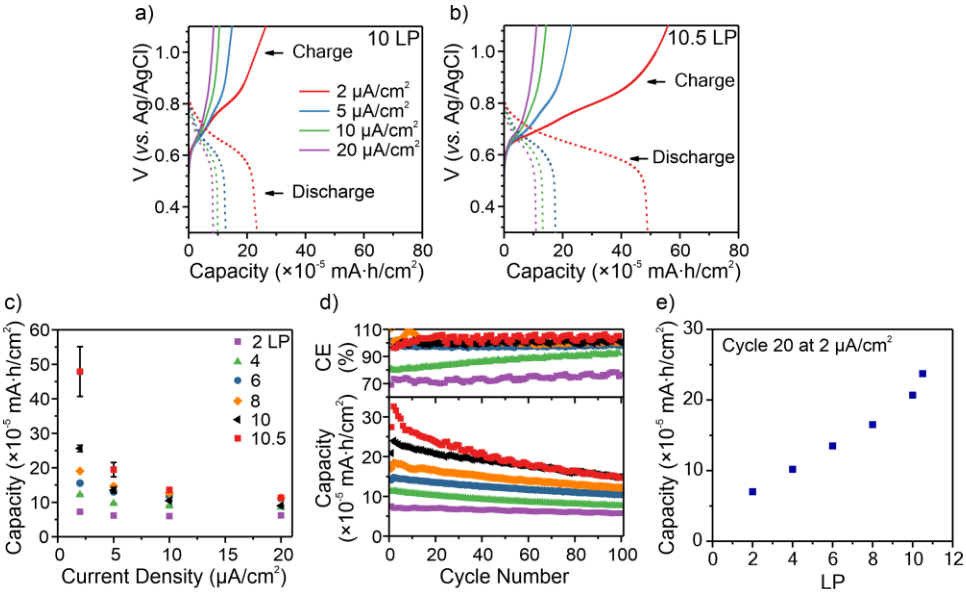

Figure 3.7. Galvanostatic charge-discharge profiles for a) 10 LP and b) 10.5 LP LbL films consisting of the nitroxide polycation and the nitroxide polyanion. Comparison of c) the rate capability and d) the coulombic efficiency cycling stability for LbL with different LPs. e) Capacity *vs.* LP number for cycle 20 of the galvanostatic charge-discharge at a current density of 2 µA/cm^2 from (d). The legend in (c) also applies to the curves shown in (d).

The capacity performance was also considered for a varying number of layer pairs. As the number of LPs increased, there was an increase in capacity (**Figure 3.7 c**). This increase in capacity with LP was particularly notable at low current densities. These films were then cycled for 100 cycles at 2 µA/cm^2 (**Figure 3.7 d**). With increasing LPs, the capacity increased fairly linearly with respect to layer pair number (**Figure 3.7 e**) and coulombic efficiency also increased. The film with 2 LPs exhibited a poor coulombic efficiency of ~70%, likely because the film was patchy and not well formed in the first few cycles of LbL assembly. For 6 LPs and greater, the Coulombic efficiency was ~100%, which we attribute to the formation of an electrochemically percolating film over the substrate. As for capacity retention, LbL films of 6 and 8 LPs exhibited the best retention, but higher LP films (10 and 10.5) showed more pronounced capacity fade. The reason for this is not immediately clear but may arise from side reactions or irreversible swelling of the film.

3.3.4. Electrochemical impedance spectroscopy (EIS).

To evaluate the charge transfer characteristics of the 10 and 10.5 LP films, EIS was used. An equivalent circuit consisting of a solution resistance (R_s), charge transfer resistance (R_{CT}), Warburg diffusion element (W_O), and constant phase element (CPE) (**Figure 3.8 a**) was utilized to represent the electrolyte and LbL thin film. The Nyquist plots for both the 10 and 10.5 LP films exhibited characteristic semi-circle shapes associated with the films' R_{CT} (**Figure 3.8 b**), where the radius was slightly larger for the 10 LP film when compared to the 10.5 LP film. There was little difference between the Bode plots for the 10 and 10.5 LP films (**Figure 3.8 c**). **Table 3.2** presents the parameters from the equivalent circuit model for both films and two control films (only the nitroxide polycation and 2 LP). Specifically, R_{CT} for the 10 LP film was slightly higher than the 10.5 LP film, which we attribute to the lower activation barrier allowed by the polyanion-terminating layer that can participate in self-doping.

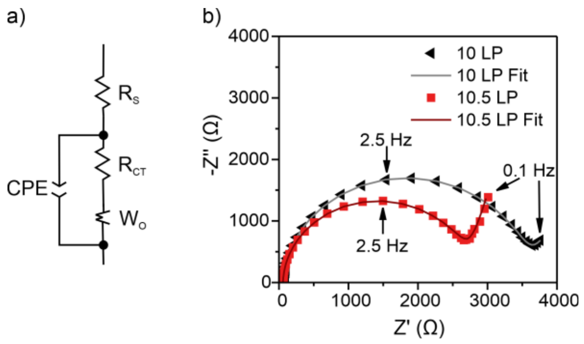

Figure 3.8. a) The equivalent circuit use to model the to the EIS data. b) Nyquist plots for 10 LP and 10.5 LP with their fit lines. EIS was conducted at a potential of 0.8 V *vs.* Ag/AgCl (sat.) with an amplitude of 10 mV in a frequency range of 5 × 10^6 Hz to 0.1 Hz (10 steps per decade). Bode plots can be found in **Figure S3.7**.

Table 3.2. Equivalent circuit modeling parameters for the 2, 10, and 10.5 LP films. Thin film nitroxide polycation on a glassy carbon was used as a control sample. The Nyquist plots for the nitroxide polycation and 2 LP films are found in **Figure S3.8**.

EIS Fit Parameter	**10 LP (cation-terminated), 262 nm thick**	**10.5 LP (anion-terminated), 362 nm thick**	**Nitroxide Polycation on Glassy Carbon, *ca.* 570 nm thick**	**2 LP (cation-terminated), 29 nm thick**
R_S (Ω)	59 ± 0.1	58 ± 0.1	44 ± 0.1	55 ± 0.1
R_{CT} (Ω)	3519 ± 22	2692 ± 6	6117 ± 62	982 ± 5
W_O	0.36 ± 0.01	0.42 ± 0.01	0.18 ± 0.1	0.45 ± 0.1
CPE (μF)	18 ± 0.1	17 ± 0.1	15 ± 0.1	22 ± 0.1

3.4. Conclusions

In conclusion, the synthesis and solution state electrochemical characterization of a nitroxide-based polycation and polyanion were presented. From solution state electrochemical characterization, it was determined that the nitroxide polyanion's redox reaction is slightly less reversible and exhibits a pronounced shoulder in oxidation and reduction associated with anion self-doping. The nitroxide polyanion also exhibited significantly higher D_{et}, $k_{ex,app}$, and k^0 values compared to the nitroxide polycation. In addition to solution state characterization, the nitroxide polyanion and nitroxide polycation were LbL-assembled to fabricate thin films of tunable thickness (28 nm/LP). QCM and profilometry showed that the growth of the films was linear. The ion transport mechanism of the LbL films during the redox reaction differed depending on the terminating layer, where the nitroxide polyanion can participate in self-doping, which leads to a contribution from cation transport. However, the LbL film with the nitroxide polyanion terminating layer led to an improved capacity at 2 $\mu A/cm^2$. Finally, electrochemical impedance spectroscopy was utilized to study charge transfer within the LbL films. The nitroxide polyanion terminating layer led to a slightly reduced charge transfer resistance.

Taken together, these films show the promise of nitroxide-containing polyelectrolytes for EACs, but more work is needed to realize their full potential. Looking to the future, further work should be conducted to produce thicker films that are fully electrochemically accessible. The films produced here were 300-400 nm thick, and depositing more layer pairs could, in principle, increase the areal capacity. However, this might manifest in capacity fade during cycle, as we observed for the 10 and 10.5 LP films. To address this, one might consider adding conductive particles during the LbL assembly process to promote electron transfer from the redox-active polymer to the current collector. With future improvements, nitroxide-based polyelectrolytes might provide EACs that are conformal, adherent, and functional for applications ranging from energy storage to sensing.

3.5. References

19. Wang, S., Easley, A. D. & Lutkenhaus, J. L. 100th Anniversary of Macromolecular Science Viewpoint: Fundamentals for the Future of Macromolecular Nitroxide Radicals. *ACS Macro Letters* **9**, 358-370 (2020).

20. Sato, K., Ichinoi, R., Mizukami, R., Serikawa, T., Sasaki, Y., Lutkenhaus, J., Nishide, H. & Oyaizu, K. Diffusion-Cooperative Model for Charge Transport by Redox-Active Nonconjugated Polymers. *Journal of the American Chemical Society* **140**, 1049-1056 (2018).

24. Wang, S., Li, F., Easley, A. D. & Lutkenhaus, J. L. Real-time insight into the doping mechanism of redox-active organic radical polymers. *Nature Materials* **18**, 69-75 (2019).

87. Easley, A., Shaligram, S., Echols, I., Nixon, K., Regen, S. & Lutkenhaus, J. L. Layer-by-Layer Nanoarchitectonics of Electrochemically Active Thin Films Comprised of Radical-Containing Polymers. *J. Electrochem. Soc.* (2022).

88. Jun, K., Kim, J. & Oh, I.-K. An Electroactive and Transparent Haptic Interface Utilizing Soft Elastomer Actuators with Silver Nanowire Electrodes. *Small* **14**, 1801603 (2018).

89. Wałęsa-Chorab, M. & Skene, W. G. Visible-to-NIR Electrochromic Device Prepared from a Thermally Polymerizable Electroactive Organic Monomer. *ACS Applied Materials & Interfaces* **9**, 21524-21531 (2017).

90. Ariga, K., Lvov, Y. & Decher, G. There is still plenty of room for layer-by-layer assembly for constructing nanoarchitectonics-based materials and devices. *Physical Chemistry Chemical Physics* (2022).

91. Tebyetekerwa, M., Xu, Z., Li, W., Wang, X., Marriam, I., Peng, S., Ramkrishna, S., Yang, S. & Zhu, M. Surface Self-Assembly of Functional Electroactive Nanofibers on Textile Yarns as a Facile Approach toward Super Flexible Energy Storage. *ACS Applied Energy Materials* **1**, 377-386 (2018).

92. Gu, M. & Kim, B.-S. Electrochemistry of Multilayer Electrodes: From the Basics to Energy Applications. *Accounts of Chemical Research* **54**, 57-69 (2021).

93. Rohland, P., Schröter, E., Nolte, O., Newkome, G. R., Hager, M. D. & Schubert, U. S. Redox-active polymers: The magic key towards energy storage – a polymer design guideline progress in polymer science. *Prog. Polym. Sci.* **125**, 101474 (2022).

94. Gerlach, P. & Balducci, A. The influence of current density, rest time and electrolyte composition on the self-discharge of organic radical polymers. *Electrochim. Acta* **377**, 138070 (2021).

95. Hung, M.-K., Wang, Y.-H., Lin, C.-H., Lin, H.-C. & Lee, J.-T. Synthesis and electrochemical behaviour of nitroxide polymer brush thin-film electrodes for organic radical batteries. *J. Mater. Chem.* **22**, 1570-1577 (2012).

96. Hauffman, G., Vlad, A., Janoschka, T., Schubert, U. S. & Gohy, J. F. Nanostructured organic radical cathodes from self-assembled nitroxide-containing block copolymer thin films. *Journal of Materials Chemistry A* **3**, 19575-19581 (2015).

97. Tokue, H., Murata, T., Agatsuma, H., Nishide, H. & Oyaizu, K. Charge–Discharge with Rocking-Chair-Type Li+ Migration Characteristics in a Zwitterionic Radical Copolymer Composed of TEMPO and Trifluoromethanesulfonylimide with Carbonate Electrolytes for a High-Rate Li-Ion Battery. *Macromolecules* **50**, 1950-1958 (2017).

98. Aqil, M., Ouhib, F., Aqil, A., El Idrissi, A., Detrembleur, C. & Jérôme, C. Polymer ionic liquid bearing radicals as an active material for organic batteries with ultrafast charge-discharge rate. *Eur. Polym. J.* **106**, 242-248 (2018).

99. Aqil, M., Aqil, A., Ouhib, F., El Idrissi, A., Dahbi, M., Detrembleur, C. & Jérôme, C. Nitroxide TEMPO-containing PILs: Kinetics study and electrochemical characterizations. *Eur. Polym. J.* **152**, 110453 (2021).

100. Wang, S., Park, A. M. G., Flouda, P., Easley, A. D., Li, F., Ma, T., Fuchs, G. D. & Lutkenhaus, J. L. Solution-Processable Thermally Crosslinked Organic Radical Polymer Battery Cathodes. *ChemSusChem* **13**, 2371-2378 (2020).

101. Jeon, J.-W., O’Neal, J., Shao, L. & Lutkenhaus, J. L. Charge Storage in Polymer Acid-Doped Polyaniline-Based Layer-by-Layer Electrodes. *ACS Applied Materials & Interfaces* **5**, 10127-10136 (2013).

102. Jeon, J.-W., Kwon, S. R. & Lutkenhaus, J. L. Polyaniline nanofiber/electrochemically reduced graphene oxide layer-by-layer electrodes for electrochemical energy storage. *Journal of Materials Chemistry A* **3**, 3757-3767 (2015).

103. Yun, J., Echols, I., Flouda, P., Wang, S., Easley, A., Zhao, X., Tan, Z., Prehn, E., Zi, G., Radovic, M., Green, M. J. & Lutkenhaus, J. L. Layer-by-Layer Assembly of Polyaniline Nanofibers and MXene Thin-Film Electrodes for Electrochemical Energy Storage. *ACS Applied Materials & Interfaces* **11**, 47929-47938 (2019).

104. Pandey, M., Sadakata, S., Nagamatsu, S., Pandey, S. S., Hayase, S. & Takashima, W. Layer-by-layer coating of oriented conjugated polymer films towards anisotropic electronics. *Synth. Met.* **227**, 29-36 (2017).

105. Zhang, K., Hu, Z., Xu, R., Jiang, X.-F., Yip, H.-L., Huang, F. & Cao, Y. High-Performance Polymer Solar Cells with Electrostatic Layer-by-Layer Self-Assembled Conjugated Polyelectrolytes as the Cathode Interlayer. *Adv. Mater.* **27**, 3607-3613 (2015).

106. Jang, M., Kim, S. H., Lee, H.-K., Kim, Y.-H. & Yang, H. Layer-by-Layer Conjugated Extension of a Semiconducting Polymer for High-Performance Organic Field-Effect Transistor. *Adv. Funct. Mater.* **25**, 3833-3839 (2015).

107. Li, Y., Wang, X. & Sun, J. Layer-by-layer assembly for rapid fabrication of thick polymeric films. *Chem. Soc. Rev.* **41**, 5998-6009 (2012).

108. Richardson, J. J., Cui, J., Björnmalm, M., Braunger, J. A., Ejima, H. & Caruso, F. Innovation in Layer-by-Layer Assembly. *Chem. Rev.* **116**, 14828-14867 (2016).

109. Ghostine, R. A., Jisr, R. M., Lehaf, A. & Schlenoff, J. B. Roughness and Salt Annealing in a Polyelectrolyte Multilayer. *Langmuir* **29**, 11742-11750 (2013).

110. Soltwedel, O., Ivanova, O., Nestler, P., Müller, M., Köhler, R. & Helm, C. A. Interdiffusion in Polyelectrolyte Multilayers. *Macromolecules* **43**, 7288-7293 (2010).

111. Zahn, R., Coullerez, G., Vörös, J. & Zambelli, T. Effect of polyelectrolyte interdiffusion on electron transport in redox-active polyelectrolyte multilayers. *J. Mater. Chem.* **22**, 11073-11078 (2012).

112. Takahashi, S., Aikawa, Y., Kudo, T., Ono, T., Kashiwagi, Y. & Anzai, J.-i. Electrochemical decomposition of layer-by-layer thin films composed of TEMPO-modified poly(acrylic acid) and poly(ethyleneimine). *Colloid. Polym. Sci.* **292**, 771-776 (2014).

113. Fu, Q., Zoudanov, I., Gustafsson, E., Yang, D., Soleymani, L. & Pelton, R. H. Redox Properties of Polyvinylamine-g-TEMPO in Multilayer Films with Sodium Poly(styrenesulfonate). *ACS Applied Materials & Interfaces* **9**, 5622-5628 (2017).

114. de Vries, W., Doerenkamp, C., Zeng, Z., de Oliveira, M., Niehaus, O., Pöttgen, R., Studer, A. & Eckert, H. Synthesis and characterization of amorphous mesoporous silica using TEMPO-functionalized amphiphilic templates. *J. Solid State Chem.* **237**, 93-98 (2016).

115. Lappan, U., Wiesner, B., Zschoche, S. & Scheler, U. Polyelectrolyte Multilayers Studied by Electron Paramagnetic Resonance (EPR) Spin-Label Technique. *Appl. Magn. Reson.* **44**, 181-188 (2013).

116. Sato, K., Ono, T., Sasano, Y., Sato, F., Kumano, M., Yoshida, K., Dairaku, T., Iwabuchi, Y. & Kashiwagi, Y. Electrochemical Oxidation of Amines Using a Nitroxyl Radical Catalyst and the Electroanalysis of Lidocaine. *Catalysts* **8** (2018).

117. Nelsen, S. F. & Hintz, P. J. Electrochemical oxidation of tertiary amines. Effect of structure upon reversibility. *Journal of the American Chemical Society* **94**, 7114-7117 (1972).

118. Calvo, E. J. & Wolosiuk, A. Donnan Permselectivity in Layer-by-Layer Self-Assembled Redox Polyelectrolye Thin Films. *Journal of the American Chemical Society* **124**, 8490-8497 (2002).

119. Lappan, U., Rau, C., Naas, C. & Scheler, U. Odd–Even Effect on Rotational Dynamics of Spin-Labeled Polyacid Chain Segments in Polyelectrolyte Multilayers. *Macromolecules* **52**, 2384-2392 (2019).

120. Sato, H. & Anzai, J.-i. Preparation of Layer-by-Layer Thin Films Composed of DNA and Ferrocene-Bearing Poly(amine)s and Their Redox Properties. *Biomacromolecules* **7**, 2072-2076 (2006).

121. Yu, I., Jeon, D., Boudouris, B. & Joo, Y. Mixed Ionic and Electronic Conduction in Radical Polymers. *Macromolecules* **53**, 4435-4441 (2020).

4. POLYPEPTIDE ORGANIC RADICAL BATTERIES*

4.1. Introduction

In only a few decades, lithium-ion batteries have revolutionized technologies, enabling the proliferation of portable devices and electric vehicles, with substantial benefits for society. However, the rapid growth in technology has highlighted the ethical and environmental challenges of mining lithium, cobalt and other mineral ore resources, and the issues associated with the safe usage and non-hazardous disposal of batteries.[1] Only a small fraction of lithium-ion batteries are recycled, further exacerbating global material supply of strategic elements.[6,7,13] A potential alternative is to use organic-based redox-active materials to develop rechargeable batteries that originate from ethically sourced, sustainable materials and enable on-demand deconstruction and reconstruction.[123-125] Making such batteries is challenging because the active materials must be stable during operation but degradable at end of life. Further, the degradation products should be either environmentally benign or recyclable for reconstruction into a new battery. Here we demonstrate a metal-free, polypeptide-based battery, in which viologens and nitroxide radicals are incorporated as redox-active groups along polypeptide backbones to function as anode and cathode materials, respectively. These redox-active polypeptides perform as active materials that are stable during battery operation and

---

* Modified from ref. 122. Nguyen, T. P., Easley, A. D., Kang, N., Khan, S., Lim, S.-M., Rezenom, Y. H., Wang, S., Tran, D. K., Fan, J., Letteri, R. A., He, X., Su, L., Yu, C.-H., Lutkenhaus, J. L. & Wooley, K. L. Polypeptide organic radical batteries. *Nature* **593**, 61-66 (2021).

subsequently degrade on demand in acidic conditions to generate amino acids, other building blocks and degradation products. Such a polypeptide-based battery is a first step to addressing the need for alternative chemistries for green and sustainable batteries in a future circular economy.

Organic radical batteries promise increased environmental friendliness, independence from strategic metals and faster charging rates compared to lithium-ion batteries.[6,7,12,22,27,126-128] However, a key challenge, even taking into account the beneficial aspects of organic polymer materials, is the design of functional plastics with an end-of-life consideration.[129] he most-studied active materials in organic radical batteries are polymers that carry redox-active pendant groups,[4,12,22,128,130] —such as 2,2,6,6-tetramethyl-4-piperidine-1-oxyl (TEMPO) and 4,4'-bipyridine derivatives (viologen),[4,126,131-133] —along non-degradable, aliphatic backbones.[13,133-136] Although a few studies have investigated redox-active degradable polymers and others have explored fully polymeric batteries (**Table 4.1**),[126,127,137-141] none has combined these two concepts to create fully polymeric metal-free batteries that degrade on demand, which would be a first step towards the design of sustainable, recyclable batteries.[126,127,137-140] We postulate that redox-active pendant groups along a polypeptide backbone might provide a suitable material platform for degradable organic radical batteries.[142]

Table 4.1. Performance of Select Polymer-based Batteries.

Anode	**Cathode**	**Output Potential (V)**	**C_{spec} (mA·h·g^{-1})[*]**	**E_{spec} (mW·h·g^{-1})**	**Degradable**	**Ref.**
Poly(vinyldibenzothiophenesulfone)	Poly(TEMPO methacrylate)	2.6	~200[†]	541	No	136
Viologen-chloride Polypeptide	BiTEMPO Polypeptide	1.1 and 1.6	38	60[‡]	Yes	This Work
Polyviologen hydrogel	Poly(TEMPO acrylamide)	1.1 and 1.5	165	248[‡]	No	133
Poly(2-methacrylamide-TCAQ)	Poly(2-vinylthianthrene)	1.3	105	137[‡]	No	13
Poly(anthraquinone-substituted ethyleneimine)	Poly(TEMPO acrylamide)	1.1	80	88[‡]	No	141
Poly(viologen dibromide)	Poly(TEMPO acrylamide)	1.2	~100[†]	120	No	124
hydroquinonesulfonic acid potassium salt[§]	*p*-benzoquinone[§]	0.8	~42[†]	32	Yes	125§
Poly(galvinoxylstyrene)	Poly(TEMPO-substituted norbornene)	0.7	32	22[‡]	No	134
Poly(nitronylnitroxylstyrene)	Poly(galvinoxylstyrene)	0.6	29	17[‡]	No	135

TCAQ =11,11,12,12-tetracyano-9,10-anthraquinonedimethane

* Value taken from first charge/discharge cycle.

† The value was not provided in text but estimated from graph.

‡ Value calculated by multiplying specific capacity by output voltage (largest voltage if two are listed).

§ Small molecule organic redox-flow battery

Here we report an on-demand-degradable, polypeptide-based battery (**Figure 4.1**). We designed and synthesized polypeptide anodes and cathodes that contain redox-active pendant groups, determined their redox activities, and established their behaviours in all-polypeptide batteries. First, each polypeptide was assembled into a lithium metal half-cell battery to elucidate its fundamental energy-storage characteristics. Then, we constructed a metal-free, polypeptide-based battery. As a demonstration of recyclability, we conducted hydrolytic degradation under acidic conditions and determined the degradation products. In addition, we quantified the effects of the intact redox-active polypeptides and their degradation products on the viabilities of three different cell types. By merging degradable polypeptide backbones with the energy-storage properties of the redox-active moieties, this bioinspired polypeptide-based battery addresses some of the challenges of conventional lithium-ion batteries (for example, the use of scarce resources, safety concerns and high-cost recycling).

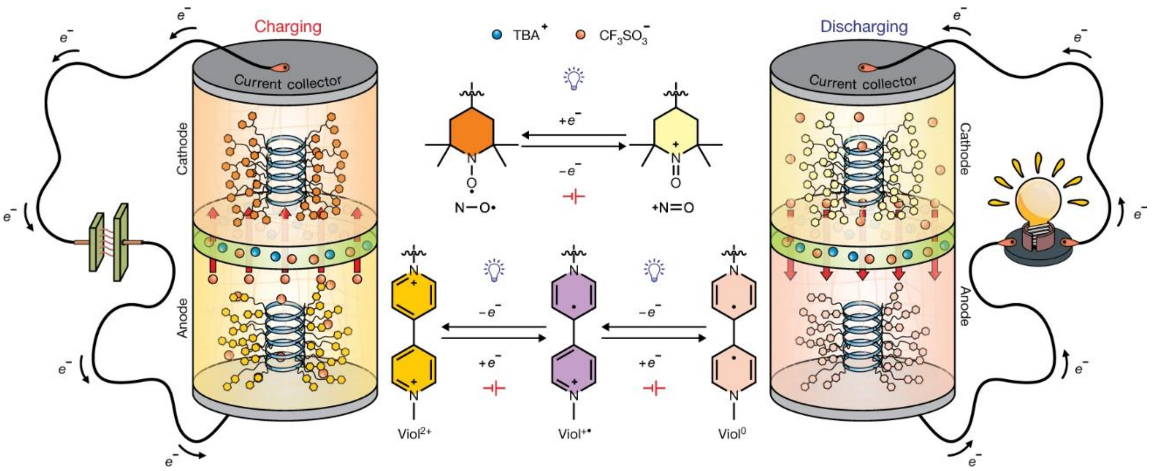

Figure 4.1. Schematics of a polypeptide-based organic radical battery and the reactions that occur during charging and discharging are shown on the left and right, respectively. The redox reactions for the TEMPO (top) and viologen (bottom) pendant groups are shown in the middle. For example, during charging, nitroxide radical functional groups at the cathode oxidize to oxoammonium cations, and viologen functional groups at the anode reduce to their neutral forms.

4.2. Syntheses of Redox-active Polypeptides

The redox-active polypeptides were synthesized by the Wooley Group. Synthetic details and the chemical and thermal characterization of all intermediates can be found in previous work.[122,143] The final polypeptides used for electrochemical characterization are shown in **Figure 4.2**. Chemical characterization performed by the Wooley lab confirmed both the viologen-chloride (viol-Cl) and biTEMPO polypeptides exhibited α-helical conformations.[122]

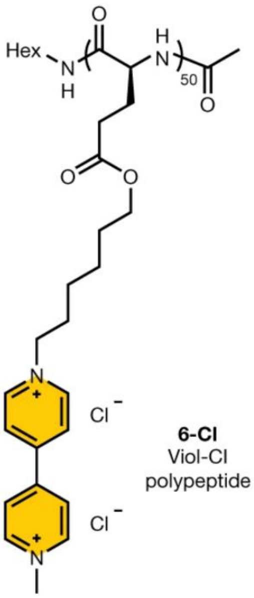

6-Cl
Viol-Cl
polypeptide

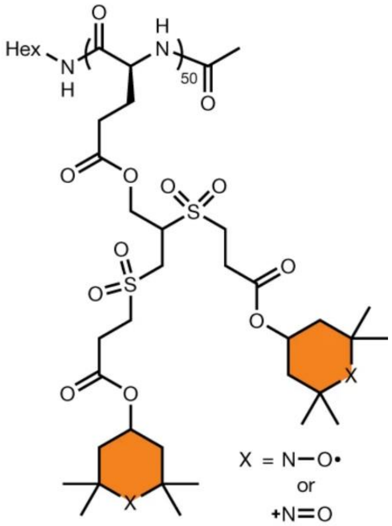

14
BiTEMPO polypeptide

Figure 4.2. Viologen-chloride and BiTEMPO Polypeptides. The chemical structures of the polypeptides provide by the Wooley Group.

4.3. Electrochemical Characterization

We used cyclic voltammetry of viol-Cl and biTEMPO polypeptide thin films (1 μm thick, 0.5–0.6 mg cm^{-2}) to assess the electrochemical response of the polypeptides in a metal-free electrolyte (0.5 M tetrabutylammonium triflate ($TBACF_3SO_3$) in propylene carbonate; **Figure 4.3**). The viol-Cl polypeptide exhibited two quasi-reversible redox peaks, at 2.23 V and 2.69 V versus Li/Li$^+$ (**Figure 4.3 a**). The lower potential (2.23V) is assigned to the reversible reaction between viologen$^{+\bullet}$ (Viol$^{+\bullet}$) and viologen^0 (Viol^0); the higher potential (2.69 V) is associated with the reversible reaction between viologen^{2+} (Viol^{2+}) and Viol$^{+\bullet}$.[131,133,144] The biTEMPO polypeptide exhibited one quasi-reversible redox peak, at 3.69 V versus Li/Li$^+$, which is associated with the reversible reaction between the nitroxide radical (N–O•) and oxoammonium cation ($^+$N=O; **Figure 4.3 b**).[4] The peak current and peak separation for both the viol-Cl and biTEMPO polypeptide thin films scaled with the square-root of the scan rate, which is indicative of a diffusion-limited reaction (**Figure S4.4 - Figure S4.5**).[4,145] Solution-state cyclic voltammetry of the viologen and biTEMPO analogues (**Figure S4.2**) exhibited a similar response.

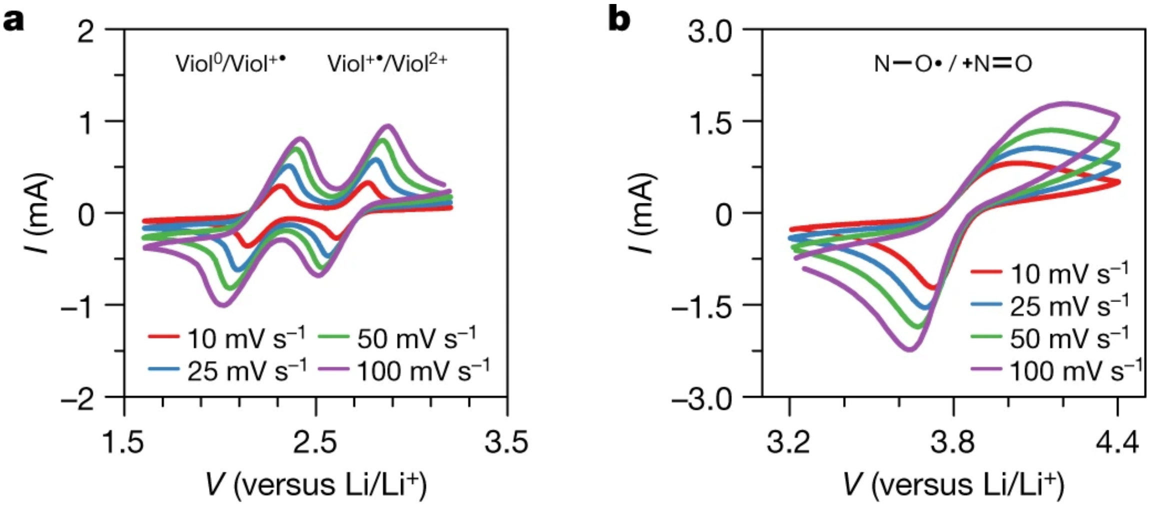

Figure 4.3. Cyclic voltammograms of viol-Cl (**a**) and biTEMPO (**b**) polypeptide thin films on ITO-coated glass substrates in a three-electrode beaker cell configuration. The supporting electrolyte was 0.5 M TBACF$_3$SO$_3$ in propylene carbonate. Lithium metal was used as counter and reference electrodes.

Next, we fabricated polypeptide composite electrodes (carbon black and polyvinylidene fluoride; 6–7 μm thick, 0.4–0.5 mg polypeptide cm^{-2}) for evaluation in lithium metal half-cells. The theoretical capacities for the viol-Cl and biTEMPO polypeptides are 118.3 mA h g^{-1} and 71.3 mA h g^{-1}, respectively (**Equation S4.1**). The viol-Cl polypeptide composite electrode (**Figure 4.4 a-c**) exhibited two quasi-reversible redox couples, at 2.13 V and 2.56 V versus Li/Li^{+}, and a discharge capacity of 74.2 mA h g^{-1} (per gram of polypeptide) at 1*C* (the current required to reach full charge in 1 h), which decreased to 68.0 mA h g^{-1} after 30 cycles (91% capacity retention). The biTEMPO polypeptide composite electrode exhibited one quasi-reversible redox peak, at 3.67 V versus Li/Li^{+}, and a charge capacity of 16.5 mA h g^{-1} at 1*C*, which faded to 11.6 mA h g^{-1} after 30 cycles (70% capacity retention; **Figure 4.4 d-f**). The main mechanism of capacity fade is dissolution of the polypeptides into the electrolyte, as verified by solution-state cyclic voltammetry of the electrolyte after galvanostatic cycling (**Figure S4.6**).[35]

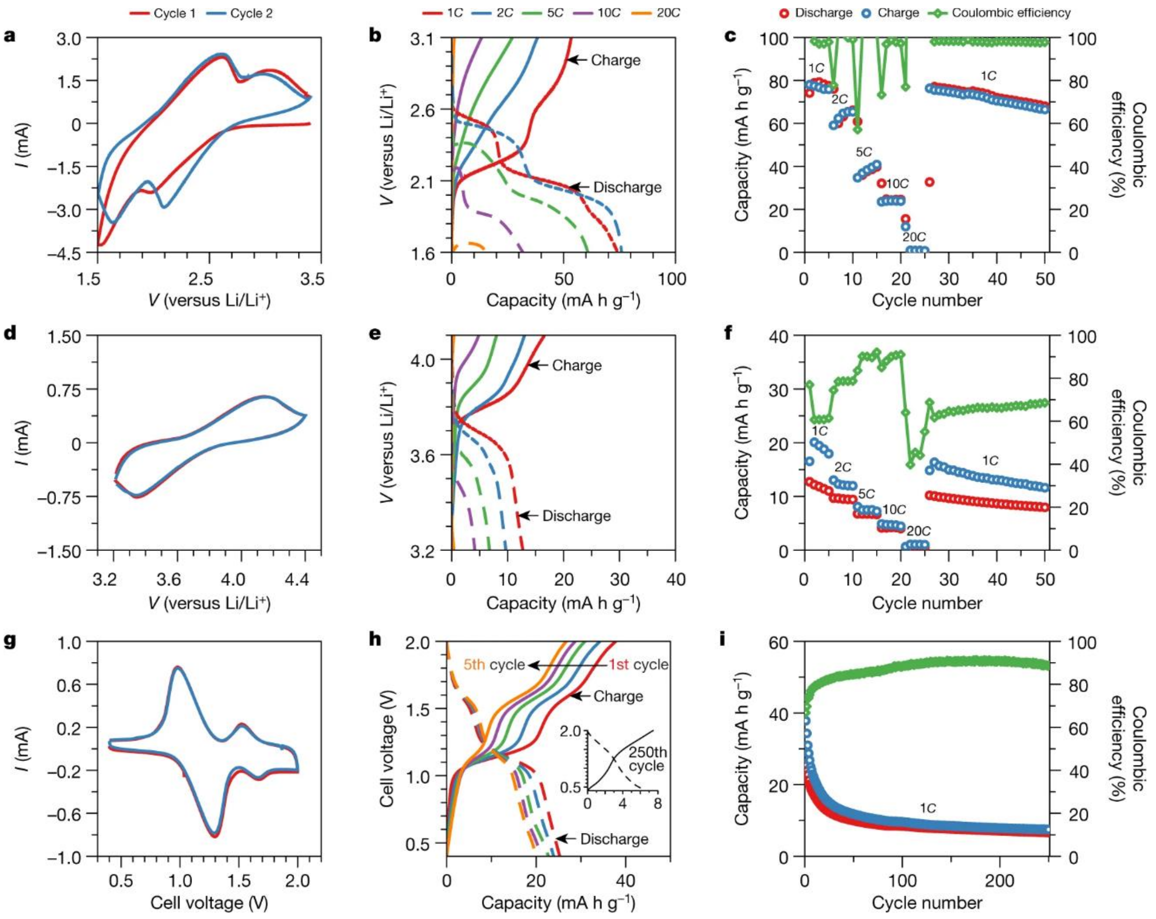

Figure 4.4. Electrochemical characterization of the viol-Cl polypeptide composite half-cell (**a**–**c**), the biTEMPO polypeptide composite half-cell (**d**–**f**) and the viol-Cl–biTEMPO polypeptide full cell (**g**–**i**), including their cyclic voltammograms (**a**, **d**, **g**), charge–discharge curves (**b**, **e**, **h**; solid, charge; dashed, discharge) and cycling response (**c**, **f**, **i**; left axis, charge or discharge capacity; right axis, Coulombic efficiency). For **a**–**f**, we used a viol-Cl (**a**–**c**) or biTEMPO (**d**–**f**) polypeptide composite electrode separated from a lithium metal reference electrode by filter paper soaked in 0.5 M $TBACF_3SO_3$ in propylene carbonate. For **g**–**i**, we used a viol-Cl polypeptide composite electrode separated from a biTEMPO polypeptide composite electrode by filter paper soaked in 0.5 M $TBACF_3SO_3$ in propylene carbonate. The composite electrodes were composed of 30 wt% active polypeptide, 60 wt% carbon black and 10 wt% polyvinylidene fluoride on ITO-coated glass. In **c** and **f**, the *C* rates were varied; in **i**, the *C* rate was constant at 1*C*.

Finally, we prepared metal-free, fully polypeptide-based cells with viol-Cl polypeptide composite anodes and biTEMPO polypeptide composite cathodes using filter paper soaked with electrolyte as the separator in a sandwich-cell configuration. The theoretical capacity for the fully polypeptide-based cell was calculated to be 44.5 mA h g^{-1} (per gram of viol-Cl polypeptide; **Equation S4.2**). Cyclic voltammetry resulted in two pairs of peaks, centred around 1.3 V and 1.6 V, consistent with the difference in redox potentials of the polypeptide composite anode and cathode. Cycling stability of the polypeptide-based battery was determined over 250 cycles of galvanostatic charging at 1*C*. In the charge–discharge curves, two plateaus occurred, at 1.1 V and 1.6 V (**Figure S4.7**). The charge capacity of the full cell at 1*C* faded from an initial value of 37.8 mA h g^{-1} (85% theoretical capacity) to 7.5 mA h g^{-1} after 250 cycles (**Figure 4.4 g-i**). The Coulombic efficiency was less than 100% for all cycles, owing to the dissolution of viol-Cl and biTEMPO polypeptides into the electrolyte.[146] Although dissolution occurred, the post-cycling capacity remained larger than that of the control full cell (without polypeptides), which confirms the activity of the remaining polypeptides even after 250 cycles (**Figure S4.9**). There was no visible delamination or morphological change in either composite electrode after 50 cycles (**Figure S4.10**). A lithium-ion-based electrolyte battery was tested separately (**Figure S4.8**).

4.4. Degradation of Viologen and BiTEMPO Polypeptides

The Wooley Lab designed the viologen and biTEMPO polypeptides to contain amide links in the backbone and ester links in the side chains, which are prone to degradation in enzymatic, basic, and acidic conditions. They were able to demonstrate, using ^{1}H NMR, that L-glutamic acid was regenerated in near quantitative amounts for both the viologen-iodide and biTEMPO polypeptides.

Reconstructing the polymers from the degradation products would be the ultimate demonstration of recyclability. We found that the primary issue with achieving this was separating the degradation products on a scale large enough for subsequent reconstruction into the original polymers. In principle, the redox-active polymers would be reconstituted by the following: (1) the regenerated glutamic acid could be fed directly back into the syntheses of the viologen and biTEMPO polypeptides as primary synthons; (2) the 4-OH-TEMPO radicals could be retrieved upon separation, neutralization and oxidation of the degradation products, then fed into the synthetic route of the biTEMPO polypeptide; and (3) the degradation product of the viologen polypeptide side chains could be conjugated with poly(L-glutamates) to regenerate the viologen polypeptide. Alternatively, a milder degradation process, for instance, enzymatic breakdown, might provide a simpler route to a full cycle of recyclability.

4.5. Conclusions

We have designed a metal-free, all-polypeptide organic radical battery comprising redox-active amino-acid macromolecules that degrade on demand. This concept represents a first step towards sustainable, recyclable batteries and minimizing global dependence on strategic metals. Viologen and biTEMPO polypeptide anodes and cathodes, respectively, were synthesized via ring-opening polymerization of highly reactive cyclic *N*-carboxyanhydrides, followed by sequential post-polymerization modifications to incorporate the redox-active groups. The polypeptide battery reached a maximum charge capacity of 37.8 mA h g^{-1} (theoretical capacity, 44.5 mA h g^{-1}). The active components degraded on demand in the presence of acid to regenerate the starting amino acids and other building blocks. Looking forward, the main challenges are preventing dissolution of the active material and boosting the overall cell capacity. Future studies should focus on preventing dissolution of the polypeptides by crosslinking,[147] by post-processing modification[148] or by taking advantage of the solubility of the polypeptides in flow battery cells.

4.6. Experimental

4.6.1. Reagents

Acetonitrile (MeCN), 3,3-dithiodipropionic acid, 4,4′-dipyridine, *meta*-chloroperoxybenzoic acid (*m*-CPBA; 77% purity), dichloromethane (DCM), *N*,*N*′-dicyclohexylcarbodiimide (DCC), 4-dimethylaminopyridine (DMAP), 2,2-dimethoxy-2-phenylacetophenone (DMPA), *N*,*N*-dimethylformamide (DMF), dimethylsulfoxide (DMSO), 4-hydroxy-2,2,6,6-tetramethylpiperidine-1-oxyl (4-OH-TEMPO, TEMPOL), diphosgene, hexanes, *n*-hexylamine, hydrocinnamic acid, iodomethane, iron(II) sulfate heptahydrate ($FeSO_4 \cdot 7H_2O$), L-glutamic acid, methanol, propargyl alcohol, sodium iodide (NaI), triethylamine (TEA), trifluoroethanol (TFE), trimethylsilyl chloride (TMSCl) and triphosgene were purchased from Sigma-Aldrich. DL-Dithiothreitol (DTT) was purchased from Tokyo Chemical Industry. 6-Chloro-1-hexanol and acetic anhydride were purchased from Alfa-Aesar. All reagents were used as received, except for propargyl alcohol, which was distilled under an atmosphere of N_2 before use. Ultrapure water was collected from a Milli-Q integral water purification system (18 MΩ cm). Lithium triflate ($LiCF_3SO_3$), tetrabutyammonium triflate (TBACF_3SO_3), methanol, *N*-methyl-2-pyrrolidinone (NMP) and propylene carbonate (PC) were purchased from Sigma-Aldrich. DCM and chloroform were purchased from VWR. Super P carbon black (CB) was purchased from TIMCAL Graphite & Carbon. Polyvinylidene fluoride (PVDF; 600,000 g mol^{-1}) was purchased from MTI. ITO-coated glass substrates were purchased from Delta Technologies, and cleaned by subsequent sonication in soap water, ultrapure water, acetone, and isopropyl alcohol, followed by drying with N_2 and ozone plasma treatment for 10 min. Lithium metal was purchased from Alfa-Aesar.

4.6.2. Electrochemical characterization

Polypeptide thin films were prepared by drop-casting 300 μl of the polypeptide solution onto clean ITO-coated glass substrates. The polypeptide solution was composed of 4 mg of polypeptide in 1 ml of MeOH/H_2O (1/1 v/v) for viol-Cl polypeptide or $CHCl_3$ for biTEMPO polypeptide. After drop-casting, the thin films were dried at ambient conditions for 24 h, followed by drying under vacuum at room temperature for 24 h before electrochemical testing. Composite electrodes for both polymers were fabricated by preparing a solution of CB (60 wt%), biTEMPO polypeptide or viol-Cl polypeptide (30 wt%) and PVDF binder polymer (10 wt%) in NMP (1 ml). 300 μl of the slurry was then drop-cast onto a clean ITO-coated glass substrate. After drop-casting the slurry onto the substrates, the electrodes were dried at 40 °C under ambient pressure for two days before drying under vacuum at room temperature for 24 h. After drying, the electrode thickness was determined with a TESA μ-HITE instrument. All electrochemical measurements were performed in an argon-filled glovebox with a Solartron Electrochemical Interface 1287 potentiostat/galvanostat unless otherwise noted.

The polypeptide thin films on ITO-coated glass substrates were used in a three-electrode beaker cell as the working electrode with lithium metal counter and reference electrodes, and 20 ml of 0.5 M $TBACF_3SO_3$ or $LiCF_3SO_3$ in PC for the electrolyte. The thin films were conditioned using three cyclic voltammetry cycles at 10 mV s^{-1} followed by cyclic voltammetry at different scan rates (10 mV s^{-1}, 25 mV s^{-1}, 50 mV s^{-1} or 100 mV s^{-1}).

The composite electrodes were used in a half sandwich cell as working electrodes, with a lithium metal reference electrode and filter paper pre-soaked with 0.5 M $TBACF_3SO_3$ or $LiCF_3SO_3$ in PC as the separator. Cyclic voltammetry (10 mV s^{-1}) and galvanostatic charge–discharge (five cycles each at 1*C*, 2*C*, 5*C*, 10*C* and 20*C* followed by 25 cycles at 1*C*) were performed. The current (I, mA) for each *C* rate was calculated using the theoretical capacity and coated mass (X, g polypeptide) of the polypeptide. For example, for a biTEMPO composite electrode at 1*C*: I [mA] = 71.3 [mA h (g biTEMPO)$^{-1}$] × X [g biTEMPO] × 1 [h^{-1}].

All-polypeptide electrochemical sandwich cells were assembled with viol-Cl polypeptide composite anodes, biTEMPO polypeptide composite cathodes and electrolyte-soaked filter-paper separators. The electrolyte was 0.5 M $TBACF_3SO_3$ or $LiCF_3SO_3$ in PC. Before sandwich-cell assembly, the viol-Cl polypeptide electrodes were conditioned with three cyclic voltammetry cycles at 10 mV s^{-1} in a three-electrode beaker cell containing 0.5 M $TBACF_3SO_3$ or $LiCF_3SO_3$ in PC electrolyte with lithium metal counter and reference electrodes. Cyclic voltammetry of the full sandwich cell was conducted at 10 mV s^{-1} before galvanostatic charge–discharge at 1*C* for 250 cycles. We also conducted electrochemical characterization of the polypeptides as composite electrodes in three-electrode cell configuration (**Table S4.1 and Table S4.2**).

4.7. References

1. Turcheniuk, K., Bondarev, D., Singhal, V. & Yushin, G. Ten years left to redesign lithium-ion batteries. *Nature* **559**, 467-470 (2018).

4. Muench, S., Wild, A., Friebe, C., Häupler, B., Janoschka, T. & Schubert, U. S. Polymer-Based Organic Batteries. *Chem. Rev.* **116**, 9438-9484 (2016).

6. Zeng, X., Li, J. & Singh, N. Recycling of Spent Lithium-Ion Battery: A Critical Review. *Critical Reviews in Environmental Science and Technology* **44**, 1129-1165 (2014).

7. Olivetti, E. A., Ceder, G., Gaustad, G. G. & Fu, X. Lithium-Ion Battery Supply Chain Considerations: Analysis of Potential Bottlenecks in Critical Metals. *Joule* **1**, 229-243 (2017).

12. Janoschka, T., Hager, M. D. & Schubert, U. S. Powering up the Future: Radical Polymers for Battery Applications. *Adv. Mater.* **24**, 6397-6409 (2012).

13. Wild, A., Strumpf, M., Häupler, B., Hager, M. D. & Schubert, U. S. All-Organic Battery Composed of Thianthrene- and TCAQ-Based Polymers. *Advanced Energy Materials* **7**, 1601415 (2017).

22. Joo, Y., Agarkar, V., Sung, S. H., Savoie, B. M. & Boudouris, B. W. A nonconjugated radical polymer glass with high electrical conductivity. *Science* **359**, 1391 (2018).

27. Schubert, U. S., Friebe, C. & Lex-Balducci, A. Sustainable Energy Storage: Recent Trends and Developments toward Fully Organic Batteries. *ChemSusChem* **0** (2019).

35. Bugnon, L., Morton, C. J. H., Novak, P., Vetter, J. & Nesvadba, P. Synthesis of Poly(4-methacryloyloxy-TEMPO) via Group-Transfer Polymerization and Its Evaluation in Organic Radical Battery. *Chem. Mater.* **19**, 2910-2914 (2007).

122. Nguyen, T. P., Easley, A. D., Kang, N., Khan, S., Lim, S.-M., Rezenom, Y. H., Wang, S., Tran, D. K., Fan, J., Letteri, R. A., He, X., Su, L., Yu, C.-H.,

Lutkenhaus, J. L. & Wooley, K. L. Polypeptide organic radical batteries. *Nature* **593**, 61-66 (2021).

123. Banza Lubaba Nkulu, C., Casas, L., Haufroid, V., De Putter, T., Saenen, N. D., Kayembe-Kitenge, T., Musa Obadia, P., Kyanika Wa Mukoma, D., Lunda Ilunga, J.-M., Nawrot, T. S., Luboya Numbi, O., Smolders, E. & Nemery, B. Sustainability of artisanal mining of cobalt in DR Congo. *Nature Sustainability* **1**, 495-504 (2018).

124. Koshika, K., Chikushi, N., Sano, N., Oyaizu, K. & Nishide, H. A TEMPO-substituted polyacrylamide as a new cathode material: an organic rechargeable device composed of polymer electrodes and aqueous electrolyte. *Green Chemistry* **12**, 1573-1575 (2010).

125. Esquivel, J. P., Alday, P., Ibrahim, O. A., Fernández, B., Kjeang, E. & Sabaté, N. A Metal-Free and Biotically Degradable Battery for Portable Single-Use Applications. *Advanced Energy Materials* **7**, 1700275 (2017).

126. Kim, J., Kim, J. H. & Ariga, K. Redox-Active Polymers for Energy Storage Nanoarchitectonics. *Joule* **1**, 739-768 (2017).

127. Tomlinson, E. P., Hay, M. E. & Boudouris, B. W. Radical Polymers and Their Application to Organic Electronic Devices. *Macromolecules* **47**, 6145-6158 (2014).

128. Lutkenhaus, J. A radical advance for conducting polymers. *Science* **359**, 1334 (2018).

129. Coates, G. W. & Getzler, Y. D. Y. L. Chemical recycling to monomer for an ideal, circular polymer economy. *Nature Reviews Materials* (2020).

130. Zhang, K., Monteiro, M. J. & Jia, Z. Stable organic radical polymers: synthesis and applications. *Polymer Chemistry* **7**, 5589-5614 (2016).

131. Janoschka, T., Martin, N., Martin, U., Friebe, C., Morgenstern, S., Hiller, H., Hager, M. D. & Schubert, U. S. An aqueous, polymer-based redox-flow battery using non-corrosive, safe, and low-cost materials. *Nature* **527**, 78 (2015).

132. Koshika, K., Sano, N., Oyaizu, K. & Nishide, H. An Aqueous, Electrolyte-Type, Rechargeable Device Utilizing a Hydrophilic Radical Polymer-Cathode. *Macromol. Chem. Phys.* **210**, 1989-1995 (2009).

133. Sano, N., Tomita, W., Hara, S., Min, C.-M., Lee, J.-S., Oyaizu, K. & Nishide, H. Polyviologen Hydrogel with High-Rate Capability for Anodes toward an Aqueous Electrolyte-Type and Organic-Based Rechargeable Device. *ACS Applied Materials & Interfaces* **5**, 1355-1361 (2013).

134. Suga, T., Ohshiro, H., Sugita, S., Oyaizu, K. & Nishide, H. Emerging N-Type Redox-Active Radical Polymer for a Totally Organic Polymer-Based Rechargeable Battery. *Adv. Mater.* **21**, 1627-1630 (2009).

135. Suga, T., Sugita, S., Ohshiro, H., Oyaizu, K. & Nishide, H. p- and n-Type Bipolar Redox-Active Radical Polymer: Toward Totally Organic Polymer-Based Rechargeable Devices with Variable Configuration. *Adv. Mater.* **23**, 751-754 (2011).

136. Oka, K., Kato, R., Oyaizu, K. & Nishide, H. Poly(vinyldibenzothiophenesulfone): Its Redox Capability at Very Negative Potential Toward an All-Organic Rechargeable Device with High-Energy Density. *Adv. Funct. Mater.* **28**, 1805858 (2018).

137. Qu, J., Morita, R., Satoh, M., Wada, J., Terakura, F., Mizoguchi, K., Ogata, N. & Masuda, T. Synthesis and Properties of DNA Complexes Containing 2,2,6,6-Tetramethyl-1-piperidinoxy (TEMPO) Moieties as Organic Radical Battery Materials. *Chemistry – A European Journal* **14**, 3250-3259 (2008).

138. Ibe, T., Frings, R. B., Lachowicz, A., Kyo, S. & Nishide, H. Nitroxide polymer networks formed by Michael addition: on site-cured electrode-active organic coating. *Chem. Commun.* **46**, 3475-3477 (2010).

139. Qu, J., Fujii, T., Katsumata, T., Suzuki, Y., Shiotsuki, M., Sanda, F., Satoh, M., Wada, J. & Masuda, T. Helical polyacetylenes carrying 2,2,6,6-tetramethyl-1-piperidinyloxy and 2,2,5,5-tetramethyl-1-pyrrolidinyloxy moieties: Their synthesis, properties, and function. *J. Polym. Sci., Part A: Polym. Chem.* **45**, 5431-5445 (2007).

140. Otaki, M. & Goto, H. Helical Spin Polymer with Magneto-Electro-Optical Activity. *Macromolecules* **52**, 3199-3209 (2019).

141. Hatakeyama-Sato, K., Wakamatsu, H., Katagiri, R., Oyaizu, K. & Nishide, H. An Ultrahigh Output Rechargeable Electrode of a Hydrophilic Radical Polymer/Nanocarbon Hybrid with an Exceptionally Large Current Density beyond 1 A cm^{-2}. *Adv. Mater.* **30**, 1800900 (2018).

142. Hiejima, T. & Kaneko, J. Spiral Configuration of Nitroxide Radicals Along the Polypeptide Helix and Their Magnetic Properties. *Macromolecules* **46**, 1713-1722 (2013).

143. Nguyen, T. P.-D. *Advanced Functional Polypeptides for Biological, Energy and Electronic Applications* Ph.D. thesis, Texas A&M University, (2020).

144. Shpilevaya, I. & Foord, J. S. Electrochemistry of Methyl Viologen and Anthraquinonedisulfonate at Diamond and Diamond Powder Electrodes: The Influence of Surface Chemistry. *Electroanalysis* **26**, 2088-2099 (2014).

145. Bard, A. J. & Faulkner, L. R. *Electrochemical Methods: Fundamentals and Applications, 2nd Edition*. (Wiley Textbooks, 2000).

146. Janoschka, T., Teichler, A., Häupler, B., Jähnert, T., Hager, M. D. & Schubert, U. S. Reactive Inkjet Printing of Cathodes for Organic Radical Batteries. *Advanced Energy Materials* **3**, 1025-1028 (2013).

147. Vlad, A., Rolland, J., Hauffman, G., Ernould, B. & Gohy, J.-F. Melt-Polymerization of TEMPO Methacrylates with Nano Carbons Enables Superior Battery Materials. *ChemSusChem* **8**, 1692-1696 (2015).

148. Lutkenhaus, J., Wang, S., Park, A. M. G., Ma, T., Li, F., Easley, A. & Fuchs, G. D. Solution-processable thermally crosslinked organic radical polymer battery cathodes. *ChemSusChem* (2020).

5. ELECTRON TRANSPORT KINETICS FOR VIOLOGEN CONTAINING POLYPEPTIDES WITH VARYING SIDE GROUP LINKER SPACING*

5.1. Introduction

With the increase demand for lithium-ion batteries and the depleting supply of strategic elements alternative active materials are needed for battery electrodes. One such material class of interest is redox-active polymers (RAPs), which include both conjugated polymers and polymers with redox-active pendant groups.[4,27,126,150,151] Extensive work has been done to investigate the structure-property relationship for conjugated polymers in the solid-state, due to their known conduction mechanism and synthetic control over regiochemistry and crystallinity.[152-155] However, there has been significantly less work done for RAPs with pendant redox-active groups, due to their random coil and amorphous nature. For cathodic RAPs with pendant redox-active groups, such as 2,2,6,6-tetramethylpiperidin1oxyl (TEMPO) containing polymers, there have been several studies investigating the electron transport mechanism[20,93,156], however, there has been less work on anodic pendant RAPs, such as viologen containing polymers.[157,158] Given the complex structure-property relationship for RAPs with pendant groups, several charge transfer mechanisms have been proposed.

---

* Reproduced from ref. 149. Easley, A. D., Li, C.-H., Li, S.-G., Nguyen, T., Echols, I., Wooley, K., Tabor, D. & Lutkenhaus, J. Electron Transport Kinetics for Viologen Containing Polypeptides with Varying Side Group Linker Spacing. (In preparation).

Much like solutions of redox-active molecules, the transfer of electrons between polymer-bound redox moieties follows similar steps. The main steps involve the diffusion of redox active species to a distance for electron transfer, the ionic and atomic rearrangement and solvent dipole orientation, and spontaneous electron transfer. Three main theories exist to consider the diffusion of polymer-bound redox active moieties: Dahms-Ruff (D-R) theory,[159,160] Laviron-Andrieux-Savéant (LAS) theory,[161,162] and the diffusion cooperative model (**Figure 5.1**).[20] D-R theory describes the electron transfer of freely diffusion redox active groups.[159,160] In this model, charge transport is limited by the diffusion of the molecules, where electron transfer can only occur as rapidly as the molecules will come in close contact. Explicitly stated, this model is applied in systems where the physical diffusion (D_{phys}) of the redox-active moieties is larger than the diffusion of electron transfer (D_e). Experimental studies have shown D-R theory accurately describes electron transfer in metal complexes,[163] viologen-polymer and dimer solutions,[158,164] ferrocene polymer solutions,[164] and viologen-based ionic liquids.[165]

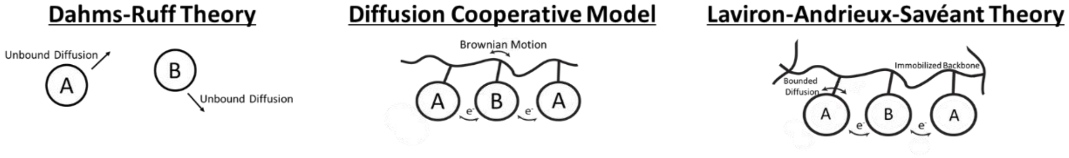

Figure 5.1. Representation of the observed diffusion in the three main theories of electron-transfer.

As the physical diffusion (D_{phys}) of the redox-active moieties is further restricted and the redox-active moieties are immobilized ($D_{phys} \approx 0$) LAS theory is used (D_e is larger than D_{phys}).[161,162] Previously, LAS theory has been used to describe electron transfer of thin film of TEMPO-containing polyether,[166] ferrocene containing polyacrylamide gels,[167] crosslinked TEMO-containing polynorbornene,[168] ferrocene-based metal-organic frameworks,[169] and viologen and TEMPO nanoparticles.[170] Recently, Burgess *et al.* and Sato *et al.* reported deviation from both D-R and LAS theory for viologen-based polymeric solutions and TEMPO-based polymer thin films, respectively.[20,158]

To account for this deviation, Sato *et al*. proposed the diffusion cooperative model, which considers effects the Brownian motion of the polymer has on the transport kinetics.[20] In this model, the diffusion of electron transfer has contributions from both D_e and D_{phys} (from the Brownian motion of the backbone). The D_{phys} considered here is significantly reduced to compared to the free diffusion of the D-R theory but greater than the lack of D_{phys} assumed in LAS theory. This intermediate D_{phys} model has also been applied to an immobilized TEMPO-containing polyamine,[171] TEMPO-substituted poly(ethylene sulfide),[172] and a variety nitroxide containing polymers with varying backbone and linker groups.[20] However, much of the work described here considers physically restricted crosslinked polymers or polymers with a lack of backbone structure (i.e. random coil).

Previously, our group has reported the use of redox-active polypeptides in solid-state and redox flow batteries.[122,173] Both works presented the use of a degradable α-helical polypeptide as a backbone for anodic and cathodic redox-active moieties. Akhoury *et al.*

studied non-crosslinked and crosslinked ferrocene-based grafts on carbon particles.[174] The authors found bounded diffusion and electron hopping influenced the rate of electron transfer for the non-crosslinked grafts, whereas only electron hopping contributed in the crosslinked grafts due to reduced mobility.[174] Similarly, Whiting *et al.* studied poly(triphenylamine acrylate) brushes and spin coated films and found that the more ordered brushes led to increased rate of electron transfer as compared to the more disordered spin-coated films.[175] In addition to the influence of the helical polypeptide backbone on electron transfer among redox-active pendant groups, electron tunneling through the helical backbone could also influence electron transport. Arikuma *et al.* demonstrated that for short ferrocene-terminated helical polypeptides (less than 16 repeat units), electron tunneling contributed to the overall rate of electron transfer.[176] Deng *et al.* reported the synthesis of viologen containing helical polyacetylenes, however, the effect of the helical backbone and pendant group spacing on the electron transport mechanism has not studied.[177]

Here, we report the synthesis of viologen-based polypeptides with varying spacing between the backbone and viologen pendant group. The influence of backbone structure is also considered through testing of a helical polypeptide backbone and control aliphatic backbone. The polymers were processed to produce thin-film coatings and the electron transfer rate constants were determined from chronoamperometry and cyclic voltammetry. The determined rate constants included the apparent diffusion coefficient (D_{ap}), rate constant for electron self-exchange between pendant viologen groups (k_{ex}), and heterogenous charge transfer (k^0). The physical diffusion coefficients (D_{phys}) for the polymers in solution and the viologen pendant group relative to the backbone were determined using dynamic light scattering and computation methods, respectively. The relationship between D_e and D_{phys} was analyzed to determine the predominate mechanism of electron transport in the system. Finally, we evaluated the performance of the viologen-based polypeptides in half-cell batteries to relate the electron transfer kinetics to battery performance. Overall, these results present the dominate theory and redox couple for charge transport in viologen-based polypeptides.

5.2. Methods

5.2.1. Materials

Lithium chloride (LiCl), γ-butyrolactone (GBL), and 4-vinylbenzyl chloride (VBC) were used as received from Sigma Aldrich. Ultrapure water (MQ water) was collected from a Milli-Q® integral water purification system (18 MΩ·cm). 4-cyano-4-(((dodecylthio)carbonothioyl)thio)pentanoic acid (CTA) was used as received from Boron Molecular. Methanol was used as received from VWR. Lithium metal was purchased from Alfa-Aesar. ITO-coated glass (ITO glass) was purchased from Delta Technologies, and cleaned by subsequent sonication in soap water, water, acetone, and isopropyl alcohol, followed by drying with N_2 and ozone plasma treatment for 10 min.

Chemical characterization

Attenuated total reflectance-Fourier transform infrared (ATR-FTIR) spectra were recorded for powder samples on an IR Prestige 21 system (Shimadzu Corp.). The data was analyzed using IRsolution v. 1.40 software. Circular dichroism (CD) spectra of the viologen polypeptide solutions in a quartz cell were recorded, between 180 and 280 nm, using a wavelength step of 1.0 nm, and had a path length of 1.0 cm, on a Chirascan CD spectrometer from Applied Photophysics, Ltd. (Leatherhead, UK) equipped with a 150-Watt xenon arc lamp. The viologen polypeptides were dissolved at 3 mM of repeat unit in H_2O to generate solutions for analysis. The resulting CD spectra were analyzed using Pro-Data v. 5 software. ^{1}H and ^{13}C nuclear magnetic resonance (NMR) spectra were recorded on a Bruker 400 spectrometer. Glass transition temperatures (T_g) were determined from the inflection point of the second heating cycle measured using modulated differential scanning calorimetry (MDSC) on a Q200 DSC (TA Instruments) with a heat-cool-heat cycle. The samples were ramped from -40 °C to 200 °C at a rate of 5 $°C \cdot min^{-1}$ with amplitude of 1.272 °C for a period of 60 s with nitrogen purge at 50 $mL \cdot min^{-1}$. Finally, dynamic light scattering (DLS) data was collected, using the same CD solutions, on a Malvern Zetasizer Nano ZS and analyzed with Zetasizer v7.13 to get the hydrodynamic radius. Using the Stokes-Einstein equation, **Equation 5.1**, the solution state polymer diffusion coefficient (D_{DLS}) can be calculated from the measured hydrodynamic radius (r_h) in DLS.

$$D_{DLS} = \frac{k_B T}{6\pi\eta r_h}$$

Equation 5.1

where k_B is Boltzmann's constant, T is the temperature (in K), and η is the viscosity of the medium (H_2O).

5.2.2. Synthesis of viologen polypeptides with varying alkyl spacer lengths

The viologen polypeptides were synthesized following the method of Nguyen *et al.*[122] For the C3 and C9 viologen polypeptides the method was altered slightly. Instead of 6-Chlorohexanol in the first synthetic step, 3-Choloropropanol and 9-Chlorononanol were used to produce the C3 and C9 viologen polypeptides, respectively. Details of the synthetic steps can be found in the Supplementary Information.

5.2.3. Synthesis of the control viologen polymer

Poly(vinylbenzyl methyl viologen) was synthesized following a modified method as reported by Nagarjuna *et al*.[178] First, methyl viologen chloride (MV-Cl) was synthesized following the procedure reported by Nguyen *et al*. followed by ion exchange with using Dowex® A2 ion exchange resin.[122] In parallel, poly(vinylbenzyl chloride) (PVBC) was synthesized *via* reversible addition–fragmentation chain-transfer (RAFT) polymerization. In a 25-mL Schlenk flask 5.0 g (32 mmol) of VBC, 11 mg of AIBN (0.07 mmol), 54 mg (0.14 mmol) of CTA, and 7.78 mL of toluene were combined at ambient conditions. Resulting in a monomer : initiator : CTA molar ratio of 228 : 0.5 : 1. The flask was then sealed, and three freeze-pump-thaw cycles were carried out with N_2 gas and liquid N_2. After the final thaw, the flask was sealed and heated to 75°C allowed to react for 24 hrs. After 24hrs, the reaction was cooled to room temperature and exposed to ambient air to terminate the reaction. The reaction solution was then precipitated in hexanes and the resulting PVBC was collected *via* vacuum filtration and dried overnight at r.t. under vacuum.

Following a procedure similar to Nagarjuna *et al*, 500 mg (18.7 mmol of repeat unit) of PVBC, 4.8 g of MV-Cl (3.3 mmol), and 15 mL of dry DMF were combined in a

100-mL Schlenk flask equipped with a condenser.[178] The reaction was then heated to 90 °C and allowed to react for 6 days. The reaction solution was precipitated in methanol and the resulting poly(vinylbenzyl methyl viologen) (PV) was collected *via* vacuum filtration and vacuum dried overnight.

5.2.4. Experimental determination of rate constants

Thin films of each viologen polypeptide were prepared by dissolving 8 mM of repeat unit for each polypeptide in 1:1 (v:v) methanol: MQ water. 80 μL of the prepared solution were drop casted on ITO glass (coating area ≈ 1.3 cm^2) and allowed to dry at ambient conditions for 24 h, followed by drying under vacuum at r.t. for 24 h. After drying, the mass of each film was measured to determine mass loading and the thickness was determined using profilometry (KLA Alpha-Step D-500). Finally, the fabricated electrodes were utilized in a three-electrode cell (coated ITO glass working electrode with lithium metal reference and counter electrodes) with 10 mL of 0.5 M LiCl in GBL as the electrolyte. All electrochemical measurements were performed using a Solartron potentiostat (Solartron Electrochemical Interface 1287). Chronoamperometry (CA) was performed in two steps (1) from 3 V to 2.2 V *vs.* Li/Li^+ and (2) from 2.2 V to 1.6 V *vs.* Li/Li^+ to determine the properties for both redox couples separately and cyclic voltammetry (CV) was performed from 3.2 V to 1.5 V *vs.* Li/Li^+ at 10, 25, 50, and 100 mV s^{-1}.

The CA data was further analyzed to estimate the apparent diffusion coefficient (D_{ap}) by fitting using the Cottrell equation (**Equation 5.2**) assuming semi-infinite condition.[20]

$$i = \frac{nFAC_0^*}{\sqrt{\pi t}}\sqrt{D_{ap}} = \tau\frac{nFAC_0^*}{\sqrt{\pi}}\sqrt{D_{ap}}$$

Equation 5.2

where i is the current output from CA (in mA), n is the number of electrons transferred per repeat unit, A is the electrode area (in cm^2), and C_0^* is the total concentration of redox sites (or repeat units in mol/cm^3). If $D_{ap} \geq D_{phys}$, the rate constant for electron self-exchange, k_{ex} was found using the Dahms-Ruff equation (**Equation 5.3**).

$$k_{ex} = \frac{6(D_{ap} - D_{phys})}{C_0^* \delta^2}$$

Equation 5.3

where δ is the average site distance, which is determined from MD simulations as discussed below. However, if $D_{phys} < D_{ap}$ and $D_{phys} \approx 0$, k_{ex} was calculated using the Laviron−Andrieux−Savéant equation (**Equation 5.4**).

$$k_{ex} = \frac{6D_{ap}}{C_0^* \delta^2}$$

Equation 5.4

From the peak separation of the CV data at 10 mV s^{-1}, the heterogeneous rate constant, k^0, was calculated using the simplified method of Nicholson, **Equation 5.5**. The simplified form assumed the diffusion coefficient of the oxidized and reduced species are equal to D_{et}.

$$\psi = \frac{k^0}{\left(\pi D_{ap} f v\right)^{1/2}}$$

Equation 5.5

where ψ is a dimensionless rate parameter from the method of Nicholson, *v* is the scan rate of CV (in V s^{-1}), and D_{ap} is the apparent diffusion coefficient from CA (in cm^2/s), respectively. *f* = F/RT, where F is Faraday constant (or 96585 C/mol e^-), R is the gas constant (or 8.3124 J/mol K), and T is the temperature (in K).

5.2.5. Evaluation of the capacity performance

The fabricated films were also used as working electrodes in a half cell with a lithium metal reference and filter paper soaked in 0.5 M LiCl in GBL as the separator and electrolyte, respectively. Galvanostatic charge-discharge (GCD) was performed on the half cells at different c-rates (1 C is the current required to completely charge the battery in 1 h). GCD was performed for 5 cycles at 0.2, 0.4, 0.6, 0.8, 1.0, and 1.2. C followed by 10 cycles at 0.2 C.

5.3. Results and Discussion

5.3.1. Synthesis and chemical characterization of viologen polypeptides and control viologen polymer.

The three viologen polypeptides were synthesized through the post-polymerization modification of iodo-containing polypeptide precursors. The spacing between the polypeptide backbone and the viologen redox-active group was changed by the incorporation of alkyl chains of varying lengths (**Figure 5.2 a**) to systematically study side chain effects. In addition to these polypeptides, poly(vinylbenzyl methyl viologen) (PV) was synthesized as a control (**Figure 5.2 b**) using post-polymerization modification of a chloro-containing PVBC precursor. PV was selected as the control because it bears a hydrocarbon (non-peptide) backbone and because it has been extensively studied in the literature.[178-181] By this design, the effect of having a peptide and non-peptide backbone can be compared.

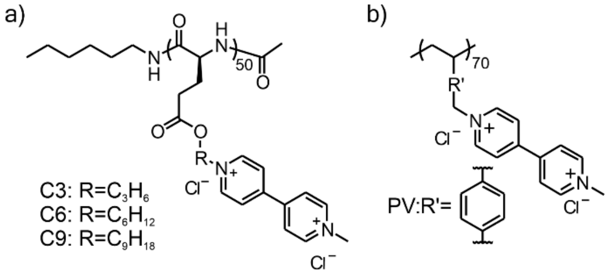

Figure 5.2. The chemical structure of a) viologen-based polypeptides with alkyl spacer lengths of three (C3), six (C6), or nine (C9) carbons. b) The chemical structure of the control viologen (PV), bearing a non-peptide backbone.

To understand how the side chain length affects the nature of the polypeptides' redox response, cyclic voltammetry (CV) was conducted using thin films on ITO glass (mass loadings: 0.25 to 0.40 mg/cm^2 and thicknesses: 200 to 275 nm), **Figure 5.3**. For the CVs obtained at 10 mV/s, the three polypeptides exhibited two redox couples at similar potentials ($E_{1/2}$ = 2.12 and 2.54 V *vs.* Li/Li$^+$), consistent with that of PV and previous literature.[178] For C3 and C6, the MV^{2+}/ $MV^{\bullet+}$ redox couple was more reversible with a peak separation (ΔE_p) of *ca.* 0.25 V as compared to 0.42 V *ca* for the $MV^{\bullet+}/MV^0$ redox couple. C9 exhibited the same ΔE_p of 0.32 V for both redox couples. PV exhibited a ΔE_p consistent with C3 and C6. These results generally follow past literature for PV, for which $MV^{\bullet+}/MV^0$ is less reversible than MV^{2+}/ $MV^{\bullet+}$.[20] All polymers exhibited diffusion limited redox reactions, as indicated by the linear fit of peak current *vs.* square-root of scan rate (**Figure S5.1**).

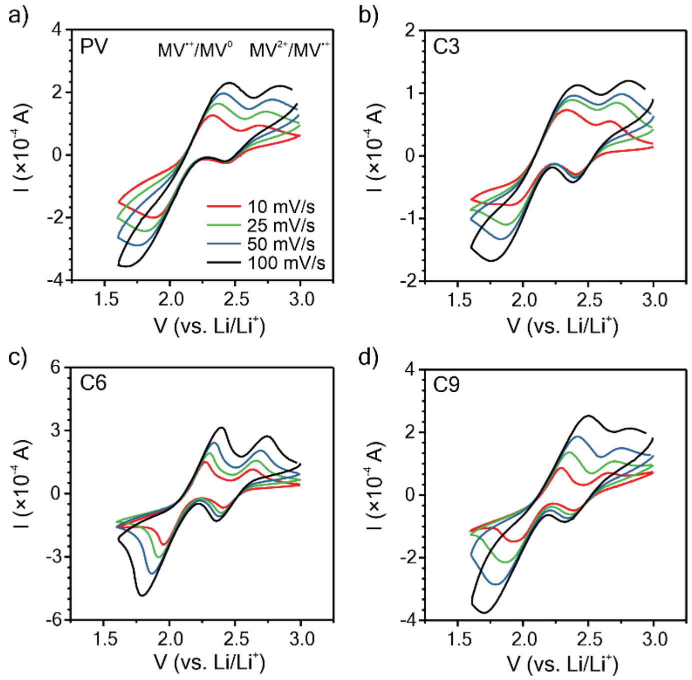

Figure 5.3. Cyclic voltammograms at 10, 25, 50, and 100 mV·s^{-1}for a) PV, b) C3, c) C6, and d) C9 thin films on ITO-coated glass as working electrodes in a three-electrode beaker cell configuration. The supporting electrolyte was 0.5 M LiCl in γ-butyrolactone (GBL). Lithium metal was used as counter and reference electrodes.

5.3.2. Experimental determination of rate constants.

To elucidate how the side chain lengths affect the rate constants of electron transfer of the polypeptides', thin films were investigated experimentally using chronoamperometry (CA). Specifically, Cottrell plots of CA data were used to determine the apparent diffusion coefficient (D_{ap}), which was then used to calculate the rate constant for electron self-exchange (k_{ex}). Additionally, the peak separation from CV was used to calculate the heterogeneous rate constant (k^0) using the method of Nicholson.

From CA, the Cottrell plots for the three polypeptides were determined for oxidation and reduction and decoupled for MV^{2+}/ $MV^{•+}$ and $MV^{•+}/MV^0$, **Figure 4.** We adopted an abbreviation for referring to the reduction/oxidation of each redox couple, for example $R^{2+/1+}$ refers to the reduction from MV^{2+}/ $MV^{\bullet+}$. The raw input/output data is found in **Figure S5.2** and the Cottrell plots for PV are found in **Figure S5.3**. In general, PV and all three polypeptides exhibited similar CA responses for both $R^{2+/1+}$ and $O^{2+/1+}$, which is consistent with previous literature for reduction (**Figure 5.4 a-c** and **Figure S5.3**).[158,182] The similar response slope for all the polymers is indicative of similar rates of electron transfer. In contrast, the $O^{\bullet+/0}$ slope for PV and the three polypeptides showed similar, however, for $R^{\bullet+/0}$ the slope increases in magnitude with increased spacer length (**Figure 5.4d-f** and **Figure S5.3**). Explicitly, the slopes for reduction from $MV^{\bullet+}/MV^0$ followed the trend of PV < C3 < C6 < C9, which would suggest C9 will exhibit the highest electron transfer rate.

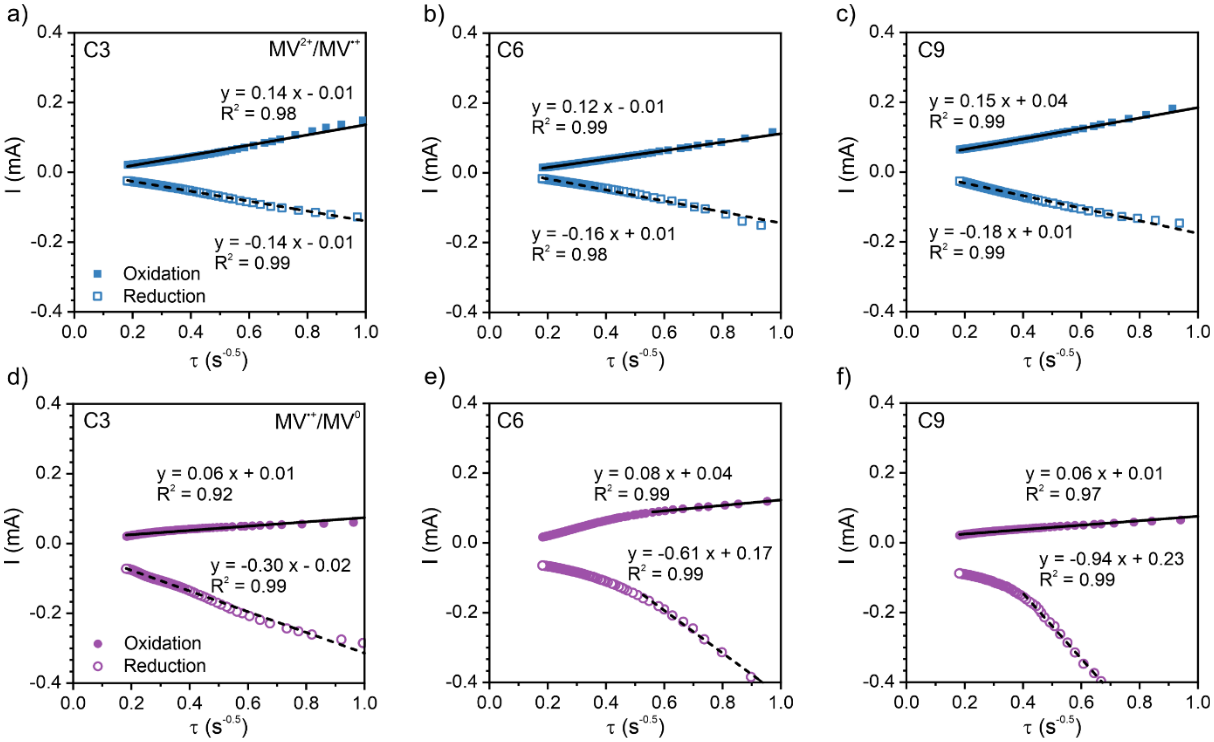

Figure 5.4. Chronoamperometry (CA) Cottrell plots for the two redox couples of the three polypeptides. (a-c) show the CA output data for the MV^{2+}/ $MV^{\bullet+}$ redox couple. (d-f) show the CA output data for the $MV^{\bullet+}/MV^0$ redox couple. Viologen polypeptides coated on ITO glass were used as the working electrodes in a three-electrode beaker cell configuration. The supporting electrolyte was 0.5 M LiCl in γ-butyrolactone. Lithium metal was used as counter and reference electrodes. The Cottrell plots for PV are found in **Figure S5.3**.

The slopes from the Cottrell plots were used to estimate the apparent diffusion coefficient (D_{ap}) using **Equation 5.2**. C_0^* was determined as 2.03 M for PV, 2.92 M for C3, 2.65 for C6, and 2.42 for C9. The site distance (δ) of the pendant viologen groups in all three polypeptides was determined to be 4 Å using MD simulations, which is consistent with previous reports for PV.[158,182] The D_{ap} values were similar for all the polymers investigated and on the order of 10^{-13} cm^2/s (**Figure S5.4**). Within a single redox process (i.e., $R^{2+/1+}$), there is very little effect of linker group on D_{ap}. However, we saw that all polymers follow a similar trend where $R^{1+/0} > R^{2+/1+}$ and $O^{2+/1+} > O^{1+/0}$.

To determine the mechanism of electron transfer in the system, the physical diffusion coefficient of the system must be compared to D_{ap}. Two different methods were used to approximate the diffusion of the viologen polypeptides within their thin film. The first method was to determine the solution state diffusion coefficient from DLS (D_{DLS}) and the second was using MD simulations to get the physical diffusion of the viologen pendant groups (D_{phys}). The obtained D_{DLS} and D_{phys} values were on the order of 10^{-7} cm^2/s (**Table S5.1**). However, both approximations had excess of solvent compared to the electrochemical testing conditions and result in overestimates of D_{DLS} and D_{phys}. Previous studies on charged polymers and protein hydrogels suggest that the solution state diffusion coefficient is approximately 10 orders of magnitude larger than thin film diffusion (*ca.* 10^{-12} to 10^{-19} cm^2/s).[183,184] Using this approximation, the diffusion of the viologen polypeptides would be *ca.* 10^{-17} cm^2/s. This value was smaller than the D_{ap} (10^{-13} cm^2/s) suggesting Laviron-Andrieux-Savéant theory is the appropriate mechanism of electron transport in the viologen polypeptides. k_{ex} was determined using **Equation 5.4**.

Table S5.2 and **Figure 5.5** show the summary of log(k_{ex}) values for all the polymers studied. For all the polymers studied (independent of linker group), k_{ex} of $R^{1+/0} > R^{2+/1+}$ and $O^{2+/1+} > O^{1+/0}$. This trend was also observed by Dalton *et al*. and Hatozaki *et al*. for an electrolyte swollen viologen film, where k_{ex} for $MV^{\bullet+}/MV^0$ was larger than $MV^{2+}/ MV^{\bullet+}$.[182,185,186] When only considering k_{ex} for $R^{1+/0}$, C9 exhibited the largest value (4.8×10^7 M^{-1} s^{-1}), whereas C3 was the smallest (3.5×10^6 M^{-1} s^{-1}). The larger k_{ex} value for C9 could be due to the longer alkyl chain allowing for greater diffusion, from the D_{phys} values in **Table S5.1**, and enhanced dimerization leading to the higher rate of electron transfer.

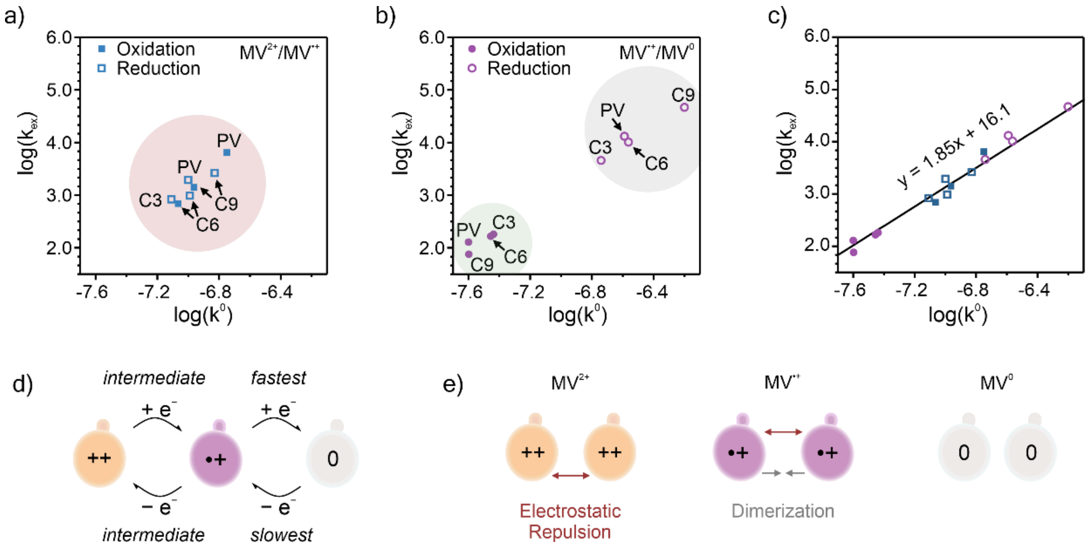

Figure 5.5. Summary of the $\log(k_{ex})$ and $\log(k^0)$ for PV, C3, C6, and C9. The results are presented as separate experimental values of oxidation and reduction for the a) $MV^{2+}/MV^{\bullet+}$ and b) $MV^{\bullet+}/MV^0$ redox couples. c) Plot showing all the $\log(k_{ex})$ *vs*. $\log(k^0)$ for experimental data for both redox couples. Panels a) and b) show the enlarged region containing the CV/CA-determined rate constants for the polypeptides studied in this work. d) Schematic showing the relative k_{ex} values and e) the intermolecular forces between viologen groups in each oxidation state.

Using the previously discussed ΔE_p values from CV at 10 mV/s, the heterogeneous rate constant (k^0) was determined using **Equation 5.4**. The calculated k^0 values are summarized in **Figure 5.5 a-b** and show little variation among the different redox couples and polymers (*ca.* $10^{-7} – 10^{-8}$ cm/s). The values for $MV^{\bullet+}/MV^0$ were slightly smaller than $MV^{2+}/ MV^{\bullet+}$. The similarity among the thin films studied is likely dominated by the consistent substrate and redox group utilized in the study.

Further confirmation of the electron transport mechanism was evaluated by considering the slope of the relationship between $\log(k_{ex})$ and $\log(k^0)$ in **Figure 5.5 c**, which was determined to be 1.85. This slope was then compared to the slopes from Marcus-Hush theory and the diffusion cooperative model. First, the relationship from Marcus *et al*. is presented in **Equation 5.6**, similar to the relation found in LAS theory.[187]

$$\left(\frac{k_{ex}}{A_{ex}}\right)^{\frac{1}{2}} = \frac{k^0}{A_{el}}$$

Equation 5.6

A_{ex} and A_{el} are the pre-exponential factors for self-exchange and the electrode reaction. When reorganized, a linear relationship between k_{ex} and k^0 emerges as $\log(k_{ex,app}) = 2\cdot\log(k^0) + b$, where $b = -2\log(A_{el}) + \log(A_{ex})$. From this linear relationship, if electron transfer follows Marcus-Hush theory with diffusion limitations or LAS theory, it is expected that the slope for $\log(k_{ex,app})$ *vs.* $\log(k^0)$ is 2. From the diffusion cooperative model, a relationship between k_{ex} and k^0 is found when substituting for D_{phys}, **Equation 5.7**.[20]

$$\frac{k_{ex}}{16\pi a N_a} = \frac{k^0 2L}{3\kappa_{el} e^{\left(-\frac{\lambda}{4k_bT}\right)}}$$

Equation 5.7

When reorganized, the linear relationship is $\log(k_{ex,app}) = \log(k^0) + \log(b)$, where $b = 2L16\pi aN_a/3\kappa_{el}\exp(-\lambda/4k_bT)$. For the diffusion cooperative model, the expected slope from the log (k_{ex}) *vs.* $\log(k^0)$ is 1. Given the slope analysis of 1.85, we conclude that the studied viologen polymers do not follow the diffusion cooperative model, where the Brownian motion of the backbone contributes to the electron transport. However, the slope was slightly smaller than the slope seen for Marcus-Hush theory, which supports the diffusion limitations we conclude for applying LAS theory and those seen in cyclic voltammetry (**Figure S5.1**).

An additional consideration for the mechanism of electron transfer in the viologen polypeptides is the electron tunneling through the helical backbone. According to LAS theory, k_{ex} should be equal to the activation-limited rate constant (k_{act}) determined from Marcus-Hush theory (**Equation S5.2**). However, if electron tunneling occurs it would manifest in an enhanced experimentally determined k_{ex} compared to k_{act}. Here, k_{act} values were using H_{AB} and λ determined from DFT calculations., which is described in detail in the supplementary information. k_{act} was *ca.* 10^9 $M^{-1} \cdot s^{-1}$, which slightly larger than the experimentally determined k_{ex} values and previously studied TEMPO-based monomer (*ca.* 10^8 $M^{-1} \cdot s^{-1}$).[20] Suggesting that there is no significant electron tunneling observed in the viologen polypeptide thin films, which is consistent with previous results for alanine and aminoisobutyric acid α helical polypeptides with 48 repeat units (3.1×10^{-14} s^{-1}).[176]

In the k_{ex} data, three main clusters appear (**Figure 5.5 d - e**). The data in the red shaded area was dominated by electrostatic repulsion of the MV^{2+} and/or the $MV^{\bullet+}$ groups, which lead to the smallest observed k_{ex} values. In the gray shaded region, dimerization leads to ordering and close packing to facilitate rapid electron transfer, leading to the largest k_{ex} values. Finally, in the green shaded area an entropy loss due to the dimerization leads to slow electron transfer and the smallest k_{ex} values.

From the trends in k_{ex}, the future design of methyl viologen RAPs (utilizing both redox couples) should target longer linker groups to enhance the electron transfer of $R^{1+/0}$. However, this will also lead to a decrease in electron transfer for $O^{1+/0}$. If being used in energy storage applications, such as a redox flow battery, different currents could be used for discharge (reduction) and charge (oxidation). For example, a smaller current could be used for oxidation to prevent a low coulombic efficiency. However, if only the MV^{2+}/ $MV^{\bullet+}$ redox couple is desired, then the RAPs linker group does not have a profound effect. For energy storage, this would result in a high coulombic efficiency with the same currents of charge and discharge.

5.3.3. Impact of transfer kinetics on electrode performance.

An important consideration for the future design of RAPs is the relationship between electron transfer rates and the charge-discharge performance. To determine the capacity performance of the viologen polypeptides, galvanostatic charge-discharge (GCD) was utilized at a variety of C-rates on a half cell with lithium metal, where 1 C is the current required to charge the battery in 1 hour. The theoretical capacities for the studied polymers were 149.2 mAh/g for PV, 130.3 mAh/g for C3, 118.3 mAh/g for C6, and 108.0 mAh/g for C9. For the half cells, all the polymers studied exhibited two peaks in CV at 2.2 – 2.5 V and 1.7 – 2.1 V *vs.* Li/Li^+ (**Figure S5.5**), which was similar to those observed in the three-electrode beaker cells (**Figure 5.3**). In addition to CV, two characteristic plateaus at 2.15 and 2.55 V *vs.* Li/Li^+ were observed in the GCD curves at 0.2 C associated with the two redox couples (**Figure S5.6**).

Figure 5.6a summarizes the discharge capacity at varying C-rates for the viologen polypeptides and control viologen polymer. All the polymers exhibited capacities significantly lower than theoretical (C6 exhibited the maximum at *ca.* 40% of theoretical), due to the lack of conductive additive and insulating backbones. Additionally, all the polymers exhibited capacity fade and low coulombic efficiencies likely due to dissolution of the polymer into the electrolyte (**Figure S5.7**). For all the polymers, as the C-rate increased there was a decrease in capacity and the two plateaus became less pronounced.

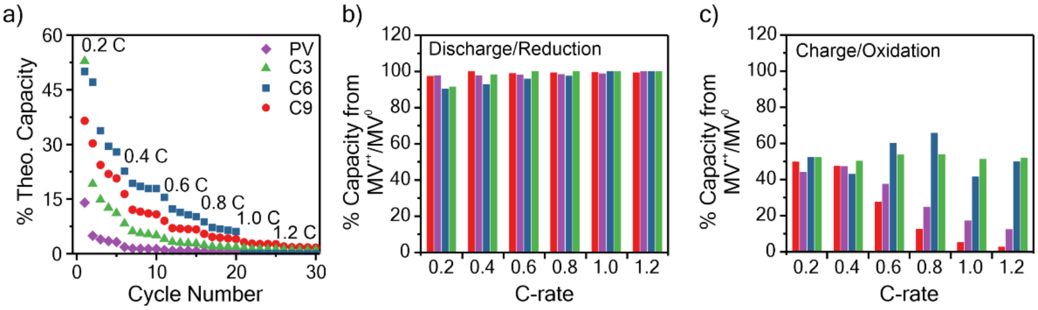

Figure 5.6. a) Discharge capacity summary for the polymers studied at the varied c-rates. The percent of total capacity from the $MV^{\bullet+}/MV^0$ redox couple for b) discharge (reduction) and c) for charge (oxidation) for all polymers studied. The data is taken from the first cycle in **Figure S5.6**. The legend in panel a) are applicable to panels b) and c).

At C-rates less than 1 C, C6 showed the best performance followed by C9, C3, and PV. After 1C, all polymers show significantly lower capacity, however, C9 exhibited the highest capacity. At 0.2 C, C6 exhibited the highest capacity of 1.28×10^{-2} mAh/cm^2 and PV exhibited the lowest (0.45×10^{-2} mAh/cm^2). This suggests that although the backbone does not influence the electron transfer kinetics, similar k_{ex} seen for the viologen polypeptides and PV, it improves the capacity performance.

The capacity contributions of $MV^{\bullet+}/MV^0$ were considered by identifying the inflection point in the second derivative of the charge-discharge curves (**Figure S5.6**). **Figure 5.6b-c** shows the percent of total capacity from $MV^{\bullet+}/MV^0$ in both discharge and charge, respectively. In discharge (reduction), $MV^{\bullet+}/MV^{0+}$ contributes almost entirely to the observed discharge capacity for all the polymers. However, in charge (oxidation), $MV^{\bullet+}/MV^{0+}$ contributes to about half of the observed charge capacity for C-rates less than 1C for all polymers. Above 1 C, C9 and PV exhibited decreased contribution from $MV^{\bullet+}/MV^{0+}$ to the charge capacity, whereas for C3 and C6 the contribution remains approximately 50% (**Figure 5.6 c**). These observed trends in capacity contribution for $MV^{\bullet+}/MV^{0+}$ mirror similar trends to those observed for k_{ex}. Specifically, k_{ex} for $R^{1+/0} > R^{2+/1+}$, meaning in reduction the electron transfer rate of $MV^{\bullet+}/MV^0$ is much higher than $MV^{2+}/ MV^{\bullet}$. However, upon charging $k_{ex,app}$ for $O^{2+/1+}$ is only slightly larger than $O^{1+/0}$, so the two redox couples contributed equally to the charge capacity.

5.4. Conclusion

In conclusion, the successful synthesis of viologen-containing polypeptides with varying linker lengths were demonstrated and confirmed using a variety of spectroscopic methods. The polymers were cast into thin films that were used in three-electrode beaker cells to study the electron transfer kinetics using cyclic voltammetry (CV) and chronoamperometry (CA). From CV studies of C3, C6, and PV it was found that $MV^{\bullet+}/MV^{0}$ is less reversible than $MV^{2+}/ MV^{\bullet+}$, whereas for C9 the two redox couples exhibited the same reversibility. Additional investigation using Cottrell analysis of the CA data led to determination of D_{ap} and k_{ex}. k_{ex} for all the polymers studied followed the pattern of $R^{1+/0} > R^{2+/1+}$ and $O^{2+/1+} > O^{1+/0}$. The largest difference in k_{ex} for the studied polymers was for $R^{1+/0}$, where C9 exhibited the highest k_{ex} and C3 exhibited the smallest. Upon analysis of the linear relationship between $\log(k_{ex})$ and $\log(k^{0})$, we conclude that the slope of 2 indicated Marcus-Hush theory of electron transfer was the best description of electron transfer in the studied polymers. Finally, galvanostatic-charge discharge of lithium metal half cells was used to evaluate the capacity performance. C6 showed highest capacity at C-rates less than 1 C, whereas at higher C-rates C9 showed highest capacity. It was also observed that since k_{ex} for $R^{1+/0} > R^{2+/1+}$, $MV^{\bullet+}/MV^{0}$ dominated the discharge capacity. However, upon charging k_{ex} for $O^{2+/1+} > O^{1+/0}$ but similar, so the two redox couples contributed equally to the charge capacity.

Taken together this suggests that variation of linker group for viologen-based RAPs has a larger impact on the $MV^{\bullet+}/MV^{0}$ and should be considered when selecting battery charge-discharge rates. However, additional studies are needed to confirm the structure-property relationship for anodic RAPs. Specifically, further work should be done to identify high throughput backbone-side group systems. The three viologen-polypeptides studied here required the synthesis of three different precursor polymers followed by installation of the same viologen moiety. Future work should consider utilizing one precursor polymer with the installation of different redox-active moieties. This could help to improve the variety of polymers studied in the future while reducing the synthetic time. With future synthetic variety, structure-property relationships for anodic RAPs can be used to design the next generation of fully polymeric batteries with improved design criteria.

5.5. References

4. Muench, S., Wild, A., Friebe, C., Häupler, B., Janoschka, T. & Schubert, U. S. Polymer-Based Organic Batteries. *Chem. Rev.* **116**, 9438-9484 (2016).

20. Sato, K., Ichinoi, R., Mizukami, R., Serikawa, T., Sasaki, Y., Lutkenhaus, J., Nishide, H. & Oyaizu, K. Diffusion-Cooperative Model for Charge Transport by Redox-Active Nonconjugated Polymers. *Journal of the American Chemical Society* **140**, 1049-1056 (2018).

27. Schubert, U. S., Friebe, C. & Lex-Balducci, A. Sustainable Energy Storage: Recent Trends and Developments toward Fully Organic Batteries. *ChemSusChem* **0** (2019).

93. Rohland, P., Schröter, E., Nolte, O., Newkome, G. R., Hager, M. D. & Schubert, U. S. Redox-active polymers: The magic key towards energy storage – a polymer design guideline progress in polymer science. *Prog. Polym. Sci.* **125**, 101474 (2022).

122. Nguyen, T. P., Easley, A. D., Kang, N., Khan, S., Lim, S.-M., Rezenom, Y. H., Wang, S., Tran, D. K., Fan, J., Letteri, R. A., He, X., Su, L., Yu, C.-H., Lutkenhaus, J. L. & Wooley, K. L. Polypeptide organic radical batteries. *Nature* **593**, 61-66 (2021).

126. Kim, J., Kim, J. H. & Ariga, K. Redox-Active Polymers for Energy Storage Nanoarchitectonics. *Joule* **1**, 739-768 (2017).

149. Easley, A. D., Li, C.-H., Li, S.-G., Nguyen, T., Echols, I., Wooley, K., Tabor, D. & Lutkenhaus, J. Electron Transport Kinetics for Viologen Containing Polypeptides with Varying Side Group Linker Spacing. (In preparation).

150. Gannett, C. N., Melecio-Zambrano, L., Theibault, M. J., Peterson, B. M., Fors, B. P. & Abruña, H. D. Organic electrode materials for fast-rate, high-power battery applications. *Materials Reports: Energy* **1**, 100008 (2021).

151. Casado, N., Hernández, G., Sardon, H. & Mecerreyes, D. Current trends in redox polymers for energy and medicine. *Progress in Polymer Science* **52**, 107-135 (2016).

152. Noriega, R., Rivnay, J., Vandewal, K., Koch, F. P. V., Stingelin, N., Smith, P., Toney, M. F. & Salleo, A. A general relationship between disorder, aggregation and charge transport in conjugated polymers. *Nature Materials* **12**, 1038-1044 (2013).

153. Salleo, A., Kline, R. J., DeLongchamp, D. M. & Chabinyc, M. L. Microstructural Characterization and Charge Transport in Thin Films of Conjugated Polymers. *Advanced Materials* **22**, 3812-3838 (2010).

154. Hernández-Burgos, K., Barton, Z. J. & Rodríguez-López, J. Finding Harmony between Ions and Electrons: New Tools and Concepts for Emerging Energy Storage Materials. *Chemistry of Materials* **29**, 8918-8931 (2017).

155. Casado, N. & Mecerreyes, D. in *Redox Polymers for Energy and Nanomedicine* 1-26 (The Royal Society of Chemistry, 2021).

156. Karlsson, C., Suga, T. & Nishide, H. Quantifying TEMPO Redox Polymer Charge Transport toward the Organic Radical Battery. *ACS Applied Materials & Interfaces* **9**, 10692-10698 (2017).

157. Dalton, E. F., Surridge, N. A., Jernigan, J. C., Wilbourn, K. O., Facci, J. S. & Murray, R. W. Charge transport in electroactive polymers consisting of fixed molecular redox sites. *Chemical Physics* **141**, 143-157 (1990).

158. Burgess, M., Chénard, E., Hernández-Burgos, K., Nagarjuna, G., Assary, R. S., Hui, J., Moore, J. S. & Rodríguez-López, J. Impact of Backbone Tether Length and Structure on the Electrochemical Performance of Viologen Redox Active Polymers. *Chemistry of Materials* **28**, 7362-7374 (2016).

159. Ruff, I. & Friedrich, V. J. Transfer diffusion. I. Theoretical. *The Journal of Physical Chemistry* **75**, 3297-3302 (1971).

160. Dahms, H. Electronic conduction in aqueous solution. *The Journal of Physical Chemistry* **72**, 362-364 (1968).

161. Andrieux, C. P. & Savéant, J. M. Electron transfer through redox polymer films. *Journal of Electroanalytical Chemistry and Interfacial Electrochemistry* **111**, 377-381 (1980).

162. Laviron, E. A multilayer model for the study of space distributed redox modified electrodes: Part I. Description and discussion of the model. *Journal of Electroanalytical Chemistry and Interfacial Electrochemistry* **112**, 1-9 (1980).

163. Kim, T.-Y., Wang, Y., Raithel, A. L. & Hamann, T. W. Real-Time Observation of the Diffusion Mechanism Progression from Liquid to Solid State of Transition Metal Complexes. *ACS Energy Letters* **5**, 583-588 (2020).

164. Burgess, M., Hernández-Burgos, K., Schuh, J. K., Davila, J., Montoto, E. C., Ewoldt, R. H. & Rodríguez-López, J. Modulation of the Electrochemical Reactivity of Solubilized Redox Active Polymers via Polyelectrolyte Dynamics. *Journal of the American Chemical Society* **140**, 2093-2104 (2018).

165. Bodappa, N., Fu, Y.-C., Broekmann, P., Furrer, J., Zick, K., Vesztergom, S., Tahara, H. & Sagara, T. Electron transfer controlled by solvent and counter-anion dynamics in electrochemistry of viologen-type ionic liquid. *Electrochim. Acta* **320**, 134559 (2019).

166. Oyaizu, K., Kawamoto, T., Suga, T. & Nishide, H. Synthesis and Charge Transport Properties of Redox-Active Nitroxide Polyethers with Large Site Density. *Macromolecules* **43**, 10382-10389 (2010).

167. Bu, H.-z., English, A. M. & Mikkelsen, S. R. Charge Transport in Ferrocene-Containing Polyacrylamide-Based Redox Gels. *The Journal of Physical Chemistry B* **101**, 9593-9599 (1997).

168. Oyaizu, K., Ando, Y., Konishi, H. & Nishide, H. Nernstian Adsorbate-like Bulk Layer of Organic Radical Polymers for High-Density Charge Storage Purposes. *Journal of the American Chemical Society* **130**, 14459-14461 (2008).

169. Mohammad-Pour, G. S., Hatfield, K. O., Fairchild, D. C., Hernandez-Burgos, K., Rodríguez-López, J. & Uribe-Romo, F. J. A Solid-Solution Approach for Redox Active Metal–Organic Frameworks with Tunable Redox Conductivity. *Journal of the American Chemical Society* **141**, 19978-19982 (2019).

170. Hatakeyama-Sato, K., Nagano, T., Noguchi, S., Sugai, Y., Du, J., Nishide, H. & Oyaizu, K. Hydrophilic Organic Redox-Active Polymer Nanoparticles for Higher Energy Density Flow Batteries. *ACS Applied Polymer Materials* **1**, 188-196 (2019).

171. Place, S. D. & Kavanagh, P. Electroactivity of PIPO nitroxide radical polymer films. *Electrochim. Acta* **392**, 139044 (2021).

172. Hatakeyama-Sato, K., Wakamatsu, H., Matsumoto, S., Sadakuni, K., Matsuoka, K., Nagatsuka, T. & Oyaizu, K. TEMPO-Substituted Poly(ethylene sulfide) for Solid-State Electro-Chemical Charge Storage. *Macromol. Rapid Commun.* **42**, 2000607 (2021).

173. Liang, Z., Nguyen, T. P., Attanayake, N. H., Easley, A. D., Lutkenhaus, J. L., Wooley, K. L. & Odom, S. A. Metal-free Polypeptide Redox Flow Batteries. *Submitted*.

174. Akhoury, A., Bromberg, L. & Hatton, T. A. Interplay of Electron Hopping and Bounded Diffusion during Charge Transport in Redox Polymer Electrodes. *The Journal of Physical Chemistry B* **117**, 333-342 (2013).

175. Whiting, G. L., Snaith, H. J., Khodabakhsh, S., Andreasen, J. W., Breiby, D. W., Nielsen, M. M., Greenham, N. C., Friend, R. H. & Huck, W. T. S. Enhancement of Charge-Transport Characteristics in Polymeric Films Using Polymer Brushes. *Nano Lett.* **6**, 573-578 (2006).

176. Arikuma, Y., Nakayama, H., Morita, T. & Kimura, S. Electron Hopping over 100 Å Along an α Helix. *Angew. Chem. Int. Ed.* **49**, 1800-1804 (2010).

177. Deng, J., Zhou, C. & Song, N. Chiroptically Active Photonics Polymers: Synthesis and Chiroptically Switching Properties of Helical Polyacetylene Bearing Electrochromic Viologens in the Side Chains. *Macromolecules* **42**, 6865-6872 (2009).

178. Nagarjuna, G., Hui, J., Cheng, K. J., Lichtenstein, T., Shen, M., Moore, J. S. & Rodríguez-López, J. Impact of Redox-Active Polymer Molecular Weight on the Electrochemical Properties and Transport Across Porous Separators in

Nonaqueous Solvents. *Journal of the American Chemical Society* **136**, 16309-16316 (2014).

179. Janoschka, T., Morgenstern, S., Hiller, H., Friebe, C., Wolkersdörfer, K., Häupler, B., Hager, M. D. & Schubert, U. S. Synthesis and characterization of TEMPO- and viologen-polymers for water-based redox-flow batteries. *Polymer Chemistry* **6**, 7801-7811 (2015).

180. Oyama, N., Ohsaka, T., Yamamoto, H. & Kaneko, M. Charge-transfer reactions in pendant viologen polymers coated on graphite electrodes and at electrode/pendant viologen polymer film interfaces. *The Journal of Physical Chemistry* **90**, 3850-3856 (1986).

181. Ohsaka, T., Yamamoto, H. & Oyama, N. Thermodynamic parameters for charge-transfer reactions in pendant viologen polymers coated on graphite electrodes and at electrode/pendant viologen polymer film interfaces. *The Journal of Physical Chemistry* **91**, 3775-3779 (1987).

182. Dalton, E. F. & Murray, R. W. Viologen(2+/1+) and viologen(1+/0) electron-self-exchange reactions in a redox polymer. *The Journal of Physical Chemistry* **95**, 6383-6389 (1991).

183. Manoj Lalwani, S., Eneh, C. I. & Lutkenhaus, J. L. Emerging trends in the dynamics of polyelectrolyte complexes. *Physical Chemistry Chemical Physics* **22**, 24157-24177 (2020).

184. Tang, S., Wang, M. & Olsen, B. D. Anomalous Self-Diffusion and Sticky Rouse Dynamics in Associative Protein Hydrogels. *Journal of the American Chemical Society* **137**, 3946-3957 (2015).

185. Lewis, T. J., White, H. S. & Wrighton, M. S. Comparison of the charge-transport rate in two redox levels of polymers derived from N,N'-dibenzyl-4,4'-bipyridinium and N,N'-dialkyl-4,4'-bipyridinium. *Journal of the American Chemical Society* **106**, 6947-6952 (1984).

186. Hatozaki, O., Ohsaka, T. & Oyama, N. Charge-transport properties of polymer complex films composed of poly(alkyleneviologen) and poly(p-styrenesulfonate). *The Journal of Physical Chemistry* **96**, 10492-10497 (1992).

187. Marcus, R. A. On the Theory of Oxidation-Reduction Reactions Involving Electron Transfer. I. *The Journal of Chemical Physics* **24**, 966-978 (1956).

6. ONGOING WORK

The work presented in **Chapters 2 – 5** laid the groundwork for the future of macromolecular-based energy storage devices. Much of the focus in literature has followed the mass transport of cathodic macromolecular radicals. This information must be determined for anodic macromolecular radicals to allow for electrolyte design to optimize mass transport in both electrodes. Additionally, most work in the dissertation was focused on thin film characterization which will impact the design of solid-state batteries. However, additional experimentation on macromolecular radical-based solutions is needed to provide redox flow battery design criteria. The preliminary results have tried to address these unknowns through the ongoing work discussed below.

6.1. Water-Coupled Anion Transport in Polyviologen Network Films

One important consideration for redox-active polymers used in electroactive coatings and as polymer-based electrodes, is the volume change during reduction and oxidation. The volume change is usually coupled with the solvation shell of the counter ions diffusing in and out of the redox-active polymer film throughout the redox process. Previous studies have focused on the mass (ion and solvent) transport have focused on cathodic polymers. Specifically, polymers with pendant nitroxide radicals and quinones have been the most investigated.[24,188-191] Some work has been done on viologen-based polymers, however, many studies saw minimal mass change,[133] focused on only the first redox couple,[192,193] or investigated monolayers,[194] which are not ideal representation of mass transport in battery electrodes. To design polymer-based batteries that do not exhibit diffusion limitations, the mass transport in both the cathodic and anodic polymers should be balanced.

Here, the mass transport in polyviologen-based network thin films were studied. The monomer was synthesized through a simple one-step reaction and subsequently used for electropolymerization on conductive substrates to fabricate working electrodes. The electropolymerization and mass transport were then investigated using electrochemical quartz crystal microbalance with dissipation, which provides real time mass change with change in redox state. Additionally, the change in charge transfer resistance with viologen oxidation state was considered using electrochemical impedance spectroscopy. For both characterization techniques, two anions (chloride and sulfate) were considered to investigate the effect of differing valences (monovalent and divalent) on mass transport. Ongoing work is considering a third anion (tetrafluoroborate), which has been shown to have the smallest solvation shell and lowest thickness change for a nitroxide-based polymer.[188]

6.1.1. Methods

6.1.1.1. Materials.

Sodium chloride (NaCl), 4-pyridinecarbonitrile, acetonitrile (MeCN), sodium tetrafluoroborate ($NaBF_4$), 1,3,5-Tris(bromomethyl)benzene (TBMB), and methanol were received from Millipore Sigma. Sodium sulfate (Na_2SO_4) was received by VWR. Ultrapure water (MQ water) was collected from a Milli-Q® water purification system (18

MΩ·cm). Indium tin oxide (ITO)-coated glass (CUV5B) was purchased from Delta Technologies. Au-coated QSense quartz crystal microbalance sensors with a Ti adhesion layer (QSX 338) were purchased from Biolin Scientific and cleaned with 5:1:1 MQ H_2O:ammonium hydroxide:hydrogen peroxide at 75 °C for 5 mins before use. All chemicals were used as received.

6.1.1.2. Characterization.

^{1}H-NMR spectra were conducted on D_2O solutions using a 400 MHz Bruker NMR. UV-vis spectra were collected in 1 nm increments from 800 to 250 nm using a Hitachi U-4100 UV-Vis-NIR spectrophotometer (341-F).

6.1.1.3. Synthesis of 1,3,5-Tris(4-cyanopyridinio)mesitylene (TPM) Bromide Salt.

The TMP bromide salt was synthetized following a modified protocol from Sano *et al.* and is described briefly (**Figure 6.1 a**).[133] TBMB (2.25 g, 6.3 mmol) and 4-pyridinecarbonitrile (6.5 g, 62.4 mmol) were refluxed in acetonitrile (20 mL) for 24 h under nitrogen. The resulting, yellow-colored solid was recovered by filtration, washed with acetonitrile, and recrystallized from methanol to yield yellow needlelike crystals. This afforded 1.24 g of the final product (yield = 62 %).

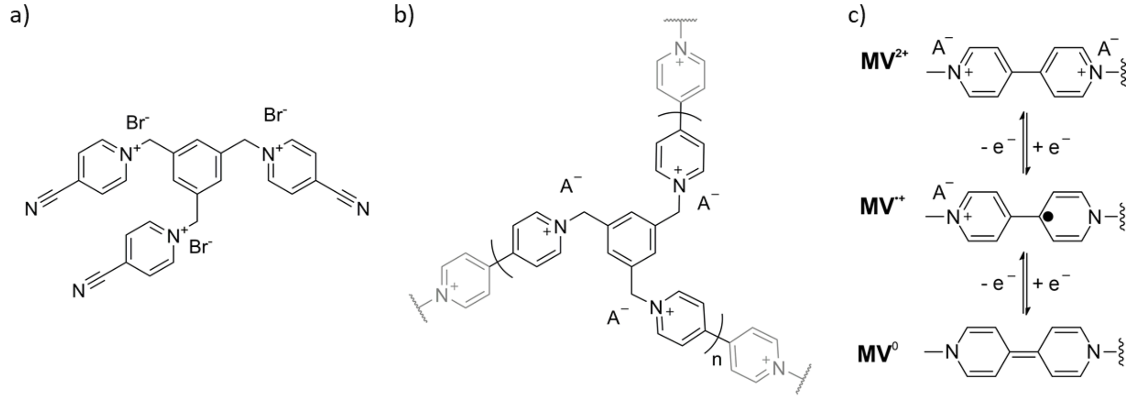

Figure 6.1. a) TMP monomer used for electropolymerization, b) the viologen crosslinked network from electropolymerization of TMP salt. c) The redox mechanism of the viologen pendant group with both charge and ion transport, where A^- is an anion.

6.1.1.4. Electrochemical Measurements.

TMP was electropolymerized from a 5 mM TMP in 0.1 M NaCl aqueous solution onto ITO glass in a three-electrode beaker cell with a platinum wire counter electrode and Ag/AgCl (sat.) reference electrode. The electropolymerization was carried out using a potentiostatic hold at -0.75 V *vs.* Ag/AgCl for 10 minutes. After deposition, the film was soaked in the testing electrolyte for 20 minutes to remove any unreacted TMP. The testing electrolytes were 0.5 NaCl, 0.5 M $NaBF_4$, and 0.25 M Na_2SO_4. After soaking, conditioning cyclic voltammetry (CV) was carried out for three cycles at 50 mV/s, followed by two cycles of CV at each of the following scan rates: 5, 10, 25, 50, 100, and 200 mV/s. Finally, a 10-minute potentiostatic hold was used to equilibrate the sample before conducting electrochemical impedance spectroscopy (EIS). 10 mV in a frequency range of 0.1 to 5×10^6 Hz (10 steps per decade). Equilibration and EIS was conducted at two potentials: (1) -0.45 V *vs.* Ag/AgCl and (2) -0.90 V *vs.* Ag/AgCl. All electrochemical data was collecting using a Gamry Interface 1000 unless otherwise noted.

6.1.1.5. Electrochemical Quartz Crystal Microbalance with Dissipation (EQCM-D).

In-situ mass changes during electrochemistry was conducted using a QSense E1 module (Biolin Scientific) to determine the mass changes during electrodeposition and CV. First, an air baseline was collected on the blank Au/Ti sensor for 2 minutes. After 2 minutes, the 5 mM TMP in 0.1 M NaCl aqueous solution was flowed (150 µL/min) into the EQCM-D cell and the flow was stopped for the electropolymerization. The electropolymerization was then carried out using a potentiostatic hold at -0.75 V *vs.* Ag/AgCl for 4 minutes. After deposition, the testing electrolyte was continuously flowed at 150 µL/min into the cell for 20 minutes to remove any unreacted TMP. The testing electrolytes were 0.5 NaCl, 0.5 M $NaBF_4$, and 0.25 M Na_2SO_4. After 20 minutes the electrolyte was held static and conditioning cyclic voltammetry (CV) was carried out for three cycles at 50 mV/s, followed by two cycles of CV at each of the following scan rates: 5, 10, 25, 50, 100, and 200 mV/s. The QCM-D data was analyzed using Dfind (Biolin Scientific), where the reference period was taken as the static solution of 5 mM TMP in 0.1 M NaCl aqueous solution before the electropolymerization began. The estimated film thickness after electropolymerization was *ca.* 120 nm.

6.1.1.6. EQCM-D Data Modeling.

The QCM-D data was modeled in Dfind using the composite Sauerbrey equation, which relates the normalized change in frequency ($\Delta f/n$) to change in mass (**Equation 6.1**). For fitting, the solution density was assumed to match that of water (1 mg/mL) and the polymer layer was taken to be 1.2 mg/mg. Overtones 3, 5, 7, and 9 were used to obtain accurate fits.

$$\Delta m = -C \frac{\Delta f}{n}$$

Equation 6.1

The mass change is then related to the charge transferred to determine the mass per charge relationship (Δm/e) and then compared to the ideal value obtained from Faraday's law.

6.1.2. Results and Discussion

6.1.2.1. TMP Synthesis and Electropolymerization.

Following a previously described protocol, 1,3,5-Tris(4-cyanopyridinio)mesitylene (TPM) bromide salt was synthesized through the coupling of 4-pyridinecarbonitrile and 1,3,5-Tris(bromomethyl)benzene.[133,195] The successfully synthesis of TMP was confirmed using ^{1}H-NMR spectroscopy (**Figure 6.2 a**). The resulting TMP bromide salt was a trifunctional monomer that could undergo cathodic electropolymerization to produce a fully crosslinked polyviologen film (**Figure 6.1 b**). **Figure 6.2 c** shows the current response during the potentiostatic electropolymerization at -0.75 V *vs.* Ag/AgCl.

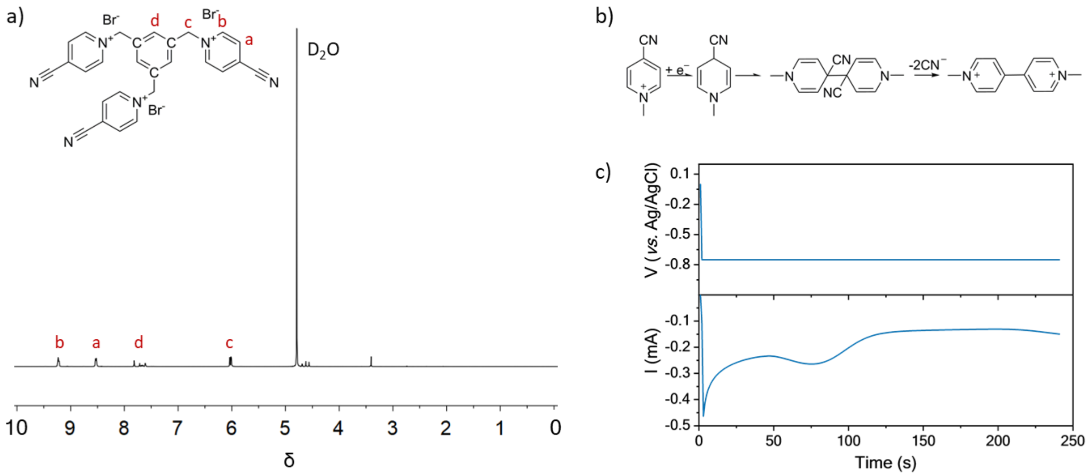

Figure 6.2. a) ^{1}H-NMR spectra of TMP bromide salt. b) The electropolymerization mechanism proposed by Saika *et al*.[195] c) The output current during the potentiostatic electropolymerization onto the Au/Ti EQCM-D sensor. The supporting electrolyte was 5 mM TMP in aqueous 0.1 M NaCl. Au/Ti crystal was the working electrode with a Ag/AgCl reference electrode and platinum plate counter electrode.

After confirmation of successful synthesis, the electrochemical properties of the resulting polyviologen films were considered in different electrolytes. The electrolytes considered were sodium chloride (NaCl) and sodium sulfate ($NaSO_4$), which were selected to vary the anion. **Figure 6.3** shows cyclic voltammograms of the polyviologen films in the two electrolytes. At 100 mV/s, the polyviologen films exhibited half wave potentials ($E_{1/2}$) of -0.8 V and -0.1 V *vs.* Ag/AgCl in the chloride and sulfate-based electrolytes. Additionally, all redox couples exhibited peak separation (ΔE_p) of 100 mV indicating the redox couples are quasi-reversible.

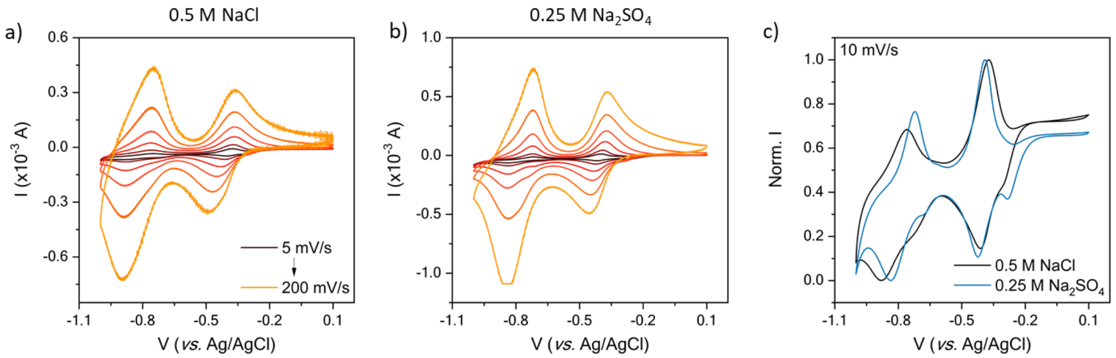

Figure 6.3. Cyclic voltammograms at varying scan rates for PTMP thin films in a) 0.5 M NaCl and b) 0.25 M Na_2SO_4 aqueous solutions as the supporting electrolyte. c) Shows the normalized cyclic voltammograms at 10 mV/s for all three electrolytes. PTMP electropolymerized on the Au/Ti EQCM-D crystal was the working electrode with a Ag/AgCl reference electrode and platinum plate counter electrode. The legend in a) applies to b).

At low scan rates, the polyviologen film in the Na_2SO_4 electrolyte exhibited peak splitting in reduction, whereas the film did not in the NaCl electrolyte (**Figure 6c**). The observed peak splitting in Na_2SO_4 could be attributed to the influx of sodium ions when viologen exists as radical cations (1+ state), since the anion is divalent sodium is needed for charge balance. However peak splitting is not large, which suggests that the sulfate ion might act as a counter ion for two radical cation viologen groups. It is also of interest that peak splitting does not occur in oxidation with either supporting electrolyte, suggesting the mass transport mechanism differ in reduction and oxidation. Further details from real time mass change may clarify the ion compensation mechanism and differences in reduction and oxidation.

6.1.2.2. EQCM-D Characterization of PTMP Thin Films.

Given the differences in cyclic voltammogram shape for polyviologen in the two electrolytes, it is of interest to study the real time mass-coupled electron transfer to provide greater insight. Using the cyclic voltammetry data for 25 mV/s, the charge transferred during oxidation and reduction is determined by integration (**Figure 6.4**). The polyviologen film exhibited a higher oxidation peak current in Na_2SO_4, compared to that in NaCl, corresponding to more charge transferred (**Figure 6.4 a-b**). However, both exhibited similar profiles exhibiting charge plateaus away from the redox peaks.

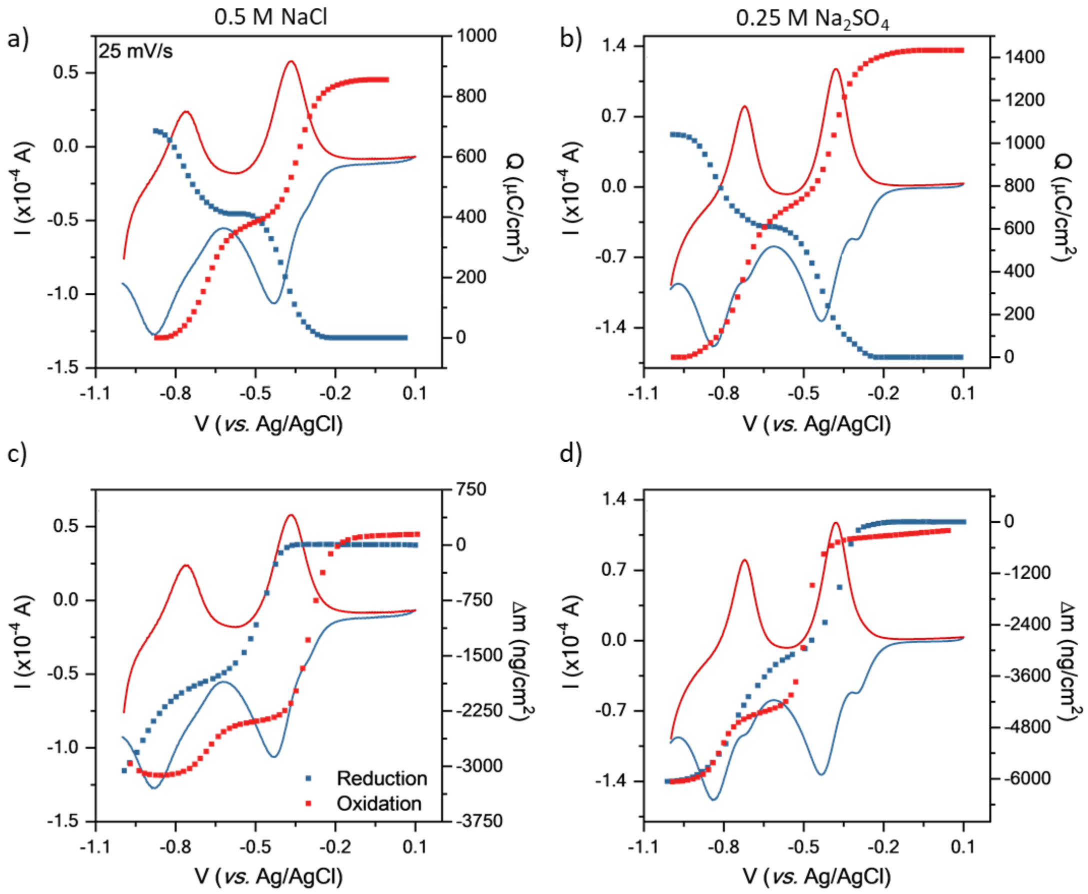

Figure 6.4. Cyclic voltammograms at 25 mV/s with overlaid charge profiles (a-b) and mass profiles (c-d). The supporting electrolyte was a) and c) 0.5 M NaCl or b) and d) 0.25 M Na_2SO_4. PTMP electropolymerized on the Au/Ti EQCM-D crystal was the working electrode with a Ag/AgCl reference electrode and platinum plate counter electrode. The legend in d) applies to all panels.

Additionally, using the EQCM-D data the mass change during CV was calculated from the Sauerbrey equation. During reduction, both films exhibited a mass decrease, associated with ion and/or solvent expulsion from the film. In oxidation the opposite behavior was observed; the mass increased associated with ion and/or solvent uptake. However, to gain insight into the detailed mass transport process, the mass change with change in charge should be considered. For example, in an ideal system for every electron transferred in reduction is coupled with the expulsion of an anion from the film, since it is no longer needed for charge balance. For both electrolytes, the slope between mass change (Δm) and charge (e) was negative for the entire reduction period (**Figure 6.5 a-b**). This was indicative of mass loss throughout the process. In contrast, during oxidation the slop was positive, which was indicative of mass gain (**Figure 6.5 c-d**).

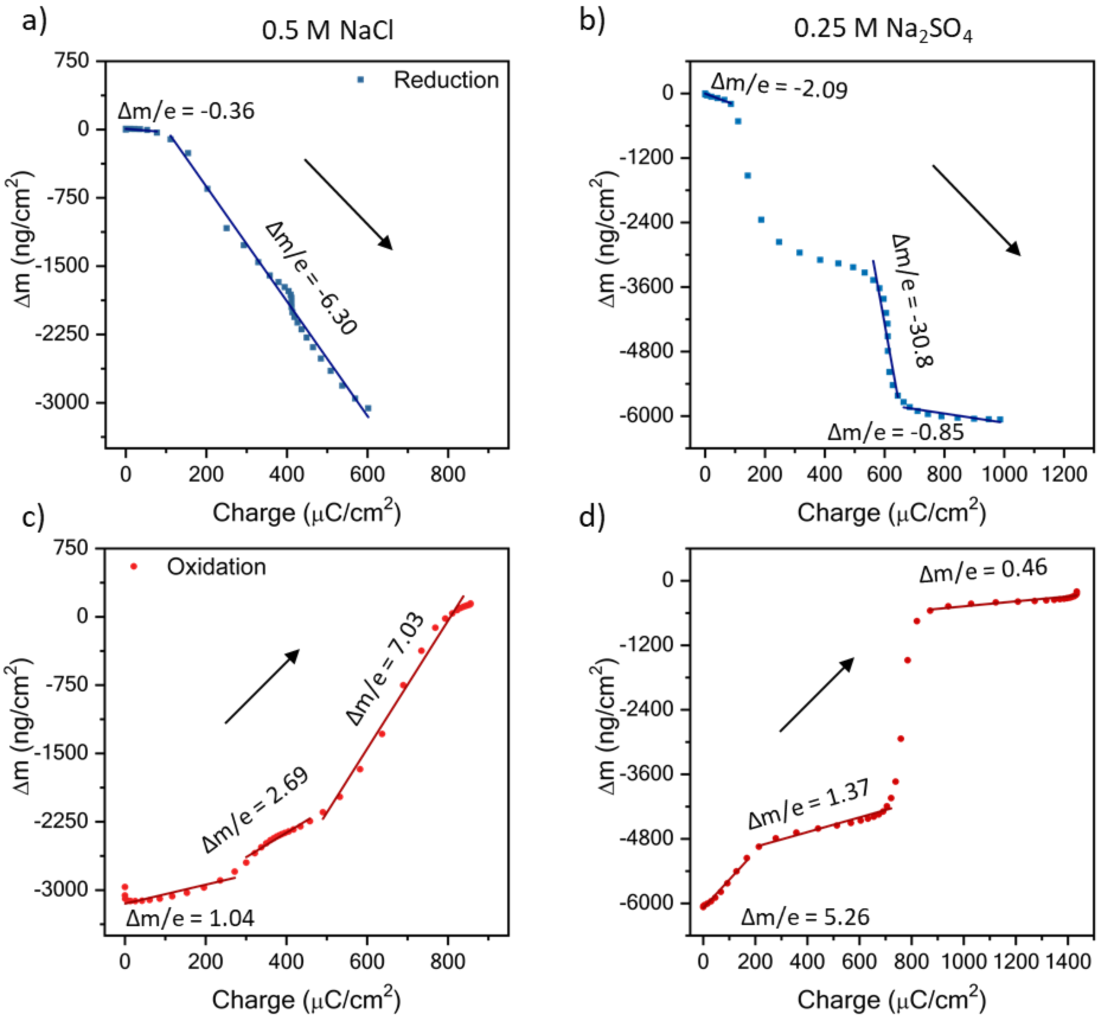

Figure 6.5. Mass change *vs.* charge transferred plots during cyclic voltammetry at 25 mV/s with a) 0.5 M NaCl and b) 0.25 M Na_2SO_4 supporting electrolyte. The mass change and charge transferred as a function of potential in **Figure 6.4**. PTMP electropolymerized on the Au/Ti EQCM-D crystal was the working electrode with a Ag/AgCl reference electrode and platinum plate counter electrode. The legend in d) applies to all panels.

Using Faraday's law, the theoretical mass per charge ratio (in mg/C) was determined to be 0.39 for chloride and 1.00 for sulfate. If the experimentally determined slope from **Figure 6.5** is larger than the theoretical value, there are additional transporting species such as sodium cation or water. The theoretical slope for sodium is 0.24 and 0.19 for water. The experimental slopes are sign dependent, where a negative sign is mass loss/expulsion, and a positive slope is mass gain/uptake.

For the viologen film in reduction, there were two major slope regimes observed in the NaCl electrolyte (**Figure 6.5 a**). The initial regime had a magnitude of 0.36, which is similar to the theoretical value the chloride ion, suggesting it is the only species being expelled. After the initial regime, the slope drastically increases to 6.30, suggesting a large amount of water (approximately 32 water molecules per chloride ion) was also expelled. In oxidation (**Figure 6.5 c**), there were three major regimes observed, each with an increasing magnitude. This suggests an increasing number of water molecules transports in each regime, specifically 4 water molecules, then 12 water molecules, and finally 36 water molecules. Due to the dicationic nature of the viologen and the large amount of water transport, a divalent anion may provide an appealing alternative.

The mass transport within the viologen film in the sodium sulfate electrolyte is more complex, due to the divalent nature of the sulfate anion. In reduction, there are two possible routes of ion transport (**Figure 6.6**). In route one (**Figure 6.6 a**), upon reduction from MV^{2+} to $MV^{\bullet+}$ a sulfate ($SO4^{-2}$) anion is expelled, and one sulfate ion is used to balance the charge of two $MV^{\bullet+}$ groups. Next, the reduction from $MV^{\bullet+}$ to MV^{0} results in the expulsion of another $SO4^{-2}$. In contrast, in route two upon reduction from MV^{2+} to $MV^{\bullet+}$ sodium (Na+) cation uptake occurs to balance the charge. Followed by expulsion of both $SO4^{-2}$ and Na^{+} during reduction from $MV^{\bullet+}$ to MV^{0}.

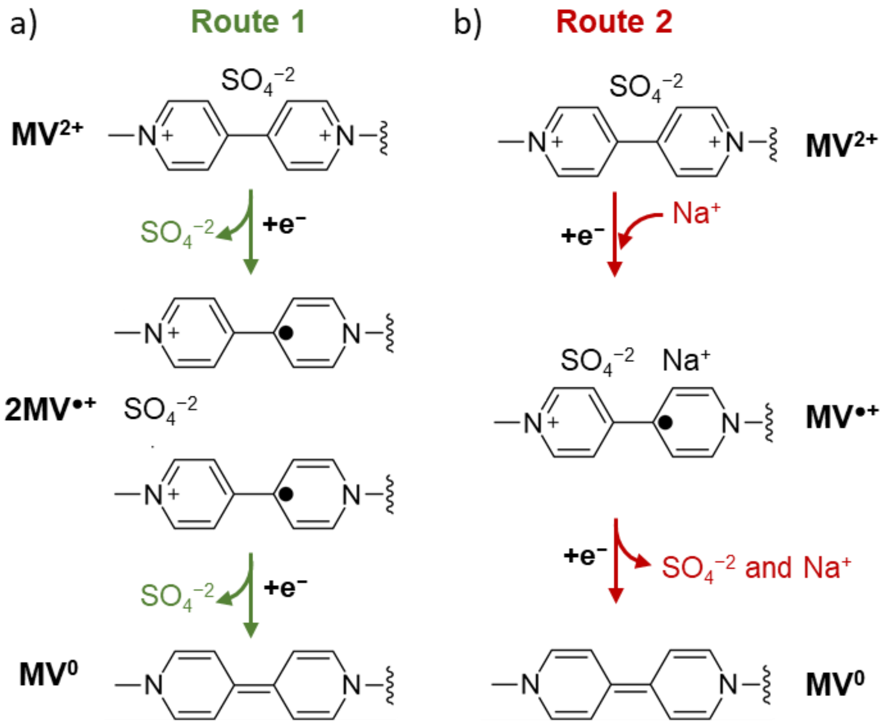

Figure 6.6. Possible ion transport for sodium sulfate in the polyviologen film. a) In route 1, upon reduction from MV^{2+} to $MV^{\bullet+}$ a sulfate (SO_4^{-2}) anion is expelled, and one sulfate ion is used to balance the charge of two $MV^{\bullet+}$ groups. The final step in route 1 during the reduction from $MV^{\bullet+}$ to MV^0 results in the expulsion of another SO_4^{-2}. b) In route 2, upon reduction from MV^{2+} to $MV^{\bullet+}$ sodium (Na^+) cation uptake occurs to balance the charge. The final step in route 1 during reduction from $MV^{\bullet+}$ to MV^0 results in the expulsion of both SO_4^{-2} and Na^+.

Although two routes are possible, the mass *vs*. charge data from reduction in the Na_2SO_4 electrolytes suggests that route one was more probable (**Figure 6.5 b**). During reduction, the slope throughout was negative suggesting that there was only mass loss. The consistent negative slope follows more with route one, where mass uptake (or a positive slope) would be expected if route two was observed. There was an initial regime followed by two regimes for each redox peak. The initial regime and beginning regime for each redox peak had a magnitude of 2.09 and 30.8, respectively. This suggests that a large amount of water (6 and 160 water molecules, respectively). The second regime's for each redox peak drastically decreases to 0.85, which is similar to the theoretical value of the sulfate ion, suggesting it is the only species being expelled. In oxidation (**Figure 6.5 d**), an initial regime was observed, followed by one for each redox peak (with a slight transition region between). The initial regime had a slope of 5.26 corresponding to the uptake of a sulfate anion and 23 water molecules. The regimes for each redox couple had smaller slopes with decreasing values, 1.37 and 0.46, respectively. These slopes correspond with the uptake of two water molecules per sulfate followed by the expulsion of three water molecules per sulfate in the regimes for the $MV^{2+}/MV^{\bullet+}$ and $MV^{\bullet+}/MV^{0}$, respectively. This suggests that most of the water uptake occurs in the initial regime and short transition regime between redox couples with some water expulsion in the final regime.

When comparing the two electrolytes, it was observed that for the NaCl electrolyte there was more water uptake during oxidation than the water expulsion observed in reduction. In contrast, for the Na_2SO_4 electrolyte similar water movement occurred in both oxidation and reduction, however, some water expulsion was observed in oxidation. For battery applications, reduced water movement is preferred to prevent large thickness changes that could impact the electrode resistance.

6.1.2.3. Electrochemical Impedance Spectroscopy Characterization.

As discussed, there was a large amount of water movement occurring in both electrolytes. One concern when there are large amounts of water uptake is that the charge transfer resistance (R_{CT}) could increase due to an increased thickness. To determine R_{CT} for the viologen films in each electrolyte, electrochemical impedance spectroscopy (EIS) was utilized, and the resulting data was modeled using the equivalent circuit presented in **Figure 6.7 a**. The EIS curves for the NaCl electrolyte exhibited clear semi-circle behavior typical of redox-active polymers (**Figure 6.7 b**). However, the Na_2SO_4 electrolyte did not exhibit a clear semi-circle, which could be associated with large resistance or diffusion limitations affecting the semi-circle behavior (**Figure 6.7 c**).

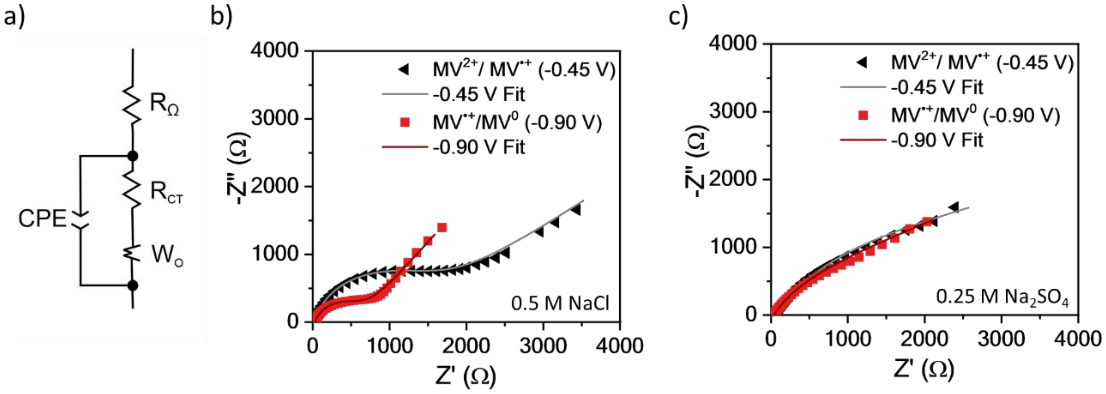

Figure 6.7. a) The equivalent circuit used to model the EIS data. Nyquist plots for polyviologen films in b) 0.5 M NaCl and c) 0.25 M Na_2SO_4 with their fit lines. EIS was conducted at -0.45 V and -0.90 V *vs.* Ag/AgCl (sat.) with an amplitude of 10 mV in a frequency range of 5 × 106 Hz to 0.1 Hz (10 steps per decade).

From the equivalent circuit parameters (**Table 6.1**), the viologen film exhibits a larger R_{CT} for the $MV^{2+}/MV^{+\bullet}$ redox couple compared to the $MV^{+\bullet}/MV^0$ for both electrolytes. However, the polyviologen exhibited significantly smaller R_{CT} in NaCl compared to Na_2SO_4.

Table 6.1. EIS equivalent circuit fit parameters at -0.45 V *vs.* Ag/AgCl ($MV^{2+}/ MV^{\bullet+}$ redox couple) and at -0.90 V *vs.* Ag/AgCl (the $MV^{\bullet+}/MV^0$ redox couple).

	$MV^{2+}/ MV^{\bullet+}$ (-0.45 V *vs.* Ag/AgCl)		**$MV^{\bullet+}/MV^0$ (-0.90 V *vs.* Ag/AgCl)**	
EIS Fit Parameter	**0.5 M NaCl**	**0.25 M Na_2SO_4**	**0.5 M NaCl**	**0.25 M Na_2SO_4**
R_Ω (Ω)	35 ± 0.2	40 ± 0.1	34 ± 0.2	40 ± 0.2
R_{CT} (Ω)	1331 ± 81	3515 ± 348	648 ± 27	1165 ± 335
W_O	0.21 ± 0.01	0.22 ± 0.04	0.29 ± 0.01	0.33 ± 0.04
CPE (μF)	59 ± 1	713 ± 9	76 ± 2	518 ± 19

6.2. Mark-Houwink Sakarada Constants for PTMA in Selected Solvents

Using solution-state viscosity measurements the Mark-Houwink-Sakurada (MHS) equation constants (a and K) were determined for PTMA in a variety of solvents.[196] To determine the MHS equation constants, viscosity measurements were conducted for PTMA with four different degrees of polymerization: 15, 44, 122, and 277. Here present the preliminary data for PTMA dissolved in 2-butoxyethyl acetate (BCA) at 2 mg/mL, which was selected due to our previous solubility parameter work (**Figure 6.8 d**).[23] The viscosity results showed a moderately linear relationship between the log (intrinsic viscosity) and log (polymer molar mass) (**Figure 6.8 a-c**). Here, the steady state viscosity was considered for each polymer solution, however, it is suggested by some that zero-shear viscosity be utilized.[197] Additionally, Tam *et al.* stress the importance of utilizing an appropriate shear rate regime to determine the zero shear viscosity for charged polymers.[198] Future analysis of the collected data will identify appropriate shear rate regimes to determine the zero-shear viscosity.

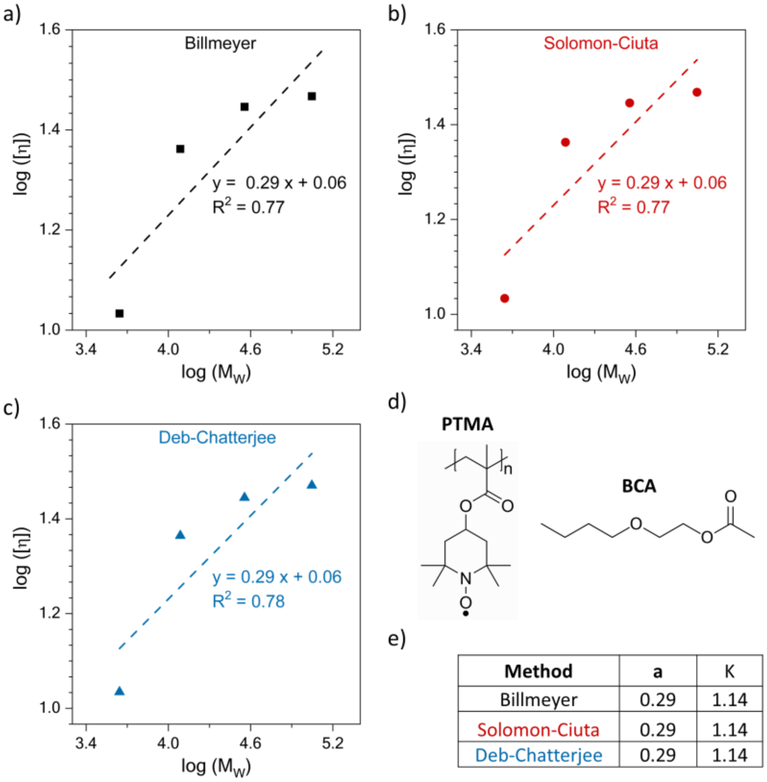

Method	a	K
Billmeyer	0.29	1.14
Solomon-Ciuta	0.29	1.14
Deb-Chatterjee	0.29	1.14

Figure 6.8. log (intrinsic viscosity) vs. log (molar mass) data determined using the a) Billmeyer, b) Solomon-Ciuta. and c)Deb-Chatterjee methods. d) The chemical structures of PTMA and 2-butoxyethyl acetate (BCA), which were used to produce solutions at 2 mg/mL for analysis. e) The determined Mark-Houwink-Sakurada equation constants, a and K, for the three methods.

In general, this linear relationship indicates that the solution viscosity increases with increasing molar mass, at a constant solution concentration. Moreover, the viscosity results for these solutions indicate that at the selected concentration the Billmeyer,[199] Solomon-Ciuta,[200] and Deb-Chatterjee[201] methods were more descriptive than the Huggins[202] or Kramer[203] methods. Additionally, all three methods provided the same slope and intercept, which are related to a and K, respectively (**Figure 6.8 e**). The determined a value indicates that small aggregates of PTMA may be formed at 2 mg/mL in BCA, since it is less than the value typically associated with a good solvent (a ≈ 0.8). Additional analysis with a variety of concentrations is required to fully evaluate the solvent quality. In addition to BCA, battery related solvents, such as *N*-methyl-2-pyrrolidone (NMP) and ethylene carbonate/dimethyl carbonate (EC/DMC, 1/1, v/v), are also being analyzed. Future investigations will focus on using the PTMA MHS equation constants to determine the optimal molar mass and solvent for non-aqueous flow battery applications.

6.3. Small Angle Neutron Scattering of Nitroxide-based Macromolecular Radicals

To study the solution conformation and dynamics of PTMA dilute solutions, small-angle neutron scattering (SANS) with deuterated solvents was performed in collaboration with Prof. Mark Dadmun of University of Tennessee Knoxville. A variety of PTMA samples with varying molar masses were studied in deuterated NMP. NMP was selected because it is the prominent solvent for electrode casting in literature. Our solution state SANS results, show that PTMA is soluble in NMP and exhibits increased scattering intensity with increased molar mass.[204] From the raw scattering data, the Guinier model was used to determine the radius of gyration (R_g) for varying molar-masses of PTMA in deuterated NMP. **Figure 6.9** shows the R_g as a function of scattering intensity, I(0), for the PTMA samples (data points are labeled with the number of repeat units). I(0) was used to minimize any form of effects on the accuracy of the analysis. The plot shows that the dependence of $Rg \propto I(0)^{0.63}$. For an ideal gaussian chain, this dependence is expected to be in the range of 0.5-0.6.[6] However, a dependence of 0.63 indicates that PTMA oxidized with H_2O_2 is slightly rigid along the backbone of the polymer chain. Solution state SANS data provides insight of PTMAs solution state conformation; however, the thin film pendant group packing is also of interest.

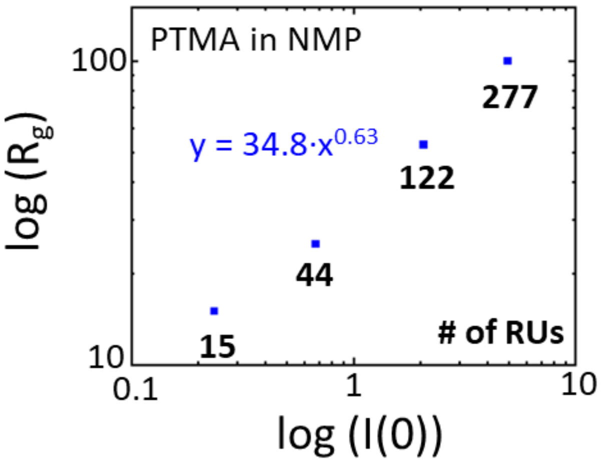

Figure 6.9. log R_g vs log I(0) for PTMA of different molecular weights and similar oxidation levels (~98%). The data point labels correspond to the number of repeat units.

6.4. References

23. Easley, A. D., Vukin, L. M., Flouda, P., Howard, D. L., Pena, J. L. & Lutkenhaus, J. L. Nitroxide Radical Polymer–Solvent Interactions and Solubility Parameter Determination. *Macromolecules* **53**, 7997-8008 (2020).

24. Wang, S., Li, F., Easley, A. D. & Lutkenhaus, J. L. Real-time insight into the doping mechanism of redox-active organic radical polymers. *Nature Materials* **18**, 69-75 (2019).

133. Sano, N., Tomita, W., Hara, S., Min, C.-M., Lee, J.-S., Oyaizu, K. & Nishide, H. Polyviologen Hydrogel with High-Rate Capability for Anodes toward an Aqueous Electrolyte-Type and Organic-Based Rechargeable Device. *ACS Applied Materials & Interfaces* **5**, 1355-1361 (2013).

188. Ma, T., Easley, A. D., Wang, S., Flouda, P. & Lutkenhaus, J. L. Mixed electron-ion-water transfer in macromolecular radicals for metal-free aqueous batteries. *Cell Reports Physical Science* **2**, 100414 (2021).

189. Karlsson, C., Huang, H., Strømme, M., Gogoll, A. & Sjödin, M. Impact of linker in polypyrrole/quinone conducting redox polymers. *RSC Advances* **5**, 11309-11316 (2015).

190. Sterby, M., Emanuelsson, R., Huang, X., Gogoll, A., Strømme, M. & Sjödin, M. Characterization of PEDOT-Quinone Conducting Redox Polymers for Water Based Secondary Batteries. *Electrochim. Acta* **235**, 356-364 (2017).

191. Wang, H., Emanuelsson, R., Liu, H., Edström, K., Mamedov, F., Strømme, M. & Sjödin, M. Redox-State-Dependent Interplay between Pendant Group and Conducting Polymer Backbone in Quinone-Based Conducting Redox Polymers for Lithium Ion Batteries. *ACS Applied Energy Materials* **2**, 7162-7170 (2019).

192. Lee, D.-Y., Kafi, A. K. M., Park, S.-H., Qian, D.-J. & Kwon, Y.-S. Influence of Anions on Electrochemical Redox Reactions and Electrical Properties using a Viologen Derivative. *Japanese Journal of Applied Physics* **45**, 3772-3775 (2006).

193. Corrêa, C. M., Córdoba de Torresi, S. I., Benedetti, T. M. & Torresi, R. M. Viologen-functionalized poly(ionic liquids): Spectroelectrochemical and QCM-D studies. *J. Electroanal. Chem.* **819**, 365-373 (2018).

194. De Long, H. C. & Buttry, D. A. Environmental effects on redox potentials of viologen groups embedded in electroactive self-assembled monolayers. *Langmuir* **8**, 2491-2496 (1992).

195. Saika, T., Iyoda, T. & Shimidzu, T. Electropolymerization of Bis(4-cyano-1-pyridinio) Derivatives for the Preparation of Polyviologen Films on Electrodes. *Bull. Chem. Soc. Jpn.* **66**, 2054-2060 (1993).

196. Easley, A. D., Weems, A. C. & Lutkenhauss, J. L. Mark-Houwink-Sakurada Constants for PTMA in selected solvents. (In preparation.).

197. Takahashi, Y., Sakakura, D., Wakutsu, M., Yamaguchi, M. & Noda, I. Effects of Molecular Weight Distribution on Zero-Shear Viscosity of Linear Polymers in Dilute and Semidilute Regions. *Polym. J.* **24**, 987-990 (1992).

198. Tam, K. C., Tiu, C. & Fang, T. N. Comments on the accuracy of zero shear intrinsic viscosity of high molecular weight polyacrylamide. *Polym. Int.* **24**, 15-22 (1991).

199. Billmeyer Jr, F. W. Methods for estimating intrinsic viscosity. *Journal of Polymer Science* **4**, 83-86 (1949).

200. Solomon, O. F. & Ciută, I. Z. Détermination de la viscosité intrinsèque de solutions de polymères par une simple détermination de la viscosité. *J. Appl. Polym. Sci.* **6**, 683-686 (1962).

201. Deb, P. C. & Chatterjee, S. R. On polynomial expansion of log relative viscosity. *Die Makromolekulare Chemie* **125**, 283-285 (1969).

202. Huggins, M. L. The Viscosity of Dilute Solutions of Long-Chain Molecules. IV. Dependence on Concentration. *Journal of the American Chemical Society* **64**, 2716-2718 (1942).

203. Kraemer, E. O. Molecular Weights of Celluloses and Cellulose Derivates. *Industrial & Engineering Chemistry* **30**, 1200-1203 (1938).

204. Haque, A., Easley, A., Lutkenhaus, J. & Dadmun, M. Investigating the Effect of Radical Content on the Conformation of Organic Radical Polymer in Solution State via Small-Angle Neutron Scattering. (In preparation).

7. CONCLUSIONS AND FUTURE WORK

In the projects described in **Chapters 2 – 6**, many advances were made in the fundamental design and understanding of macromolecular radicals and their integration into thin films and electrodes. Specifically, the interactions between composite electrode components were quantified and resulted improved performance of PTMA-based cathodes. Additionally, the assembly of nanoarchitectonics composed of charged nitroxide-based polymers was demonstrated for thin electroactive coatings, with control over their mass transport mechanism. Degradable macromolecular radicals were synthesized by collaborators and utilized in fully polymeric batteries and their structure-electron transport relationship was considered. Finally, the mass transport control from ion valency was considered. Taken together, this work has laid the groundwork for the future of macromolecular-based energy storage devices. Although these results are the first step electrode design and in the development of degradable fully polymeric batteries additional areas of focus should be considered to improve battery performance. Some future areas of interest are described below with short discussions on the influence on battery performance.

7.1. Development of electropolymerizable hydrogels with degradable functionalities.

Most dramatically, a redesign of the degradable repeat unit and synthetic route presents the greatest potential for performance improvement. One way to accomplish this is to combine the degradable functionalities presented in **Chapter 4** into the electropolymerizable monomer studied in **Chapter 6.1.** The electropolymerizable monomer is targeted because of the promising results from Sano *et* al, where the authors reported high rate capabilities (C-rates up to 1200 C) and were able to achieve capacities of 150 mAh/g at 1 C.[133] However, it is desired to modify the previously reported electropolymerizable monomer to include on-demand degradable functionalities. One possible route to produce the degradable monomer would through a two-step synthetic route proposed below (**Figure 7.1 a**).

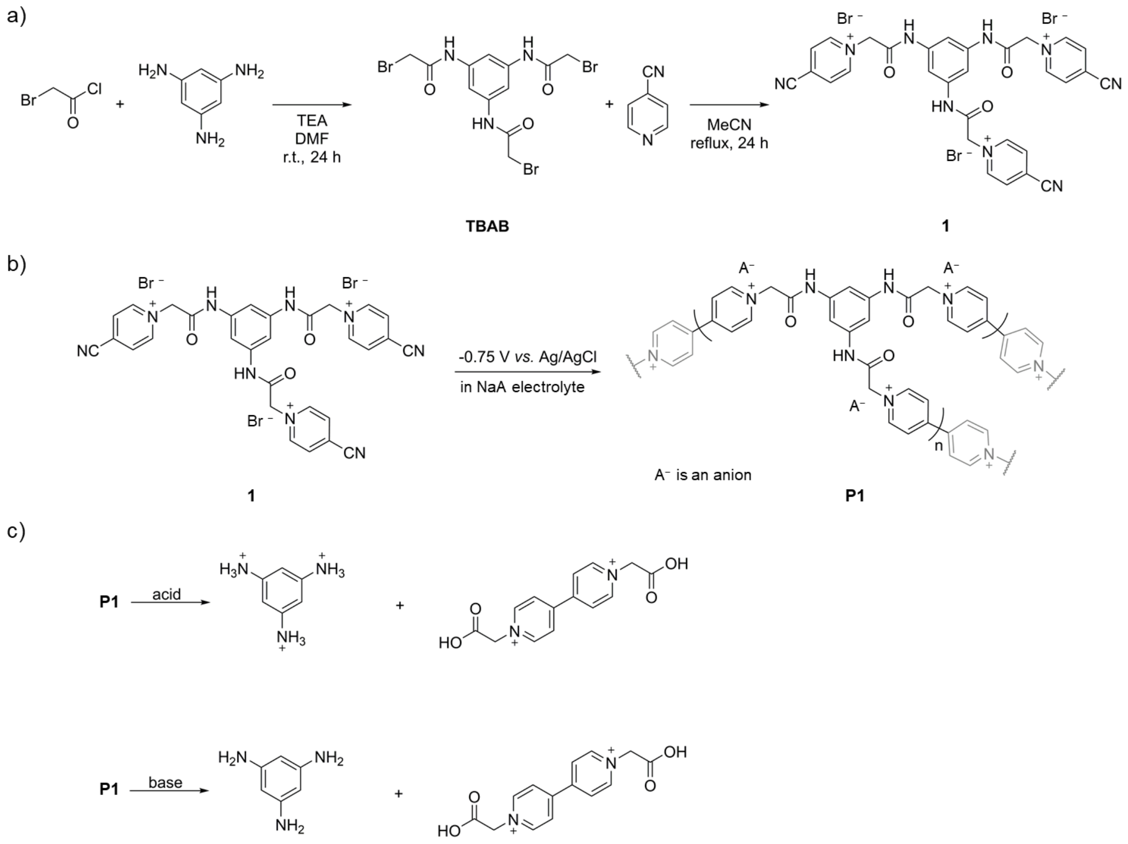

Figure 7.1. a) The proposed two-step synthetic route resulting in the production of a degradable and electropolymerizable viologen monomer (**1**). b) The proposed electropolymerization process and obtained network viologen polymer (**P1**) of the salt produced in panel a). c) The proposed degradation products from both acidic and basic degradation of **P1**.

In the first step, N,N′,N″-(Benzene-1,3,5-triyl)tris(2-bromoacetamide) (TBAB) can be synthesized with decent yield (*ca.* 82%) following a procedure from Chen *et al.*[205] In the second step, the procedure used in **Chapter 6.1** (from Sano *et al.*[133]) could be modified couple 4-pyridinecarbonitrile with TBAB to produce the hypothesized monomer **1**. The resulting salt can then be utilized for electropolymerization to produce a electroactive thin film P1 that can be utilized as a battery anode. The theoretical capacity of **P1** would be approximately 137 mAh/g and should exhibit redox peaks below 0 V *vs.* Ag/AgCl. After operation acid or base could be used to catalyze amide hydrolysis[206] of **P1** to degrade the above material to likely form a viologen-based carboxylic acid and an aromatic triamine.

The proposed system solves two main problems previously observed for degradable polymers in batteries: 1) the repeat unit molar mass is reduced compared to the polypeptides, which leads to an increased theoretical capacity and 2) the network nature of **P1** prevents the dissolution of the active material thus this should help prevent the capacity fade of the full battery and lead to an improved performance for long term cycling.

The major challenge remaining for the proposed system will be identifying a method to produce thick electrodes (> 6 µm) with a carbon additive, which is critical for high performance battery electrodes. Additionally, a similar method should be considered to produce a network polymer for the cathode. For example, the synthetic protocol presented by Ji *et al.* could also be modified to include degradable functionalities in the monomer.[207]

7.2. Replace the electrolyte with an ionic solid electrolyte.

Another alternative to improve the performance of polymer based batteries, is through the selection and design of the electrolyte. For example, the steep capacity fade of the batteries presented in **Chapters 2** and **4** were attributed to the dissolution of the active material into the liquid electrolytes. The liquid electrolyte and separator could be replaced with an ion conducting solid electrolyte. A solid electrolyte would help to prevent capacity fade, thus improving the long-term capacity of the full battery. However, it should be noted that solid electrolytes typically exhibit lower conductivities than their liquid counter parts and could limit the charge-discharge rates due to increase diffusion limitations.

7.3. References

133. Sano, N., Tomita, W., Hara, S., Min, C.-M., Lee, J.-S., Oyaizu, K. & Nishide, H. Polyviologen Hydrogel with High-Rate Capability for Anodes toward an Aqueous Electrolyte-Type and Organic-Based Rechargeable Device. *ACS Applied Materials & Interfaces* **5**, 1355-1361 (2013).

205. Chen, S., Morales-Sanfrutos, J., Angelini, A., Cutting, B. & Heinis, C. Structurally Diverse Cyclisation Linkers Impose Different Backbone Conformations in Bicyclic Peptides. *ChemBioChem* **13**, 1032-1038 (2012).

206. O'Connor, C. Acidic and basic amide hydrolysis. *Quarterly Reviews, Chemical Society* **24**, 553-564 (1970).

207. Ji, L., Dai, Y., Yan, S., Lv, X., Su, C., Xu, L., Lv, Y., Ouyang, M., Chen, Z. & Zhang, C. A fast electrochromic polymer based on TEMPO substituted polytriphenylamine. *Scientific Reports* **6**, 30068 (2016).

APPENDIX A

SUPPLEMENTAL INFORMATION

The supplementary information is presented by chapter.

Chapter 2: Nitroxide Radical Polymer–Solvent Interactions and Solubility Parameter Determination

Reprinted with permission from ref. [23] Copyright 2020 American Chemical Society.

Table S2.1. PTMA-based electrodes, electrolyte utilized, and cycling stability of the cell from literature. See ref. [12] for a complete review with additional examples.

Electrode System	Electrolyte (v/v)	Capacity Fade/Dissolution	Reference
10 % PTMA with graphite and binding powder	1 M $LiPF_6$ in EC/DEC (3/7)	Initial: 77 $mA{\cdot}h{\cdot}g^{-1}$ “No significant fade after 500 cycles”	28
PTMA:acetylene black:PVDF = 77:15:8 wt%	1 M $LiPF_6$ in EC/DMC (1/1)	Initial: 78.4 $mA{\cdot}h{\cdot}g^{-1}$ 98% of the initial capacity was obtained after 100 cycles	74
PTMA:graphite:PVDF = 10:80:10 wt%	0.1 M $TBABF_4$ in DCM or ACN	Initial: 77 $mA{\cdot}h{\cdot}g^{-1}$ “no significant deterioration in the capacity was observed up to 1000 cycles”	10
PTMA:VGCF:CMC:PTFE = 50:45:4:1 wt%	1 M $LiPF_6$ in EC/DEC (3/7)	Initial: 147 $mA{\cdot}h{\cdot}g^{-1}$ 82% of the initial capacity remained after 100 cycles	32
PTMA:VGCF:PVDF = 30:60:10 wt%	1 M $LiPF_6$ in EC/DEC (3/7)	Initial: 100[a] $mA{\cdot}h{\cdot}g^{-1}$ 89% of the initial capacity remained after 1000 cycles	33
PTMA:VGCF:CMC:PTFE = 50:45:4:1 wt%	1 M $LiPF_6$ in EC/DEC (3/7)	Initial: 110 $mA{\cdot}h{\cdot}g^{-1}$ 87% of the initial capacity was obtained after 25 cycles	29

Table S2.1. Continued

Electrode System	**Electrolyte (v/v)**	**Capacity Fade/Dissolution**	**Reference**
PTMA:Super P:PVDF = 40:50:10 wt%	P(VdF-HFP) membrane swollen with 1 M $LiPF_6$ in EC/DMC (1/1)	Initial: 111 mA·h·g^{-1} 91% of the initial capacity was obtained after 100 cycles	75
PTMA:Super P:PVDF = 40:50:10 wt%	1 M $LiPF_6$ in EC/DMC (1/1)	Initial: 111 mA·h·g^{-1} ~90% of the initial capacity was obtained after 100 cycles	31
PTMA:graphite:Carbon black:PVDF	1 M $LiPF_6$ in EC/DMC (1/1)	Initial: 76.7 mA·h·g^{-1} "a rapid fading of the capacity is observed" to 26%[a] of initial capacity after 25 cycles	35
PTMA:Super P:PVDF = 60:30:10 wt%	1 M $LiPF_6$ in EC/DMC (1/1)	Initial: 80 mA·h·g^{-1} ~87% of the initial capacity was obtained after 200 cycles	18
PTMA:Super P:PVDF = 40:50:10 wt%	1 M $LiPF_6$ in EC/DMC (1/1)	Initial: 110 mA·h·g^{-1} 96% of the initial capacity was obtained after 400 cycles	11
PTMA:Super P = 25:75 wt%	1 M $LiClO_4$ in EC/DEC (1/1)	Initial: 100[a] mA·h·g^{-1} 82% of the initial capacity was obtained after 300 cycles (PTMA brushes were also fabricated to prevent dissolution)	208
PTMA:carbon black:graphene:PVDF = 10:20:60:10 %	1 M $LiPF_6$ in EC/DEC/DMC (1/1/1)	Initial: 120[b] mA·h·g^{-1} 63% of the initial capacity was obtained after 100 cycles	77
PTMA composite:Super P:PVDF = 80:10:10 wt%	1 M $LiPF_6$ in EC/DMC (1/1)	Initial: 110 mA·h·g^{-1} 90% of the initial capacity was obtained after 50 cycles	76

Table S2.1. Continued

Electrode System	**Electrolyte (v/v)**	**Capacity Fade/Dissolution**	**Reference**
PTMA brushes on ITO glass	1 M LiTFSI in EC/DEC (1/1)	Initial: 94 mA·h·g^{-1} 97% of the initial capacity was obtained after 100 cycles (brushes to prevent dissolution)	95
PTMA:Super P:PVDF = 25:65:10 wt%	1 M $LiPF_6$ in DMC	Initial: 30 to 67 mA·h·g^{-1} 0.017% to 0.11% capacity loss per cycle	25
PTMA	0.5 M $LiCF_3SO_3$ in PC	14 wt% mass loss over 200 s during cyclic voltammetry	24
PTMA copolymer:VGCF:PVDF = 30:60:10 wt%	1 M $LiPF_6$ in EC/DMC (1/1)	Initial: 75^a mA·h·g^{-1} 86% to 94% of the initial capacity was retained after 50 cycles (crosslinked PTMA was also demonstrated to prevent dissolution)	209

Table S2.1. Continued

Electrode System	**Electrolyte (v/v)**	**Capacity Fade/Dissolution**	**Reference**
PTMA: Super P:PVDF = 10:80:10 wt%	1 M $LiPF_6$ in EC/DMC (1/1)	Initial: ~77.4 mA·h·g^{-1} "the capacity of PTMA-oxidation dropped dramatically within the first 30 cycles to ~62 mA·h·g^{-1}"	[210]
PTMA: Super P:PVDF = 30:60:10 wt%	**1 M $LiPF_6$ in EC/DMC (1/1)**	**Initial: 28.5 mA·h·g^{-1}** **92% of the initial capacity was retained after 35 cycles**	**This Work**
PTMA: Super P:PMMA = 30:60:10 wt%	**1 M $LiPF_6$ in EC/DMC (1/1)**	**Initial: 54.9 mA·h·g^{-1}** **89% of the initial capacity was retained after 35 cycles**	**This Work**

EC: ethylene carbonate
DEC: diethyl carbonate
VGCF: vapor-grown carbon fiber
PVDF: poly(vinylidene difluoride)
CMC: carboxymethyl cellulose
PTFE: poly(tetrafluoroethylene)
TBA: tetrabutylammonium
DCM: dichloromethane
ACN: acetonitrile
PC: propylene carbonate
DMC: dimethyl carbonate
[a]Estimated from plot
[b]Accessed the three redox states of PTMA with a two-electron process

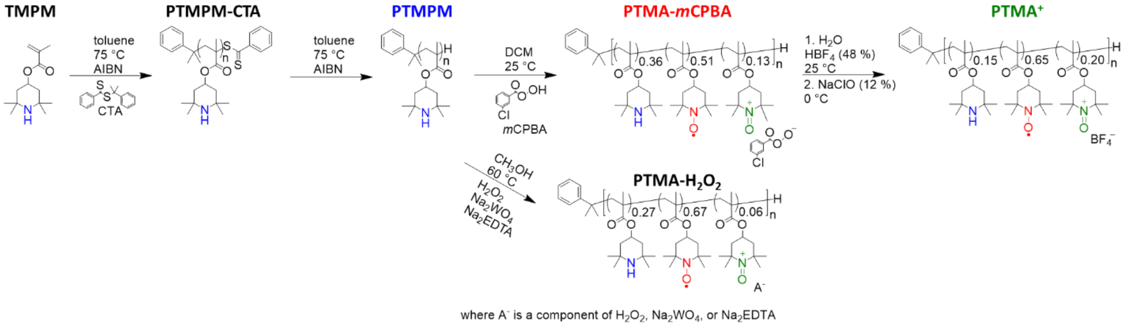

Figure S2.1. Synthetic route for PTMPM, PTMA-mCPBA, PTMA-H_2O_2, and PTMA$^+$.

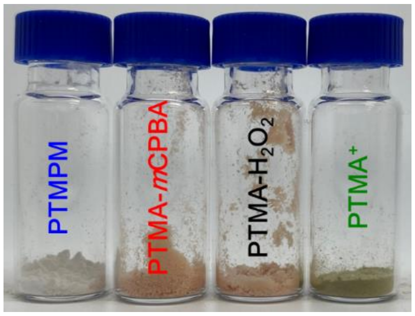

Figure S2.2. PTMPM, PTMA-mCPBA, PTMA-H_2O_2, and PTMA$^+$ powders collected after the final vacuum filtration step.

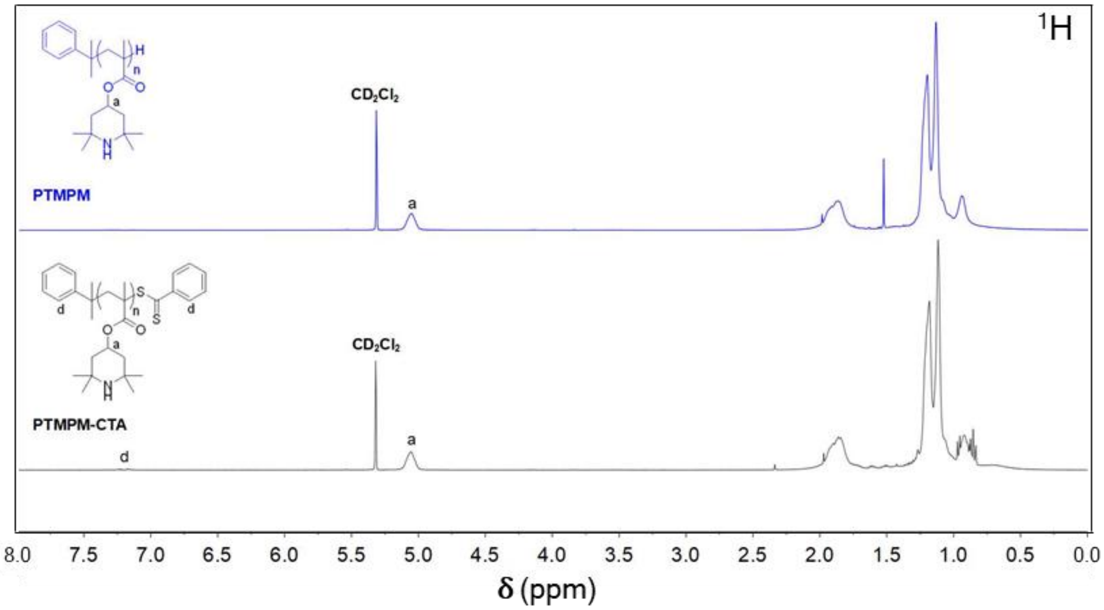

Figure S2.3. The ^{1}H-NMR of PTMPM-CTA and PTMPM, showing a loss in the signal between 7.0 and 7.5 ppm to confirm the successful removal of the CTA end group.

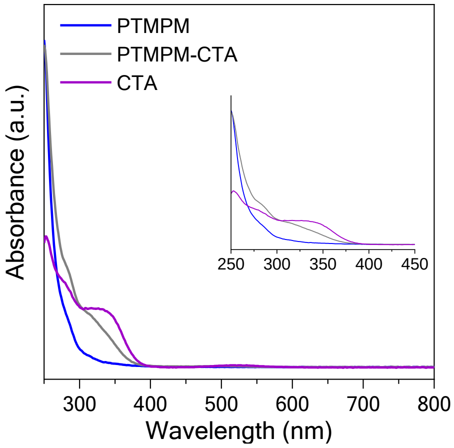

Figure S2.4. UV-Vis spectra of PTMPM-RAFT and PTMPM, confirming the successful removal of the CTA end group due to the loss of the shoulder between 300 and 400 nm.

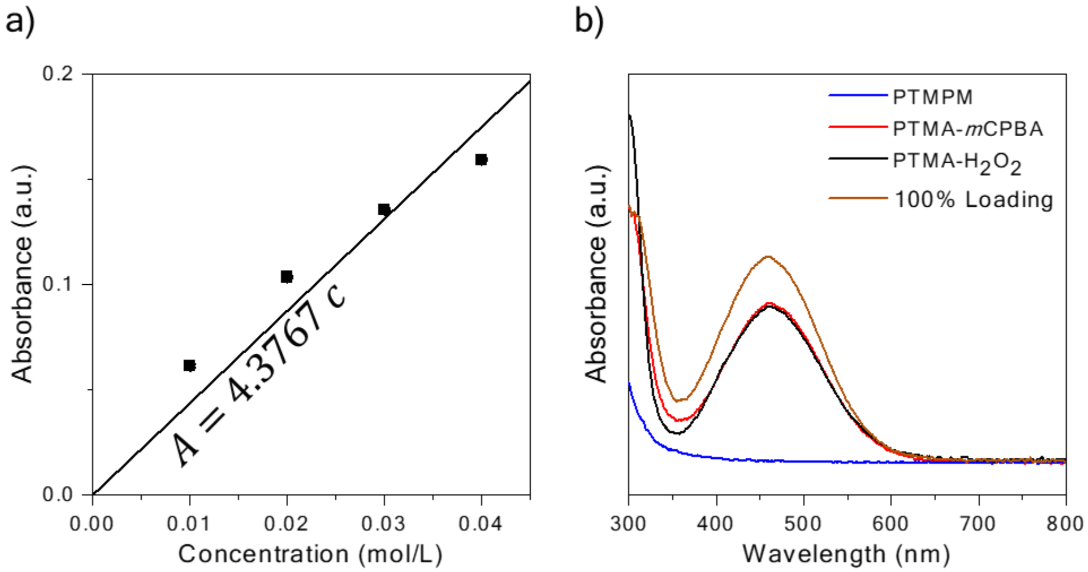

Figure S2.5. a) The calibration curve for the standard, 4-hydroxy-TEMPO, in chloroform used to determine the radical content of PTMA, and b) the UV-Vis spectra for the standard (or 100% radical loading) and utilized polymers.

Table S2.2. Radical loading percentage determined using UV-Vis spectroscopy, EPR spectroscopy, and XPS.

Method of Measurement	**PTMPM**	**PTMA-*m*CPBA**	**PTMA-H_2O_2**	**PTMA$^+$**
UV-Vis	0	68	67	NA
EPR	0	67	73	13
XPS	0	51	67	65
Avg. Radical Loading	0	62 ± 10	69 ± 3	39 ± 37

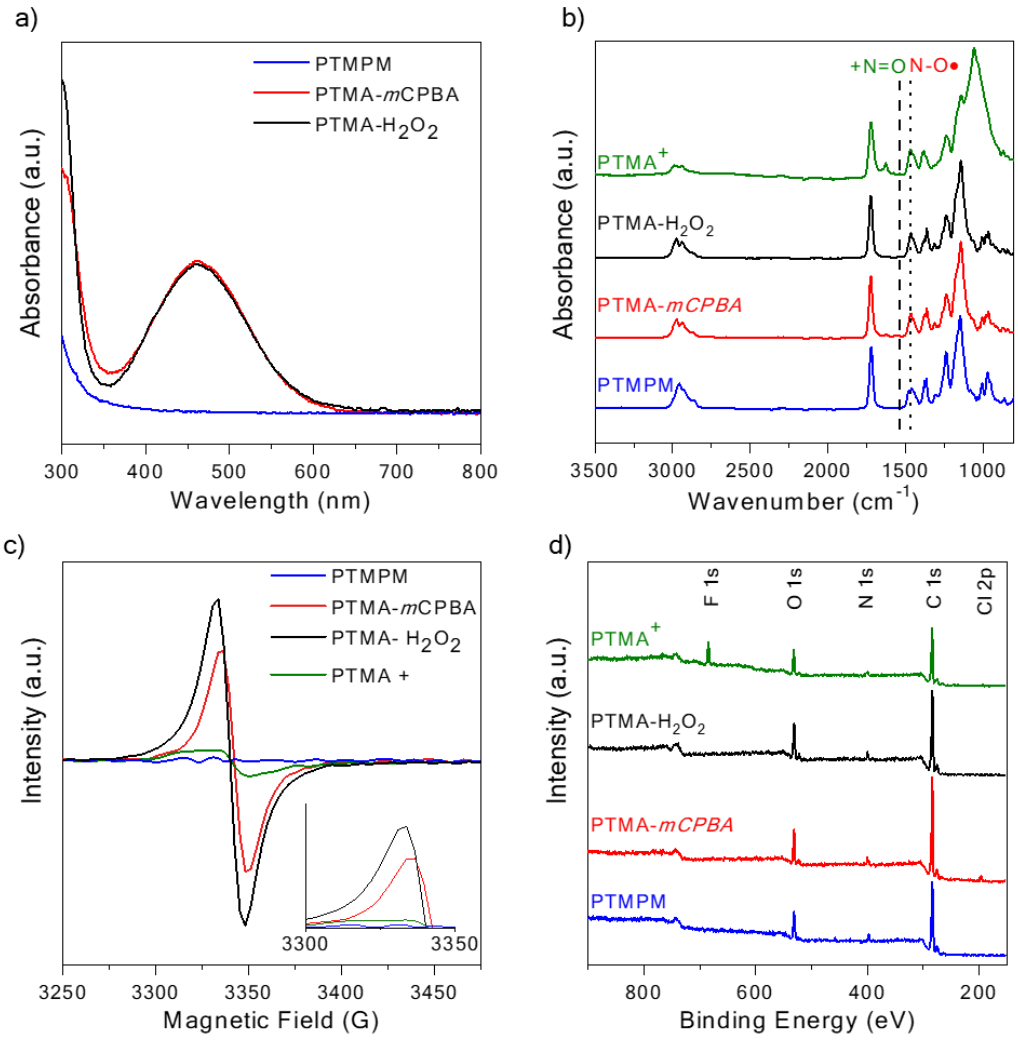

Figure S2.6. a) UV-Vis spectra, b) FTIR spectra, c) EPR spectra, and d) XPS survey scans for PTMPM, PTMA-*m*CPBA, PTMA-H_2O_2, and PTMA$^+$. PTMA$^+$ UV-Vis spectra are not shown because PTMA$^+$ was not soluble in chloroform at the studied concentration. FTIR and XPS spectra were collected for powder samples (except for XPS on PTMA-*m*CPBA, which was conducted on a thin film on ITO glass).

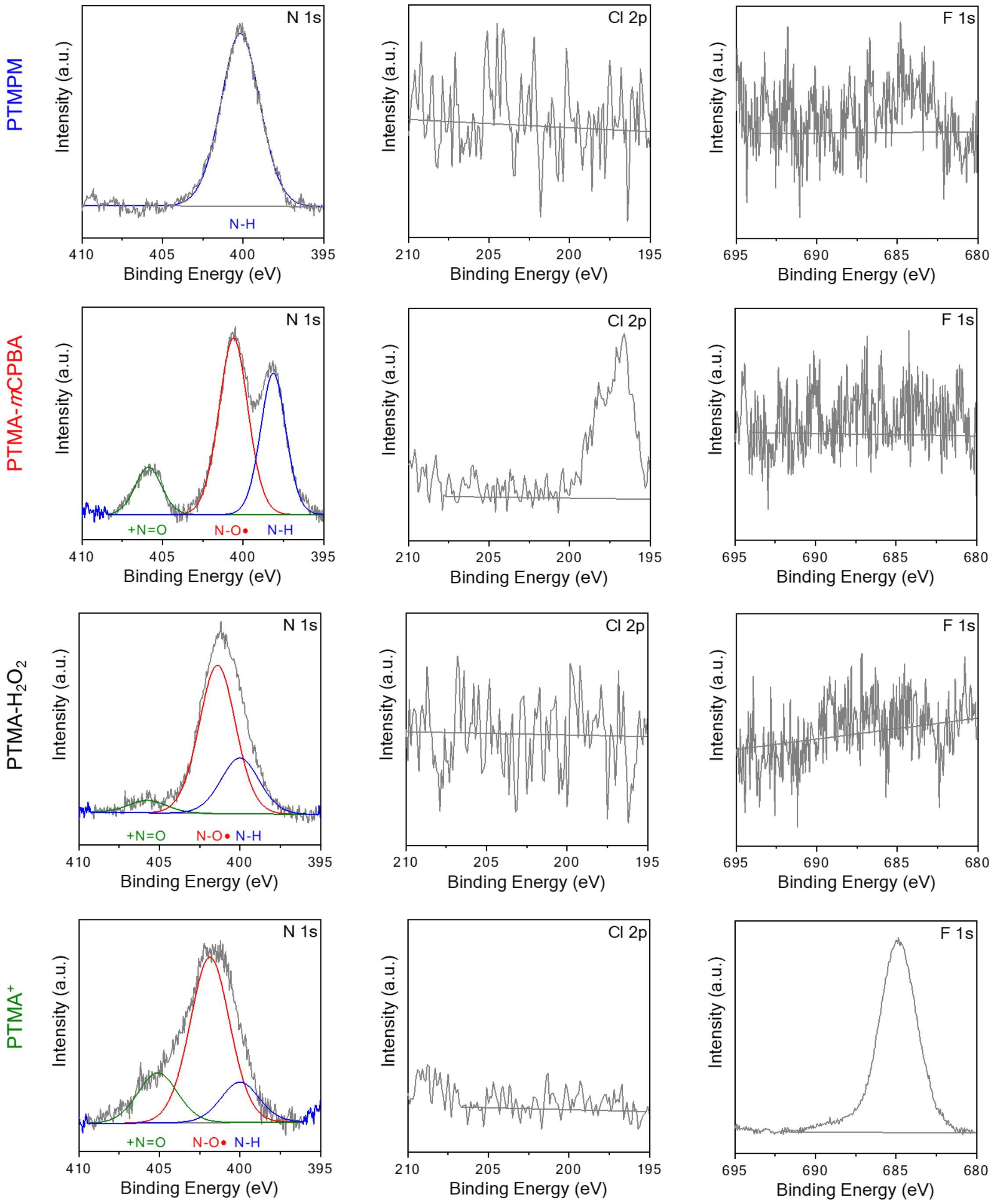

Figure S2.7. High resolution N 1s, Cl 2p, and F 1s XPS for PTMPM, PTMA-*m*CPBA, PTMA-H_2O_2, and PTMA$^+$. All data was collected from powder samples, except for PTMA-*m*CPBA, which was a thin film on ITO glass.

Table S2.3. Summary of XPS results from deconvolution of the N 1s peak to determine the functional group distribution of the polymers studied.

	PTMPM	**PTMA-*m*CPBA**	**PTMA-H_2O_2**	**PTMA$^+$**
C (at %)	84	83	83	76
O (at %)	15	11	13	13
N (at %)	4	4	4	4
N-H (~399.8 eV)	100 %	36 %	27 %	15 %
N-O• (~401.3 eV)	0 %	51 %	67 %	65 %
+N=O (~405.6 eV)	0 %	13 %	6 %	20 %
Cl (at %)	0	2	0	0
F (at %)	0	0	0	7

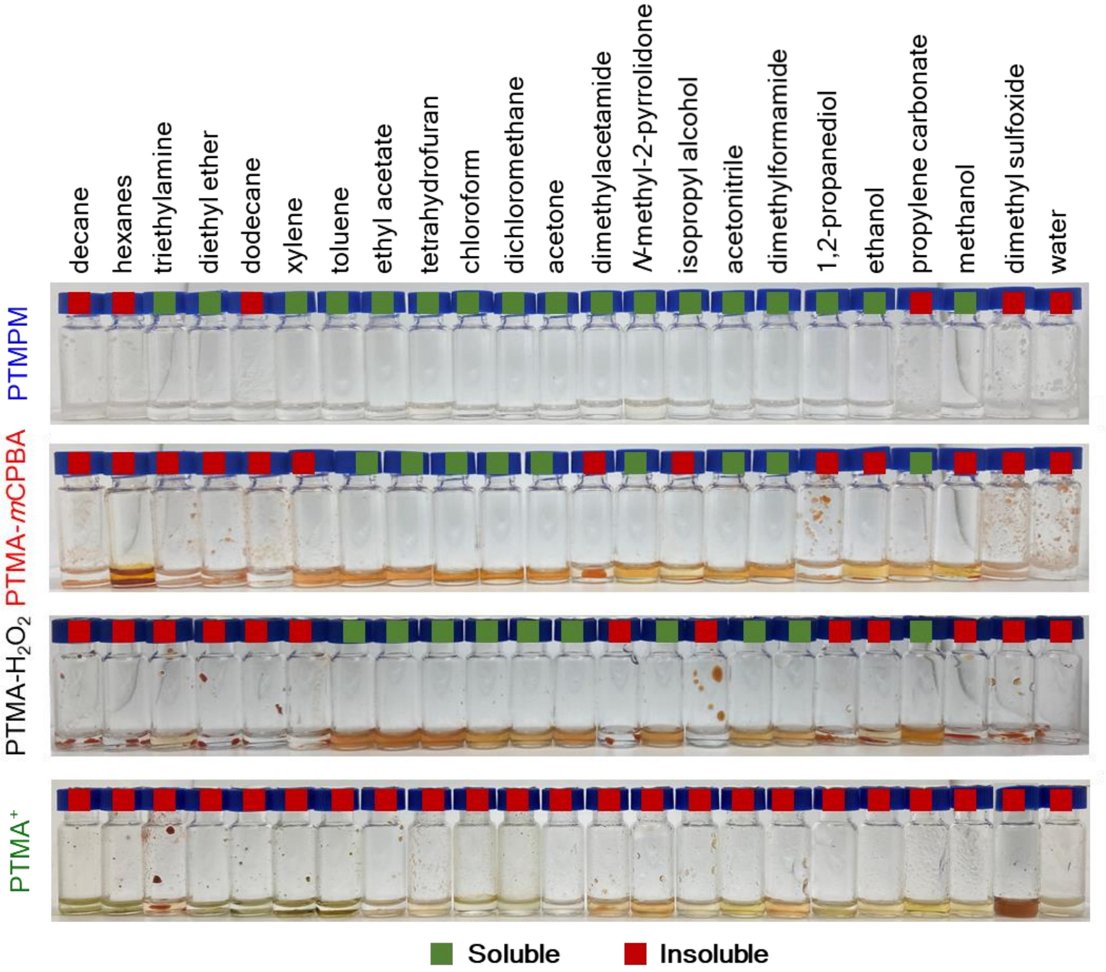

Figure S2.8. The solubility spectrum for PTMPM, PTMA-*m*CPBA, PTMA-H_2O_2, and PTMA$^+$. Green indicates the solvents which dissolve the polymer and red indicates those which do not. The Hildebrand solubility parameters vary from 13.5 (decane) to 47.9 (water) MPa$^{1/2}$.

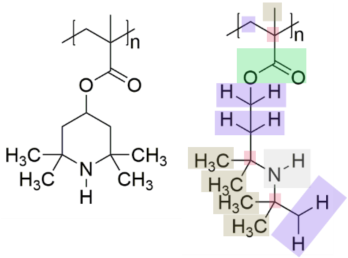

Group	# in structure	Hoy		Fedors		Hansen			
		U (kJ/mol)	V (cm^3/mol)	F ($J^{1/2} cm^{3/2} mol^{-1}$)	V (cm^3/mol)	F_d ($J^{1/2}cm^{3/2}mol^{-1}$)	F_p ($J^{1/2}cm^{3/2}mol^{-1}$)	U_h (J/mol)	V (cm^3/mol)
—C—	3	65.5	3.562	1.47	-19.2	-70	0	0	-19.2
H_2C	4	269.0	15.553	4.94	16.1	270	0	0	16.6
—CH_3	5	303.4	21.548	4.71	33.5	419	0	0	31.7
—CO_2	1	668.1	23.728	18.00	18.0	667	511	7000	8.2
H N	1	368.2	11.017	8.40	4.5	160	211	3100	4.5
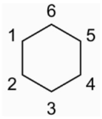	1	-48.0	0	1.05	16.0	190	0	0	13.5
Total	16	3777.8	215.383	75.17	212.8	3169	1766	12000	183.8

Figure S2.9. The Hoy, Fedors, and Hansen group contribution calculation for homopolymer PTMPM.

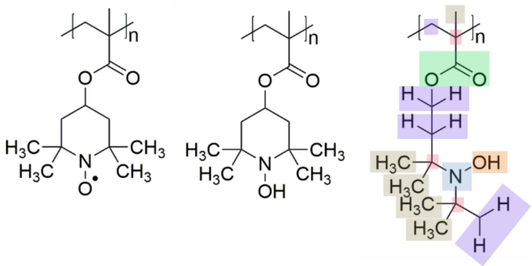

		Hoy		Fedors		Hansen			
Group	# in structure	U (kJ/mol)	V (cm^3/mol)	F ($J^{1/2}$ $cm^{3/2}$ mol^{-1})	V (cm^3/mol)	F_d ($J^{1/2}cm^{3/2}mol^{-1}$)	F_p ($J^{1/2}cm^{3/2}mol^{-1}$)	U_h (J/mol)	V (cm^3/mol)
$-\overset{\vert}{\underset{\vert}{C}}-$	3	65.5	3.562	1.47	-19.2	-70	0	0	-19.2
$\overset{H_2}{C}$	4	269.0	15.553	4.94	16.1	270	0	0	16.6
$-CH_3$	5	303.4	21.548	4.71	33.5	419	0	0	31.7
$-CO_2$	1	668.1	23.728	18.00	18.0	667	511	7000	8.2
$\overset{\vert}{N}$	1	125.0	12.569	4.20	-9.0	31	149	5000	-9.00
$-OH$	1	798.6	12.457	29.80	10.0	211	499	20000	10.5
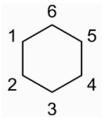	1	-48.0	0	1.05	16.0	190	0	0	13.5
Total	16	4333.2	229.392	100.77	209.3	4064	730	32000	190.5

Figure S2.10. The Hoy, Fedors, and Hansen group contribution calculation for homopolymer PTMA.

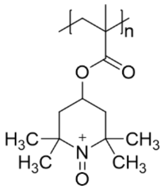

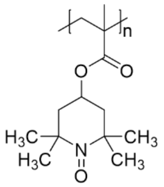

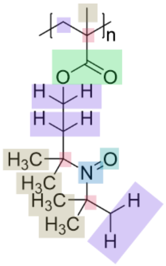

		Hoy		Fedors		Hansen			
Group	# in structure	U (kJ/mol)	V (cm^3/mol)	F ($J^{1/2}$ $cm^{3/2}$ mol^{-1})	V (cm^3/mol)	F_d ($J^{1/2}cm^{3/2}mol^{-1}$)	F_p ($J^{1/2}cm^{3/2}mol^{-1}$)	U_h (J/mol)	V (cm^3/mol)
$-\overset{\vert}{\underset{\vert}{C}}-$	3	65.5	3.562	1.47	-19.2	-70	0	0	-19.2
$\overset{H_2}{C}$	4	269.0	15.553	4.94	16.1	270	0	0	16.6
$-CH_3$	5	303.4	21.548	4.71	33.5	419	0	0	31.7
$-CO_2$	1	668.1	23.728	18.00	18.0	667	511	7000	8.2
$-N=$	1	125.0	12.569	4.20	-9.0	164	1323	5000	4.0
$-O-$	1	235.2	6.462	3.35	3.8	100	401	300	3.8
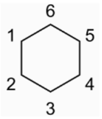	1	-48.0	0	1.05	16.0	190	0	0	13.5
Total	16	3769.8	223.397	74.32	203.1	4086	1473.856	15000	196.8

Figure S2.11. The Hoy, Fedors, and Hansen group contribution calculation for homopolymer PTMA$^+$.

Table S2.4. Group contribution of the studied polymers with adjustment for the different fractions of comonomers in the tri-copolymers (PTMA-*m*CPBA, PTMA-H_2O_2, and PTMA$^+$).

			Hoy		**Fedors**		**Hansen**			
	Group	**Fraction**	**F ($J^{1/2}$ $cm^{3/2}$ mol^{-1})**	**V (cm^3/mol)**	**U (kJ/mol)**	**V (cm^3/mol)**	**F_d ($J^{1/2}$ $cm^{3/2}$ mol^{-1})**	**F_p ($J^{1/2}$ $cm^{3/2}$ mol^{-1})**	**U_h (J mol^{-1})**	**V (cm^3/mol)**
PTMPM	N-H	1.00	3777.8	215.4	75.2	212.8	3982	552.8	10100	193.5
	N-O•	0	0	0	0	0	0	0	0	0
	+N=O	0	0	0	0	0	0	0	0	0
	Sum		3777.8	215.4	75.2	212.8	3982	552.8	10100	193.5
PTMA-*m*CPBA	N-H	0.36	1360.0	77.6	27.1	76.6	1433.5	199.0	3636	69.7
	N-O•	0.51	2209.9	117.0	51.4	106.7	2072.6	372.1	16320	97.1
	+N=O	0.13	490.1	29.0	9.7	26.4	531.2	191.6	1950	25.6
	Sum		4060.0	223.7	88.1	209.8	4037.3	762.7	21906	192.4
PTMA-H_2O_2	N-H	0.27	1020.0	58.2	20.3	57.5	1075.1	149.3	2727	52.2
	N-O•	0.67	2903.2	153.7	67.5	140.2	2722.9	488.8	21440	127.6
	+N=O	0.06	226.2	13.4	4.5	12.2	245.2	88.4	900	11.8

Table S2.4. Continued.

			Hoy		Fedors		Hansen			
	Group	**Fraction**	**F ($J^{1/2}$ $cm^{3/2}$ mol^{-1})**	**V (cm^3/mol)**	**U (kJ/mol)**	**V (cm^3/mol)**	**F_d ($J^{1/2}$ $cm^{3/2}$ mol^{-1})**	**F_p ($J^{1/2}$ $cm^{3/2}$ mol^{-1})**	**U_h (J mol^{-1})**	**V (cm^3/mol)**
PTMA-H_2O_2	Sum		4149.4	225.2	92.3	209.9	4043.2	726.5	25067	191.7
$PTMA^+$	N-H	0.15	566.7	32.3	11.3	31.9	597.3	82.9	1515	29.0
	N-O•	0.65	2816.6	149.1	65.5	136.0	2641.6	474.2	20800	123.8
	+N=O	0.2	754.0	44.7	14.9	40.6	817.2	294.8	3000	39.4
	Sum		4137.2	226.1	91.6	208.6	4056.1	851.9	25315	192.2

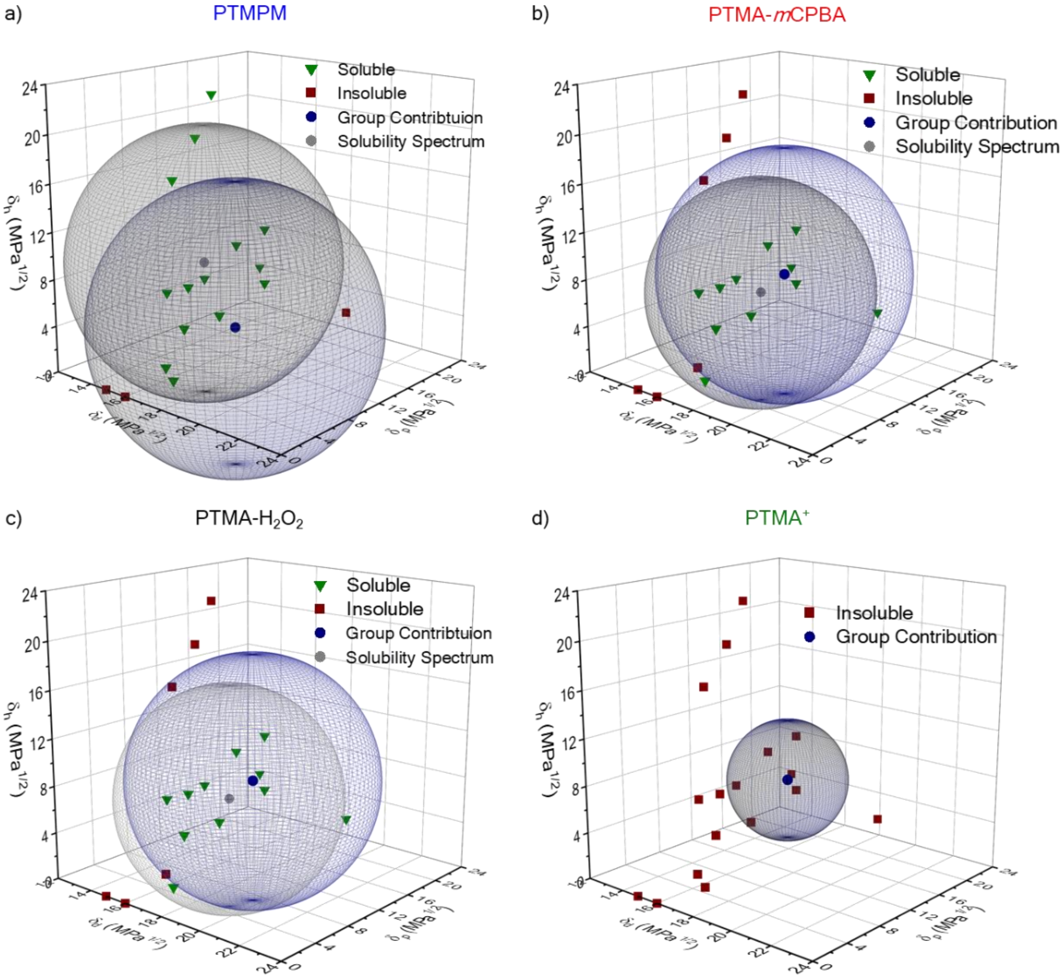

Figure S2.12. The Hansen solubility spheres for PTMPM, PTMA-*m*CPBA, PTMA-H$_2$O$_2$, and PTMA$^+$. The 2D projections can be found in **Figure 2.3**. Water is off the scale of the graphs due a large δ_h value of 42.4 MPa$^{1/2}$.

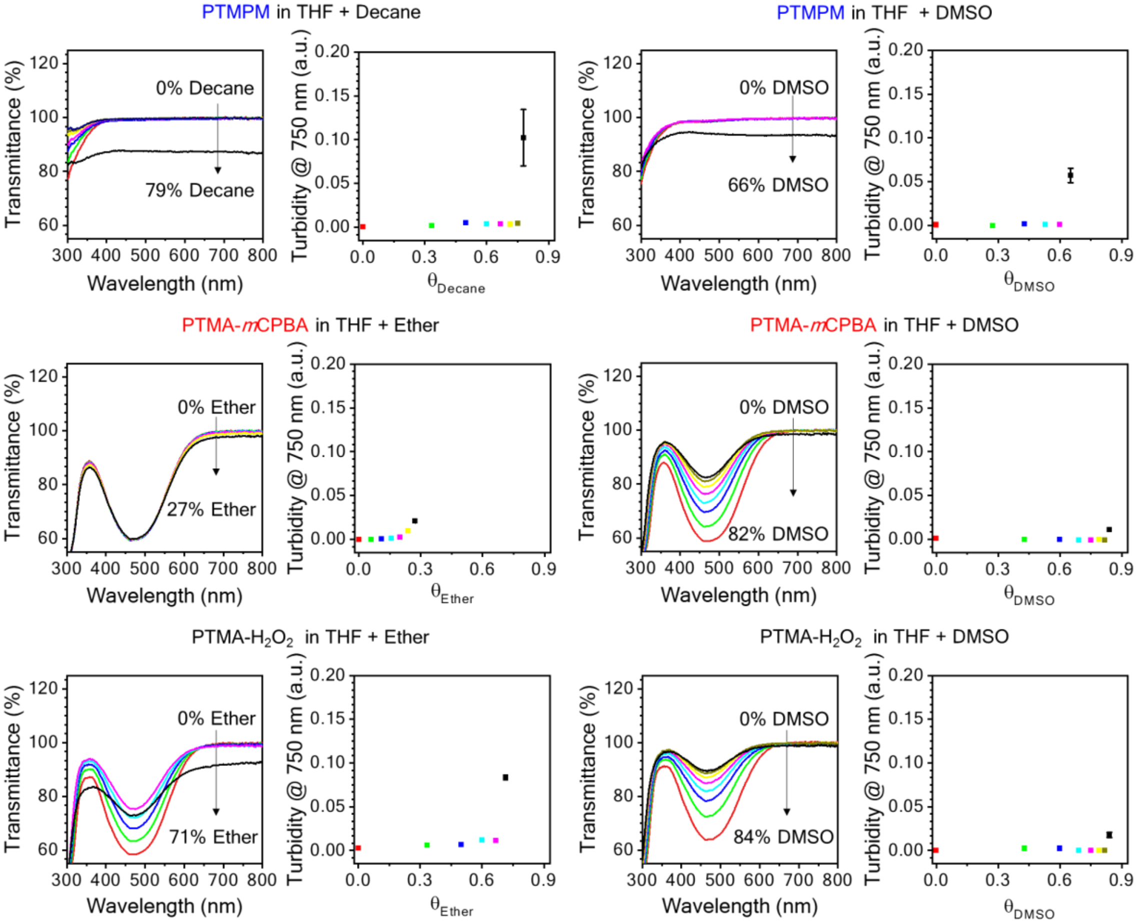

Figure S2.13. The UV-Vis spectra and corresponding turbidity plots (at 750 nm) calculated as a function of the volume fraction of poor solvent added during the titration for polymer solutions in tetrahydrofuran (THF).

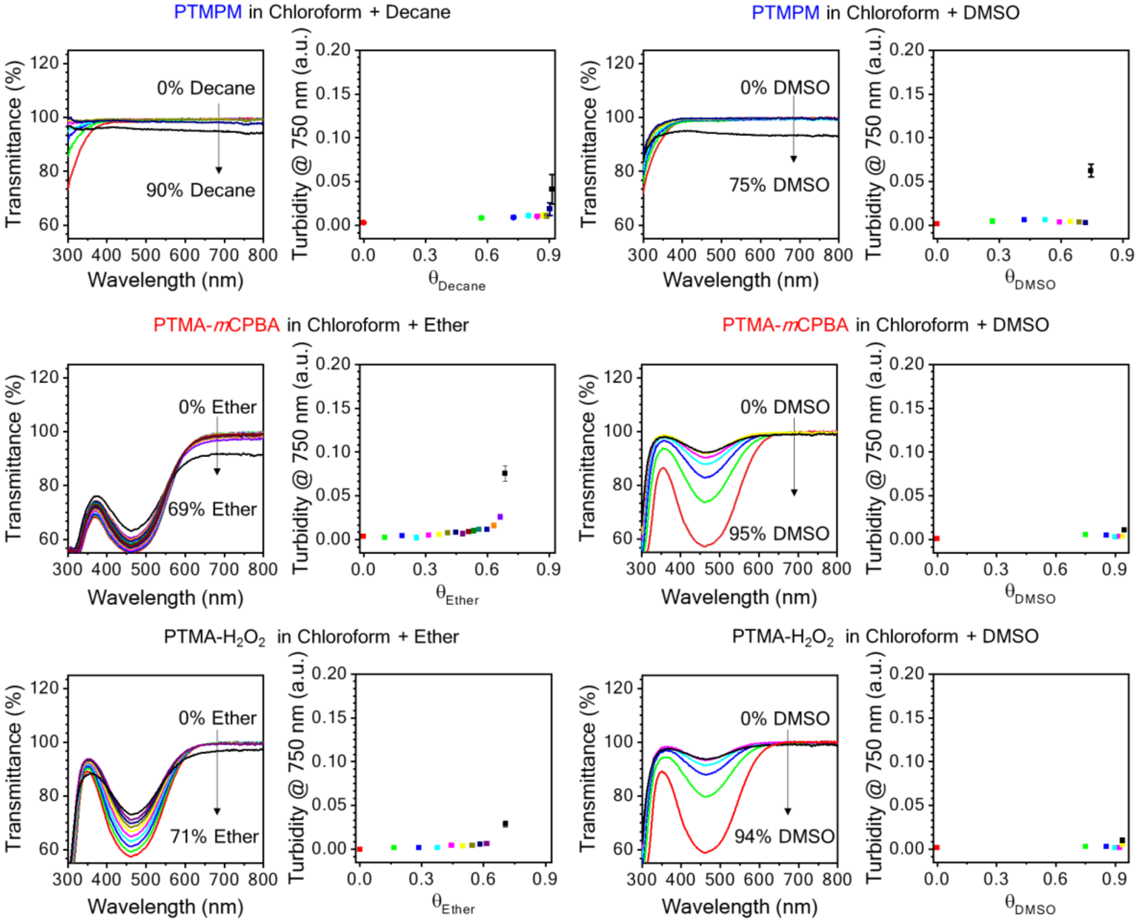

Figure S2.14. The UV-Vis spectra and corresponding turbidity plots (at 750 nm) calculated as a function of the volume fraction of poor solvent added during the titration for polymer solutions in chloroform.

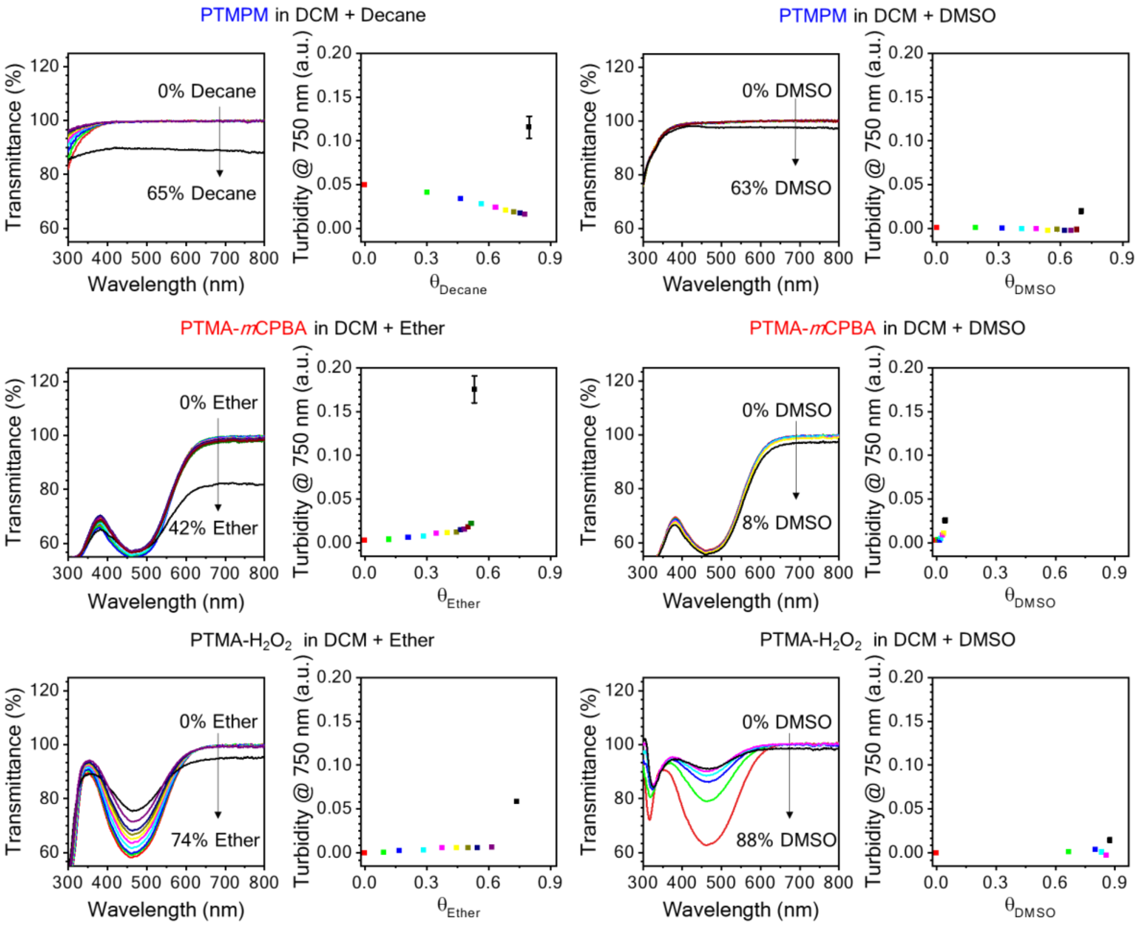

Figure S2.15. The UV-Vis spectra and corresponding turbidity plots (at 750 nm) calculated as a function of the volume fraction of poor solvent added during the titration for polymer solutions in dichloromethane (DCM).

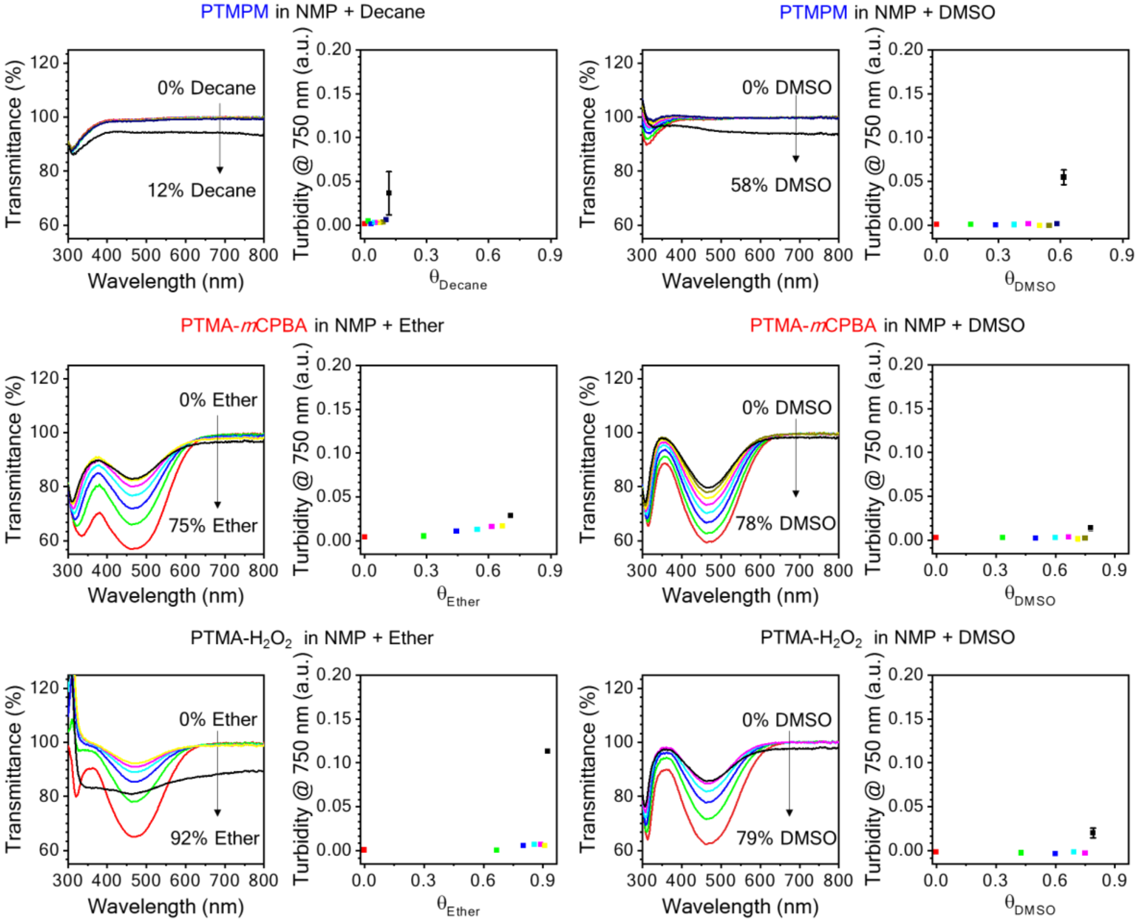

Figure S2.16. The UV-Vis spectra and corresponding turbidity plots (at 750 nm) calculated as a function of the volume fraction of poor solvent added during the titration for polymer solutions in *N*-methyl-2-pyrrolidinone (NMP).

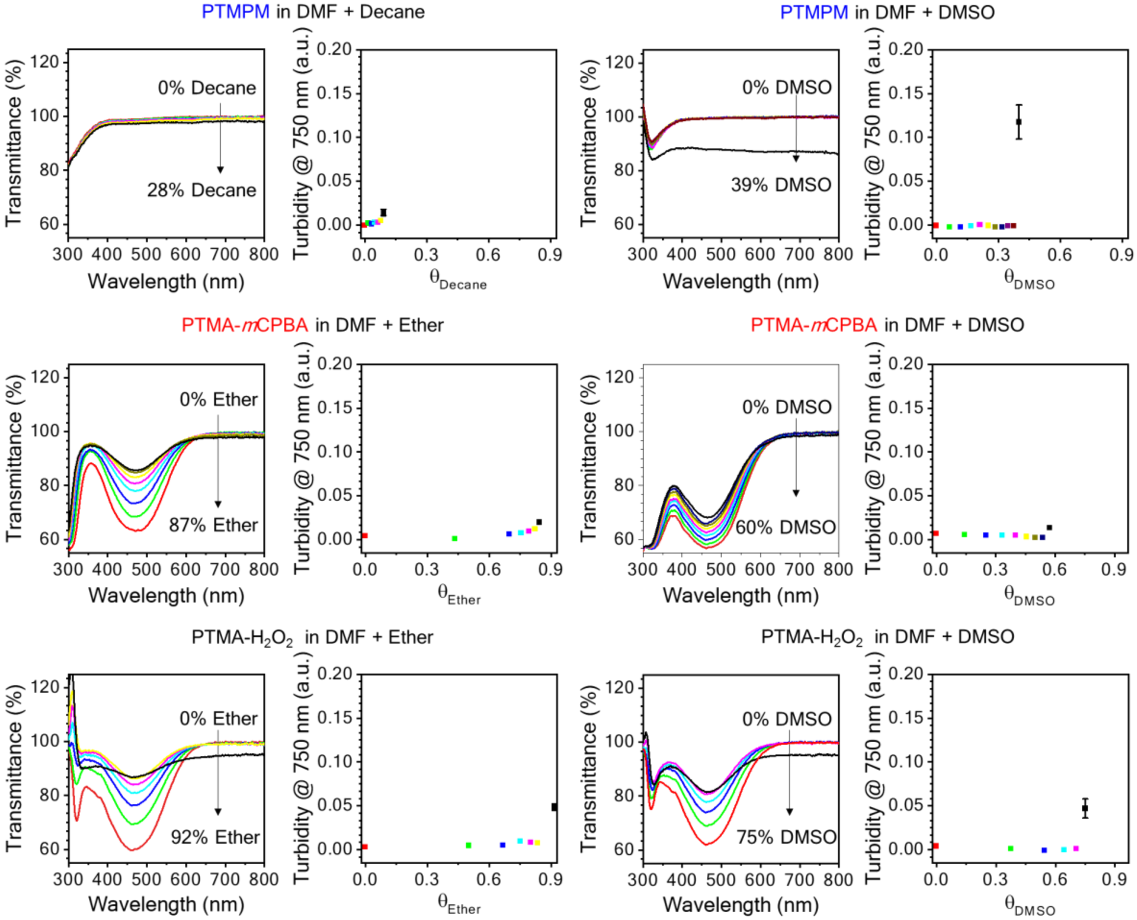

Figure S2.17. The UV-Vis spectra and corresponding turbidity plots (at 750 nm) calculated as a function of the volume fraction of poor solvent added during the titration for polymer solutions in dimethylformamide (DMF).

Table S2.5. A summary of the turbidity titration results for PTMPM.

Solvent	**δ_1 (MPa$^{1/2}$)**	**V (cm^3·mol^{-1})**	**Φ**		**δ_2' (MPa$^{1/2}$)**
			Decane	**DMSO**	
THF	18.6	81.7	0.79 ± 0.01	0.66 ± 0.04	19.2 ± 0.74
Chloroform	19.0	80.7	0.90 ± 0.01	0.75 ± 0.02	19.2 ± 0.37
DCM	19.8	63.9	0.65 ± 0.04	0.63 ± 0.05	20.2 ± 1.25
Acetone	20.3	74.0	0.57 ± 0.04	0.60 ± 0.03	20.7 ± 0.86
NMP	23.1	96.5	0.12 ± 0.01	0.58 ± 0.04	24.3 ± 0.93
DMF	24.8	77.0	0.20 ± 0.08	0.39 ± 0.02	24.5 ± 1.39

Table S2.6. A summary of the turbidity titration results for PTMA-*m*CPBA.

Solvent	**δ_1 (MPa$^{1/2}$)**	**V (cm^3·mol^{-1})**	**Φ**		**δ_2' (MPa$^{1/2}$)**
			Ether	**DMSO**	
THF	18.6	81.7	0.27 ± 0.01	0.82 ± 0.02	22.5 ± 0.44
Chloroform	19.0	80.7	0.69 ± 0.01	0.95 ± 0.01	22.3 ± 0.17
DCM	19.8	63.9	0.50 ± 0.03	0.08 ± 0.07	18.9 ± 1.47
Acetone	20.3	74.0	0.59 ± 0.02	0.82 ± 0.05	22.3 ± 1.10
NMP	23.1	96.5	0.75 ± 0.05	0.78 ± 0.01	22.2 ± 0.87
DMF	24.8	77.0	0.87 ± 0.02	0.60 ± 0.08	21.6 ± 1.75

Table S2.7. A summary of the turbidity titration results for PTMA-H_2O_2.

Solvent	**δ_1 ($MPa^{1/2}$)**	**V ($cm^3 \cdot mol^{-1}$)**	**Φ**		**δ_2' ($MPa^{1/2}$)**
			Ether	**DMSO**	
THF	18.6	81.7	0.75 ± 0.03	0.81 ± 0.03	21.4 ± 0.82
Chloroform	19.0	80.7	0.72 ± 0.01	0.95 ± 0.01	22.2 ± 0.27
DCM	19.8	63.9	0.75 ± 0.01	0.89 ± 0.02	22.1 ± 0.55
Acetone	20.3	74.0	0.83 ± 0.01	0.80 ± 0.01	21.5 ± 0.10
NMP	23.1	96.5	0.91 ± 0.02	0.78 ± 0.01	21.5 ± 0.43
DMF	24.8	77.0	0.92 ± 0.02	0.70 ± 0.04	21.6 ± 0.88

For mixed solvent of acetone (dissolving solvent) and ether (non-dissolving solvent):

$$V_{nds} = V_{ether} = 89.4\ cm^3/mol$$

$$\delta_{nds} = \delta_{ether} = 15.1\ MPa^{1/2}$$

$$\Phi_{nds} = \Phi_{ether} = 0.59$$

$$V_{ds} = V_{acetone} = 74.0\ cm^3/mol$$

$$\delta_{ds} = \delta_{acetone} = 20.3\ MPa^{1/2}$$

$$\Phi_{ds} = \Phi_{acetone} = 0.41$$

$$\delta_{ml} = \Phi_{ds}\delta_{ds} + \Phi_{nds}\delta_{nds} = (0.41)\left(20.3\ MPa^{\frac{1}{2}}\right) + (0.59)\left(15.1\ MPa^{\frac{1}{2}}\right) = 17.2\ MPa^{\frac{1}{2}}$$

$$V_{ml} = \frac{V_{nds}V_{ds}}{(\Phi_{nds}V_{ds} + \Phi_{ds}V_{nds})} = \frac{(89.4\frac{cm^3}{mol})(74.0\frac{cm^3}{mol})}{\left((0.59)(74.0\frac{cm^3}{mol}) + (0.41)(\ 89.4\frac{cm^3}{mol})\right)} = 89.4\ cm^3/mol$$

For mixed solvent of acetone (dissolving solvent) and DMSO (non-dissolving solvent):

$$V_{nds} = V_{DMSO} = 71.3\ cm^3/mol$$

$$\delta_{nds} = \delta_{DMSO} = 29.7\ MPa^{1/2}$$

$$\Phi_{nds} = \Phi_{DMSO} = 0.82$$

$$V_{ds} = V_{acetone} = 74.0\ cm^3/mol$$

$$\delta_{ds} = \delta_{acetone} = 20.3\ MPa^{1/2}$$

$$\Phi_{ds} = \Phi_{acetone} = 0.18$$

$$\delta_{mh} = \Phi_{ds}\delta_{ds} + \Phi_{ds}\delta_{ds} = (0.18)\left(20.3\ MPa^{\frac{1}{2}}\right) + (0.82)\left(29.7\ MPa^{\frac{1}{2}}\right) = 28.0\ MPa^{\frac{1}{2}}$$

$$V_{mh} = \frac{V_{nds}V_{ds}}{(\Phi_{nds}V_{ds} + \Phi_{ds}V_{nds})} = = \frac{(71.3\frac{cm^3}{mol})(74.0\frac{cm^3}{mol})}{\left((0.82)(74.0\frac{cm^3}{mol}) + (0.18)(\ 71.3\frac{cm^3}{mol})\right)} = 71.8\ cm^3/mol$$

Final calculation of estimated solubility parameter for PTMA in acetone:

$$\delta_2^{'} = \frac{\left(V_{ml}^{\frac{1}{2}}\delta_{ml} + V_{mh}^{\frac{1}{2}}\delta_{mh}\right)}{\left(V_{ml}^{\frac{1}{2}} + V_{mh}^{\frac{1}{2}}\right)} = \frac{\left(\left(89.4\frac{cm^3}{mol}\right)^{\frac{1}{2}} 17.2\ MPa^{\frac{1}{2}} + \left(71.8\frac{cm^3}{mol}\right)^{\frac{1}{2}}\ 28.0\ MPa^{\frac{1}{2}}\right)}{\left(\left(89.4\frac{cm^3}{mol}\right)^{\frac{1}{2}} + \left(71.8\frac{cm^3}{mol}\right)^{\frac{1}{2}}\right)}$$

$$\delta_2^{'} = 22.3\ MPa^{\frac{1}{2}}$$

Figure S2.18. Sample Calculation for PTMA-*m*CPBA in Acetone, as seen in **Figure 2.4**.

Calculation of Nitroxide and Oxoammonium Group Contribution Values Details

To estimate the Hildebrand group contribution values for the nitroxide group, the molar volume contribution of the oxygen radical (-O•) was assumed to be the same value as an oxygen (-O-) or 6.4 $cm^3 \cdot mol^{-1}$ for the Hoy method and 3.8 $cm^3 \cdot mol^{-1}$ for the Fedors method. This resulted in values of 1325.0 $J^{1/2} \cdot cm^{3/2} \cdot mol^{-1}$ and 36.3 $kJ \cdot mol^{-1}$ for the Hoy and Fedors methods, respectively, for the oxygen radical (-O•). The assumed molar volume and estimated group contribution values were combined with the known values for a tertiary amine to estimate the values for the entire nitroxide group (N-O•), **Table 2.2**.

To estimate the Hansen group contribution values for the nitroxide group, the same procedure was applied. The molar volume contribution of the oxygen radical (-O•) was assumed to be the same value as an oxygen (-O-) or 3.8 $cm^3 \cdot mol^{-1}$. Calculations for the oxygen radical resulted in -21 $J^{1/2} \cdot cm^{3/2} \cdot mol^{-1}$ for F_d, 668 $J^{1/2} \cdot cm^{3/2} \cdot mol^{-1}$ for F_p, and 0 $J \cdot mol^{-1}$ for U_h, which can be used to calculate δ_d, δ_p, and δ_h, respectively. Solving for F_d and U_h would have resulted in 2003 $J^{1/2} \cdot cm^{3/2} \cdot mol^{-1}$ and -3476 $J \cdot mol^{-1}$, respectively, however, the F_d value was much larger than those seen for other functional groups (largest of 1528 $J^{1/2} \cdot cm^{3/2} \cdot mol^{-1}$), so the F_d was scaled (*i.e.* to a third of the calculated value).[42,49] Additionally, only positive U_h values are assigned to functional groups capable of hydrogen bonding (for -OH, U_h= 20000 $J \cdot mol^{-1}$) or 0 $J \cdot mol^{-1}$ for functional groups that do not hydrogen bond, so a value of 0 $J \cdot mol^{-1}$ was used for U_h.[42] Again, the assumed molar volume and estimated group contribution values were combined with the known values for a tertiary amine to estimate the values for the entire nitroxide group (N-O•), **Table 2.2**.

Back-calculation of the dispersion contribution (F_d) for the oxoammonium cation would have resulted in -4812 $J^{1/2}\cdot cm^{3/2}\cdot mol^{-1}$, which is much larger than other functional groups so the F_d was scaled to the largest value reported (*i.e.* -409 $J^{1/2}\cdot cm^{3/2}\cdot mol^{-1}$).[42] Additionally, calculation of the polarity contribution (F_p) for the oxoammonium cation would have resulted in 4254 $J^{1/2}\cdot cm^{3/2}\cdot mol^{-1}$, which is much larger than other functional groups (largest of 1528 $J^{1/2}\cdot cm^{3/2}\cdot mol^{-1}$), so the F_d was scaled to be more similar (*i.e.* to a third of the calculated value).[49]

For Hoy Method calculation of PTMA-*m*CPBA:

$$\delta_{mCPBA,Hoy} = 21.1\ MPa^{1/2}\ (from\ turbidity\ titrations)$$

$$\delta_{mCPBA,Hoy} = \left(\frac{0.36(F_{NH}) + 051(F_{NO\bullet}) + 0.13(F_{+NO})}{0.36(V_{NH}) + 0.51(V_{NO\bullet}) + 0.13(V_{+NO})}\right) = 21.1MPa^{1/2}$$

where *F* is the group contribution sum and *V* is the molar volume of a polymer with only the subscripted functional group. The value of F_{NH} and V_{NH} are known from published group contribution values. $V_{NO\bullet}$ and V_{+NO} were estimated as described above.

$$\delta_{mCPBA,Hoy} = \left(\frac{3882.2 + 0.51(F_{NO\bullet}) + 0.13(F_{+NO})}{220.5}\right) = 21.1MPa^{1/2}$$

For Hoy Method calculation of PTMA-H_2O_2:

$$\delta_{H2O2,Hoy} = 21.7\ MPa^{1/2}\ (from\ turbidity\ titrations)$$

$$\delta_{H2O2,Hoy} = \left(\frac{0.27(F_{NH}) + 0.67(F_{NO\bullet}) + 0.06(F_{+NO})}{0.27(V_{NH}) + 0.67(V_{NO\bullet}) + 0.06(V_{+NO})}\right) = 21.7MPa^{1/2}$$

$$\delta_{H2O2,Hoy} = \left(\frac{3869.1 + 0.67(F_{NO\bullet}) + 0.06(F_{+NO})}{221.2}\right) = 21.7MPa^{1/2}$$

Simplifying both expressions:

PTMA-*m*CPBA: $707.6 = 0.51F_{NO\bullet} + 0.13F_{+NO}$

PTMA-H_2O_2: $931.7 = 0.67F_{NO\bullet} + 0.06F_{+NO}$

Solving for PTMA-*m*CPBA equation for F_{+NO}:

$$F_{+NO} = \frac{707.6 - 0.51F_{NO\bullet}}{0.13} = 5927.7 - 3.9F_{NO\bullet}$$

Plugging the expression for F_{+NO} into PTMA-H_2O_2 equation to solve for $F_{NO\bullet}$:

$$931.7 = 0.67F_{NO\bullet} + 0.06(5927.7 - 3.9F_{NO\bullet})$$

$$576.0 = 0.4F_{NO\bullet}$$

$$F_{NO\bullet} = 1325.0\ \mathrm{J}^{1/2} \cdot \mathrm{cm}^{3/2} \cdot \mathrm{mol}^{-1}$$

Plugging $F_{NO\bullet}$ into PTMA-*m*CPBA equation to solve for F_{+NO}:

$$707.6 = 0.51(1325.0) + 0.13F_{+NO}$$

$$F_{+NO} = 243.5\ \mathrm{J}^{1/2} \cdot \mathrm{cm}^{3/2} \cdot \mathrm{mol}^{-1}$$

Figure S2.19. Example calculation of the nitroxide and oxoammonium group contribution values (for the Hoy method) from experimental input.

Table S2.8. Hydrogen bonding (δ_h), polar (δ_p), and dispersion (δ_d) and Hansen solubility parameters for the polymers studied in this work, predicted values for other macromolecular radicals, commodity polymers, binder polymers, and conductive additives.

Compound	**Abbreviation**	**δ_h (MPa$^{1/2}$)**	**δ_p (MPa$^{1/2}$)**	**δ_d (MPa$^{1/2}$)**	**Reference**
$Ti_3C_2T_x$ MXene	NA	23.2	13.4	17.8	[64,69]
graphene oxide	GO	15.7	10	17.1	[64]
Super P carbon black	Super P	12.9	2.42	17.6	[38]
poly(2,2,6,6-tetramethylpiperidine methacrylate)	PTMPM	9.7	7.5	16.8	This Work
poly(vinylidene difluoride)	PVDF	9.2	12.5	17.2	[71]
poly(TEMPO norbornene)	PTNB	8.3	3.8	21.5	Predicted from This Work
poly(methyl methacrylate)	PMMA	7.8	5.7	17.5	[42]
graphene	-	7.7	9.3	18	[68]
poly(TEMPO ethylene oxide)	PTEO	7.7	7.1	19.6	Predicted from This Work
single-walled carbon nanotubes	SWCNTs	7.6	7.5	17.8	[37,64,65]
reduced graphene oxide	rGO	7.5	8.5	18	[64]

Table S2.8. Continued.

Compound	**Abbreviation**	**δ_h (MPa$^{1/2}$)**	**δ_p (MPa$^{1/2}$)**	**δ_d (MPa$^{1/2}$)**	**Reference**
poly(TEMPO vinyl ether)	PTVE	6.9	8.0	18.9	Predicted from This Work
poly(TEMPO methacrylate) *m*CPBA oxidation	PTMA-*m*CPBA	6.8	9.6	17.2	This Work
poly(TEMPO methacrylate) H_2O_2 oxidation	PTMA-H_2O_2	6.8	9.6	17.2	This Work
poly(TEMPO acrylamide)	PTAm	6.6	7.4	18.7	Predicted from This Work
multi-walled carbon nanotubes	MWCNTs	4.8	7	18.5	[66,211]
fullerene	C60	2.7	2.9	19.7	[64,70]
polystyrene	PS	2.1	0.9	19.2	[42]
polyethylene	PE	0.0	0.0	17.3	[42]
poly(tetrafluoroethylene)	PTFE	0.0	0.0	12.7	[42]

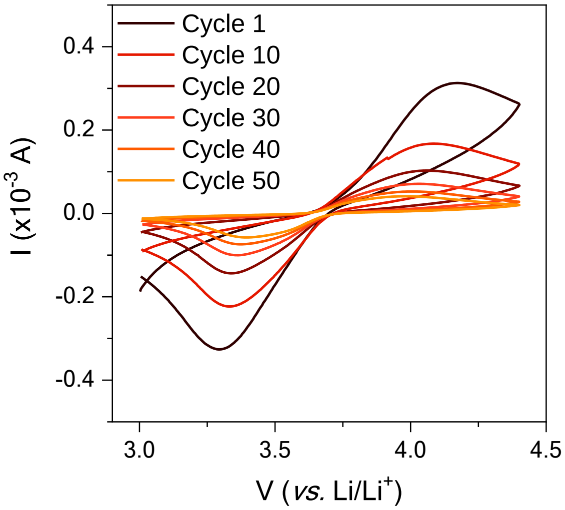

Figure S2.20. Cyclic voltammetry at 10 mV·s^{-1} for a three-electrode beaker cell. The working electrode was a PTMA thin film on ITO-coated glass. The electrolyte was 0.5M $LiCF_3SO_3$ in EC/DEC (3/7, v/v) and the counter and reference electrodes were lithium metal.

References

10. Nishide, H., Iwasa, S., Pu, Y.-J., Suga, T., Nakahara, K. & Satoh, M. Organic radical battery: nitroxide polymers as a cathode-active material. *Electrochim. Acta* **50**, 827-831 (2004).

11. Kim, J.-K., Ahn, J.-H., Cheruvally, G., Chauhan, G. S., Choi, J.-W., Kim, D.-S., Ahn, H.-J., Lee, S. H. & Song, C. E. Electrochemical properties of rechargeable organic radical battery with PTMA cathode. *Metals and Materials International* **15**, 77-82 (2009).

12. Janoschka, T., Hager, M. D. & Schubert, U. S. Powering up the Future: Radical Polymers for Battery Applications. *Adv. Mater.* **24**, 6397-6409 (2012).

18. Kim, J.-K., Cheruvally, G., Ahn, J.-H., Seo, Y.-G., Choi, D. S., Lee, S.-H. & Song, C. E. Organic radical battery with PTMA cathode: Effect of PTMA content on electrochemical properties. *Journal of Industrial and Engineering Chemistry* **14**, 371-376 (2008).

23. Easley, A. D., Vukin, L. M., Flouda, P., Howard, D. L., Pena, J. L. & Lutkenhaus, J. L. Nitroxide Radical Polymer–Solvent Interactions and Solubility Parameter Determination. *Macromolecules* **53**, 7997-8008 (2020).

24. Wang, S., Li, F., Easley, A. D. & Lutkenhaus, J. L. Real-time insight into the doping mechanism of redox-active organic radical polymers. *Nature Materials* **18**, 69-75 (2019).

25. Zhang, K., Hu, Y., Wang, L., Fan, J., Monteiro, M. J. & Jia, Z. The impact of the molecular weight on the electrochemical properties of poly(TEMPO methacrylate). *Polymer Chemistry* **8**, 1815-1823 (2017).

28. Nakahara, K., Iwasa, S., Satoh, M., Morioka, Y., Iriyama, J., Suguro, M. & Hasegawa, E. Rechargeable batteries with organic radical cathodes. *Chem. Phys. Lett.* **359**, 351-354 (2002).

29. Nakahara, K., Iriyama, J., Iwasa, S., Suguro, M., Satoh, M. & Cairns, E. J. Cell properties for modified PTMA cathodes of organic radical batteries. *J. Power Sources* **165**, 398-402 (2007).

31. Kim, J.-K., Cheruvally, G., Choi, J.-W., Ahn, J.-H., Lee, S. H., Choi, D. S. & Song, C. E. Effect of radical polymer cathode thickness on the electrochemical performance of organic radical battery. *Solid State Ionics* **178**, 1546-1551 (2007).

32. Nakahara, K., Iriyama, J., Iwasa, S., Suguro, M., Satoh, M. & Cairns, E. J. Al-laminated film packaged organic radical battery for high-power applications. *J. Power Sources* **163**, 1110-1113 (2007).

33. Nakahara, K., Iriyama, J., Iwasa, S., Suguro, M., Satoh, M. & Cairns, E. J. High-rate capable organic radical cathodes for lithium rechargeable batteries. *J. Power Sources* **165**, 870-873 (2007).

35. Bugnon, L., Morton, C. J. H., Novak, P., Vetter, J. & Nesvadba, P. Synthesis of Poly(4-methacryloyloxy-TEMPO) via Group-Transfer Polymerization and Its Evaluation in Organic Radical Battery. *Chem. Mater.* **19**, 2910-2914 (2007).

37. Ata, S., Mizuno, T., Nishizawa, A., Subramaniam, C., Futaba, D. N. & Hata, K. Influence of matching solubility parameter of polymer matrix and CNT on electrical conductivity of CNT/rubber composite. *Scientific Reports* **4**, 7232 (2014).

38. Kwon, Y. H., Huie, M. M., Choi, D., Chang, M., Marschilok, A. C., Takeuchi, K. J., Takeuchi, E. S. & Reichmanis, E. Toward Uniformly Dispersed Battery Electrode Composite Materials: Characteristics and Performance. *ACS Applied Materials & Interfaces* **8**, 3452-3463 (2016).

42. Barton, A. F. M. *CRC Handbook of Solubility Parameters and Other Cohesion Parameters, Second Edition*. (Taylor & Francis, 1991).

49. Hansen, C. M. The three dimensional solubility parameter. *Danish Technical: Copenhagen* **14** (1967).

64. Qin, J., Wang, X., Jiang, Q. & Cao, M. Optimizing Dispersion, Exfoliation, Synthesis, and Device Fabrication of Inorganic Nanomaterials Using Hansen Solubility Parameters. *ChemPhysChem* **20**, 1069-1097 (2019).

65. Bergin, S. D., Nicolosi, V., Streich, P. V., Giordani, S., Sun, Z., Windle, A. H., Ryan, P., Niraj, N. P. P., Wang, Z.-T. T., Carpenter, L., Blau, W. J., Boland, J. J., Hamilton, J. P. & Coleman, J. N. Towards Solutions of Single-Walled Carbon Nanotubes in Common Solvents. *Adv. Mater.* **20**, 1876-1881 (2008).

66. Clark, M. D. & Krishnamoorti, R. Dispersion of Functionalized Multiwalled Carbon Nanotubes. *The Journal of Physical Chemistry C* **113**, 20861-20868 (2009).

68. Hernandez, Y., Lotya, M., Rickard, D., Bergin, S. D. & Coleman, J. N. Measurement of Multicomponent Solubility Parameters for Graphene Facilitates Solvent Discovery. *Langmuir* **26**, 3208-3213 (2010).

69. Maleski, K., Mochalin, V. N. & Gogotsi, Y. Dispersions of Two-Dimensional Titanium Carbide MXene in Organic Solvents. *Chem. Mater.* **29**, 1632-1640 (2017).

70. Hansen, C. M. & Smith, A. L. Using Hansen solubility parameters to correlate solubility of C60 fullerene in organic solvents and in polymers. *Carbon* **42**, 1591-1597 (2004).

71. Bottino, A., Capannelli, G., Munari, S. & Turturro, A. Solubility parameters of poly(vinylidene fluoride). *J. Polym. Sci., Part B: Polym. Phys.* **26**, 785-794 (1988).

74. Deng, L.-f., Li, X.-h., Xiao, L.-x. & Zhang, Y.-h. Synthesis and electrochemical properties of polyradical cathode material for lithium second batteries. *Journal of Central South University of Technology* **10**, 190-194 (2003).

75. Kim, J.-K., Cheruvally, G., Choi, J.-W., Ahn, J.-H., Choi, D. S. & Song, C. E. Rechargeable Organic Radical Battery with Electrospun, Fibrous Membrane-Based Polymer Electrolyte. *J. Electrochem. Soc.* **154**, A839 (2007).

76. Kim, Y., Jo, C., Lee, J., Lee, C. W. & Yoon, S. An ordered nanocomposite of organic radical polymer and mesocellular carbon foam as cathode material in lithium ion batteries. *J. Mater. Chem.* **22**, 1453-1458 (2012).

77. Guo, W., Yin, Y.-X., Xin, S., Guo, Y.-G. & Wan, L.-J. Superior radical polymer cathode material with a two-electron process redox reaction promoted by graphene. *Energy & Environmental Science* **5**, 5221-5225 (2012).

95. Hung, M.-K., Wang, Y.-H., Lin, C.-H., Lin, H.-C. & Lee, J.-T. Synthesis and electrochemical behaviour of nitroxide polymer brush thin-film electrodes for organic radical batteries. *J. Mater. Chem.* **22**, 1570-1577 (2012).

208. Lin, H.-C., Li, C.-C. & Lee, J.-T. Nitroxide polymer brushes grafted onto silica nanoparticles as cathodes for organic radical batteries. *J. Power Sources* **196**, 8098-8103 (2011).

209. Wang, S., Park, A. M. G., Flouda, P., Easley, A. D., Li, F., Ma, T., Fuchs, G. D. & Lutkenhaus, J. L. Solution-Processable Thermally Crosslinked Organic Radical Polymer Battery Cathodes. *ChemSusChem* **n/a** (2020).

210. Xue, W., Mutlu, H. & Theato, P. Post-polymerization modification of polymeric active esters towards TEMPO containing polymers: A systematic study. *Eur. Polym. J.* **130**, 109660 (2020).

211. detriche, S., Zorzini, G., Colomer, J.-F., Fonseca, A. & B.Nagy, J. Application of the Hansen Solubility Parameters Theory to Carbon Nanotubes. *Journal of nanoscience and nanotechnology* **8**, 6082-6092 (2008).

Chapter 3: Layer-by-Layer Nanoarchitectonics of Electrochemically Active Thin Films Comprised of Radical-Containing Polymers

Reprinted with permission from ref. [87]Copyright 2020.

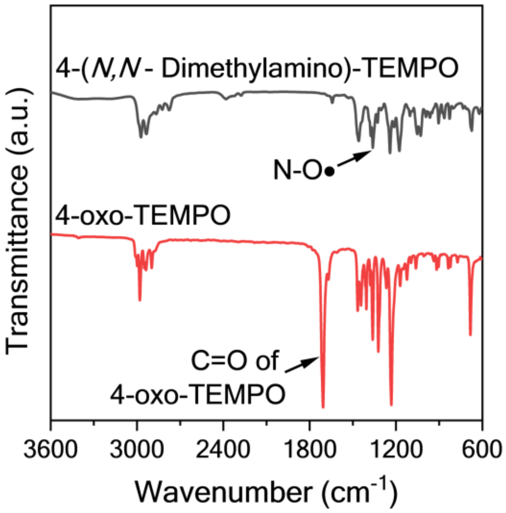

Figure S3.1. IR spectra of 4-oxo-TEMPO and 4-(*N*,*N*-Dimethylamino)-TEMPO.

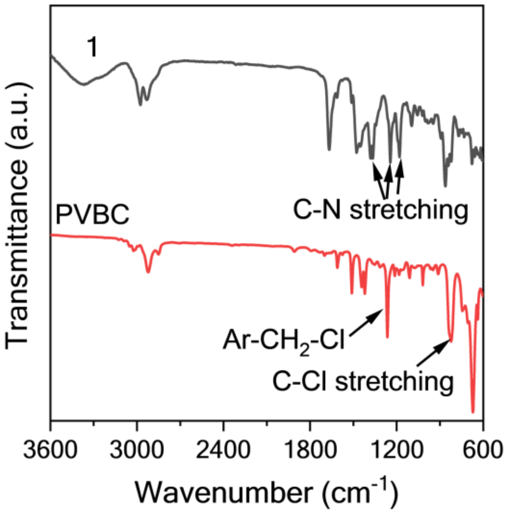

Figure S3.2. IR spectra of PVBC and the nitroxide polycation (**1**).

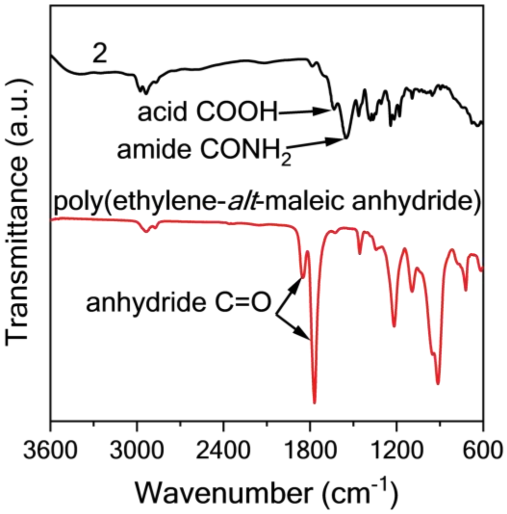

Figure S3.3. IR spectra of poly(ethylene-*alt*-maleic anhydride) and the nitroxide polyanion (**2**).

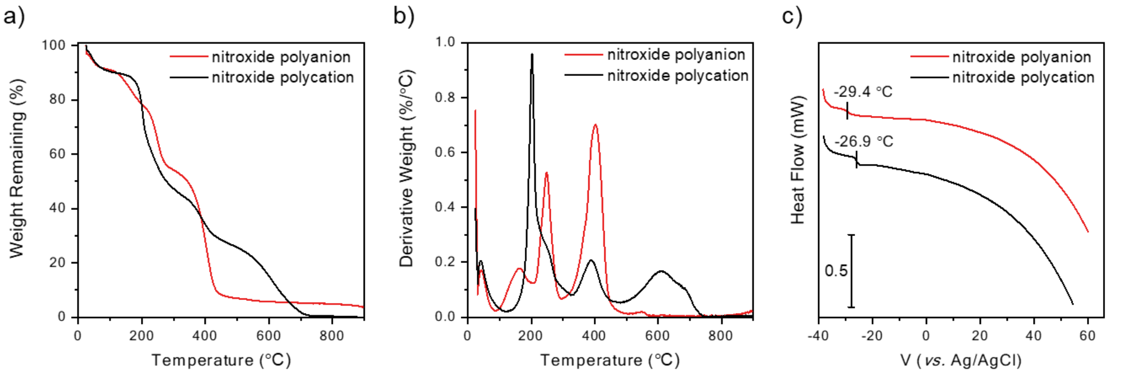

Figure S3.4. Thermogravametic analysis a) weight remaining and b) derivative weight for the nitroxide polyanion and polycation. c) Differential scanning calorimetry with indicated glass transition temperatures (T_g) for the nitroxide polyanion and polycation.

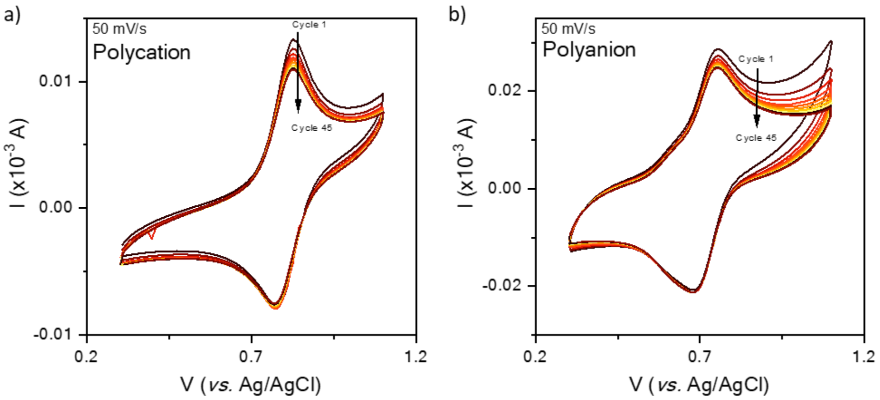

Figure S3.5. Solution state cyclic voltammograms for 45 cycles at 50 mV/s for the a) nitroxide polycation and b) nitroxide polyanion. The electrolyte solution was 1 mM of the nitroxide repeat unit in 0.1 M NaCl in H2O with a platinum wire counter electrode, Ag/AgCl (sat.) reference electrode, and a glassy carbon working electrode.

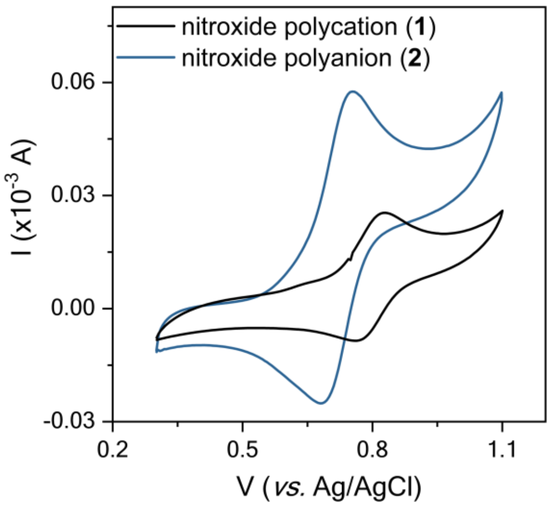

Figure S3.6. Solution state cyclic voltammograms at 2 mV/s for both the nitroxide polycation and nitroxide polyanion. The polymer was dissolved at 1 mM of repeat unit in 0.1 M NaCl aqueous solution. The polymer solution was tested in a three-electrode cell with a glassy carbon working electrode, a platinum wire counter electrode, and a Ag/AgCl (sat.) reference electrode.

Table S3.1. Comparison previous studies of LbL films using nitroxide-modified polyelectrolytes.

Polycation	**Polyanion**	**LPs**	**Thickness (nm)**	**Oxidation Potential**[b] **(*vs.* Ag/AgCl)**	**Peak Oxidation Current**[b]	**Ref.**
nitroxide polycation	nitroxide polyanion	10.5	363	0.73	230 μA	This Work
poly(ethyleneimine)	TEMPO-modified poly(acrylic acid)	4.5	12[c]	0.66	175 μA[a]	112
polyvinylamine-g-TEMPO	Poly(styrenesulfonate)	4	5[a]	0.59 V	3 μA[a]	113

[a] Estimated from graph in corresponding reference.

[b] Scan rate of 50 mV/s.

[c] Thickness from a 9 LP film.

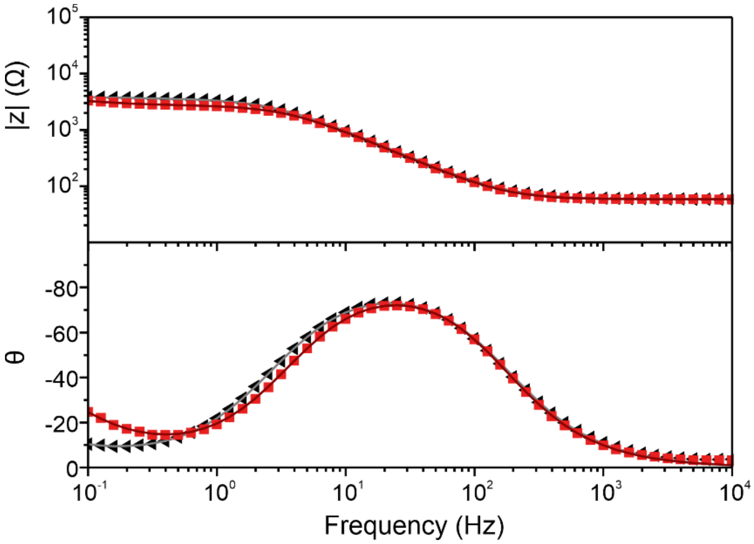

Figure S3.7. Bode plots for 10 LP and 10.5 LP with their fit lines. EIS was conducted at a potential of 0.8 V *vs.* Ag/AgCl (sat.) with an amplitude of 10 mV in a frequency range of 5 × 10^6 Hz to 0.1 Hz (10 steps per decade).

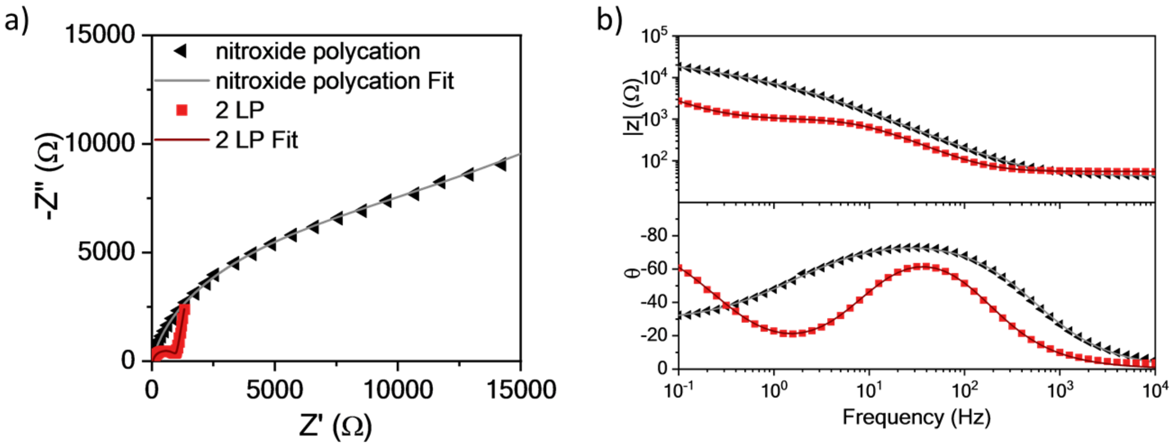

Figure S3.8. a) Nyquist and b) Bode plots for nitroxide polycation and 2 LP films with their fit lines using the equivalent circuit model in **Figure 3.8a**. EIS was conducted at a potential of 0.8 V *vs.* Ag/AgCl (sat.) with an amplitude of 10 mV in a frequency range of 5 × 10^6 Hz to 0.1 Hz (10 steps per decade).

References

87. Easley, A., Shaligram, S., Echols, I., Nixon, K., Regen, S. & Lutkenhaus, J. L. Layer-by-Layer Nanoarchitectonics of Electrochemically Active Thin Films Comprised of Radical-Containing Polymers. *J. Electrochem. Soc.* (2022).

112. Takahashi, S., Aikawa, Y., Kudo, T., Ono, T., Kashiwagi, Y. & Anzai, J.-i. Electrochemical decomposition of layer-by-layer thin films composed of TEMPO-modified poly(acrylic acid) and poly(ethyleneimine). *Colloid. Polym. Sci.* **292**, 771-776 (2014).

113. Fu, Q., Zoudanov, I., Gustafsson, E., Yang, D., Soleymani, L. & Pelton, R. H. Redox Properties of Polyvinylamine-g-TEMPO in Multilayer Films with Sodium Poly(styrenesulfonate). *ACS Applied Materials & Interfaces* **9**, 5622-5628 (2017).

Chapter 4: Polypeptide Organic Radical Batteries

Modified from ref. [122]

Theoretical Capacity Calculation

The theoretical capacities of the analogs and polypeptides were calculated using

$$Theoretical\ Capacity\ = \left(\frac{nF}{3600\ M}\right) \cdot 1000 \quad \left(\frac{\mathrm{mA \cdot h}}{\mathrm{g}}\right)$$

Equation S4.1

where n is the moles of electrons transferred per molecule or repeat unit, F is Faraday constant (≈ 96,485 s·A·mol^{-1}), M is the molar mass (g·mol^{-1}) of the molecule or polymer repeat unit. Capacities were calculated using the discharged states for both pendant groups (TEMPO and viologen^{2+}). For the viologen analog and viologen-chloride polypeptide, the counterions (iodide and chloride, respectively) were considered for the molar mass of the repeat unit. The theoretical capacities were 81.4 mA·h·g^{-1} for the viologen analog and 69.4 mA·h·g^{-1} for the biTEMPO analog.

The theoretical capacity of the full cell composed of a biTEMPO polypeptide-based cathode and a viologen-chloride polypeptide-based anode was calculated using

$$Cell\ Theoretical\ Capacity\ = \frac{1}{\left(\frac{1}{C_{cathode}} + \frac{1}{C_{anode}}\right)} \quad \left(\frac{\mathrm{mA \cdot h}}{\mathrm{g}}\right)$$

Equation S4.2

where $C_{cathode}$ is the theoretical capacity for the cathode (calculated in **Equation S4.1**) and C_{anode} is the theoretical capacity for the anode (calculated in **Equation S4.2**).

Electrochemical Characterization of Analog Solutions in Three-electrode Beaker Cells

Solution state CV was conducted for the viologen and biTEMPO analogs. The analogs were dissolved at 1 mM in 20 mL of 0.5 M $LiCF_3SO_3$ in PC electrolyte. In the three-electrode beaker cell for solution state CV, a glassy carbon working electrode was used with lithium metal counter and reference electrodes (**Figure S4.1 A**). After three conditioning cyclic voltammetry (CV) cycles at 10 $mV \cdot s^{-1}$, CV was performed at different scan rates (10, 25, 50 and 100 $mV \cdot s^{-1}$). All electrochemical measurements were performed in an argon filled glovebox with a Solartron Electrochemical Interface 1287 potentiostat/galvanostat unless otherwise noted.

Fabrication and Electrochemical Characterization of Polypeptide Composite Electrodes in Three-electrode Beaker Cells

Composite electrodes for both polypeptides were fabricated by preparing a slurry of viologen-chloride polypeptide or biTEMPO polypeptide (30 wt%), CB (60 wt%) and PVDF binder polymer (10 wt%) in NMP (1 mL). 200 μL (for viologen-chloride polypeptide slurry) or 300 μL (for viologen-chloride polypeptide slurry) of the slurry was then drop-casted onto a clean ITO-coated glass. After drop-casting, the electrodes were dried at 40 °C for 2 d before drying under vacuum at r.t. for 24 h. The fabricated electrodes were utilized in a three-electrode beaker cell as working electrodes with lithium metal reference and counter electrodes and 20 mL of 0.5 M $LiCF_3SO_3$ or 0.5 M $TBACF_3SO_3$ in PC as electrolyte (**Figure S4.1 B**). Three conditioning CV cycles at 10 mV·s^{-1} followed two CV cycles at each scan rate (10, 25, 50, and 100 mV·s^{-1}).

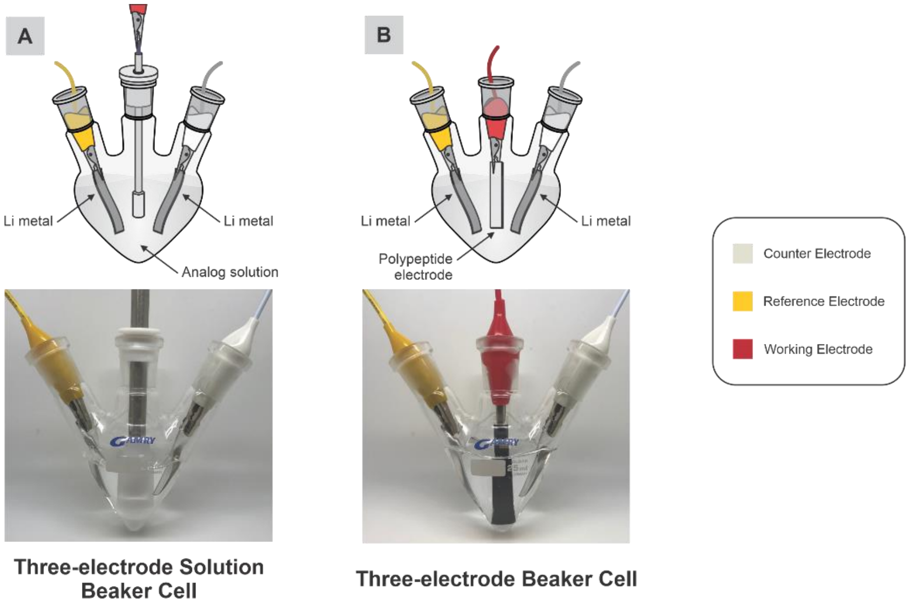

Figure S4.1. Electrochemical characterization set-ups discussed in the manuscript. (**A**) The three-electrode solution beaker cell: glassy carbon working electrode and lithium metal counter/reference electrodes. (**B**) The three-electrode beaker cell: polypeptide composite working electrode and lithium metal counter/reference electrodes.

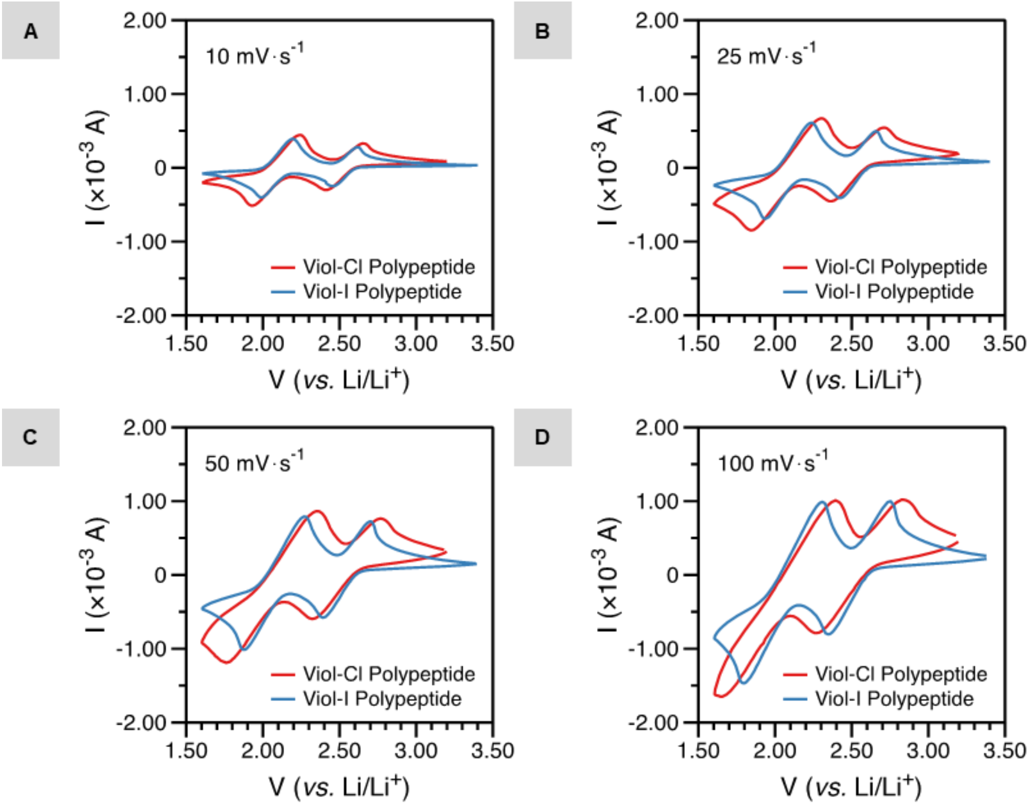

Figure S4.2. Cyclic voltammograms at (**A**) 10 mV$^{\cdot s-1}$, (**B**) 25 mV$^{\cdot s-1}$, (**C**) 50 mV$\cdot$s^{-1}, and (**D**) 100 mV$\cdot$s^{-1} for the viol-Cl polypeptide and viol-I polypeptide thin films on ITO-coated glass in a three-electrode beaker cell configuration. The supporting electrolyte was 0.5 M $LiCF_3SO_3$ in propylene carbonate. Lithium metal was used as counter and reference electrodes.

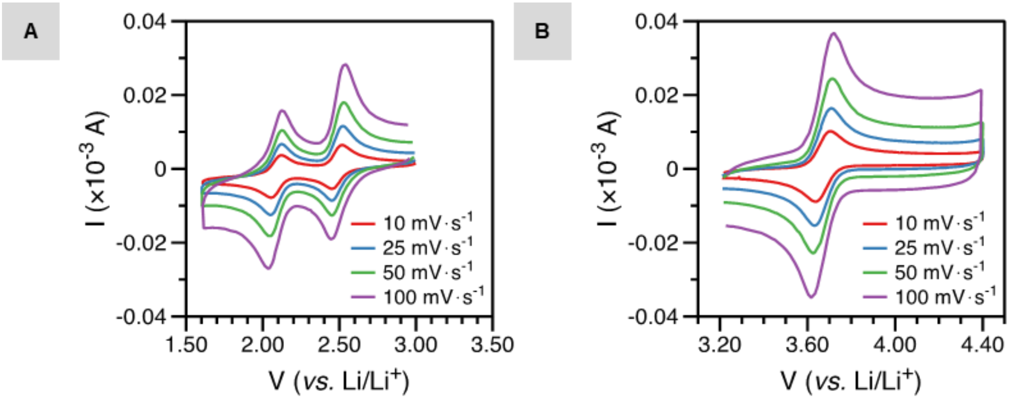

Figure S4.3. Solution state cyclic voltammetry of (**A**) viologen analog and (**B**) biTEMPO analog at 1 mM in 0.5 M LiCF3SO3 in PC electrolyte. A glassy carbon electrode was utilized as the working electrode in a three-electrode beaker cell with lithium metal reference and counter electrodes.

Table S4.1. Comparison of the oxidation/reduction peak potential (E_o/E_R), the peak separation (ΔE_p), half-wave potential ($E_{1/2}$), oxidation/reduction peak width (W_o/W_R), and oxidation/reduction peak area (A_o/A_R) for the biTEMPO analog, biTEMPO polypeptide thin film and biTEMPO polypeptide composite electrode at 10 mV·s^{-1} in a three-electrode beaker cell.

Parameter	**BiTEMPO Analog Solution**[a]	**BiTEMPO Polypeptide Thin Film**[a]	**BiTEMPO Polypeptide Thin Film**[b]	**BiTEMPO Polypeptide Composite Electrode**[a]	**BiTEMPO Polypeptide Composite Electrode**[b]
E_O (V)	3.70	3.77	3.98	3.80	3.91
E_R (V)	3.69	3.60	3.73	3.56	3.73
ΔE_p (V)	0.06	0.17	0.25	0.24	0.18
$E_{1/2}$ (V)	3.67	3.69	3.86	3.68	3.67
W_O (V)	0.26	0.24	0.70	0.26	0.65
W_R (V)	0.19	0.19	0.76	0.24	0.47
A_O (W)	4.13×10^{-6}	1.23×10^{-4}	2.47×10^{-5}	2.36×10^{-4}	5.29×10^{-4}
A_R (W)	2.07×10^{-6}	8.43×10^{-5}	3.29×10^{-5}	1.46×10^{-4}	6.04×10^{-4}

[a] 0.5 M $LiCF_3SO_3$ in PC utilized as the supporting electrolyte
[b] 0.5 M $TBACF_3SO_3$ in PC utilized as the supporting electrolyte

Table S4.2. Comparison of the oxidation/reduction peak potential (E_o/E_R), the peak separation (ΔE_p), half-wave potential ($E_{1/2}$), oxidation/reduction peak width (W_o/W_R), and oxidation/reduction peak area (A_o/A_R) for both peaks of the viologen analog, viologen-chloride polypeptide thin film and viologen-chloride polypeptide composite electrode at 10 mV·s^{-1} in a three-electrode beaker cell.

Reaction	**Parameter**	**Viologen Analog Solution**^{a}	**Viologen-chloride Polypeptide Thin Film**^{a}	**Viologen-chloride Polypeptide Thin Film**^{b}	**Viologen-chloride Polypeptide Composite Electrode**^{a}	**Viologen-chloride Polypeptide Composite Electrode**^{b}
$Viol^{+\bullet}/Viol^{2+}$	**E_O (V)**	2.51	2.64	2.77	2.99	2.86
	E_R (V)	2.46	2.42	2.61	2.17	2.52
	ΔE_p (V)	0.05	0.22	0.16	0.82	0.34
	$E_{1/2}$ (V)	2.49	2.53	2.69	2.58	2.69
	W_O (V)	0.17	0.62	0.61	0.56	0.47
	W_R (V)	0.15	0.44	0.44	0.62	0.46
	A_O (W)	1.31×10^{-6}	3.44×10^{-4}	4.87×10^{-5}	3.37×10^{-4}	2.81×10^{-4}
	A_R (W)	8.20×10^{-7}	3.47×10^{-4}	4.28×10^{-5}	2.50×10^{-4}	2.29×10^{-4}
$Viol^{0}/Viol^{+\bullet}$	**E_O (V)**	2.12	2.22	2.31	2.43	2.39
	E_R (V)	2.06	1.93	2.14	1.74	2.07
	ΔE_p (V)	0.06	0.29	0.17	0.69	0.32
	$E_{1/2}$ (V)	2.09	2.08	2.23	2.09	2.23

Table S4.2. Continued.

Reaction	Parameter	Viologen Analog Solution[a]	Viologen-chloride Polypeptide Thin Film[a]	Viologen-chloride Polypeptide Thin Film[b]	Viologen-chloride Polypeptide Composite Electrode[a]	Viologen-chloride Polypeptide Composite Electrode[b]
$\text{Viol}^0/\text{Viol}^{+\bullet}$	**W_O (V)**	0.15	0.54	0.47	0.64	0.59
	W_R (V)	0.18	0.57	0.75	0.41	0.60
	A_O (W)	8.57×10^{-7}	6.91×10^{-4}	5.15×10^{-5}	3.09×10^{-4}	6.27×10^{-4}
	A_R (W)	1.18×10^{-6}	5.67×10^{-4}	5.81×10^{-5}	4.04×10^{-5}	2.44×10^{-4}

[a] 0.5 M $LiCF_3SO_3$ in PC utilized as the supporting electrolyte

[b] 0.5 M $TBACF_3SO_3$ in PC utilized as the supporting electrolyte

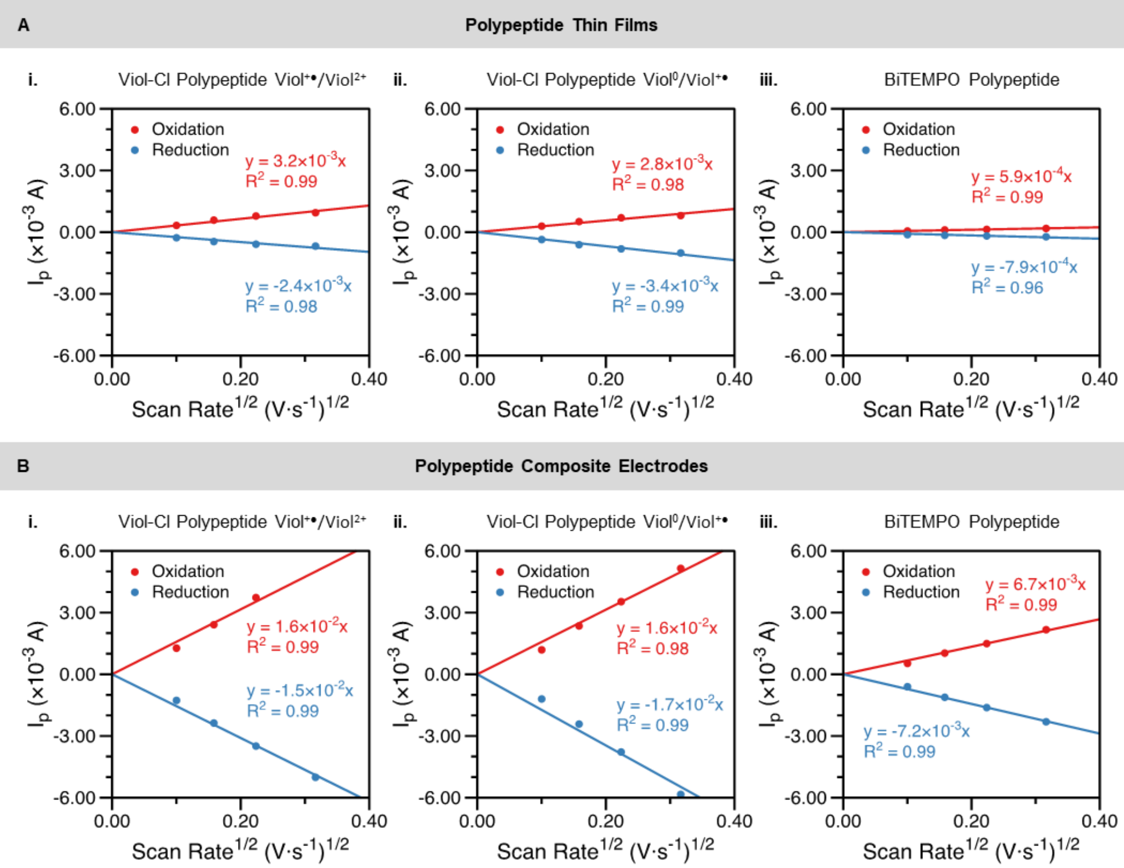

Figure S4.4. Peak current *vs.* square-root of scan rate from the cyclic voltammograms for (**A**) polypeptide thin film electrodes and (**B**) polypeptide composite electrodes of **i.** $Viol^{+•}/Viol^{2+}$ and **ii.** $Viol^{0}/Viol^{+•}$ for the viol-Cl polypeptide and **iii.** for the biTEMPO polypeptide. The viol-Cl polypeptide composite electrode did not exhibit a $Viol^{+•}/Viol^{2+}$ oxidation peak at 100 $mV·s^{-1}$.

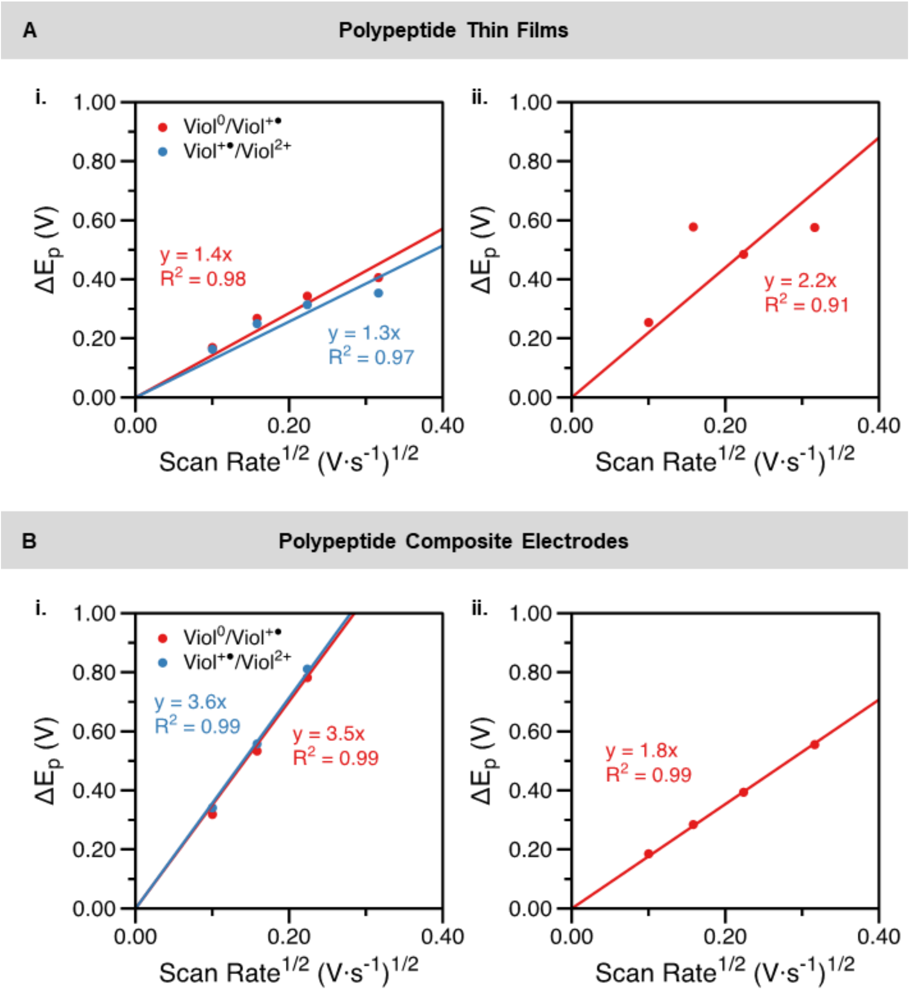

Figure S4.5. Peak separation *vs.* square-root of scan rate from the cyclic voltammograms for (**A**) polypeptide thin film electrodes and (**B**) polypeptide composite electrodes of **i.** the viologen-chloride polypeptide and **ii.** the biTEMPO polypeptide. The viol-Cl polypeptide composite electrode did not exhibit a Viol$^{+\bullet}$/Viol^{2+} oxidation peak at 100 mV·s^{-1}.

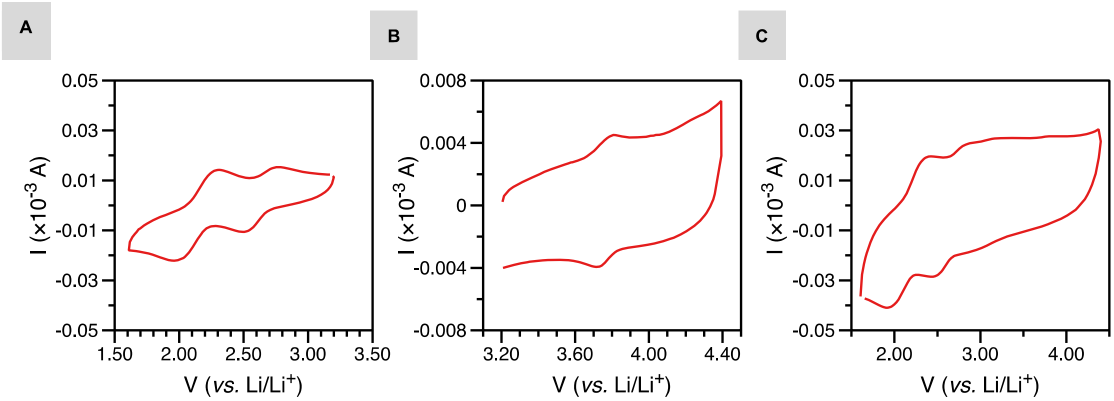

Figure S4.6. Solution state CV after testing (**A**) the viol-Cl polypeptide half sandwich cell (**B**) the BiTEMPO polypeptide half sandwich cell and (**C**) the full sandwich cell (with both composite electrodes). After half or full sandwich cell testing, the separator was soaked in 15 mL of 0.5 M $TBACF_3SO_3$ in PC after electrochemical testing and the resulting solution was used for solution state CV testing. The CV was conducted at 100 $mV \cdot s^{-1}$ in a three-electrode beaker cell with a glassy carbon working electrode and lithium metal counter and reference electrodes.

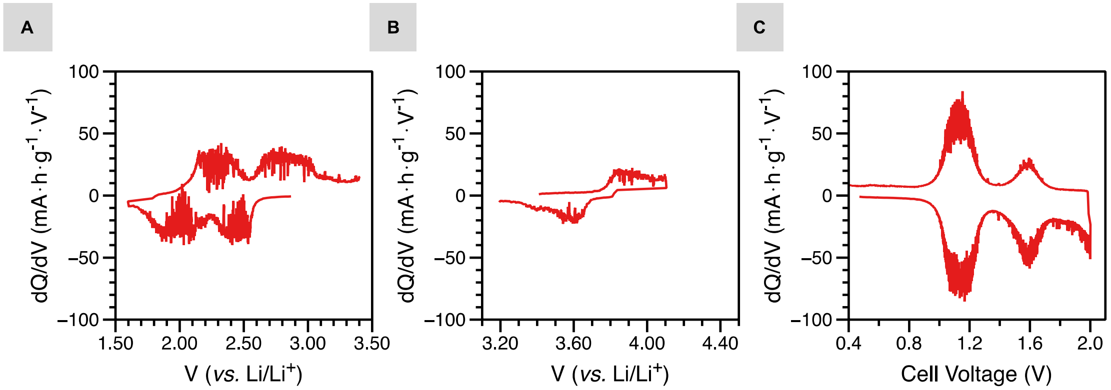

Figure S4.7. Differential capacity curves from galvanostatic cycling curves of (**A**) the viol-Cl polypeptide composite electrode half sandwich cell at 10 C, (**B**) the biTEMPO polypeptide composite electrode half sandwich cell at 10 C and (**C**) the filter paper sandwich cell at 1C. The composition of the composite electrode was 30 wt% active polypeptide with 60 wt% CB and 10 wt% PVDF) on ITO glass. An adjacent-averaging filter with a 5-point window was applied in OriginPro 2020 to remove noise in the data.

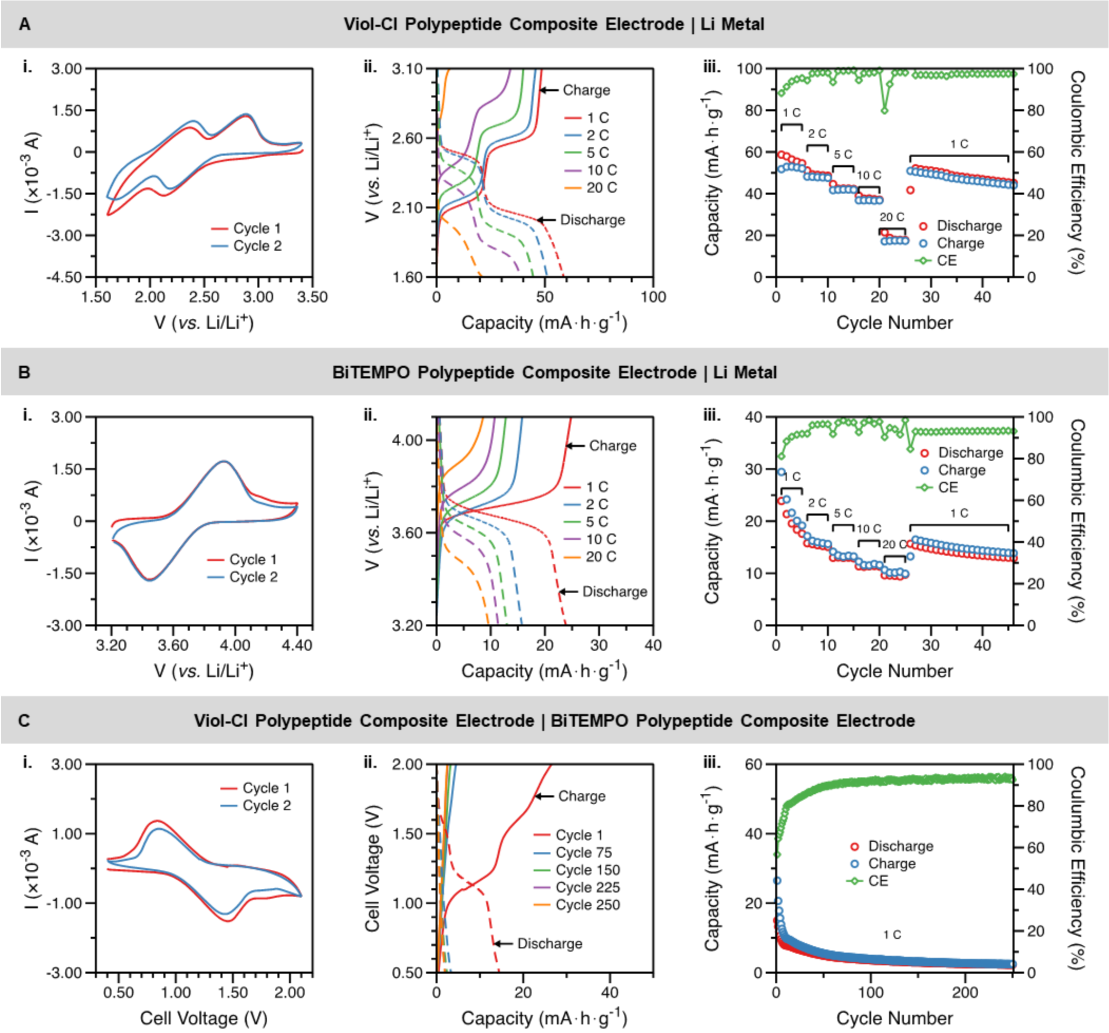

Figure S4.8. Electrochemical characterization of (**A**) the viol-Cl polypeptide composite half cell, (**B**) the biTEMPO polypeptide composite half cell and (**C**) the viol-Cl/biTEMPO polypeptide full cell, including their **i.** cyclic voltammograms, **ii.** charge-discharge curves and **iii.** cycling response. (**A**) and (**B**) utilized a polypeptide composite electrode | 0.5 M $LiCF_3SO_3$ in PC + filter paper | lithium metal configuration while (**C**) utilized a viol-Cl polypeptide composite electrode | 0.5 M $LiCF_3SO_3$ in PC + filter paper | biTEMPO polypeptide composite electrode configuration. The composite electrodes were composed of 30 wt% active polypeptide with 60 wt% CB and 10 wt% PVDF on ITO-coated glass. In **Aiii.** and **Biii.**, the C rates were varied, while in **Ciii.** the C-rate was constant at 1 C.

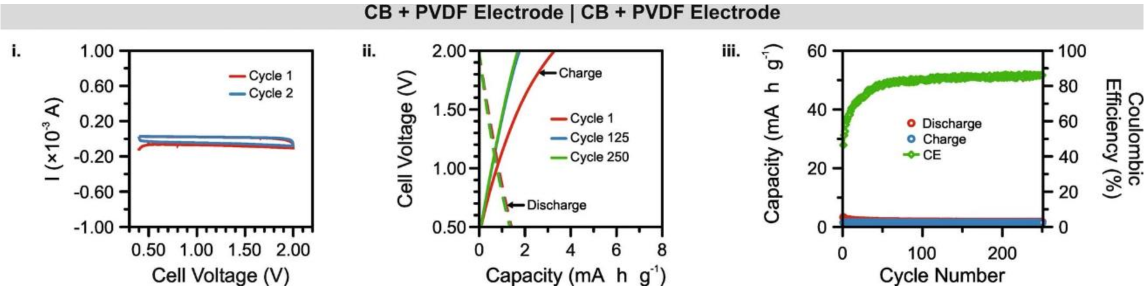

Figure S4.9. Electrochemical characterization of a PVDF + CB symmetric full cell is shown, including cyclic voltammograms (**i**), charge–discharge curves (**ii**) and cycling response at 1C (**iii**) (PVDF + CB composite electrode, 0.5 M TBACF$_3$SO$_3$ in PC and filter paper, PVDF + CB composite electrode). The composite electrodes were cast in an identical manner to the polypeptide composite electrodes, with a composition of 86 wt% CB and 14 wt% PVDF on ITO-coated glass substrates. After 250 cycles, the capacity was 1.7 mA h g^{-1}, whereas the capacity of the polypeptide-based full cell was 7.5 mA h g^{-1} (**Figure 4.4 g-i**).

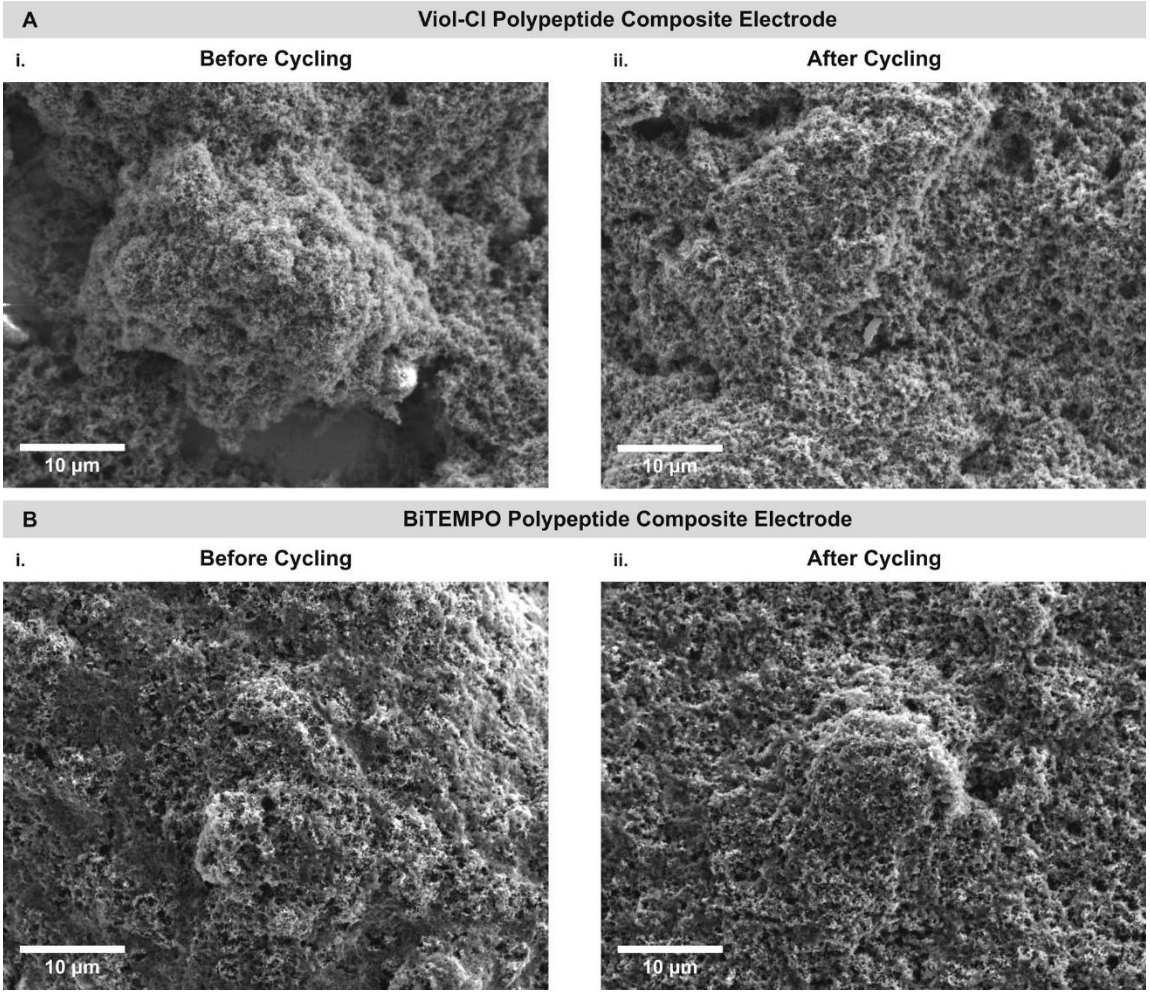

Figure S4.10. Scanning electron micrographs of the viol-Cl polypeptide composite electrode (**a**) and the biTEMPO polypeptide composite electrode (**b**), before (**i**) and after (**ii**) 50 charge–discharge cycles in the full sandwich cell configuration (viol-Cl polypeptide composite electrode, 0.5 M $TBACF_3SO_3$ in PC and filter paper, biTEMPO polypeptide composite electrode).

References

122. Nguyen, T. P., Easley, A. D., Kang, N., Khan, S., Lim, S.-M., Rezenom, Y. H., Wang, S., Tran, D. K., Fan, J., Letteri, R. A., He, X., Su, L., Yu, C.-H., Lutkenhaus, J. L. & Wooley, K. L. Polypeptide organic radical batteries. *Nature* **593**, 61-66 (2021).

Chapter 5: Electron Transport Kinetics for Viologen Containing Polypeptides with Varying Side Group Linker Spacing

Reproduce from ref [149].

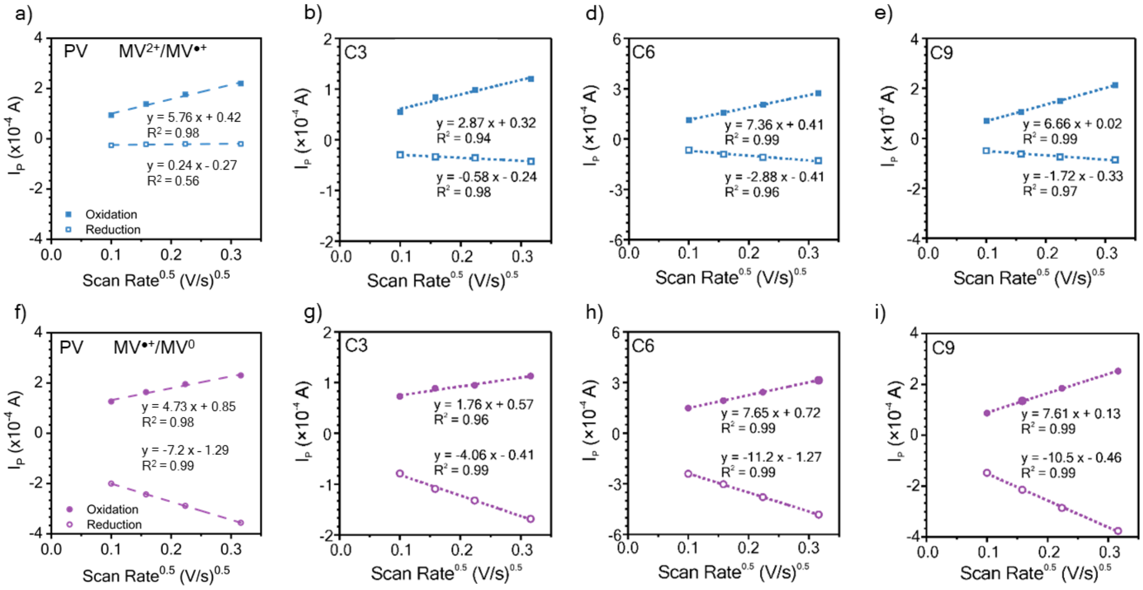

Figure S5.1. Peak current *vs.* square-root of scan rate from the cyclic voltammograms for PV (a,f), C3 (b,g), C6 (d,h), and C9 (e,i).

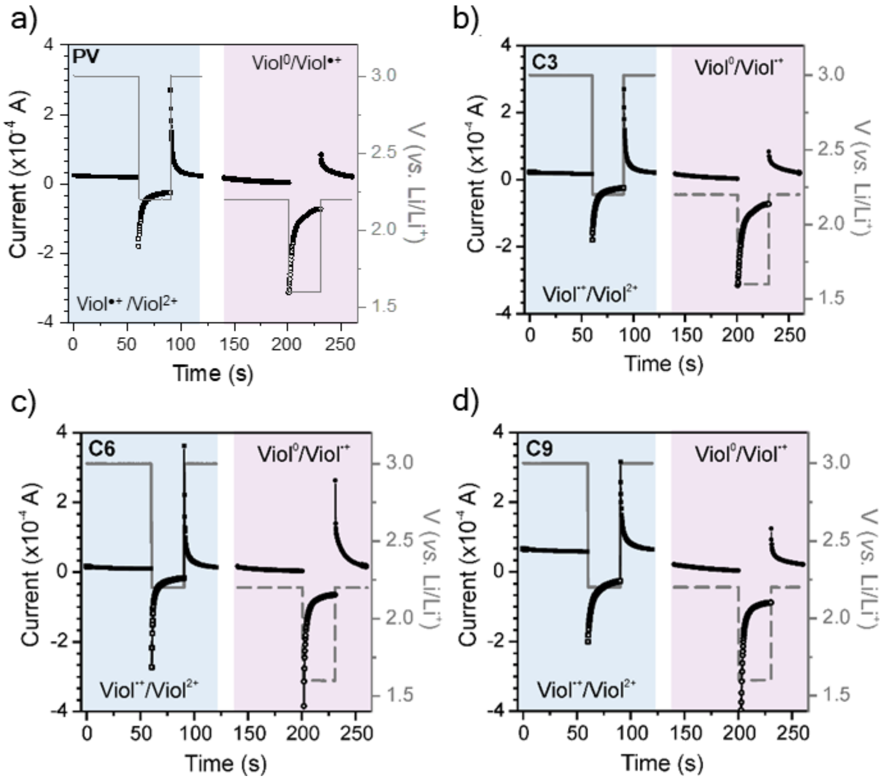

Figure S5.2. Chronoamperometry (CA) input and output data for a) PV, b) C3, c) C6, and d) C9.

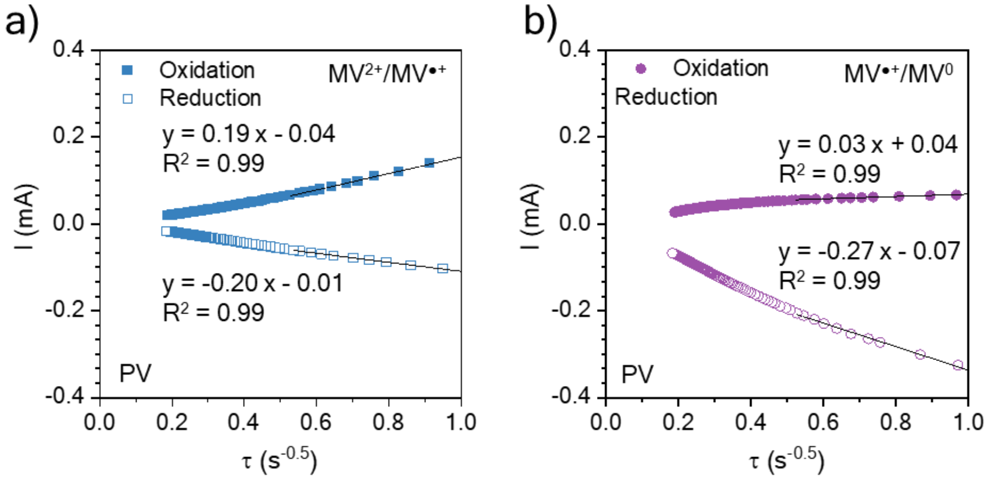

Figure S5.3. Chronoamperometry (CA) Cottrell plots for the two redox couples of the control viologen polymer (PV). (a) shows the CA output data for the MV^{2+}/ $MV^{\bullet+}$ redox couple. (b) shows the CA output data for the $MV^{\bullet+}/MV^0$ redox couple. Polymer coated on ITO glass was used as the working electrodes in a three-electrode beaker cell configuration. The supporting electrolyte was 0.5 M LiCl in γ-butyrolactone. Lithium metal was used as counter and reference electrodes

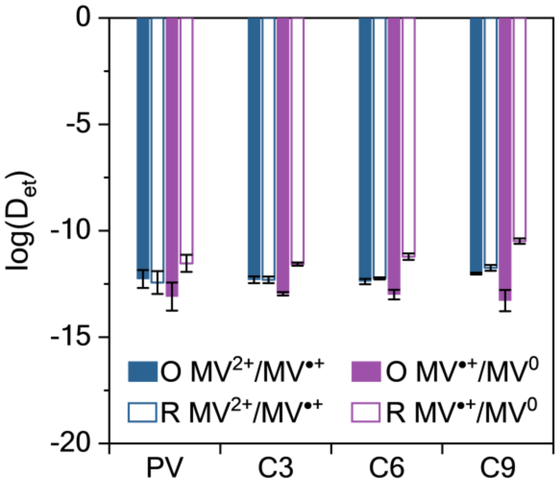

Figure S5.4. log(D_{et}) values for the considered polymers. The values are separated for the oxidation and reduction of both redox couples.

Diffusion coefficients of the viologen-based polymers. An important factor influencing the rate of electron transport in swollen RAPs is the physical diffusion of the pendant redox-active group. Dynamic light scattering (DLS) is one experimental option to measure the diffusion coefficient of a polymer chain, but it does not directly measure the diffusion of the redox-active pendant group, yet past literature assumes their equivalency.[20] Additionally, the diffusion coefficients of the redox-active methyl viologen groups (D_{phys}) were extracted from the trajectories of MD simulations of the oligomers in either swollen or solvated states, taking GBL as the solvent. **Table S5.1** shows the diffusion coefficients (D_{phys}) of the redox groups for the two different redox processes (MV^{2+}/ $MV^{\bullet+}$ and $MV^{\bullet+}/MV^{0}$) calculated using MD simulations. For comparison, the DLS-measured r_h of the polypeptides in the MV^{2+} form and **Equation 5.1** were used to experimentally estimate the diffusion coefficient of the polymer in solution (D_{DLS}).

Table S5.1. Experimentally determined D_{DLS} and MD calculated D_{phys} constant values ($\times 10^{-7}$ cm^2/s) for both redox couples.

	D_{DLS} and D_{phys}						
	MV^{2+}			**MV$^{\bullet+}$**		**MV^{0}**	
$\times 10^{-7}$ cm^2/s	**D_{DLS}**	**D_{phys} (swollen)**	**D_{phys} (solvated)**	**D_{phys} (swollen)**	**D_{phys} (solvated)**	**D_{phys} (swollen)**	**D_{phys} (solvated)**
PV	0.8 ± 0.10	N/A	N/A	N/A	N/A	N/A	N/A
C3	1.2 ± 0.25	5.2 ± 3.5	2.2 ± 0.91	0.7 ± 0.38	3.0 ± 0.86	5.2 ± 1.0	11.9 ± 3.1
C6	1.0 ± 0.12	0.1 ± 0.17	1.3 ± 0.64	0.6 ± 0.13	8.9 ± 3.0	8.1 ± 1.4	11.1 ± 2.7
C9	4.6 ± 0.74	4.4 ± 2.1	4.0 ± 1.8	2.1 ± 0.93	9.2 ± 3.3	7.7 ± 2.0	11.9 ± 3.5

Determination of k_{act} from Marcus-Hush Theory. In additional to the dynamics of the polymer backbone and redox active groups in pendant RAPs, the energy barrier to electron transfer between redox centers needs to be considered to properly estimate k_{act} and k^0. More explicitly, the electron transfer mechanism between methyl viologen groups is best represented by a consecutive reaction mechanism, such as between a donor (D) and an acceptor (A):

$$D + A \underset{-k_{diff}}{\overset{k_{diff}}{\rightleftharpoons}} DA \xrightarrow{k_{act}} D^{+} + A^{-}$$

Equation S5.1

where k_{diff} is the diffusion-limited rate constant and k_{act} is the activation-limited rate constant. k_{act} can be determined from Marcus-Hush theory following:

$$k_{act} = K_a\left[\left(-\frac{\pi}{\lambda k_b T}\right)^{1/2}\left(-\frac{H_{AB}^2}{\hbar}\right)exp\left(-\frac{\Delta G^{\ddagger}}{k_b T}\right)\right]$$

Equation S5.2

where K_a is the association constant (*ca*. 0.38 M^{-1} for viologen),[212] λ is the reorganization energy, k_b is the Boltzmann constant, T is temperature, H_{AB} is the electronic coupling, $\hbar$ is the reduced Planck constant, and $\Delta G^{\ddagger}$ is the activation energy for the transition state. For self-exchange electron transfer, $\Delta G^{\ddagger}$ can be further approximated by $(\lambda - 2H_{AB})^2/ 4\lambda$.[181] To calculate k_{act}, H_{AB} and λ were first determined by DFT methods. The calculations resulted in estimates of the λ between $MV^{2+}/ MV^{\bullet+}$ and $MV^{\bullet+}/MV^0$ of 1.65 and 1.31 eV, respectively.

Table S5.2. log (k_{ex}) (L/ mol s) values determined experimentally using CA and **Equation 5.4.**

	log (k_{ex})			
	$MV^{2+}/MV^{\bullet+}$		**$MV^{\bullet+}/ MV^0$**	
	CA Ox.	**CA Red.**	**CA Ox.**	**CA Red.**
PV	3.1 ± 0.42	3.3 ± 0.54	2.1 ± 0.66	4.1 ± 0.40
C3	2.9 ± 0.16	2.9 ± 0.16	2.3 ± 0.08	3.7 ± 0.07
C6	2.8 ± 0.13	3.0 ± 0.05	2.2 ± 0.22	4.0 ± 0.15
C9	3.2 ± 0.04	3.4 ± 0.14	1.9 ± 0.50	4.7 ± 0.12

Table S5.3. Experimentally determined log (k^0) (cm/s) values for both reduction and oxidation for both redox couples (using **Equation 5.5**).

	log (k^0)			
	$MV^{2+}/MV^{\bullet+}$		**$MV^{\bullet+}/MV^0$**	
	CV Ox.	**CV Red.**	**CV Ox.**	**CV Red.**
PV	-6.8 ± 0.21	-7.0 ± 0.27	-7.6 ± 0.33	-6.6± 0.20
C3	-7.1 ± 0.08	-7.1 ± 0.08	-7.4 ± 0.04	-6.7 ± 0.04
C6	-7.1 ± 0.06	-7.0 ± 0.03	-7.5 ± 0.14	-6.5 ± 0.04
C9	-7.0 ± 0.02	-6.8± 0.07	-7.6 ± 0.25	-6.2 ± 0.31

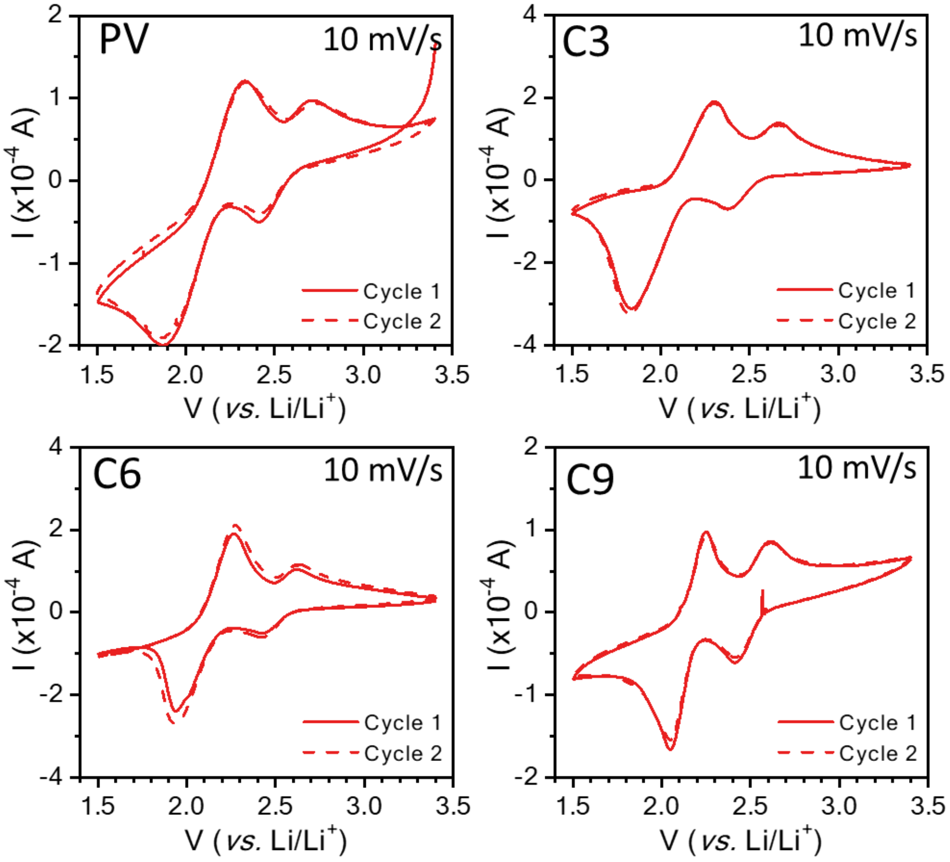

Figure S5.5. Cyclic voltammograms of a half-sandwich cell for a) PV, b) C3, c) C6, and d) C9. The working electrode was a thin film on ITO glass in a half cell with lithium metal. The separator was filter paper soaked in 0.5 M LiCl in GBL electrolyte.

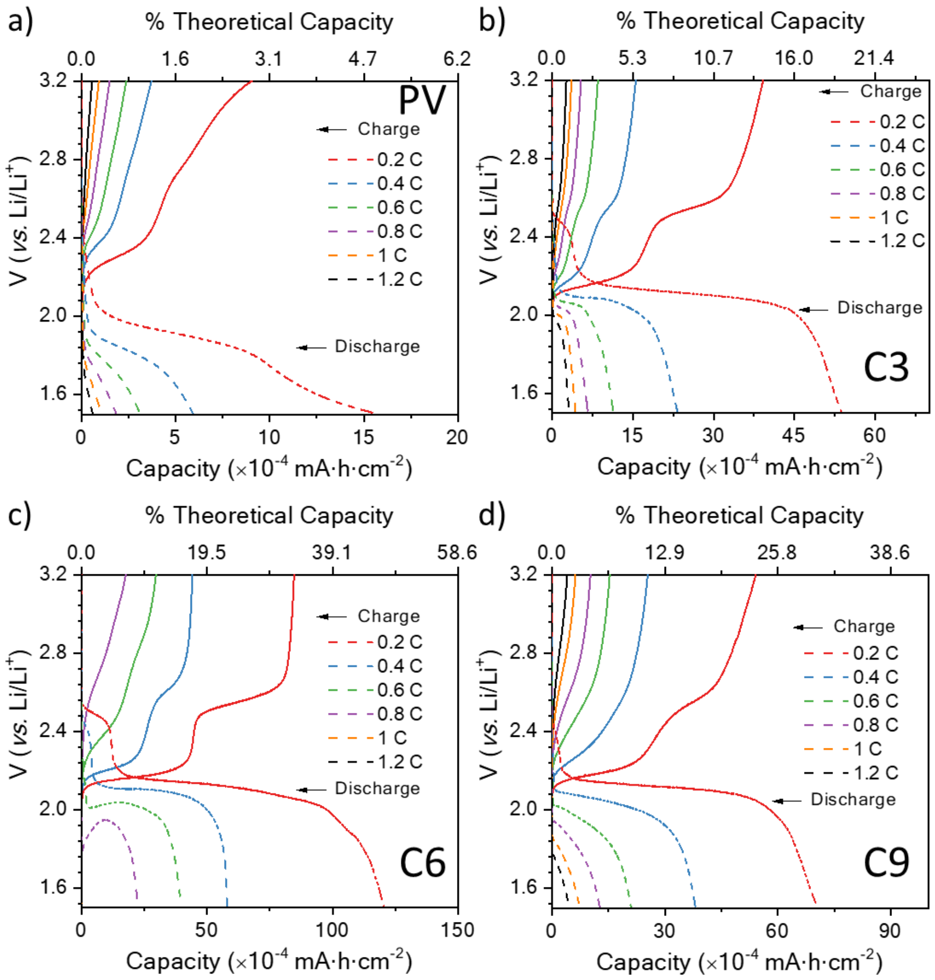

Figure S5.6. Galvanostatic charge-discharge curves for the a) PV, b) C3, c) C6, and d) C9 half cells against lithium metal. The working electrode was a polymer thin film on ITO-coated glass and 0.5 M LiCl in GBL on filter paper as the supporting electrolyte and separator, respectively.

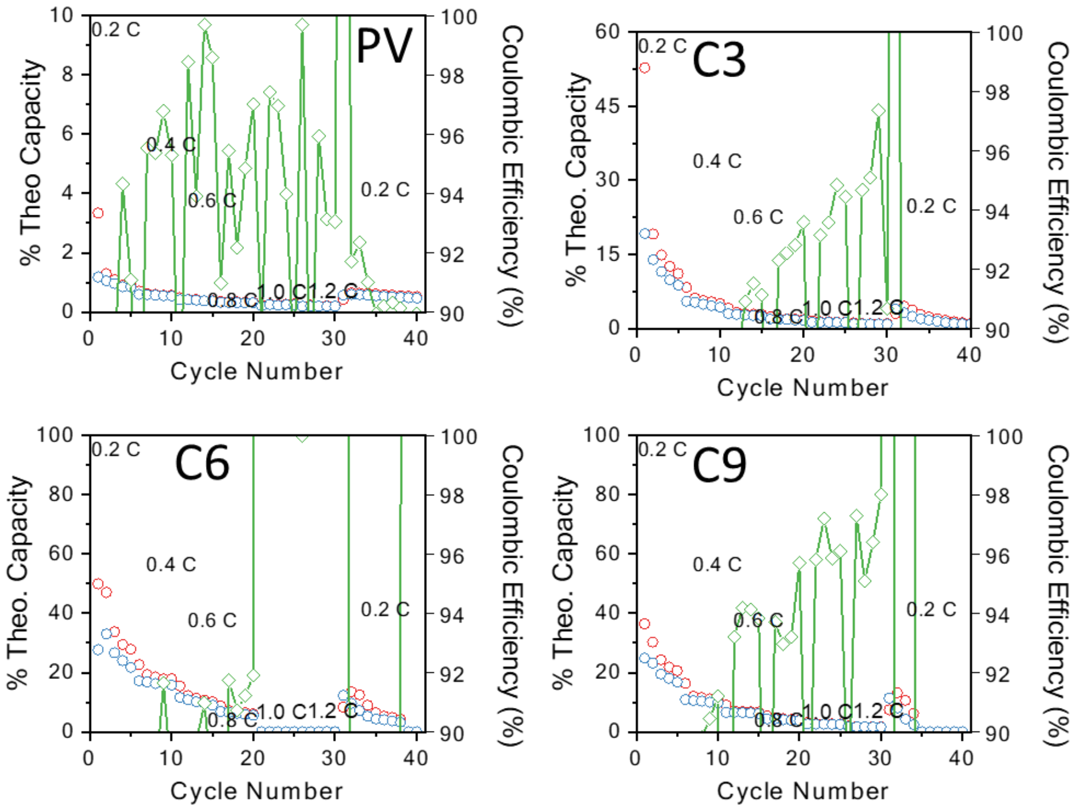

Figure S5.7. GCD Summary plots of a half-sandwich cell for a) PV, b) C3, c) C6, and d) C9. The working electrode was a thin film on ITO glass in a half cell with lithium metal. The separator was filter paper soaked in 0.5 M LiCl in GBL electrolyte.

References

20. Sato, K., Ichinoi, R., Mizukami, R., Serikawa, T., Sasaki, Y., Lutkenhaus, J., Nishide, H. & Oyaizu, K. Diffusion-Cooperative Model for Charge Transport by Redox-Active Nonconjugated Polymers. *Journal of the American Chemical Society* **140**, 1049-1056 (2018).

149. Easley, A. D., Li, C.-H., Li, S.-G., Nguyen, T., Echols, I., Wooley, K., Tabor, D. & Lutkenhaus, J. Electron Transport Kinetics for Viologen Containing Polypeptides with Varying Side Group Linker Spacing. (In preparation).

181. Ohsaka, T., Yamamoto, H. & Oyama, N. Thermodynamic parameters for charge-transfer reactions in pendant viologen polymers coated on graphite electrodes and at electrode/pendant viologen polymer film interfaces. *The Journal of Physical Chemistry* **91**, 3775-3779 (1987).

212. Neta, P., Richoux, M.-C. & Harriman, A. Intramolecular association of covalently linked viologen radicals. *Journal of the Chemical Society, Faraday Transactions 2: Molecular and Chemical Physics* **81**, 1427-1443 (1985).